UNIVERSITAT DE
BARCELONA

Development of $Cu_2ZnSnSe_4$ Based Thin Film Solar Cells by PVD and Chemical Based Processes

Markus Neuschitzer

ADVERTIMENT. La consulta d’aquesta tesi queda condicionada a l’acceptació de les següents condicions d'ús: La difusió d’aquesta tesi per mitjà del servei TDX (**www.tdx.cat**) i a través del Dipòsit Digital de la UB (**diposit.ub.edu**) ha estat autoritzada pels titulars dels drets de propietat intel·lectual únicament per a usos privats emmarcats en activitats d’investigació i docència. No s’autoritza la seva reproducció amb finalitats de lucre ni la seva difusió i posada a disposició des d’un lloc aliè al servei TDX ni al Dipòsit Digital de la UB. No s’autoritza la presentació del seu contingut en una finestra o marc aliè a TDX o al Dipòsit Digital de la UB (framing). Aquesta reserva de drets afecta tant al resum de presentació de la tesi com als seus continguts. En la utilització o cita de parts de la tesi és obligat indicar el nom de la persona autora.

ADVERTENCIA. La consulta de esta tesis queda condicionada a la aceptación de las siguientes condiciones de uso: La difusión de esta tesis por medio del servicio TDR (**www.tdx.cat**) y a través del Repositorio Digital de la UB (**diposit.ub.edu**) ha sido autorizada por los titulares de los derechos de propiedad intelectual únicamente para usos privados enmarcados en actividades de investigación y docencia. No se autoriza su reproducción con finalidades de lucro ni su difusión y puesta a disposición desde un sitio ajeno al servicio TDR o al Repositorio Digital de la UB. No se autoriza la presentación de su contenido en una ventana o marco ajeno a TDR o al Repositorio Digital de la UB (framing). Esta reserva de derechos afecta tanto al resumen de presentación de la tesis como a sus contenidos. En la utilización o cita de partes de la tesis es obligado indicar el nombre de la persona autora.

WARNING. On having consulted this thesis you’re accepting the following use conditions: Spreading this thesis by the TDX (**www.tdx.cat**) service and by the UB Digital Repository (**diposit.ub.edu**) has been authorized by the titular of the intellectual property rights only for private uses placed in investigation and teaching activities. Reproduction with lucrative aims is not authorized nor its spreading and availability from a site foreign to the TDX service or to the UB Digital Repository. Introducing its content in a window or frame foreign to the TDX service or to the UB Digital Repository is not authorized (framing). Those rights affect to the presentation summary of the thesis as well as to its contents. In the using or citation of parts of the thesis it’s obliged to indicate the name of the author.

UNIVERSITAT DE BARCELONA

IREC
Institut de Recerca en Energia de Catalunya
Catalonia Institute for Energy Research

Development of $Cu_2ZnSnSe_4$ Based Thin Film Solar Cells by PVD and Chemical Based Processes

Doctoral thesis presented by
Markus Neuschitzer

Thesis supervisors:
Dr. Edgardo Saucedo Silva
Prof. Dr. Alejandro Pérez Rodríguez

Thesis tutor: **Prof. Dr. Alejandro Pérez Rodríguez**

Thesis submitted in July 2016
Programa de Doctorat: Enginyeria i Tecnologies Avançades

Universitat de Barcelona
Facultat de Física, Department d'Electrònica

Für meine Mädels
Ari, Lola & Kala

CONTENTS

LIST OF TABLES

List of Figures

LIST OF ABBREVIATIONS AND ACRONYMS

AZO – aluminium doped zinc oxide
CBD – chemical bath deposition
CIGS – $Cu(In,Ga)Se_2$
COP – Conference of the Parties
CZTS – Cu_2ZnSnS_4
CZTSe – $Cu_2ZnSnSe_4$
CZTSSe – $Cu_2ZnSn(S_{1-x}Se_x)_4$
EPBT – energy payback time
EQE – external quantum efficiency
EROI – energy return on energy investment
FF – fill factor
ITO – indium doped tin oxide
IPCC – Intergovernmental Panel on Climate Change
IEA – international energy agency
Jsc – short circuit current density
JV – current density voltage
PL – photoluminescence
PV – photovoltaic
SEM – scanning electron microscope
SLG – soda lime glass
TCO – transparent conductive oxide
TEM – transmission electron microscopy
Voc – open circuit voltage
XPS – X-ray photoelectron spectroscopy
XRD – X-ray diffraction
XRF – X-ray fluorescence

LIST OF APPENDICES

PREFACE: *PUBLICATIONS AND SUMMARY OF THE THESIS*

The work presented in this thesis was carried out at the Catalonian Institute for Energy Research (IREC) in the frame of the Marie Curie Initial Training Network KESTCELLS (FP7-PEOPLE-2012-ITN-316488). The main goal of this thesis was to develop and optimize heterostructure solar cells based on kesterite ($Cu_2ZnSnSe_4$) absorbers, a semiconducting compound consisting of earth abundant materials, by cost effective physical vapour deposition (PVD) and chemical based processes.
The thesis is structured around several articles published in high impact peer review journals. According to the requirements to obtain a Doctor of Philosophy in Engineering and Applied Sciences at the University of Barcelona this thesis is based on following four articles:

Neuschitzer, M.; Sanchez, Y.; Olar, T.; Thersleff, T.; Lopez-Marino, S.; Oliva, F.; Espindola-Rodriguez, M.; Xie, H.; Placidi, M.; Izquierdo-Roca, V.; Lauermann, I.; Leifer, K.; Pérez-Rodriguez, A.; Saucedo, E. "Complex Surface Chemistry of Kesterites: Cu/Zn Reordering after Low Temperature Postdeposition Annealing and Its Role in High Performance Devices", *Chemistry of Materials,* 2015, 27 (15), 5279–5287. **(Impact factor = 9.407)**

Neuschitzer, M.; Sanchez, Y.; López-Marino, S.; Xie, H.; Fairbrother, A.; Placidi, M.; Haass, S.; Izquierdo-Roca, V.; Perez-Rodriguez, A.; Saucedo, E. "Optimization of CdS Buffer Layer for High-Performance $Cu_2ZnSnSe_4$ Solar Cells and the Effects of Light Soaking: Elimination of Crossover and Red Kink", *Progress in Photovoltaics: Research and Application*, 2015, 23 (11), 1660–1667. **(Impact factor = 7.365)**

Neuschitzer, M.; Lienau, K.; Guc, M.; Barrio, L. C.; Haass, S.; Prieto, J. M.; Sanchez, Y.; Espindola-Rodriguez, M.; Romanyuk, Y.; Perez-Rodriguez, A.; Izquierdo-Roca, V.; Saucedo, E. "Towards High Performance Cd-Free CZTSe Solar Cells with a ZnS(O,OH) Buffer Layer: The Influence of Thiourea Concentration on Chemical Bath Deposition", *Journal of Physics D: Applied Physics*, 2016, 49 (12), 125602. **(Impact factor = 2.772)**

Neuschitzer, M.; Marquez, J.; Giraldo, S.; Dimitrievska, M.; Placidi, M.; Forbes, I.; Izquierdo-Roca, V.; Pérez-Rodriguez, A.; Saucedo, E. "V_{oc} Boosting and Grain Growth Enhancing Ge-Doping Strategy for $Cu_2ZnSnSe_4$ Photovoltaic Absorbers", *Journal of Physical Chemistry C*, 2016, 120 (18), 9661-9670. **(Impact factor = 4.509)**

The first chapter of this thesis gives an overview over the current status of photovoltaic (PV) technology and points out the need for a decarbonisation of the energy sector where PV plays a major role. The different technologies available on the market are introduced. Mono- and multicrystalline silicon have the highest market share of all PV technologies but thin film solar cells based on CdTe or Cu(In,Ga)Se_2 (CIGS) absorbers recently show promising high power conversion efficiency values and due to their short energy payback time, minimal use of high purity material and low cost, they attract more and more attention. However, one concern of thin film PV based on CdTe or CIGS is the use of scare elements like tellurium or indium and gallium which could become a bottleneck if the technology wants to scale up to the terawatt level. Therefore, there is a high interest to replace these scare elements by more abundant ones and find suitable earth abundant photovoltaic absorbers. $Cu_2ZnSnSe_4$ (CZTSe) or Cu_2ZnSnS_4 (CZTS) and its sulphur-selenide solid solution are promising candidates to replace CIGS as absorber material due to its composition of more earth abundant elements. However, there is still a large gap between power conversion efficiencies of solar cells based on this absorber material and more established thin film solar cells, thus intensive research is still necessary to close this gap.

In literature CZTSe and CZTS are referred to as kesterite due to its crystal structure. Details regarding crystalline and materials properties as well as a short overview of the history of kesterites are given in Chapter 2. The kesterite crystal structure is flexible towards compositional variation from stoichiometry, and highest device performance is obtained for absorbers with Cu-poor and Zn-rich composition. The reason for this can be found in the intrinsic defect structure of the material. Furthermore, a Cu/Zn disorder was found in CuZn planes of the kesterite structure which can be modified by low temperature annealings around 200ºC. Additionally, insights into the growth of kesterite as well as deep defects mostly related to Sn antisites are given in this Chapter and the aim of this thesis is presented.

In Chapter 3 the peculiarities of kesterite based heterostructure solar cells are introduced. Different to Si solar cells, where in most cases a homojunction is created by doping, kesterite based solar cells use a p-type absorber n-type buffer/window heterostructure to form a pn-junction for the separation of light generated electron hole pairs. The role of the buffer layer is to provide a favourable band alignment with the kesterite absorber layer, where a small spike like alignment is ideal. This means that the conduction band minimum of the buffer is slightly higher than the one of the absorber, whereas the valence band maximum is lower. CdS deposited by chemical bath deposition (CBD) is widely used as buffer layer in kesterite solar cells due to its favourable band alignment. An overview of all other functional layers used in kesterite based heterostructures like molybdenum back contact and transparent conducting window layer is presented as well. Furthermore, the theory necessary for opto-electronic characterization of thin film solar cells by illuminated and dark current voltage measurements as well as external quantum efficiency and capacitive measurements is discussed. Finally, the status of kesterite based solar cells as well as current efficiency limiting bottlenecks are presented.

Chapter 4 is focused on the optimization of the front interface of CZTSe solar cells and is based on three different publications. First a study entitled "Complex Surface Chemistry of Kesterites: Cu/Zn Reordering after Low Temperature Postdeposition Annealing and Its Role in High Performance Devices" is presented. In this study the influence of the surface chemistry on device performance is investigated. After a chemical etching to remove unwanted ZnSe secondary phases formed during CZTSe absorber synthesis a low temperature post deposition annealing at 200ºC of the full solar cell is necessary to improve device efficiencies from below 3% to over 8%. X-ray photoelectron spectroscopy (XPS) surface analysis showed that this post deposition annealing promotes the diffusion of Zn towards the surface and Cu towards the bulk resulting in a Zn enriched and Cu depleted surface region. Furthermore, transmission electron microscopy (TEM)

investigations evidenced a change in grain boundary composition, which tend to be Cu rich prior the post deposition annealing. Additionally TEM showed a significant Cu diffusion into the CdS buffer layer which further enhances the Cu depletion of the absorber surface. Improved device performance can be explained by an increased formation of beneficial [V_{Cu}+Zn_{Cu}] defect cluster due to Cu depletion and Zn enrichment of the surface near region that was also confirmed by Raman measurements. Additionally improvements in the CdS and a change of grain boundary towards a more benign composition contribute to increased performance. Furthermore, different other chemical and physical surface treatments presented in this work confirm the necessity of a Cu depleted and Zn enriched surface composition for high performance kesterite based solar cells.
As second part of the front interface optimization a study entitled "Optimization of CdS Buffer Layer for High-Performance $Cu_2ZnSnSe_4$ Solar Cells and the Effects of Light Soaking: Elimination of Crossover and Red Kink" is presented. The spike like conduction band alignment of CdS buffer layer and CZTSe absorber is one of the key factors for high device performance. However, it can also be the origin of fill factor and current-reducing distortions in current–voltage curves, such as light/dark curve crossover, or an s-like curve shape for long wavelength monochromatic illumination (red kink) if light-dependent defect states are present in the buffer layer. An optimization of the CdS buffer layer growth by chemical bath deposition using different cadmium salts resulted in a great improvement of this crossover (which was eliminated entirely after light soaking) and furthermore increased fill factor and device efficiency. As cause of the JV curve distortion light-sensitive compensating acceptor defects, most likely cadmium vacancies could be identified. Any JV curve distortions could be drastically reduced by implementing a slow and controlled CdS growth process with cadmium nitrate, as opposed to the more commonly used cadmium sulphate as cadmium source employed during chemical bath deposition. Furthermore, the effects of light soaking are discussed in this work.
As third part of Chapter 4 a study entitled "Towards High Performance Cd-Free CZTSe Solar Cells with a ZnS(O,OH) Buffer Layer: The Influence of Thiourea Concentration on Chemical Bath Deposition" is presented. Since CdS used as buffer layer in high performance kesterite devices is highly toxic and has a bandgap of 2.4 eV which causes losses due to absorption of short wavelength photons there is a high interest to replace it by less toxic and more transparent alternatives. ZnS(O,OH) is one of the most promising candidates, since it is non-toxic, has a higher band gap, and its band alignment with the kesterite absorber layer can be tuned by the S/O ratio. High sulphur content ZnS(O,OH) buffer leads to an unfavourable high spike like buffer/absorber conduction band alignment which led to JV curve distortion and low efficiencies. By adjusting the thiourea concentration, i.e. sulphur source, during the CBD process of ZnS(O,OH) layers this distortion could be eliminated and devices with similar efficiencies compared to CdS reference cells were obtained.

Chapter 5 the beneficial effects on device performance of Ge doping of CZTSe absorbers is investigated. The first part is based on a study entitled "V_{oc} Boosting and Grain Growth Enhancing Ge-Doping Strategy for $Cu_2ZnSnSe_4$ Photovoltaic Absorbers". One of the main challenges of kesterite based solar cells is the low open circuit voltage (V_{oc}) compared to more mature thin film technologies. The presence of deep defects is proposed to be partly responsible for the lack in V_{oc}. Most intrinsic deep defects are related to Sn antisites which could form during synthesis due to the multi-charge states of Sn or the volatility of Sn-chalcogenide intermediate species. Germanium (Ge) is form the same main group as tin and can substitute it in the kesterite structure. By adding a low amount of Ge during the crystallization of nanocrystalline precursor the device performance and especially the V_{oc} could largely be improved, while keeping the Ge/(Ge+Sn) ratio below 2% to still ensure maximum abundancy of all elements used. Interestingly the addition of larger Ge amounts during crystallization result in largely increased grain growth. Despite the largely increased grain size and bandgap widening due to Ge incorporation device performance and V_{oc} could not be further improved compared to the lower Ge doped devices. Defect characterization by admittance spectroscopy showed the presence of a deep defect for the highest Ge content. This deep midgap defect may be assigned to Sn_{Cu} or Ge_{Cu} antisite donor defects, formed under Cu poor and group IV element-rich growth condition and is likely to act as an electron-hole recombination centre, which could explaining the deterioration of the solar cell performance.

In the second part of chapter 5 a more in depth opto-electrical and defect characterization of optimal and high Ge doped as well as non-doped reference CZTSe solar cells is presented. Furthermore, the interaction of Ge and sodium (Na), a well-known dopant for chalcogenide based solar cells is demonstrated. The Ge added during crystallization seems to moderate the Na content of the absorber layer and the supply of excessive Na for absorbers synthesized under high Ge addition could recover device performance. Defect spectroscopy revealed that the formation of the deep defect normally observed for these high Ge and Na doped absorbers could be reduced, which could be explained by the fact that Na favourably occupies copper vacancies (V_{Cu},) thus prevents the formation of Sn_{Cu} or Ge_{Cu} antisites. A careful control of group IV elemental composition seems mandatory to obtain high performance kesterite devices. The tuning of the group IV element composition during crystallization of nanocrystalline precursors by Ge-doping as well as additional Na supply has shown to be an efficient way to avoid the formation of this deep defect, and enabled to significantly increase V_{oc} and reduce the V_{oc} - deficit.

Finally in the last Chapter a conclusion of the work and a further outlook for kesterite technology is given.

Additionally following publications which are co-authored by Markus Neuschitzer contributed in the preparation of the thesis but are not included in the text:

(1) Placidi, M.; Espindola-Rodriguez, M.; Lopez-Marino, S.; Sanchez, Y.; Giraldo, S.; Acebo, L.; **Neuschitzer, M.**; Alcobé, X.; Pérez-Rodríguez, A.; Saucedo, E. “Effect of Rapid Thermal Annealing on the Mo Back Contact Properties for $Cu_2ZnSnSe_4$ Solar Cells”, *J. Alloys Compd.* 2016, *675*, 158–162.

(2) Lopez-Marino, S.; Espíndola-Rodríguez, M.; Sánchez, Y.; Alcobé, X.; Oliva, F.; Xie, H.; **Neuschitzer, M.**; Giraldo, S.; Placidi, M.; Caballero, R.; Izquierdo-Roca, V.; Pérez-Rodríguez, A.; Saucedo, E. “The Importance of Back Contact Modification in $Cu_2ZnSnSe_4$ Solar Cells: The Role of a Thin MoO_2 Layer”. *Nano Energy* 2016, DOI:10.1016/j.nanoen.2016.06.034 .

(3) Espindola-Rodriguez, M.; Sanchez, Y.; López-Marino, S.; Sylla, D.; Placidi, M.; **Neuschitzer, M.**; Xie, H.; Izquierdo-Roca, V.; Vigil-Galán, O.; Saucedo, E. “Selenization of Cu_2ZnSnS_4 Thin Films Obtained by Pneumatic Spray Pyrolysis”. *J. Anal. Appl. Pyrolysis* 2016, doi:10.1016/j.jaap.2016.04.008.

(4) Giraldo, S.; **Neuschitzer, M.**; Placidi, M.; Pistor, P.; Perez-Rodrıguez, A.; Saucedo, E. “$Cu_2ZnSnSe_4$-Based Solar Cells With Efficiency Exceeding 10% by Adding a Superficial Ge Nanolayer: The Interaction Between Ge and Na”. *IEEE Journal of Photovoltaics* 2016, *6* (3), 754–759.

(5) Xie, H.; Lopez-Marino, S.; Olar, T.; Sánchez González, Y.; **Neuschitzer, M.**; Oliva, F.; Giraldo, S.; Izquierdo-Roca, V.; Lauermann, I.; Pérez-Rodríguez, A.; Saucedo, E. “On the Impact of Na Dynamics at the $Cu_2ZnSn(S,Se)_4$/CdS Interface During Post Low Temperature Treatment of Absorbers”. *ACS Appl. Mater. Interfaces* **2016**, *8* (7), 5017–5024.

(6) Márquez, J.; **Neuschitzer, M.**; Dimitrievska, M.; Gunder, R.; Haass, S.; Werner, M.; Romanyuk, Y. E.; Schorr, S.; Pearsall, N. M.; Forbes, I. “Systematic Compositional Changes and Their Influence on Lattice and Optoelectronic Properties of $Cu_2ZnSnSe_4$ Kesterite Solar Cells”. *Sol. Energy Mater. Sol. Cells* 2016, *144*, 579–585.

(7) Kask, E.; Krustok, J.; Giraldo, S.; **Neuschitzer, M.**; López-Marino, S.; Saucedo, E. “Temperature Dependent Electrical Characterization of Thin Film $Cu_2ZnSnSe_4$ Solar Cells”. *J. Phys. D: Appl. Phys.* 2016, *49* (8), 85101.

(8) Sánchez, Y.; Espíndola-Rodríguez, M.; Xie, H.; López-Marino, S.; **Neuschitzer, M.**; Giraldo, S.; Dimitrievska, M.; Placidi, M.; Izquierdo-Roca, V.; Pulgarín-Agudelo, F. A.; Vigil-Galán, O.; Saucedo, E. “Ultra-Thin CdS for Highly Performing Chalcogenides Thin Film Based Solar Cells”. *Sol. Energy Mater. Sol. Cells* 2016.

(9) Guc, M.; **Neuschitzer, M.**; Hariskos, D.; Bauer, A.; Witte, W.; Hempel, W.; Calvo-Barrio, L.; Pistor, P.; Perez-Rodriguez, A.; Izquierdo-Roca, V. “Raman Scattering Quantitative Assessment of the Anion Composition Ratio in Zn(O,S) Layers for Cd-Free Chalcogenide-Based Solar Cells”. *RSC Adv* 2016, *6* (29), 24536–24542.

(10) López-Marino, S.; Sánchez, Y.; Espíndola-Rodríguez, M.; Alcobé, X.; Xie, H.; **Neuschitzer, M.**; Becerril, I.; Giraldo, S.; Dimitrievska, M.; Placidi, M.; Fourdrinier, L.; Izquierdo-Roca, V.; Pérez-Rodríguez, A.; Saucedo, E. “Alkali Doping Strategies for Flexible and Light-Weight $Cu_2ZnSnSe_4$ Solar Cells”. *J Mater Chem A* 2016, *4* (5), 1895–1907.

(11) Insignares-Cuello, C.; Oliva, F.; **Neuschitzer, M.**; X. Fontané; Broussillou, C.; Goislard de Monsabert, T.; Saucedo, E.; Ruiz, C. M.; Pérez-Rodríguez, A.; Izquierdo-Roca, V. “Advanced Characterization of Electrodeposition-Based High Efficiency Solar Cells: Non-Destructive Raman Scattering Quantitative Assessment of the Anion Chemical Composition in Cu(In,Ga)(S,Se)2 Absorbers”. *Sol. Energy Mater. Sol. Cells* 2015, *143*, 212–217.

(12) Krustok, J.; Raadik, T.; Grossberg, M.; Giraldo, S.; **Neuschitzer, M**.; López-Marino, S.; Saucedo, E. “Temperature Dependent Electroreflectance Study of $Cu_2ZnSnSe_4$ Solar Cells”. *Mater. Sci. Semicond. Process.* 2015, *39*, 251–254.

(13) Giraldo, S.; **Neuschitzer, M.**; Thersleff, T.; López-Marino, S.; Sánchez, Y.; Xie, H.; Colina, M.; Placidi, M.; Pistor, P.; Izquierdo-Roca, V.; Leifer, K.; Pérez-Rodríguez, A.; Saucedo, E. “Large Efficiency Improvement in $Cu_2ZnSnSe_4$ Solar Cells by Introducing a Superficial Ge Nanolayer”. *Adv. Energy Mater.* 2015, *5* (21), 1501070.

(14) Placidi, M.; Dimitrievska, M.; Izquierdo-Roca, V.; Fontané, X.; Castellanos-Gomez, A.; Pérez-Tomás, A.; Mestres, N.; Espindola-Rodriguez, M.; López-Marino, S.; **Neuschitzer, M.**; Bermudez, V.; Yaremko, A.; Pérez-Rodríguez, A. “Multiwavelength Excitation Raman Scattering Analysis of Bulk and Two-Dimensional MoS_2 : Vibrational Properties of Atomically Thin MoS_2 Layers”. *2D Mater.* 2015, *2* (3), 35006.

(15) Lugo, S.; Sánchez, Y.; **Neuschitzer, M.**; Xie, H.; Insignares-Cuello, C.; Izquierdo-Roca, V.; Peña, Y.; Saucedo, E. “Chemical Bath Deposition Route for the Synthesis of Ultra-Thin $CuIn(S,Se)_2$ Based Solar Cells”. *Thin Solid Films* 2015, *582*, 74–78.

(16) Fairbrother, A.; **Neuschitzer, M.**; Saucedo, E.; Pérez-Rodríguez, A. ”Zn-Poor $Cu_2ZnSnSe_4$ Thin Films and Solar Cell Devices”. *Phys. Status Solidi A* 2015, *212* (1), 109–115.

(17) López-Marino, S.; **Neuschitzer, M.**; Sánchez, Y.; Fairbrother, A.; Espindola-Rodriguez, M.; López-García, J.; Placidi, M.; Calvo-Barrio, L.; Pérez-Rodríguez, A.; Saucedo, E. “Earth-Abundant Absorber Based Solar Cells onto Low Weight Stainless Steel Substrate”. *Sol. Energy Mater. Sol. Cells* 2014, *130*, 347–353.

(18) Xie, H.; Sánchez, Y.; López-Marino, S.; Espíndola-Rodríguez, M.; **Neuschitzer, M.**; Sylla, D.; Fairbrother, A.; Izquierdo-Roca, V.; Pérez-Rodríguez, A.; Saucedo, E. “Impact of Sn(S,Se) Secondary Phases in $Cu_2ZnSn(S,Se)_4$ Solar Cells: A Chemical Route for Their Selective Removal and Absorber Surface Passivation”. *ACS Appl. Mater. Interfaces* 2014, *6* (15), 12744–12751

Contribution of the author to publications in the thesis

The author of this work, Markus Neuschitzer, has been responsible for the design and coordination of experimental studies carried out in this thesis as well as for the interpretation of the experimental results obtained. He has prepared all kesterite absorber layers presented in this work and finished those to solar cells as well as he performed all opto-electrical characterizations. Additionally, most material characterization was carried out by him and he was intensively involved in the coordination of more advanced characterization by specific techniques performed at partner institutes.

(1) **Neuschitzer et al.**, "Complex Surface Chemistry of Kesterites: Cu/Zn Reordering after Low Temperature Postdeposition Annealing and Its Role in High Performance Devices", ***Chemistry of Materials***, 2015, 27 (15), 5279–5287.

Impact factor (2015 JCR Science Edition) = 9.407
1st quartile in categories: CHEMISTRY, PHYSICAL; MATERIALS SCIENCE, MULTIDISCIPLINARY;

This work gives important insights in the influence of the surface chemistry of kesterite absorbers on solar cell device performance. A low temperature post deposition annealing after a specific surface etching is presented which increases solar cell efficiencies from below 3% to above 8%. Besides detailed solar cell device characterization advanced techniques like transmission electron microscopy and X-ray photoelectron spectroscopy carried out in an international cooperation with research groups from Germany and Sweden are used to reveal the origins of this beneficial low temperature annealing. It was found that the post deposition annealing induces a Cu/Zn reordering of the kesterite absorber surface which results in a Cu depletion and Zn enrichment of absorber surface. Furthermore, changes in grain boundary composition as well as Cu diffusion towards the CdS layer are evidenced. Getting insights in the complex surface chemistry of CZTSe absorbers and its strong influences on solar cells performance opens up new ways to further optimize kesterite based solar cells by developing processing routes for a better and easier control of the surface composition. Markus Neuschitzer fabricated all absorber layers used in this study and was involved in finishing all solar cells. He carried out different surface treatments and postdeposition annealings and was responsible for solar cell characterization as well as the interpretation of the data. Furthermore, he was coordinating sample exchange with international research partner institutes and was writing the manuscript as well as handling the submission process.

(2) **Neuschitzer et al.**, "Optimization of CdS Buffer Layer for High-Performance $Cu_2ZnSnSe_4$ Solar Cells and the Effects of Light Soaking: Elimination of Crossover and Red Kink", ***Progress in Photovoltaics: Research and Application***, 2015, 23 (11), 1660–1667.

Impact factor (2015 JCR Science Edition) = 7.365
1st quartile in categories: ENERGY & FUELS; MATERIALS SCIENCE, MULTIDISCIPLINARY; PHYSICS, APPLIED;

This paper is highlighted in the Progress in Photovoltaics Journal web page as one of the most accessed papers during 2015.

In this work the optimization of CdS buffer layer is presented. In depth solar cell characterization found efficiency limiting problems related to the CdS buffer layer when a standard chemical bath deposition process is used. By changing the growth conditions of the CdS these interface problems could be eliminated. Markus Neuschitzer synthesized all absorber layers used in the study and was involved in buffer layer deposition and finishing of the solar cells. All solar cell device characterization and data interpretation was carried out by him and he performed temperature dependent JV characterizations during an experimental stay at EMPA in Switzerland. Furthermore, he was in charge of writing the manuscript.

(3) Neuschitzer et al., "Towards High Performance Cd-Free CZTSe Solar Cells with a ZnS(O,OH) Buffer Layer: The Influence of Thiourea Concentration on Chemical Bath Deposition", ***Journal of Physics D: Applied Physics***, 2016, 49 (12), 125602.

Impact factor (2015 JCR Science Edition) = 2.772
1st quartile in categories: PHYSICS, APPLIED;

This work was carried out as international cooperation between IREC and EMPA in Switzerland. An optimization of ZnS(O,OH) buffer layer is presented which result in device performance comparable to that of CdS containing reference cells. These results are promising since it proves that the use of non-toxic Cd-free buffer layers is possible without compromising efficiencies. Markus Neuschitzer was responsible for the experimental design and grew all CZTSe absorber layers as well as he was involved in buffer layer deposition and solar cell device finishing. Furthermore, in-depth solar cell device characterization as well as data interpretation and the preparation of the manuscript and paper submission process were carried out by him.

(4) Neuschitzer, M.; Marquez, J.; Giraldo, S.; Dimitrievska, M.; Placidi, M.; Forbes, I.; Izquierdo-Roca, V.; Pérez-Rodriguez, A.; Saucedo, E. "V_{oc} Boosting and Grain Growth Enhancing Ge-Doping Strategy for $Cu_2ZnSnSe_4$ Photovoltaic Absorbers", ***Journal of Physical Chemistry C***, 2016, 120 (18), 9661-9670.

Impact factor (2015 JCR Science Edition) = 4.509
1st quartile in categories: CHEMISTRY, PHYSICAL; MATERIALS SCIENCE, MULTIDISCIPLINARY

In this work a Ge assisted crystallization for nanocrystalline precursor is presented. By adding a small amount of Ge during crystallization device performance end especially V_{oc} could largely be improved. Since a lack of V_{oc} is one of the biggest challenges for kesterite technology these V_{oc} boosting doping strategies are from high relevance for the kesterite community. The beneficial effect can be explained by an improved crystallization due to Ge-Se phases which acts as a crystallization flux as well as by the prevention of the formation of deep defects related to Sn loss. Markus Neuschitzer was involved in the experimental design and performed all experimental work related to absorber synthesis as well as solar cell preparation. Furthermore, he performed most in depth solar cell characterization and material characterization by X-ray diffraction. During an experimental stay at Newcastle University, Markus Neuschitzer could carry out defect characterizations by capacitance measurement methods. He was involved in the interpretation of all data and was in charge of writing the manuscript as well as coordinating the paper submission process.

None of these articles have been previously used by other co-authors for their doctoral thesis.

Barcelona, 04. 07. 2016.

Prof. Alejandro Pérez Rodríguez Dr. Edgardo Saucedo

PREFACIO: *PUBLICACIONES Y RESUMEN DE LA TESIS*

El trabajo realizado en la presente tesis ha sido desarrollado en el *Institut de Recerca en Energia de Catalunya* (IREC) bajo el marco del programa Marie Curie Initial Training Network KESTCELLS (FP7-PEOPLE-2012-ITN-316488). El principal objetivo de la siguiente tesis es el desarrollo y la optimización de celdas solares de heterouniones basadas en absorbedores de kesterita mediante procesos físicos y químicos. Estos semiconductores están formados por elementos abundantes en la corteza terrestre y con nula toxicidad
La tesis se estructura en torno a una serie de artículos que han publicados en revistas científicas de alto factor de impacto. De acuerdo con los requisitos del programa de doctorado en Ingeniería y Tecnologías Avanzadas de la Universitat de Barcelona, la Tesis se basa en los siguientes cuatro artículos:

Neuschitzer, M.; Sanchez, Y.; Olar, T.; Thersleff, T.; Lopez-Marino, S.; Oliva, F.; Espindola-Rodriguez, M.; Xie, H.; Placidi, M.; Izquierdo-Roca, V.; Lauermann, I.; Leifer, K.; Pérez-Rodriguez, A.; Saucedo, E. "Complex Surface Chemistry of Kesterites: Cu/Zn Reordering after Low Temperature Postdeposition Annealing and Its Role in High Performance Devices", *Chemistry of Materials,* 2015, 27 (15), 5279–5287. **(Impact factor = 9.407)**

Neuschitzer, M.; Sanchez, Y.; López-Marino, S.; Xie, H.; Fairbrother, A.; Placidi, M.; Haass, S.; Izquierdo-Roca, V.; Perez-Rodriguez, A.; Saucedo, E. "Optimization of CdS Buffer Layer for High-Performance $Cu_2ZnSnSe_4$ Solar Cells and the Effects of Light Soaking: Elimination of Crossover and Red Kink", *Progress in Photovoltaics: Research and Application*, 2015, 23 (11), 1660–1667. **(Impact factor = 7.365)**

Neuschitzer, M.; Lienau, K.; Guc, M.; Barrio, L. C.; Haass, S.; Prieto, J. M.; Sanchez, Y.; Espindola-Rodriguez, M.; Romanyuk, Y.; Perez-Rodriguez, A.; Izquierdo-Roca, V.; Saucedo, E. "Towards High Performance Cd-Free CZTSe Solar Cells with a ZnS(O,OH) Buffer Layer: The Influence of Thiourea Concentration on Chemical Bath Deposition", *Journal of Physics D: Applied Physics*, 2016, 49 (12), 125602. **(Impact factor = 2.772)**

Neuschitzer, M.; Marquez, J.; Giraldo, S.; Dimitrievska, M.; Placidi, M.; Forbes, I.; Izquierdo-Roca, V.; Pérez-Rodriguez, A.; Saucedo, E. "V_{oc} Boosting and Grain Growth Enhancing Ge-

Doping Strategy for $Cu_2ZnSnSe_4$ Photovoltaic Absorbers", *Journal of Physical Chemistry C*, 2016, 120 (18), 9661-9670. **(Impact factor = 4.509)**

El primer capítulo de la Tesis provee de una visión general del estado actual de la tecnología fotovoltaica y describe la necesidad de desarrollar tecnologías alternativas a las basadas en el Carbono en el sector de la energía. Entre estas tecnologías, las tecnologías fotovoltaicas juegan un papel principal. Además, se introducen la situación actual del mercado y la industria fotovoltiaca, describiendo las características principales de los diferentes tipos de tecnologías fotovoltaicas que están ya en explotación industrial. Entre ellas, se incluyen las tecnologías de silicio mono y multicristalino, que poseen las mayores cuotas de mercado, asi como las nuevas tecnologías basadas en células solares de capa fina con absorbedores de CdTe o $Cu(In,Ga)(S,Se)_2$ (CIGS), que recientemente han demostrado valores muy prometedores de eficiencia. Las tecnologías de capa fina tienen un gran interés que viene determinado por su valor más reducido de "Energy Pay Back Time" (que se define como el tiempo necesario para recuperar la energía consumida para la fabricación de los dispositivos) y a su mayor potencial de reducción de costes respecto las tecnologías de Si monocristalino y multicristalino. En este sentido, es interesante destacar cómo las tecnologías de capa fina ya son competitivas en términos de costes con las tecnologías dominantes de Si, a pesar de que tienen un volumen de producción que es aún un orden de magnitud inferior al de los dispositivos basados en Si.

No obstante, las tecnologías de capa delgada de CdTe y CIGS presentan un problema potencial que puede limitar su futura extensión a los niveles de producción masiva que se requieren para substituir a las tecnologías convencionales actuales basadas en combustibles fósiles (lo que requiere la capacidad de producción en la escala de los Terawatios), debido al hecho de que contienen elementos escasos en la corteza terrestre como el In, el Ga y el Te. Además, en el caso del CdTe existe una preocupación adicional debido a la elevada toxicidad del Cd, lo que ha hecho que esta tecnología esté prohibida en países como Japón. En este sentido, existe un interés muy alto para reemplazar estos elementos escasos por elementos que sean más abundantes en la corteza terrestre y con muy baja toxicidad, que permitan el desarrollo de una tecnología que pueda crecer de forma sostenible hasta niveles de producción en masa.

En este contexto, los compuestos $Cu_2ZnSnSe_4$ (CZTSe) y Cu_2ZnSnS_4 (CZTS) y sus aleaciones sólidas de sulfo-seleniuros son candidatos muy interesantes para substituir al CIGS como absorbedor, ya que permiten substituir el In y el Ga por el Zn y el Sn, que son metales mucho más abundantes en la corteza terrestre. No obstante, pese a los grandes esfuerzos de la comunidad científica en su investigación, a día de hoy existe aún una diferencia significativa en las eficiencias de las células solares basadas en tecnología de kesterita en comparación con los dispositivos basados en tecnologías de capa fina más maduras como las de CIGS y CdTe. Esto implica la necesidad de realizar un esfuerzo significativo en la investigación en estas tecnologías que permitan explotar de forma eficiente su potencial para el desarrollo de dispositivos de alta eficiencia y bajo coste.

En la literatura científica el CZTSe y el CZTS, son referidos como kesteritas a consecuencia de su estructura cristalina. Los detalles sobre su estructura cristalina y sus propiedades intrínsecas como material, además de una pequeña introducción general a la historia de las kesteritas se presnetan en el Capítulo 2 de la tesis. La estructura cristalina de la kesterita muestra flexibilidad a variaciones de su composición respecto de la composición estequiométrica de estos compuestos. Los dispositivos con mayores eficiencias han sido obtenidos utilizando capas absorbedoras sintetizadas con una composición pobre en cobre y rica en zinc. Esto es debido a la presencia de defectos intrínsecos del material que juegan un papel determinante en el comportamiento optoelectrónico de los dispositivos. Además, se ha observado la posibilidad de modificar el desorden estructural asociado a la distribución de los átomos de cobre y de zinc en los planos de Cobre-Zinc de la estructura de la kesterita mediante procesos de recocido a temperaturas relativamente bajas (alrededor de 200ºC). El capítulo describe también el impacto de los procesos de síntesis de las capas de kesterita sobre la formación de defectos profundos, tales como los asociados a "antisites" de Sn, y finaliza con la presentación de los objetivos fundamentales de la tesis, que incluyen el desarrollo y la optimización de celdas solares de heterouniones basadas en absorbedores de kesterita mediante procesos físicos y químicos.

En el capítulo 3 se introducen las características específicas y las peculiaridades de las células solares basadas en kesteritas. Mientras que las células solares de silicio se basan en una homounión que es obtenida mediante procesos de dopado, las células solares de kesterita poseen una estructura que incluye una heterounión entre la capa absorbedora tipo p de kesterita y una capa tampón/ventana tipo n. El papel de la capa tampón es permitir una correcta alineación de las bandas de energía con la capa absorbedora en la heterounión. La situación ideal corresponde a la formación de una pequeña discontinuidad de las bandas tipo "spike" en la banda de conducción en la heterounión. Para ello es necesario que el mínimo de la banda de conducción de la capa tampón sea ligeramente superior al de la capa absorbedora, mientras que el máximo de la banda de valencia de la capa tampón ha de ser inferior a l de la capa absorbedora. En el caso de las células de CZTSe, la capa tampón utilizada normalmente corresponde a una delgada capa de CdS crecida mediante procesos de depósito por baño químico, que permite obtener una alineación favorable de las bandas.

El capítulo 3 proporciona también una visión general del resto de las otras capas funcionales utilizadas en las heteroestructuras de kesterita que incluyen un contacto posterior de molibdeno y una capa ventana conductora transparente. Además, se revisan los conceptos fundamentales para la caracterización optoelectrónica de las células solares de capa fina mediante el análisis de las medidas de corriente – tensión obtenidas bajo diferentes condiciones de iluminación, así como el estudio de la eficiencia cuántica externa y de las medidas de capacidad de los dispositivos. Para finalizar, se revisa el estado actual de estas tecnologías, identificando los principales problemas que es necesario resolver para mejorar la eficiencia de conversión fotovoltaica de estos dispositivos,

El capítulo 4 se centra en el estudio y optimización de la interfaz entre la capa absorbedora y la capa tampón en células solares de CZTSe. Este estudio se sustenta sobre tres publicaciones diferentes. La primera de estas publicaciones es el trabajo titulado "Complex Surface Chemistry of Kesterites: Cu/Zn Reordering after Low Temperature Postdeposition Annealing and Its Role in High Performance Devices". En este estudio se investiga la influencia de la química de la superficie de la capa absorbedora en el rendimiento optoelectrónico de los dispositivos. Después de la realización de un ataque químico para remover las fases secundarias no deseadas de ZnSe que se han formado durante la síntesis de la capa absorbedora, y una vez finalizada la fabricación de la célula solar es necesario someter a la célula a un tratamiento térmico de recocido a 200ºC. Este tratamiento permite aumentar la eficiencia de conversión fotovoltaica de los dispositivos desde valores inferiores al 3% hasta valores en el rango del 8%. El análisis detallado de la estructura de la superficie de las capas mediante espectroscopia de fotoelectrones de rayos X (XPS) ha permitido observar cómo este proceso de recocido final promueve la difusión del zinc hacia la superficiede la capa absorbedora y la difusión del cobre hacia el interior de la capa. Esto determina la formación de una región superficial con una composición más rica en Zn y más pobre en Cu. Además, se ha realizado un estudio de las capas procesadas mediante microscopía electrónica de transmisión (TEM) que ha puesto en evidencia la existencia de cambios en la composición de las regiones de frontera de grano en la región superficial de la capa absorbedora, que antes de este proceso de recocido final tienen a ser ricas en Cu. El análisis de las capas y los dispositivos mediante microscopia TEM ha revelado también la existencia de una difusión significativa del Cu hacia la capa tampón de CdS que colabora también en el empobrecimiento en el contenido de Cu de la región superficial de la capa absorbedora. La mejora observada en la eficiencia de conversión fotovoltaica de los dispositivos con este tratamiento ha sido interpretada gracias a la formación de clústers de defectos de [V_{Cu}+Zn_{Cu}] que se ve favorecida por el empobrecimiento de Cu y el enriquecimiento de Zn en la región cercana a la superficie. El aumento en la presencia de estos defectos ha sido corroborado también de forma independiente mediante medidas de espectroscopia Raman. Adicionalmente, los cambios observados en la composición de las regiones de frontera de grano y la mejora de la capa tampón de CdS con el tratamiento térmico contribuyen también a la mejora observada en el rendimiento. Este estudio confirma de forma clara la necesidad de tener un empobrecimiento en el contenido de Cu y un enriquecimiento en el contendió de Zn para la obtención de células solares basadas en kesterita de alto rendimiento.

La segunda parte de la optimización de la interfaz entre la capa absorbedora de kesterita y la capa tampón de CdS se describe en el trabajo titulado “Optimization of CdS Buffer Layer for High-Performance $Cu_2ZnSnSe_4$ Solar Cells and the Effects of Light Soaking: Elimination of Crossover and Red Kink”. Tal como se ha comentado previamente, un aspecto clave para la obtención de una estructura de bandas favorable en la heterounión es la formación de una discontinuidad tipo ”spike” en la banda de conducción entre la capa tampón de CdS y la capa absorbedora de CZTSe. No obstante, esta discontinuidad puede ser también el origen de diferentes tipos de distorsiones en las curvas de corriente-voltaje, como la existencia de un “crossover” entre las curvas medidas bajo condiciones de iluminación y en oscuridad, así como el efecto de “red kink” que se observa en las curvas medidas bajo iluminación de las capas con longitudes de onda elevadas cuando se tienen defectos sensibles a la iluminación en la capa tampón. La optimización de la capa tampón de CdS crecida por baño químico utilizando diferentes sales de cadmio ha permitido mejorar de forma significativa la presencia de estas distorsiones, en combinación con tratamientos adecuados de ”light soaking”. Estos tratamientos han permitido obtener una mejora relevante en el “fill factor” y la eficiencia de los dispositivos. El análisis detallado de los efectos observados en las características corriuente-voltaje de los dispositivos ha permitido identificar la presencia de defectos aceptadores que pueden ser compensados mediante iluminación de las capas asociados a vacantes de cadmio. La implementación y control de un proceso adecuado de crecimiento de la capa tampón basado en nitrato de cadmio se ha revelado como más eficiente para la reducción drástica de las distorsiones en las curvas corriente-voltaje en relación con los procesos utilizados comúnmente, que se basan en la utilización de sulfato de cadmio como fuente del cadmio durante el crecimiento de las capas. Finalmente, el trabajo presenta un estudio detallado de los efectos de los procesos de “light soaking” para la optimización de estos dispositivos.

La tercera parte del capítulo 4 incluye el estudio titulado “Towards High Performance Cd-Free CZTSe Solar Cells with a ZnS(O,OH) Buffer Layer: The Influence of Thiourea Concentration on Chemical Bath Deposition”, que se centra en el desarrollo de capas tampón alternativas al CdS libres de Cd. El interés en estas capas viene motivado tanto por el interés en eliminar la presencia de Cd en los dispositivos –por la elevada toxicidad de este elemento – como en utilizar capas que tengan una banda prohibida superior al valor de 2.4 eV del CdS, lo que permitiría disminuir la pérdidas de eficiencia asociadas a la absorción de fotones de la región UV del espectro solar en la capa tampón.

Una de las alternativas más interesantes para la sustitución de las capas de CdS como capa tampón en las células solares de kesterita son las basadas en el sistema ZnS(O,OH). El ZnS(O,OH) no incluye elementos con alta toxicidad y tiene una banda prohibida más elevada que el CdS que puede ser controlada de forma adecuada variando la composición relativa S/O en la capa. Esto permite modificar también la alineación de las bandas de energía en la heterounión. Así, un contenido elevado de azufre determina la formación de un “spike” elevado en la banda de conducción, que da lugar a efectos de distorsion importantes en las curvas corriente-potencial, mientras que un aumento en el contenido de oxígeno da liugar a la formación de una discontinuidad tipo ”cliff”. Mediante el control adecuado de la concentración de tiourea (la fuente de azufre) en el proceso de depósito por baño químico de las capas de ZnS(O,OH) es posible optimizar la composición de la capa tampón para obtener capas con un “spike” moderado en la banda de conducción que permite minimizar los efectos de distorsión en las características de los dispositivos, obteniendo células solares con eficiencias de conversión fotovoltaica similares a las de las células fabricadas con las capas tampón de CdS de referencia.

El capítulo 5 presenta un estudio detallado en la mejora de la eficiencia de conversión fotovoltaica de las células solares de kesterita mediante el desarrollo de procesos basados en la inclusión de Ge. La primera parte de este estudio se basa en el trabajo titulado “V_{oc} Boosting and Grain Growth Enhancing Ge-Doping Strategy for $Cu_2ZnSnSe_4$ Photovoltaic Absorbers”. Uno de los mayores retos que es necesario resolver para mejorar la eficiencia de las células solares de kesterita es la existencia en estos dispositivos de un valor demasiado pequeño del voltaje en circuito abierto (V_{oc}) en comparación con los obtenidos en otras tecnologías de capa fina más maduras. Una posible explicación para la presencia de este bajo valor del V_{oc} está asociada a la presencia de defectos estructurales profundos. La mayoría de los defectos estructurales reportados en las capas absorendoras de kesteritas están relacionados con “antisites” de estaño, y su presencia se ve favorecida por la elevada volatilidad de las especies intermedias de calcogenuros de estaño que se producen durante el proceso de síntesis de las capas de kesterita, lo que puede dar lugar a una pérdida significativa de este elemento, la formación de los “antisites” de estaño. El germanio (Ge) es un elemento que pertenece al mismo grupo de la Tabla Periódica que el estaño (grupo IV), y puede actuar como impureza substituyendo al estaño en la red cristalina. El estudio desarrollado en este trabajo muestra cómo la adición de una pequeña cantidad de Ge en la superficie de las capas precursoras favorece una mejor cristalización de los precursores nanocristalinos, observando una mejora importante en la calidad cristalina de las capas selenizadas con la formación de granos de mayor tamaño. La caracterización optoelectrónica de los dispositivos procesados en función de la cantidad de Ge añadida a las capas ha permitido optimizar estos procesos, obteniendo una mejora muy significativa tanto del voltaje V_{oc} como de la eficiencia de conversión fotovoltaica para contenidos relativos de Ge/(Ge+Sn) inferiores al 2%. Para contenidos mayores de Ge, y a pesar del aumento del tamaño de grano y del aumento de la banda prohibida asociado a la substitución parcial del Sn por el Ge en la red cristalina, tanto el voltaje V_{oc} como la eficiencia disminuyen respecto de los valores máximos obtenidos con concentraciones más bajas de Ge. La caracterización de los defectos electrónicos presentes en las capas mediante espectroscopia de admitancia ha revelado la presencia de defectos profundos cuya concentración aumenta para las concentraciones más elevadas de Ge. Estos defectos han sido asociados a “antisites” de tipo donador de Sn_{Cu} o Ge_{Cu}, cuya formación se ve favorecida por la composición pobre en Cu de las capas y por los procesos de crecimiento utilizados en el estudio, y que actúan como centros de recombinación de los portadores foto generados, degradando la eficiencia de conversión fotovoltaica de los dispositivos.

En la segunda parte del capítulo 5 se presenta un estudio en mayor profundidad de la caracterización opto-electrónica y de los defectos presentes tanto en las capas procesadas con un nivel óptimo de dopado con Ge como con capas procesadas con concentraciones más elevadas de Ge. El estudio incluye también dispositivos de referencia de CZTSe libres de Ge. En este estudio se ha observado la existencia de una interacción entre el Ge y las impurezas de sodio (Na). El sodio es un dopante bien conocido de las tecnologías de CZTSe, y en general se sabe que la presencia de una cantidad óptima de Na favorece los procesos de recristalización permitiendo la síntesis de capas con mayor tamaño de grano y reduciendo los efectos detrimentillos asociados a las fronteras de grano sobre la eficiencia de los dispositivos. Este estudio revela que el Ge añadido en el proceso parece moderar el contenido de sodio de la capa absorbedora. En este casi es posible mejorar el rendimiento de los dispositivos suministrando un exceso de sodio en las capas. El estudio de los dispositivos mediante técnicas de espectroscopia de admitancia ha revelado la existencia de una reducción en la formación de los defectos profundos observados en capas procesadas con contendidos altos de Ge. Este comportamiento ha sido asociado a una reducción de las vacantes de Cu debida a la introducción del Na, lo que prevendría la formación de defectos tipo "antisite" Sn_{Cu} o Ge_{Cu}. Este estudio pone de manifiesto la necesidad de realizar un control muy preciso de la composición de las capas en relación con el contenido de los elementos del grupo IV, con el objetivo de mejorar los procesos de cristalización de los precursores nanocristalinos. En este sentido, el desarrollo de procesos combinando una cantidad óptima tanto de impurezas de Ge como de Na se ha revelado como una de las estrategias con mayor potencial para minimizar la formación de defectos profundos que son responsables de los bajos valores de voltaje V_{oc} en estos dispositivos.

Finalmente, en el último capítulo se muestran las conclusiones principales del trabajo, y se da una visión sobre el futuro de la tecnologías fotovoltaicas de kesterita.

La actividad desarrollada en esta Tesis Doctoral ha dado lugar también a la participación activa de Markus Neuschitzer como coautor de un conjunto más amplio de publicaciones relevantes que se indican a continuación:

(1) Placidi, M.; Espindola-Rodriguez, M.; Lopez-Marino, S.; Sanchez, Y.; Giraldo, S.; Acebo, L.; **Neuschitzer, M.**; Alcobé, X.; Pérez-Rodríguez, A.; Saucedo, E. "Effect of Rapid Thermal Annealing on the Mo Back Contact Properties for $Cu_2ZnSnSe_4$ Solar Cells", *J. Alloys Compd.* 2016, *675*, 158–162.

(2) Lopez-Marino, S.; Espíndola-Rodríguez, M.; Sánchez, Y.; Alcobé, X.; Oliva, F.; Xie, H.; **Neuschitzer, M.**; Giraldo, S.; Placidi, M.; Caballero, R.; Izquierdo-Roca, V.; Pérez-Rodríguez, A.; Saucedo, E. "The Importance of Back Contact Modification in $Cu_2ZnSnSe_4$ Solar Cells: The Role of a Thin MoO_2 Layer". *Nano Energy* 2016, DOI:10.1016/j.nanoen.2016.06.034 .

(3) Espindola-Rodriguez, M.; Sanchez, Y.; López-Marino, S.; Sylla, D.; Placidi, M.; **Neuschitzer, M.**; Xie, H.; Izquierdo-Roca, V.; Vigil-Galán, O.; Saucedo, E. "Selenization of Cu_2ZnSnS_4 Thin Films Obtained by Pneumatic Spray Pyrolysis". *J. Anal. Appl. Pyrolysis* 2016, doi:10.1016/j.jaap.2016.04.008.

(4) Giraldo, S.; **Neuschitzer, M.**; Placidi, M.; Pistor, P.; Perez-Rodrıguez, A.; Saucedo, E. "$Cu_2ZnSnSe_4$-Based Solar Cells With Efficiency Exceeding 10% by Adding a Superficial Ge Nanolayer: The Interaction Between Ge and Na". *IEEE Journal of Photovoltaics* 2016, *6* (3), 754–759.

(5) Xie, H.; Lopez-Marino, S.; Olar, T.; Sánchez González, Y.; **Neuschitzer, M.**; Oliva, F.; Giraldo, S.; Izquierdo-Roca, V.; Lauermann, I.; Pérez-Rodríguez, A.; Saucedo, E. "On the Impact of Na Dynamics at the $Cu_2ZnSn(S,Se)_4$/CdS Interface During Post Low Temperature Treatment of Absorbers". *ACS Appl. Mater. Interfaces* **2016**, *8* (7), 5017–5024.

(6) Márquez, J.; **Neuschitzer, M.**; Dimitrievska, M.; Gunder, R.; Haass, S.; Werner, M.; Romanyuk, Y. E.; Schorr, S.; Pearsall, N. M.; Forbes, I. "Systematic Compositional Changes and Their Influence on Lattice and Optoelectronic Properties of $Cu_2ZnSnSe_4$ Kesterite Solar Cells". *Sol. Energy Mater. Sol. Cells* 2016, *144*, 579–585.

(7) Kask, E.; Krustok, J.; Giraldo, S.; **Neuschitzer, M.**; López-Marino, S.; Saucedo, E. "Temperature Dependent Electrical Characterization of Thin Film $Cu_2ZnSnSe_4$ Solar Cells". *J. Phys. D: Appl. Phys.* 2016, *49* (8), 85101.

(8) Sánchez, Y.; Espíndola-Rodríguez, M.; Xie, H.; López-Marino, S.; **Neuschitzer, M.**; Giraldo, S.; Dimitrievska, M.; Placidi, M.; Izquierdo-Roca, V.; Pulgarín-Agudelo, F. A.; Vigil-Galán, O.; Saucedo, E. "Ultra-Thin CdS for Highly Performing Chalcogenides Thin Film Based Solar Cells". *Sol. Energy Mater. Sol. Cells* 2016.

(9) Guc, M.; **Neuschitzer, M.**; Hariskos, D.; Bauer, A.; Witte, W.; Hempel, W.; Calvo-Barrio, L.; Pistor, P.; Perez-Rodriguez, A.; Izquierdo-Roca, V. “Raman Scattering Quantitative Assessment of the Anion Composition Ratio in Zn(O,S) Layers for Cd-Free Chalcogenide-Based Solar Cells”. *RSC Adv* 2016, *6* (29), 24536–24542.

(10) López-Marino, S.; Sánchez, Y.; Espíndola-Rodríguez, M.; Alcobé, X.; Xie, H.; **Neuschitzer, M.**; Becerril, I.; Giraldo, S.; Dimitrievska, M.; Placidi, M.; Fourdrinier, L.; Izquierdo-Roca, V.; Pérez-Rodríguez, A.; Saucedo, E. “Alkali Doping Strategies for Flexible and Light-Weight $Cu_2ZnSnSe_4$ Solar Cells”. *J Mater Chem A* 2016, *4* (5), 1895–1907.

(11) Insignares-Cuello, C.; Oliva, F.; **Neuschitzer, M.**; X. Fontané; Broussillou, C.; Goislard de Monsabert, T.; Saucedo, E.; Ruiz, C. M.; Pérez-Rodríguez, A.; Izquierdo-Roca, V. “Advanced Characterization of Electrodeposition-Based High Efficiency Solar Cells: Non-Destructive Raman Scattering Quantitative Assessment of the Anion Chemical Composition in Cu(In,Ga)(S,Se)2 Absorbers”. *Sol. Energy Mater. Sol. Cells* 2015, *143*, 212–217.

(12) Krustok, J.; Raadik, T.; Grossberg, M.; Giraldo, S.; **Neuschitzer, M**.; López-Marino, S.; Saucedo, E. “Temperature Dependent Electroreflectance Study of $Cu_2ZnSnSe_4$ Solar Cells”. *Mater. Sci. Semicond. Process.* 2015, *39*, 251–254.

(13) Giraldo, S.; **Neuschitzer, M.**; Thersleff, T.; López-Marino, S.; Sánchez, Y.; Xie, H.; Colina, M.; Placidi, M.; Pistor, P.; Izquierdo-Roca, V.; Leifer, K.; Pérez-Rodríguez, A.; Saucedo, E. “Large Efficiency Improvement in Cu $_2$ ZnSnSe $_4$ Solar Cells by Introducing a Superficial Ge Nanolayer”. *Adv. Energy Mater.* 2015, *5* (21), 1501070.

(14) Placidi, M.; Dimitrievska, M.; Izquierdo-Roca, V.; Fontané, X.; Castellanos-Gomez, A.; Pérez-Tomás, A.; Mestres, N.; Espindola-Rodriguez, M.; López-Marino, S.; **Neuschitzer, M.**; Bermudez, V.; Yaremko, A.; Pérez-Rodríguez, A. “Multiwavelength Excitation Raman Scattering Analysis of Bulk and Two-Dimensional MoS_2 : Vibrational Properties of Atomically Thin MoS_2 Layers”. *2D Mater.* 2015, *2* (3), 35006.

(15) Lugo, S.; Sánchez, Y.; **Neuschitzer, M.**; Xie, H.; Insignares-Cuello, C.; Izquierdo-Roca, V.; Peña, Y.; Saucedo, E. “Chemical Bath Deposition Route for the Synthesis of Ultra-Thin $CuIn(S,Se)_2$ Based Solar Cells”. *Thin Solid Films* 2015, *582*, 74–78.

(16) Fairbrother, A.; **Neuschitzer, M.**; Saucedo, E.; Pérez-Rodríguez, A. “Zn-Poor $Cu_2ZnSnSe_4$ Thin Films and Solar Cell Devices”. *Phys. Status Solidi A* 2015, *212* (1), 109–115.

(17) López-Marino, S.; **Neuschitzer, M.**; Sánchez, Y.; Fairbrother, A.; Espindola-Rodriguez, M.; López-García, J.; Placidi, M.; Calvo-Barrio, L.; Pérez-Rodríguez, A.; Saucedo, E. “Earth-Abundant Absorber Based Solar Cells onto Low Weight Stainless Steel Substrate”. *Sol. Energy Mater. Sol. Cells* 2014, *130*, 347–353.

(18) Xie, H.; Sánchez, Y.; López-Marino, S.; Espíndola-Rodríguez, M.; **Neuschitzer, M.**; Sylla, D.; Fairbrother, A.; Izquierdo-Roca, V.; Pérez-Rodríguez, A.; Saucedo, E. “Impact of Sn(S,Se) Secondary Phases in $Cu_2ZnSn(S,Se)_4$ Solar Cells: A Chemical Route for Their Selective Removal and Absorber Surface Passivation”. *ACS Appl. Mater. Interfaces* 2014, *6* (15), 12744–12751

1 PV – STATUS OF TECHNOLOGY

One of the main challenges for human mankind to face in near feature are dramatic climate changes if no measures are taken. The global average surface temperature increased around 0.86ºC from 1880 until 2012 and anthropogenic greenhouse gas emission could undoubtedly be identified as the dominant cause of this warming.[1] The latest assessment report of the Intergovernmental Panel on Climate Change (IPCC) drastically shows that if no measures are taken to reduce greenhouse gas emission in near future the global average surface temperature will most like increase over 4ºC up to 6ºC in the year 2100 compared to the average temperature between 1850-1900.[1] An increase in average surface temperature over 4ºC would have a sever irreversible impact resulting in high species extinctions, global and regional food insecurity as well as consequential constrains on human activities.[1] The Conference of the Parties (COP) on its 21st session held in Paris from 30 November to 13 December 2015 agreed to take measures to keep global warming below 2ºC and to pursue efforts to keep it even below 1.5ºC (FCCC/CP/2015/L.9/Rev.1). According to climate models of the IPCC there is a 50% probability to reach this 2ºC goal if the cumulative CO_2 emission stays below 3000 Gt CO_2.[1] However, about 1900 Gt CO_2 had already been emitted by 2011 showing that urgent actions are necessary. According, to the International Energy Agency's (IEA) special report on energy and climate change around 32 Gt of CO_2 were emitted in the year 2014 related to energy production which corresponds to more than 60% of the worlds greenhouse gas emission.[2] This value clearly emphasises that there is an urgent need to decarbonise the energy sector to reduce worldwide greenhouse gas emission. In 2013 78.1% of the global electricity generation was based on fossil fuel combustion (67.5%) and nuclear (10.6%) and the rest of 21.9% was generated by renewable energy sources.[3] This 21.9% of renewable electric energy was produced by a total installed capacity of 1701 GW of renewables, which corresponds to 28.9% of worldwide installed electric power generation capacity in 2013.[3] The main part of this 1701 GW renewable capacity comes from hydropower (66.8%), followed by wind (17.9%) and photovoltaic (8.0%) installations as can be seen in Figure 1.1. In the IEA's World Energy Outlook projections for 3 different scenarios are presented which allows insights into the expected evolution of the global energy sector.[3] The Current Policies Scenario takes just energy-related government policies adopted before mid-2015 into account. The New Policies Scenario takes additionally all relevant intentions that have been announced into account, which includes so called Intended Nationally Determined Contributions submitted by national governments as pledges to the COP 21st meeting held in Paris in December 2015. However, the measures taken in these two scenarios are still not enough to limit greenhouse gas emission to reach the 2ºC goal.

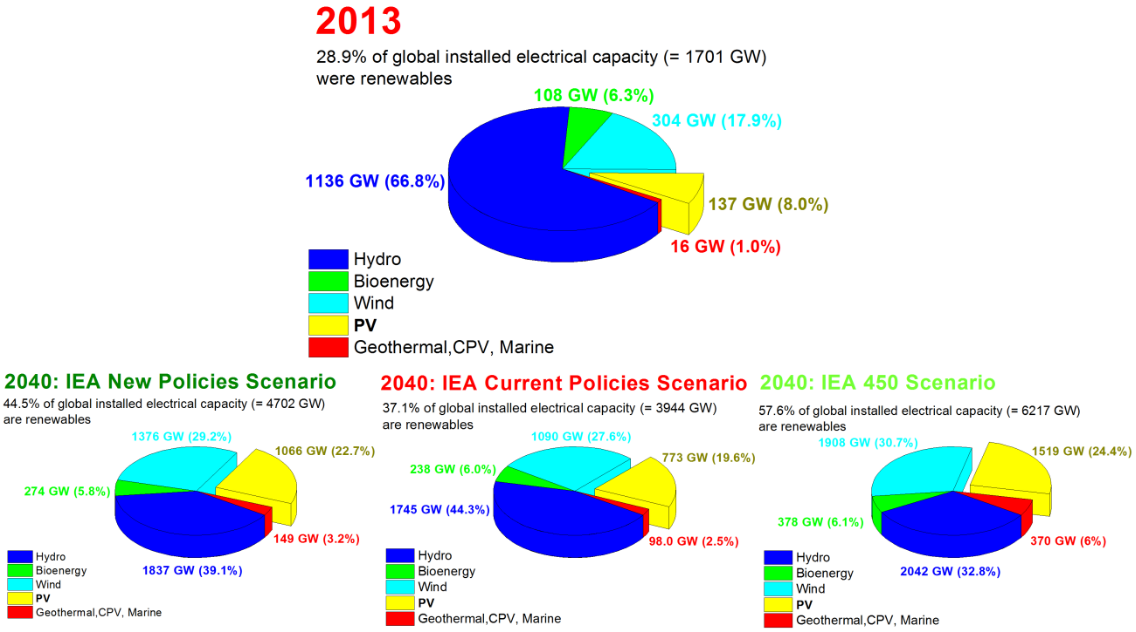

Figure 1.1. Share of different renewable technologies in global installed electrical capacity in 2013 and expected evolution for the year 2040 according to three different models of the IEA. The exploded wedge corresponds to photovoltaic installations (PV). Pie charts were created from data of the 2015 IEA World Energy outlook.[3]

Only the third scenario (450 scenario), which foresees 57.6% of global installed electrical capacity as renewable in the year 2040 would be consistent with the long term goal to limit global warming to 2ºC. As can be seen in Figure 1.1, for all projected scenarios photovoltaics (PV), together with wind power, is the key technology to achieve this shift to a decarbonised energy supply. According to these scenarios an increase of up to one order of magnitude of global installed PV capacity to over 1TW (=1000GW) can be expected until the year 2040. Already in 2014 the PV market showed another record year of growth with over 40 GW$_p$[*] of capacity added, which results in global total of 177 GW$_p$.[4] Furthermore, due to the price fell of residential PV electricity systems of over 70% from 2008 to 2014[5], electricity generated by unsubsidised PV is equal or cheaper than retail electricity prices for 79.5% of Europe’s population.[6–8] For example in southern Spain, Cyprus and Sicily the Levelised Cost of Electricity (LCOE) for unsubsidised PV, i.e. constant kWh cost that has the same present value as the overall cost of building and operating the given technology, reaches almost 0.06€/kWh[7,8] compared to 0.21€/kWh[9] average EU-28 electricity price for private households. This further demonstrates the potential of PV as an economic source of electricity. Additionally, besides being one of the most promising technologies for green energy, the solar resources worldwide are abundant and cannot be monopolised by one country in contrast to most fossil fuels.

---

[*] Photovoltaic power generation capacity is usually the subscript p for peak added since electricity is only generated when the sun is shining.

1.1 Silicon vs. thin-film technology

To the in the year 2014 already existing 177GW$_p$ of photovoltaic installation, 50 GW$_p$ are expected to be added in the year 2015, confirming the continuous growth of the PV market.[10] There are two different groups of technologies available on the market for PV installations as can be seen in Table 1.1. On the one hand, there is the silicon based technology which is the main technology in PV with a market share of 90.8% of total global production in 2014 and on the other hand thin film technology which accounts for the rest of 9.2% of total global production.

In silicon technology one has to distinguish between monocrystalline and multicrystalline (or polycrystalline) solar cells. Monocrystalline silicon solar cells use single crystal silicon wafers as light absorbing material. The highest power conversion efficiency of 25.6%[11] in laboratory scale cells and 22.8% in module size of all commercial available solar cell technologies are obtained with this technology as can be seen in Table 1. However, the growth of single crystal silicon ingots requires high amounts of energy and complex processing steps are necessary for high performance monocrystalline silicon modules which make this technology the most expensive one. Multicrystalline silicon absorber material can be produced at lower costs and is used most in solar industry with a 55.2% share of global production in 2014.

A further important benchmark for renewable energy technology is the energy performance. The two most common metrics to compare different technologies are the energy payback time (EPBT) and the energy return on energy investment (EROI). A recent study of Bhandari et al.[12] on energy performance which analyses 232 different references and harmonized several parameters found an average EPBT of 4.1 and 3.1 years for monocrystalline and multicrystalline modules, respectively, for an insolation equivalent to southern Europe. That means that after about 4 years the same amount of electricity is generated which was necessary to produce the PV panel in the case of monocrystalline Si. Considering a module lifetime of up to 30 years, these values are still sustainable, however, values as low as possible are desirable for sustainable energy sources.

Table 1.1. Overview of the performance of photovoltaic technologies available on the market

	Record lab cell efficiency	Record module efficiency	Highest commercial module efficiency in 2016	Global production in 2014[+] [GW$_p$]	Energy payback time* [years]	EROI*
Silicon technology						
monocrystalline	25.6%[11]	22.8%[a13]	21.5%[a]	16.9 (35.6%)	4.1±2.0	8.7±3.5
multicrystalline	21.3%[14]	19.2%.[b13]	16.1%[b],16.2%[c]	26.2 (55.2%)	3.1±1.3	11.6±5.2
Thin film technology						
CdTe	22.1%[15]	18.6%[16]	16.4%[d]	1.9 (4.0%)	1.0±0.4	34.2±13.5
CIGS	22.3%[17]	16.5%[f]	14.9%[e]	1.7 (3.6%)	1.7±0.7	19.9±8.2
a-Si	13.6%[13]	10.9%[13]	9.8%[g]	0.8 (1.6%)	2.3±0.7	14.5±5.1

[a]Sunpower; [b]TrinaSolar; [c]SUNTECH; [d]FirstSolar; [e]Solibro; [f]TSMC (exited the solar industry in 2015); [g]Kaneka Solar Energy - Hybride between thin film mc-Si and a-Si; – status April 2016

[+]Fraunhofer ISE: Photovoltaics Report, updated: 11 March 2016

*energy payback time (EPBT) and energy return on energy invested (EROI) are taken from Bhandari et al.[12] who use harmonised module efficiencies of 13% for monocrystalline Si, 12.3% for multicrystalline Si, 10.9% for CdTe, 11.5% for CIGS, and 6.3% for a-Si, an insolation of 1700kWh/m^2/year (corresponds to southern Europe) and 30 years of lifetime for the calculations.

The energy return of energy investment (EROI) is the ratio of the energy gained from an energy production process (e.g. lifetime energy output of solar panel) to the energy needed to obtain this energy source (e.g. energy required to obtain raw material and manufacture module as all well as all components necessary in a working PV-system to produce electricity).[18] EROIs can be calculated for any energy source and allows comparisons between them. For fossil fuels EROIs between 10-30 for oil as well as between 40-80 for coal are obtained, thus mono and multicrystalline PV with values around 9 to 12 are starting to compare to them, which proves that PV is a viable energy source.[12,18]

The second commercial available PV technology is thin film PV. Here thin, usually below 2 µm thickness, photovoltaic absorber layers are used which are deposited by different techniques. Amorphous silicon (a-Si) as absorber material has the longest history of commercial thin film PV, however, efficiencies are low compared to silicon PV and no significant improvements were observed in recent years. However, thin film PV based on CdTe or CIGS ($CuIn_{1-x}Ga_xSe_2$) absorbers recently showed promising improvements with efficiencies records of 22.1% and 22.3%, values even higher than for multicrystalline Si. The main advantages of thin film PV, besides the possibility to extent this technology to no-rigid flexible substrates, is the minimum use of high purity material which significantly reduces the EPBT and increases the EROI even closer to fossil fuel values as can be seen in Table 1.1. Therefore, thin film PV is one of the most promising truly sustainable energy source to cover parts of future energy demand. Furthermore, due to this minimal material use module prices close to 0.40 €/W_p can be achieved which is in the same range as for Si although a much lower production capacity is available today as it is the case for Si.[19] Prices are expected to decrease further if production is scaled up.[20] However, one of the main concerns of CdTe and CIGS technology is the use of scare elements. In the case of CdTe, besides the Cd toxicity, tellurium is used which is one of the rarest elements in the earth crust with an estimated abundancy of 0.005 ppm.[21] In Table 1.2 the abundancy, the world refinery production, estimated prices as well as the material requirements for PV module production for different absorber layers are summarized. For CdTe one can see that the annual production of 400 t tellurium and a material requirement of around 44 t/GWp could cause problems if this technology wants to supply PV in the TW (=1000 GW) range, as it is necessary for the future of a decarbonised energy sector until the year 2040. In the assumption of material requirements only the amount inside the absorber layers are considered, however, normally the material utilisation during a deposition process is much higher, e.g. just around 40-60% of the raw material feedstock is deposited.[22] The t/GW_p values of Table 1.2 are therefore just a lower limit. Most tellurium is mined indirectly as a by-product of copper, thus its production cannot be increased individually and the main concern about tellurium supply for PV is if the copper production can meet an increased growth in tellurium demand.[23] CIGS uses the scare element indium which has an abundancy of 0.05 ppm in the earth crust.[21] Indium as well as gallium are mined indirectly as by-product of zinc and bauxite mining and there supply is tied to the production of them.[24] With an annual indium production of 755 t in 2015, and the fact that most indium is used to produce transparent conductive oxide (ITO) coatings for displays[24], the estimated material requirements of 20 t/GW_p could led to problems in the indium supply for PV if CIGS production capacity increases towards the 1TW scale. Furthermore, all these scare elements are expensive which could increase production costs significantly if prices even more increase due to increased demand. Therefore, there is a high interest to find new thin film PV absorber materials made of more abundant elements. One of the most promising new thin film absorber is kesterite – $Cu_2ZnSnSe_4$ or it solid solution with sulphur $Cu_2ZnSn(S_xSe_{1-x})_4$. By replacing In and Ga by the more abundant elements Sn and Zn all elements of this thin film absorber material would fulfils the needs for high capacity production (see Table 1.2), thus making kesterite PV technology compatible with massive deployment up to the TW scale. However, up to now record efficiencies of $Cu_2ZnSn(S_xSe_{1-x})_4$ based solar cells reach only up to 12.6% in laboratory scale which is still much lower than it's close cousin CIGS.[25] Therefore, much more research is necessary to understand the current limitations and further improve this promising thin film PV technology.

Table 1.2. Abundancy, worldwide production, estimated prices and material requirements in module production for all elements of CdTe, CIGS as well as CZTSe photovoltaic absorbers

	abundancy[21] [ppm]	world refinery production 2015[24] [t]	price[24] [\$/kg]	material requirements in 2 µm absorber* [g/m^2]	material requirements per GW$_p$ for 14% modules* [t/GW$_p$]
Cd	0.1	24200	1	5.48	39
Te	0.005	400	200	6.23	44
Cu	25	18700000	6	2.26	16
In	0.05	755	460	2.86	20
Ga	15	435	140	0.74	5
Se	0.12	2340	50	5.61	40
Cu	25	18700000	6	2.30	16
Zn	65	13400000	2	1.18	8
Sn	2.3	270000	15	2.14	15
Se	0.12	2340	50	5.71	40
S	697	70100000	0.13	-	-

*see Appendices for details of calculation

1.2 Aim of this thesis

The aim of this thesis is to optimize pure selenide kesterite ($Cu_2ZnSnSe_4$) based solar cells grown by a cost effective two step physical vapour deposition (PVD) based route and to gain a deeper understanding in the current efficiency limiting factors. In thin film solar cells many different functional layers are used starting from the back contact, the absorber layer, buffer layer and transparent conducting window layer. Therefore, many interfaces are present which benign passivation is crucial for high device performance. This thesis focuses especially on the optimization of the front interface and the absorber layer itself. Here, detailed studies to understand the influence of kesterite surface chemistry and furthermore the role of the solar cell´s front interface (CZTSe/buffer/window - interface) on device performance were carried out with the goal to develop possible routes to modify the absorber surface and/or buffer layer properties to improve solar cell device performance. The influences of different surface treatments as well as post deposition treatments on device performance were investigated. In-depth solar cell device characterization was carried out to screen for possible efficiency limiting evidences related to the front interface, especially the buffer layer, and furthermore the absorber bulk and to find ways to overcome these.

One of the most limiting factors in kesterite based solar cell so far is the low open circuit voltage (V_{oc}). Therefore, besides different surface treatments possible absorber doping routes were developed with the goal to get a deeper understanding of the role of surface as well as absorber properties responsible for this lack of V_{oc} and develop strategies to improve V_{oc} and increase solar cell efficiencies.

2 KESTERITE A PROMISING THIN-FILM PHOTOVOLTAIC ABSORBER

In 1988 Kentaro Ito and Tatsuo Nakazawa reported the first time about the favourable optical and electrical properties for photovoltaic applications, like a direct band gap of 1.45 eV and a high absorption coefficient of 10^4 cm^{-1} of the quaternary compound Cu_2ZnSnS_4.[26] Due to the similarity of its material properties to the already more established $CuInS_2$ and $Cu(In,Ga)Se_2$ photovoltaic absorbers and a composition free of scare elements like In and Ga, this quaternary semiconductor attracted more and more attention. However, it took until 2008 when Katagiri et al. demonstrated solar cells based on Cu_2ZnSnS_4 absorbers with efficiencies over 6.7% and research in this promising absorber material started to increase rapidly.[27] Finally, in 2011 researcher of the IBM Thomas J. Watson Research succeeded in exceeding the 10% efficiency level with an absorber layer containing selenium besides sulphur and they could further improve their efficiencies to 12.6% in 2013 which is still the current world record.[25,28] In general, one distinguish between the sulphur pure quaternary compound Cu_2ZnSnS_4, abbreviated as CZTS, the selenium pure compound $Cu_2ZnSnSe_4$ (CZTSe), and the solid solution containing sulphur and selenium $Cu_2ZnSn(S_xSe_{1-x})_4$ (CZTSSe). All of these compounds together are referred to as kesterite due to its crystal structure as will be discussed in more detail in the next section.[29]

2.1 Crystal structure, material properties and defects

Quaternary compounds of the type $A_2^{I}B^{II}C^{IV}X_4^{VI}$ are known to exist in two tetragonal type crystal structures, the kesterite type and stannite type structure.[30] For Cu_2ZnSnS_4 and $Cu_2ZnSnSe_4$ (i.e. A=Cu, B=Zn, C=Sn and X=S,Se) Schorr found in a neutron powder diffraction study that both crystallize in the kesterite type structure.[31] In Figure 2.1 the unit cells of kesterite type as well as stannite type structures are shown. The main difference between these two structures is the different distribution of the cations (i.e. Cu^{+1}, Zn^{+2} and Sn^{+4}). In the kesterite type structure layers of CuSn, CuZn, CuSn and CuZn are alternated in z-direction at 0, ¼, ½, and ¾ which corresponds to the $I\bar{4}$ space group.

The asymmetric unit cell consist of a Cu atom at the 2a (0,0,0), Zn at the 2c (0,½,¼), another Cu at 2d (0,½,¾) and Sn at the 2b (0,0,½) position. In the stannite type structure ZnSn alternate with Cu_2 layers which corresponds to the $I\bar{4}2m$ space group. Thus, in the asymmetric unit cell Cu is located at 4d (0, ½, ¼), Zn at the 2a (0,0,0) and Sn as well at the 2b (0,0,½) position.[31] In both structures these planes of cations are separated by planes of anions (i.e. S^{-2} or Se^{-2}) in z-direction at 1/8, 3/8, 5/8, and 7/8. Neutron powder diffraction and further solid state nuclear magnetic resonance measurements showed that CZTS as well as CZTSe crystallize in the kesterite type structure, however, a disorder in the CuZn planes at ¼ and ¾ was found.[31,32] Thus, this Cu/Zn disorder takes place in the 2c (0,½,¼) and 2d (0,½,¾) position, leading to the formation of Cu_{Zn} and Zn_{Cu} antisites defects but should not be confused with the stannite type structure which atomic arrangement is slightly different as can be seen in Figure 2.1 (e.g. there is no Cu on the 2a (0,0,0) position in the stannite type structure).

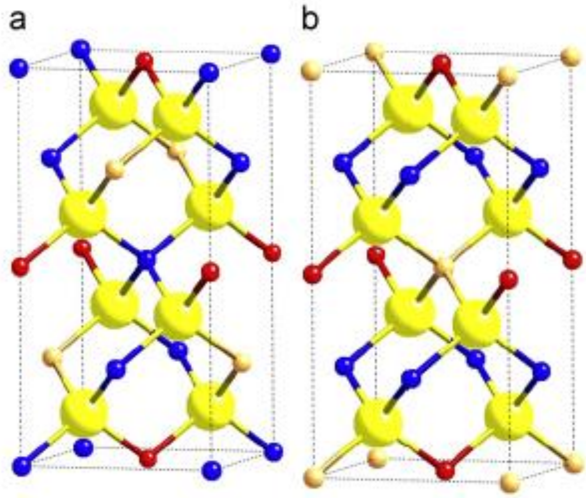

Figure 2.1. Unit cells of kesterite (a) and stannite (b) type structure. Blue=Cu, orange=Zn, red=Sn, yellow=S,Se. Picture reproduced from Schorr.[31]

Both, CZTS and CZTSe have a direct bandgap with values around 1.5eV and 1.0 eV, respectively, which varies slightly around these values depending on the degree of Cu/Zn disorder present in the layers.[29,33,34] These bandgap values are ideal for the application as photovoltaic absorbers, as highest theoretical power conversion efficiency are possible in this bandgap range assuming detailed balance (i.e. all photons with energy higher than the bandgap get absorbed and create electron-hole pairs which either contribute to the current or recombine radiative) and the sun as well as solar cell as blackbodies (Shockley-Queisser limit).[35] Furthermore, CZTS and CZTSe are highly miscible and allow the formation of the mixed anion solid solution $Cu_2ZnSn(S_xSe_{1-x})_4$ which bandgap can be tuned between 1.0 eV and 1.5 eV depending on the S/Se ratio.[36,37]

One peculiarity of kesterite based solar cells is that highest device performance is obtained for a Cu-poor and Zn-rich composition with cationic ratios around Cu/(Zn+Sn)=0.8 and Zn/Sn=1.2.[38–40] That means that the kesterite structure is flexible to compositional variations and allows deviations from stoichiometry as has been proven by XRD diffraction experiments.[41–43] For Cu-poor Zn-rich composition Cu is substituted in the kesterite lattice by the formation of Cu vacancies (V_{Cu}) and Zn_{Cu} antisites defects. This Cu-poor Zn-rich Sn-stoichiometric kesterite is referred to as A-type kesterite in literature.[42] Different other possible types of kesterite and the most probable cationic substitutions for their composition are illustrated in Figure 2.2. However, for photovoltaic absorbers Cu-poor and Zn-rich, thus A-type (Cu-poor Zn-poor Sn-stoichiometric) kesterite and in some extend B-type (Cu-poor Zn-rich Sn-poor) are the most promising. The reason for the superior solar cell performance of Cu-poor and Zn-rich kesterite absorbers can be found in the intrinsic defect structure of the material. Theoretical calculations of Chen et al. show that Cu-poor Zn-rich composition enhances the p-type conductivity due to the increased density of V_{Cu}, which act as main intrinsic shallow acceptor.[44] Furthermore, the formation of $[2Cu_{Zn}+Sn_{Zn}]$ defect clusters can be prevented in Cu-poor Zn-rich kesterite. This cluster has low formation energy in stoichiometric composition and can induce detrimental electron trapping states in the absorber, which harm solar cell performance. On the other hand a high population of $[V_{Cu}+Zn_{Cu}]$ and $[Zn_{Sn}+2Zn_{Cu}]$ defect cluster is expected for A and B type kesterite. Fortunately this defect clusters are electronically benign and do not harm solar cell performance. $[V_{Cu}+Zn_{Cu}]$ clusters can be even beneficial, as they induce a downshift of the valence band, which can enhance the separation of electron-hole pairs in the absorber.[44]

A-type: copper-poor / zinc-rich
$2Cu^+ \rightarrow V_{cu} + Zn^{2+}_{Cu}$

B-type: copper-poor / tin-poor /Zn-rich
$2Cu^+ + Sn^{4+} \rightarrow 2Zn^{2+}_{Cu} + Zn^{2+}_{Sn}$

C-type: copper-rich / tin-rich
$3Zn^{2+} \rightarrow 2Cu^+_{Zn} + Sn^{4+}_{Zn}$

D-type: copper rich/ zinc poor
$Zn^{2+} \rightarrow Cu^+_{Zn} + Cu^+_I$

E-type: Cu rich/ Zn rich
$2Cu^+ + Zn^{2+} \rightarrow 2\ V_{Cu} + Sn^{4+}_{Zn}$
$2Cu^+ + Zn^{2+} \rightarrow Sn^{4+}_{Cu} + V_{Cu} + V_{Zn}$

F-type: Cu rich/ Zn rich
$Sn^{4+} \rightarrow Zn^{2+}_{Sn} + 2\ Cu^+_i$
$Sn^{4+} \rightarrow Cu^+_{Sn} + Zn^{2+}_i + Cu^+_i$

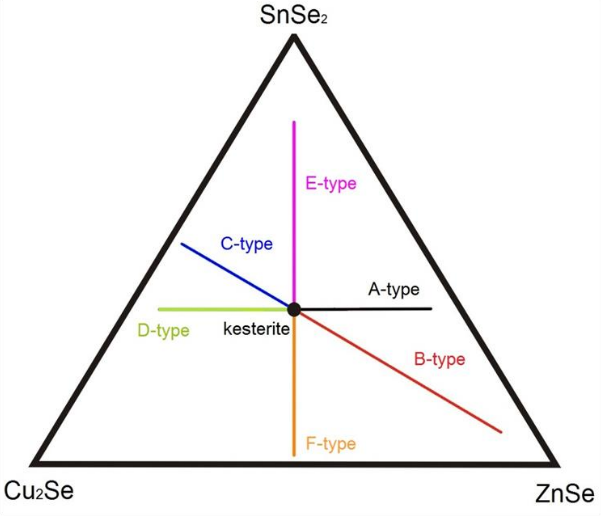

Figure 2.2. Different types of off-stoichiometric kesterite illustrated in a ternary phase diagram and the most probable cationic substitutions formed in the different compositional regions (illustration is a private communication of L. E. Valle-Rios[41]).

2.1.1 Cu/Zn disorder

As already mentioned earlier a disorder in the CuZn planes of the kesterite structure, i.e. a large density of $[Cu_{Zn}+Zn_{Cu}]$ defect clusters was found experimentally.[31,45,46] The degree of this order/disorder strongly depends on the thermal history of the sample. Choubrac et al. showed that slow cooling from the high synthesis temperature of CZTS powders can increase the Cu/Zn order.[46] Scragg et al. demonstrated the reversibility of Cu/Zn order by low temperature annealings of CZTS thin films.[33] A critical temperature of 260ºC was found for pure sulfide CZTS. Annealing below this temperature can increase order, whereas annealing above it followed by fast cooling increases disorder. For pure selenide CZTSe this temperature was found to be 200ºC.[34] Furthermore, it was shown that the degree of order has an influence of the bandgap, which increased by 110 meV from disorder to ordered pure selenide CZTSe.[34] This effect of order/disorder on the bandgap was confirmed by theoretical calculations and could lead to spacial bandgap fluctuation inside of kesterite absorber layers due to the formation of $[Cu_{Zn}+Zn_{Cu}]$ defect complexes.[47] Local bandgap fluctuations would be detrimental for solar cell performance as they reduce the bandgap of the absorber, i.e. the open circuit voltage (V_{oc}).[48] Nevertheless, experimentally there was no convincing evidence found that more ordered kesterite absorbers show better device performance than more disordered, and especially the low V_{oc} deficit, which is one of the main problems in Kesterite technology as will be discussed in more detail later on, is not improved.[49,50] One of the reason could be that best device performance is obtained with A-type kesterite absorbers, which naturally have a high population of [V_{Cu}+Zn_{Cu}] defect clusters. NMR investigations showed that [V_{Cu}+Zn_{Cu}] clusters can limit the disorder[32] and furthermore theoretical calculations suggest that [V_{Cu}+Zn_{Cu}] has the opposite effect on bandgap than [Cu_{Zn}+Zn_{Cu}], thus bandgap changes will be compensated.[47,51] Nevertheless, the reordering of Cu/Zn can be used to tailor a beneficial surface composition by chemical etchings and low temperature annealing as will be shown in more detail in Chapter 4.1.

2.1.2 Deep defects

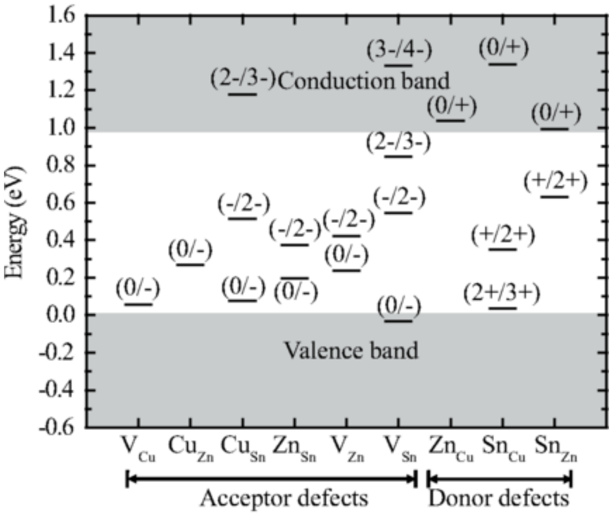

Figure 2.3. Calculated defect charge state transition levels for CZTSe (initial and final charge states in parentheses). Picture reproduced from Yee et al.[52]

In Figure 2.3 the theoretically calculated defect charge state transition of most probable cation antisites and vacancy defects in CZTSe are shown. Since the cations have the charges Cu^{+1}, Zn^{+2} and Sn^{+4} all cation vacancies are acceptor defects. V_{Cu} has the shallowest transition level of 0.06 eV of all acceptor defects and V_{Cu} together with Cu_{Zn} antisites have the lowest formation energy. Therefore they are expected to contribute mainly to the p-type conductivity of CTZSe.[44,52] On contrary to shallow defects, which can trap charge carriers for short time before thermally re-exciting them back into valence or conduction band, deep defects can be detrimental to solar cell performance as they can act as recombination centres for electron hole pairs. In p-type absorbers especially deep donor defects which are charged positively can attract minority carriers (electrons) and act as recombination centres reducing V_{oc} and thus solar cell performance. Theoretical calculations show that Sn_{Cu} and Sn_{Zn} antisites donor defects could introduce deep midgap states that could trap electrons (see Figure 2.3).[52] For example the Sn_{Cu}(+/2+) transition is calculated to be around 0.35 eV above the valence band and could act as recombination centre reducing solar cell performance.[52] This theoretical calculations are in line with observation made in the framework of this thesis. In Chapter 5.1 it is shown in detail that a careful control of Sn, which can be accomplished by Ge doping, is necessary to avoid the formation of deep defects associated with Sn antisites and increase solar cell device performance.

2.2 Growth of kesterite thin film absorbers

Besides benign intrinsic defect formation in Cu-poor Zn-rich kesterite, a further reason for superior device performances in this compositional range is the avoidance of detrimental secondary phase formation during growth since theoretical calculations show that CZTS and CZTSe have a very narrow single phase compositional region.[44,52] Therefore, compositional deviations during growth can easily led to the formation of secondary phases besides CZTS(e). Cu and Sn sulphide or selenide secondary phases easily form in Cu rich or Sn rich growth conditions and these secondary phases are expected to be especially detrimental for solar cell performance due to their lower bandgap and for the case of Cu selenides due to a semi metallic behaviour which led to shunting of solar cell devices.[29,53–55] In Zn-rich growth conditions Zn sulphide or selenide secondary phases are likely to form, however, their impact on solar cell performance seems less severe and furthermore selective etching routes were successfully developed to remove these phases if they are present on the absorber surface.[55–59] A selective chemical etching was also developed for Sn sulphur-selenide secondary phases, which furthermore is passivating the absorber surface besides removing unwanted Sn related secondary phases.[60] These etching routes were used for all solar cells processed in this thesis and are described in more details in the corresponding sections. Especially in Chapter 4.1 the impact of chemical etchings on the surface composition and its implication on device performance is discussed in detail.

All synthesis routs for high performance thin film kesterite absorbers employ a two-step approach. This two-step approach consist of 1) precursor deposition followed by 2) a high temperature (T>500ºC) annealing to convert the precursor thin film into CZTS(e) and/or promote grain growth. Concerning the precursor deposition one can distinguish between vacuum and non-vacuum processes. Non-vacuum processes rely on the solution based deposition of either nanoparticle or chemical precursor mostly metal salts dissolved in appropriate solvents to form molecular inks and deposited by spin coating, doctor blading, spray coating or printing.[25,25,40,61–65] Vacuum based precursor deposition processes rely on deposition by sputtering of metallic or compound targets or co-evaporation of all elements.[66–68] After precursor deposition the annealing step to convert the precursor layer into CZTS(e) and form large grain high crystalline layers is the most crucial one. For that propose reactive thermal annealings in sulphur and/or selenium atmosphere are carried out. During annealing a sufficient high partial pressures of sulphur or selenium as well as SnS(e) have to be provided to avoid decomposition of the kesterite layers.[69–71] Redinger et al.[69] proposed following chemical equilibrium reaction

$$Cu_2ZnSnS(e)_4(solid) \Leftrightarrow Cu_2S(e)(solid) + ZnS(e)(solid) + SnS(e)(gas) + \frac{1}{2}S(e)_2(gas)$$

That is a sufficient high chalcogen or SnS(e) partial pressure has to be provided during the annealing step to avoid decomposition because the decomposition reaction stops as soon as the partial pressure of the volatile products reaches the saturation pressure (i.e. vapour pressure).[69] The most common way to provide sulphur or selenium in the annealing atmosphere is by adding elemental chalcogen inside a semi closed graphite box. However, sulphur and selenium vapour pressures are high, thus it is difficult to provide a sufficient high partial pressure during the whole annealing step. Therefore, additionally Sn or SnS(e) can be added inside a graphite box to avoid Sn losses by providing a high SnS(e) partial pressure and shifting the equilibrium reaction towards CZTS(e).[69] Furthermore, in Chapter 5 of this thesis it will be shown that by Ge doping, which is also a group IV element as it is Sn, detrimental defects related to Sn loss can be avoided and the crystallization during a high temperature annealing step improved.

3 KESTERITE THIN-FILM HETEROSTRUCTURE SOLAR CELLS

3.1 Basic principles of heterostructure thin-film solar cells

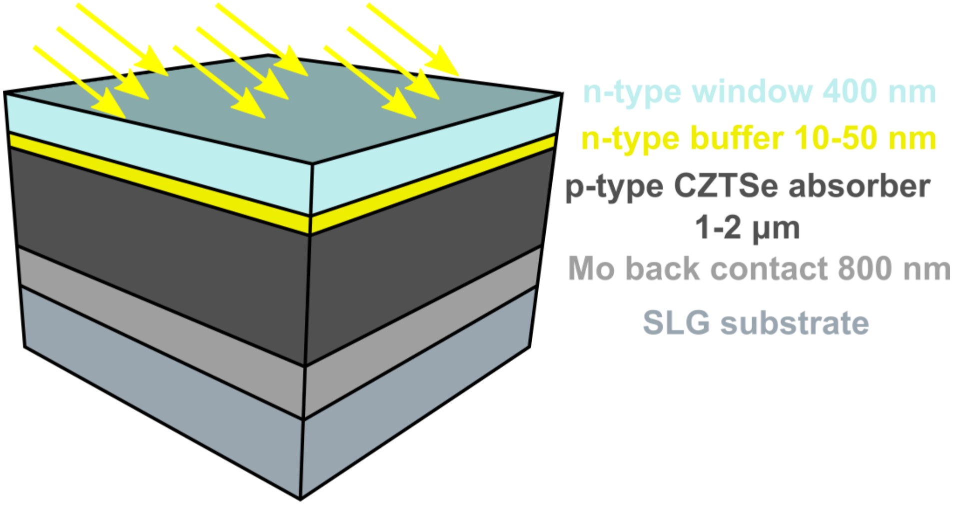

Figure 3.1. Schematic device structure of typical kesterite solar cell

A solar cell which generates current and voltage by illumination consist of an absorber that generates electron hole pairs by absorbing photons and two selective contacts. One contact allows the extraction of electrons and blocks holes, whereas the other one allows the extraction of holes and blocks electrons. For a semiconductor as absorber material, n-type and p-type doped semiconductors have exactly these properties that they have a large conductivity for electrons and a small conductivity for holes for the case of n-type and vice versa for the case of p-type material. Therefore, combining a n-type with a p-type semiconductor to form a p-n junction provides a way to separate photo generated electron hole pairs and realize a solar cell.[72] Different to most silicon solar cells where a homojunction is created by doping of the Si, chalcogenide thin film solar cells use a heterojunction architecture to create the p-n junction.[73] This heterostructure consist of a polycrystalline p-type semiconducting absorber material and some kind of n-type transparent emitter, completed with front and back contacts as it is illustrated in Figure 3.1. In the following sections a short overview of the different functional layers is given.

In a heterostructure, the electric properties of the junction strongly depend on the energy band alignment at the interface of the two different semiconducting materials. Kesterite based solar cell devices employ a p-type absorber/ n-type buffer/window heterostructure to form the p-n junction.[74] The role of the buffer layer is to provide an optimal conduction band alignment of absorber/buffer/window heterostructure which is crucial for high device performance and a so called spike like band alignment is favourable.[73,75] In a spike like alignment the conduction band minimum of the n-type buffer layer has a higher value (positive offset ΔE_c) than the conduction band minimum of the p-type absorber ,whereas the opposite occurs for the corresponding valence band maxima as it is shown in Figure 3.2. Theoretical calculations for CIGS/window heterostructures show that a slightly positive spike between 0.0-0.5 eV prevents losses in open circuit voltage (V_{oc}) due to a reduction of buffer/absorber interface recombination. Furthermore, this small spike has no negative influence on electron transport as theoretical calculation shows assuming thermionic emission across the junction.[75–77] In contrast, a too high spike in the conduction band will act as barrier for electrons, and therefore drastically reduce short circuit current (J_{sc}). The absence of a spike, i.e. a negative conduction band offset, called cliff, leads to a drastically reduction of V_{oc} due to a reduction of the interface bandgap as illustrated in Figure 3.2.[75]

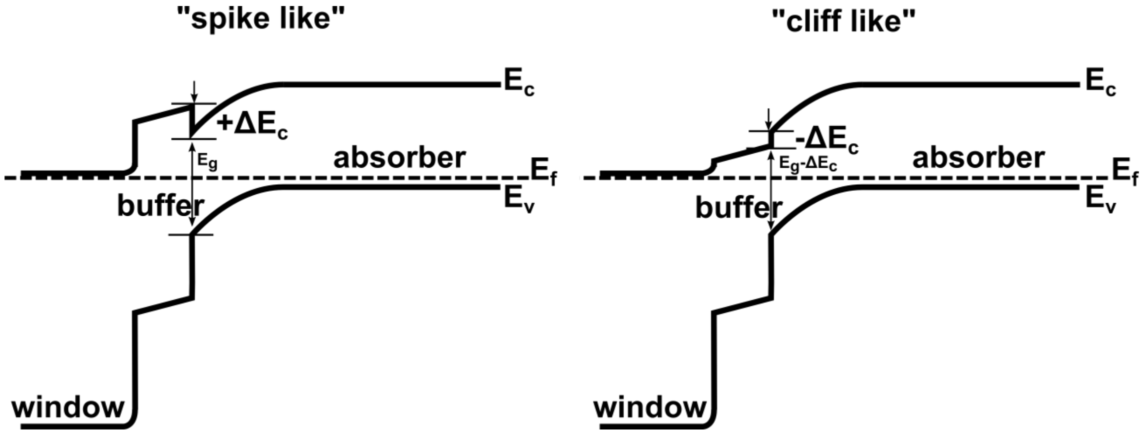

Figure 3.2. Schematics of band diagram of absorber/buffer/window heterostructure for spike and cliff like band alignment

3.1.1 Front interface and junction

As mentioned above the band alignment between p-type absorber and n-type buffer layer is crucial for high device performance, thus the front interface is one of the most critical interfaces of thin film solar cells. Up to now highest device performance in kesterite based solar cells is achieved by employing CdS as buffer layer deposited by chemical bath deposition.[25,38,74] This can be related to the favourable band alignment. For CZTSSe absorber and CdS buffer positive conduction band offsets between 0.34 eV to 0.48 eV are reported, depending on the sulphur to selenium ratio (bandgap of absorber) and CdS deposition methods, which are values in the ideal range of bandoffsets.[75,78,79] However, the deposition conditions of the buffer layer can strongly influence device performance as will be shown in Chapter 4.2 where an optimization of CdS buffer layer for CZTSe solar cells is presented. One big disadvantage of CdS is its high toxicity and its relatively low bandgap of 2.4 eV which led to absorption losses in the short wavelength region of the solar spectrum.

Therefore, there is a high interest to replace it by other non-toxic materials with higher bandgaps like Zn(O,S) which shows bandgap above 3 eV depending on the S/O ratio.[80] A further advantage of Zn(O,S) as buffer layer is that its band alignment with the kesterite absorber can be tuned depending on the S/O ratio.[81] In Chapter 4.3 an optimization of ZnS(O,OH) based buffer layer for CZTSe is presented, where by tuning the S/O ratio, i.e. the band alignment, device performance could be improved close to that of CdS reference devices.

On top of the buffer layer an n-type window layer is deposited as front contact. Here different transparent conductive oxides (TCO) are employed like indium tin oxide (ITO) or aluminium doped zinc oxide (AZO). One peculiarity in chalcogen thin film solar cell is that highest device performance is achieved by using a bi-layer front contact, which consists of a thin 50-100 nm intrinsic zinc oxide (i-ZnO) layer followed by the thicker TCO. The role of this i-ZnO layer is still under debate. The avoidance of shunt paths due to the resistive nature of this intrinsic layer and the prevention of electrical inhomogeneities are among the most plausible explanations for its beneficial nature.[82,83]

Finally, on top of the TCO a metal grid can be deposited to improve the current collection for large area cells to avoid losses due to the high sheet resistance of the TCO, as well as anti-reflective coatings are employed to reduce reflection losses.

3.1.2 Substrate and back contact

All high performance kesterite solar cells are grown in substrate configuration.[74] Highest device performance is achieved using soda lime glass as substrate followed by molybdenum back contact deposited by sputtering. Soda lime glass has the advantage that it is stable at high temperatures used during growth and more important it contains Na which can out diffuse into the kesterite absorber during synthesis.[84,85] Alkali metals especially Na and K are known from CIGS technology to be crucial dopants necessary for high device performance.[86–88] As back contact Mo is used as it is known to form a favorable ohmic contact in CIGS solar cells.[89] Since Na from the soda lime glass has to diffuse trough the Mo back contact its microstructural properties, which can be tuned by the deposition parameters like pressure or sputtering power can largely influence the Na amount in the kesterite absorber.[90,91] Several reports in literature suggest that Mo is not an ideal back contact since it decomposes the CZTS(e) layer by forming $MoS(e)_2$ and Cu, Zn and Sn binary sulfur/selenides during high temperature annealing in chalcogen atmosphere.[92–95] Different barrier layers like TiN, ZnO or TiB_2 have been proposed to overcome this problem but highest device performance so far is still reported for Mo back contacts.[96–98] However, the deposition conditions of the Mo strongly influence not only its ability to diffuse Na but also its resistivity against sulfurization/selenization, thus by employing multilayer Mo back contacts decomposition problems can be overcome.[91]

3.2 Thin film solar cell characterization

3.2.1 Basic solar cell properties

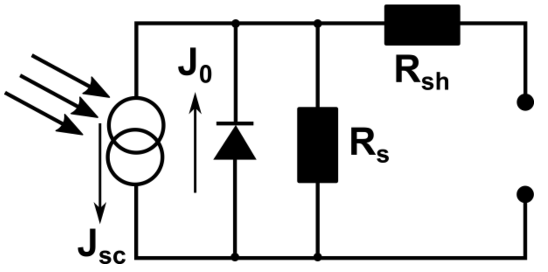

Figure 3.3. Equivalent circuit for solar cell

The current density voltage curve of a solar cell is commonly described by a 1 diode model. In Figure 3.3 the equivalent circuit is shown and the current density can be expressed by

$$J(V) = J_0\left(exp\left(\frac{q(V - R_sJ)}{AkT}\right) - 1\right) + \frac{V - R_sJ}{R_{sh}} - J_{sc} \qquad (3.1)$$

Where J_0 is the saturation current density, R_s the series resistance, k the Boltzmann constant, T the temperature, A the diode quality factor, R_{sh} the shunt resistance and J_{sc} the photo generated current which can be approximated with the short circuit current density (J_{sc}). R_s accounts for all resistive losses due to contacts and other barriers for photo current present in the solar cell. R_{sh} accounts for losses due to defects in the layers which allows alternative current path for light generated current, which leads to shunting of the solar cell. Thus, an ideal solar cell has a lowest as possible R_s and highest as possible R_{sh}. The diode quality factor gives information about the main recombination paths. For an ideal solar cell where only radiative recombination takes places its value is 1. If the main recombination path is over mid gap defects in the space charge region, i.e. Shockley Read Hall recombination in the space charge region, its value is 2.[73] The saturation current density originates from the different generation processes which are the revers processes of all present recombination processes.[72] In a general form it can be give as

$$J_0 = J_{00}\exp\left(\frac{-E_a}{AkT}\right) \qquad (3.2)$$

Where E_a describes the temperature dependence of the saturation current density and J_{00} is the reference current density which is not temperature dependent.[73] One important solar cell parameter is the open circuit voltage (V_{oc}) which corresponds to the voltage obtained when the current is zero as indicated in the JV curve in Figure 3.4 With Eq.(3.1) and (3.2) and neglecting series and shunt resistance one obtain

$$V_{oc} = \frac{E_A}{q} - \frac{AkT}{q}\ln\left(\frac{J_{00}}{J_{sc}}\right) \qquad (3.3)$$

Therefore, V_{oc} strongly depend on the dominant recombination mechanism which determines E_a and J_{00}.

For main recombination in the neutral zone of the absorber one can derive [99]

$$V_{oc} = \frac{E_g}{q} - \frac{\mathrm{k}T}{q}\ln\left(\frac{qD_nN_CN_V}{J_{sc}N_AL_D}\right) \quad (3.4)$$

where k_b is the Boltzmann constant, T the temperature, q the elementary charge, D_n the diffusion constant for electrons, $N_{C/V}$ the effective density of states in the conduction/valence band, L_D the diffusion length of electrons, N_A the acceptor density and E_g the band gap of the absorber.

For V_{oc} limitation due to recombination in the space charge region one gets[99]

$$V_{oc} = \frac{E_g}{q} - \frac{2\mathrm{k}T}{q}\ln\left(\frac{kTD_n\pi\sqrt{N_CN_V}}{J_{sc}F_mL_D}\right) \quad (3.5)$$

where $F_m = \sqrt{2qN_AV_{bm}/\varepsilon}$ is the electrical field at the position of maximum recombination (V_{bm} is the band banding). For V_{oc} limitations due to interface one gets[99]

$$V_{oc} = \frac{\Phi_b^p}{q} - \frac{\mathrm{k}T}{q}\ln\left(\frac{qS_pN_V}{J_{sc}}\right) \quad (3.6)$$

where ϕ_b^p is the barrier for holes at the interface and S_p the interface recombination velocity.
By measuring the temperature dependence of the V_{oc} and extrapolating it to 0K to obtain E_a one can see from comparing Eq. (3.3) with Eq. (3.4-6) that one can get information about the main recombination path limiting the V_{oc}.

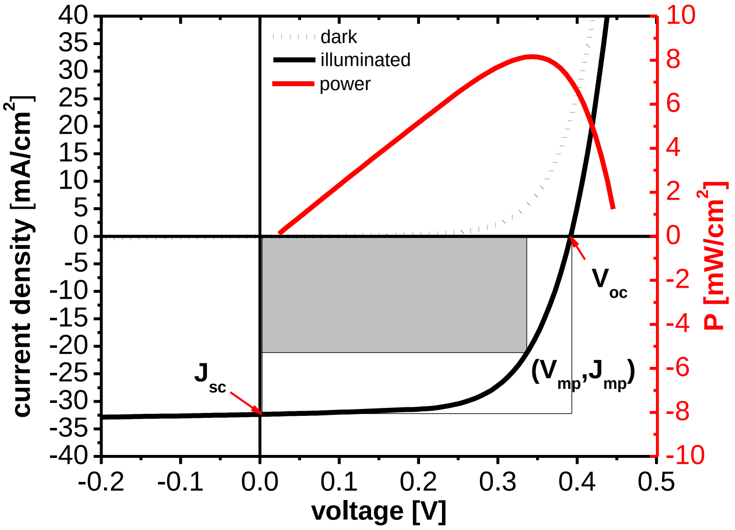

Figure 3.4. JV characteristic of CZTSe solar cell with all characteristic device parameters indicated.

To characterize solar cells in the laboratory current-voltage curves under illumination are recorded. Under standard test conditions (i.e. 25ºC) a simulated AM1.5G spectrum is used for illumination that has an integrated surface power density of 100 mW/cm^2 (=1 sun). A strong lamp together with appropriate filters to match the solar spectrum in a so called solar simulator is used for this purpose. Furthermore, by applying different wavelength filters or monochromatic light sources generation of charge carriers can be achieved just in specific layers of the heterostructure, e.g. long wavelength illumination (red light) gets absorbed just in the absorber layer due to the higher bandgap of the window and buffer layers. Therefore, by performing monochromatic or filtered JV measurements problems due to photo doping of the different layers can be investigated as will be shown in Chapter 4.2.
In Figure 3.4. a typical JV curve for a CZTSe solar cell is shown for dark and 1 sun illuminated case. The characteristic device parameters like short circuit current (J_{sc}) and open circuit voltage (V_{oc}) are indicated. Furthermore, by multiplying the current density with the applied voltage the output power can be calculated. The maximum power point (V_{mp}, J_{mp}) marks the point of maximum power that can be delivered from the solar cell. One can define then the power conversion efficiency as

$$\mathrm{eff} = \frac{P_{max}}{P_{in}} = \frac{V_{mp}J_{mp}}{P_{in}} = \frac{V_{oc}J_{sc}FF}{P_{in}} \quad (3.7)$$

where FF is called the fill factor. The fill factor is defined as the ratio of maximum power of the solar cell (product of V_{mp} and J_{mp}) to the product of J_{sc} and V_{oc}, i.e. the ratio of the gray square to the white square in Figure 3.4. Eff, J_{sc}, V_{oc} and FF are the basic device parameters to characterize the performance of a solar cell. To get more information about possible losses due to recombination or shunt and series resistance one has to analyses the JV data more deeply. Fitting JV data to the 1 diode Eq. (3.1) to obtain R_s, R_{sh}, diode quality factor A and saturation current density J_0 is not trivial. Sites and Mauk proposed a procedure based on linear fitting of $\frac{dV}{dJ}\,vs.\,(J+J_{sc})^{-1}$ with correction for shunting if necessary.[100] In this procedure one starts from a simplified 1 diode equation

$$J(V) = J_0\left(exp\left(\frac{q(V-R_sJ)}{AkT}\right)\right) + \frac{V}{R_{sh}} - J_{sc} \tag{3.8}$$

The derivative $\frac{\partial J}{\partial V}$ yields

$$\frac{\partial J}{\partial V} = \frac{1}{R_{sh}} + J_0\left(exp\left(\frac{q(V-R_sJ)}{AkT}\right)\right)\frac{q}{AkT} \tag{3.9}$$

Thus at V=0 or in reverse bias, i.e. where the exponential part is negligible small the derivative $\frac{\partial J}{\partial V}$ is equal to $\frac{1}{R_{sh}}$ or G_{sh} the shunt conductance.

Rearranging Eq. (3.8) for the voltage and building the derivate $\frac{\partial V}{\partial J}$ one gets

$$\frac{\partial V}{\partial J} = \frac{AkT}{q}\left(\frac{1-\frac{1}{R_{sh}}\frac{\partial V}{\partial J}}{J+J_{sc}-\frac{1}{R_{sh}}V}\right) + R_s \tag{3.10}$$

Therefore, by linear fitting of $\frac{\partial V}{\partial J}$ vs. $\left(\frac{1-\frac{1}{R_{sh}}\frac{\partial V}{\partial J}}{J+J_{sc}-\frac{1}{R_{sh}}V}\right)$, R_s can be derived from the intercept and A from the slope of the fit. Using the extracted R_{sh} and R_s to correct current density and voltage to plot $\left(J+J_{sc}-\frac{1}{R_{sh}}V\right)\,vs.\,(V-R_sJ)$ one can obtain J_0 and once more the diode factor A by fitting it with $y = J_0\exp(\frac{q}{AkT}x)$.

In Figure 3.5 an example for the different fittings are shown for a CZTSe solar cell.

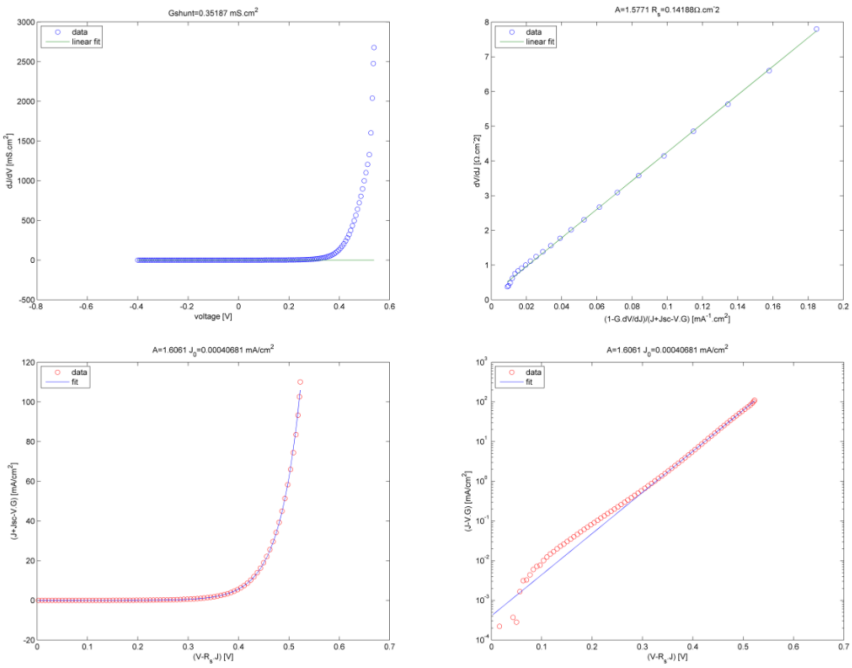

Figure 3.5. Different fitting procedures to obtain R_{sh} (G_{sh}), R_s, A, as well as J_0 from JV data CZTSe solar cell. The two lower pictures represent the same fit in linear and logarithmic scale.

3.2.2 Quantum efficiency

Besides dark and illuminated JV characterization quantum efficiency measurements give valuable information about solar cell devices. Quantum efficiency measures the number of electron-hole pairs collected at each wavelength relative to the number of photons entering the solar cell at that wavelength. Normally one measures the external quantum efficiency (EQE) which is the quantum efficiency without considering losses due to absorption in the window layer or reflection. By measuring the reflectance (R) of the solar cell one can obtain the internal quantum efficiency (IQE) as IQE=EQE/(1-R). From EQE measurements one can obtain the photo current (J_{sc}) by integrating over the desired illumination spectrum ($\Phi(\lambda)$)

$$J_{sc} = q \int EQE(\lambda)\Phi(\lambda)d\lambda \qquad (3.11)$$

The IQE can be approximated by [101]

$$IQE \cong 1 - \frac{\exp\big(-\alpha(\lambda)W(V)\big)}{\alpha(\lambda)L + 1} \qquad (3.12)$$

where $\alpha(\lambda)$ is the absorption coefficient, $W(V)$ the voltage dependent space charge region and L the minority carrier diffusion lengths. Assuming a low diffusion length L ($\alpha(\lambda)L \ll 1$), i.e. collection just in the space charge region Eq. (3.12) simplifies to

$$IQE \cong 1 - e\text{xp}(-\alpha(\lambda)W(V)) \qquad (3.13)$$

The absorption coefficient is proportional to the bandgap of the absorber by[102] $\alpha(h\upsilon) \propto \sqrt{h\upsilon - E_g}$. Thus by plotting $(\ln(1 - IQE))^2\ vs.\ h\upsilon$ and linear fitting of the long wavelength (low energy part) one can get the bandgap as the intercept with the $h\upsilon$-axis. Furthermore, the bandgap can be estimated by a peak in the derivative of the IQE $\left(\frac{dIQE}{d\lambda}\right)$ however this method can slightly overestimate the bandgap if tail states are present.[103]
From Eq. (3.12) one can also see that the IQE depends on the space charge region width W. Incomplete collection of charge carriers generated beyond W+L can be a significant loss mechanism. Applying a reverse bias enlarges W(V), thus by comparing reversed bias IQE measurements with unbiased, one can get information if incomplete collection accounts as possible loss mechanism in the device.

3.2.3 Capacitance measurements

Capacitance or more general admittance measurements are widely used to probe diode devices like solar cells.[104] Here one measures the capacitance C of the junction which is very sensitive to charge changes due to capture and emission of charge carriers from trap states. Being δQ the charge response to a small applied voltage δV, $C = \delta Q/\delta V$. In practice the measurement is performed by applying a small oscillating ac voltage with a frequency f and one measure the component of linear current response in phase with the voltage and the component which is 90º out of phase.[104] Typically this measurements are carried out using an LCR meter. From the complex admittance of the whole solar cell device measured by the LCR meter one has to determine the capacitance of the junction by employing an equivalent circuit model. The simplest model is a parallel capacitance with a parallel resistor. However, if the series resistance gets significantly high it should be considered as well to avoid errors in the interpretation of the data.[105,106] From measurements of the junction capacitance one can derive several interesting parameters of the solar cell device. One of the most prominent experimental techniques using capacitance measurements is capacitance-voltage profiling.

If one considers an n^+-p junction, that is a highly doped n side and less doped p side one can assume that the depletion only takes place in the p side. In this depletion approximation the depletion region (i.e. space charge region) is precise defined, end abruptly, and is fully depleted of free carriers. By applying a reverse bias voltage V one assumes the formation of a depletion layer thickness x and that the density of electrically active impurities (i.e. doping density) is N(x).[107] If the reverse bias voltage is then increases by dV the increase of electric field E across the junction is dE=dV/x and the increase of charges by increasing x+dx is qN(x)dx. Thus one gets[107]

$$dE = \frac{dV}{x} \;=\; \frac{q}{\varepsilon_0 \varepsilon} N(x) dx \qquad (3.14)$$

where q is the electric charge and ε the semiconductor dielectric constant. From a parallel plate capacitor which corresponds to the p-n junction in the depletion approximation the capacitance is given by

$$C = \frac{\varepsilon \varepsilon_0 A}{x} \quad \Rightarrow dx = -\frac{\varepsilon \varepsilon_0 A}{C^2} dC \qquad (3.15)$$

with A the area and ε the semiconductor dielectric constant. Combining Eq. (3.14) and (3.15) one can derive a relationship for N(x) as[104,107]

$$N(x) = -\frac{C^3}{q\varepsilon_0 \varepsilon A^2} \frac{dV}{dC} \;=\; -\frac{C^3}{q\varepsilon_0 \varepsilon A^2} \left(\frac{dC}{dV}\right)^{-1} = -\frac{2}{q\varepsilon_0 \varepsilon A^2} \left(\frac{d(C^{-2})}{dV}\right)^{-1} \qquad (3.16)$$

where x corresponds to the profiling position $x = \frac{\varepsilon \varepsilon_0 A}{C}$.

Therefore, by measuring the junction capacitance C in the dependence of the applied bias voltage V, so called CV profiling, one can derive one dimensional profiles of the doping density N(x) through the thickness of the semiconductor. However, if deep trap states are present in the absorber layer one has to be careful when interpreting CV data, because these trap states can respond to the ac voltage applied for measuring the capacitance or may adjust their charge state to the dc bias conditions and therefore create artefacts in the CV profiles.[104,108]

Besides CV profiling admittance spectroscopy (AS) is another experimental technique widely used to characterize defects in thin film solar cells. Different to CV profiling where charging and discharging of trap states by electrons create artefacts in the measurements due to the additional capacitance added, in AS one uses the fact that these capture and emission processes of electrically active traps strongly depend on the applied frequency and temperature. By applying a small oscillating voltage like it is done in admittance measurements one can modulate the occupation of trap states (defect levels). For a constant temperature a characteristic frequency can be found, where below this frequency the traps get charged and discharged and contribute to the capacitance, whereas above this frequency this defect no longer contributes to the capacitance. Therefore, a step at a characteristic frequency $\omega_0 = 2\pi f_0$ is observed in the capacitance vs. frequency sweep as can be seen in Figure 3.6 (a). Since, capturing and emission processes are also temperature dependent, one can find characteristic frequencies for each temperature. The temperature dependence of it can be given as[109,110]

$$\omega_0 = 2\nu_0 T^2 exp\left(\frac{-E_a}{kT}\right) \qquad (3.17)$$

where ν_0 is the so called attempt to escape frequency and E_a the activation energy, i.e. the energy difference between the defect level and the valence or conduction band (depending if measurements are carried out on p or n type absorbers respectively). ω_0 can be found by fitting the peak of the derivative $-dC/d\omega(\omega/kT)$ as it is shown in Figure 3.6(b). ν_0 and E_a can be extracted from an Arrhenius plot of $\ln(\omega_0/T^2) vs. \left(\frac{1}{T}\right)$, see Figure 3.6(c).

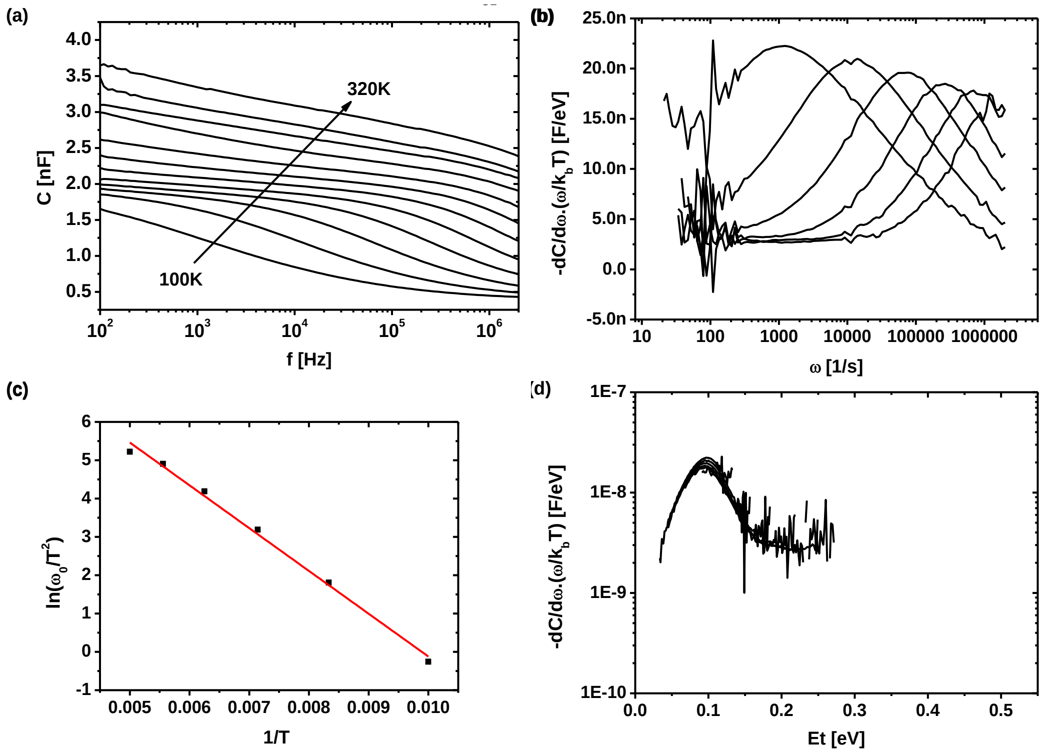

Figure 3.6. Cf measurements at different temperature (a), scaled derivative to extract ω_0 (b), Arrhenius plot to extract E_a and ν_0 (c), scaled derivative plotted against the energy E_t to illustrate defect spectra (d).

Walter et al.[109] showed that for the density of the defect one can derive

$$N_t(E_t) = -\frac{U_d^{3/2}}{W\sqrt{q}\sqrt{qU_d - (E_g - E_t)}}\frac{dC}{d\omega}\frac{\omega}{kT} \qquad (3.18)$$

where U_d is the build in voltage, W the width of the space charge region and the energy scale E_t

$$E_t = kT ln\left(\frac{\upsilon_0 T^2}{\omega}\right) \qquad (3.19)$$

If W and U_d are not known one can illustrate defect energies by plotting the scaled derivate $-dC/d\omega^*(\omega/k_b T)$ against the energy axis $E_t = kT^*\ln(\nu_0 T^2/\omega)$ as it is shown in Figure 3.6(d).

3.3 CZTSe absorber characterization

Besides characterization of kesterite based thin film solar cells, the kesterite absorber layers itself were characterized as well in detail. For morphological investigation scanning electron microscopy (SEM) is the perfect tool. Furthermore, X-ray diffraction (XRD) is the most common material characterization method. In X-ray diffraction one measured the scattered X-ray from a sample in dependence of the scattering angle. X-rays get elastically scattered from electrons and the scattered intensity is proportional to the square of the Fourier transform of the electron density of the sample. Therefore, for ordered structures like atoms in a crystal lattice, peaks at specific scattering angles are observed, which intensity depends of Fourier transform of the electron density of the atoms in the crystal.[104] Detailed structural investigation like determination of atomic positions within the crystal are not possible for Cu^+ and Zn^{2+} within the same structure because of the same amount of electrons. Neutron diffraction can help to solve this problem, due to different scattering lengths for Cu and Zn.[45] Nevertheless, from the peak positions of XRD patterns Le Bail refinements[111] can give valuable information about the lattice constants of the crystal. Furthermore, secondary phases can easily be identified from XRD measurements due to characteristic patterns for each crystal structure. However, for the case of ZnS(e) overlaps in peak position of ZnS(e) and kesterite makes its identification difficult. Here Raman spectroscopy, which theory is based on the inelastic scattering of light with vibrations of the crystal lattice can provide a solution and help to identify all possible secondary phases presented in the absorber and further probe the crystal quality.[104,112] Since the cationic composition of kesterite absorbers is crucial for device performance, compositional characterization is important. X-ray florescence (XRF) allows fast and reliable measurements. In XRF the florescence spectra of a material, which is emitted after illumination with high energy X-rays is analysed. Characteristic florescence radiation is emitted for each element, because the high energy X-ray photons can remove electrons of the inner shell of the atoms, which then is refilled by electrons from outer shells accompanied by emission of radiation of a specific wavelength.

Furthermore, more advanced characterisation techniques like transmission electron microscopy (TEM) and X-ray photoelectron spectroscopy (XPS), as well as photoluminescence (PL) measurements were used for characterization during this thesis and are explained in more detail in the specific experimental section in Chapter 4 and 5.

3.4 Current status of kesterite based thin film solar cells

Table 3.1. Selection of CZTSSe solar cells with highest device performance and comparison to record CIGS cell.

Affiliation	(Precursor) deposition method	Efficiency [%]	FF [%]	J_{sc} [mA/cm^2]	V_{oc} [mV]	E_g [eV]	$E_g/q-V_{oc}$ [V]
IBM/Solar Frontier[113]	non-vacuum	12.7	69.8	38.9	466	1.07	0.604
IBM[25]	non-vacuum	12.6[c]	69.8	35.2	513	1.13	0.617
University of Washington[114]	non-vacuum	11.8	68.1	38.8	449	1.04	0.591
EMPA[61]	non-vacuum	11.2	63.8	36.5	479	1.05	0.571
IMRA[65]	non-vacuum	10.8	65.0	32.5	510	1.18	0.670
DGIST[115]	sputtering	12.3	67.2	35.0	521	1.097	0.576
IBM[66]	co-evap.	11.6	67.3	40.6	423	1.0	0.577
IREC[67]	sputtering	10.1	66.8	33.3	453	1.04	0.587
IMEC[68]	sputtering	9.7	61.4	38.9	408	1.0	0.592
ZSW-CIGS[88]	co-evap.	21.7	79.3	36.6	746	1.13	0.384

[c] certified efficiency

In Table 3.1. an overview of the device parameters of a selection of highest performing kesterite based solar cells is shown. Currently the certified record efficiency is 12.6%.[25] All high performance devices use a two-step synthesis approach, which consist of a precursor deposition followed by a reactive thermal annealing for absorber formation and/or crystallization and grain growth. At the moment highest device performance is achieved from CZTSSe grown by a non-vacuum solution approach based on hydrazine (H_2N-NH_2) solutions.[25] However, hydrazine is highly toxic and explosive, which partly inhibit its possibility for industrial upscaling. Recently, less toxic solution approaches reach similar high efficiencies. For vacuum deposited precursors, sputtering shows most promising results, which furthermore has the advantage of possible fast upscale, due to the fact that sputtering followed by reactive thermal annealing is already successfully used in commercial CIGS module fabrication.[17,116]

However, one of the main challenges so far for kesterite solar cells is the low open circuit voltage. As was shown in Chapter 3.2.1 the V_{oc} depends on the bandgap of the absorber and is reduced due to recombination. Therefore, to compare absorbers with different bandgap a so called V_{oc} deficit is introduced, which is defined as $V_{oc\text{-}def} = E_g/q - V_{oc}$. From Table 3.1 one can clearly see that all record kesterite devices hardly overcome a V_{oc} deficit of 0.6 V, whereas record CIGS devices show V_{oc} deficits of below 0.4 V. The reasons for this lack of V_{oc} are currently intensively investigated. Besides the occurrence of detrimental secondary phases different possible explanation were proposed.

Enhanced interface recombination was proposed as one reason.[28,117–119] It could be linked to a cliff like band alignment observed for high bandgap, i.e sulphur rich kesterite absorbers and the CdS buffer layer.[120,121] However, for low bandgap, i.e. selenium rich kesterite this is not the case[68,78,121,122] and also for sulphur pure absorbers, V_{oc} losses due to the interface can be overcome by employing alternative buffer layer different than CdS with better band alignment.[123,124] Therefore, interface recombination cannot be the main cause for the high V_{oc} loss.

A low minority carrier lifetime was suggested as further reason for V_{oc} loss, however theoretical device simulation shows that low minority carrier lifetime alone does not account for all V_{oc} loss.[119,125]

Deep defects could be another reason for the lack of V_{oc}. Larramona at al. showed that by careful control of the Sn content during synthesis, the formation of deep defects related to Sn vacancies/antisites could be avoided and device performance improved. [65] Wei et al. observed a deep donor defect which compensates the CZTSSe absorber and proposed that the deep defect together with a short carrier diffusion length could be responsible for high V_{oc} deficit.[126] Furthermore, trap assisted tunnelling recombination is suggested as possible reason for low voltage.[103,127]

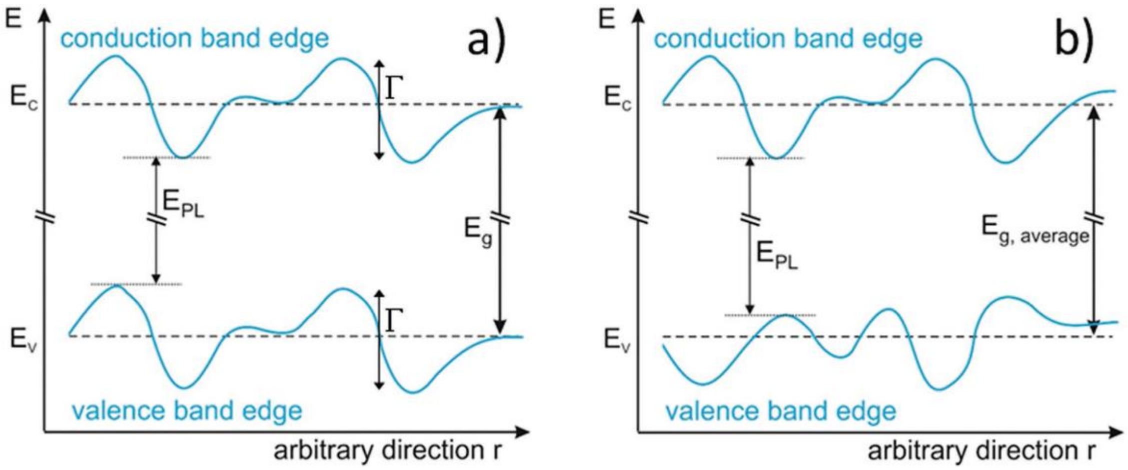

Figure 3.7. Electrostatic potential fluctuation (a) and bandgap variation (b). Picture reproduced from Bourdais et al.[49]

As a last but probably most important reason for low V_{oc} the presence of tail states were proposed.[49,119,128] Tail states are a non-zero density of states located at the bandgap edges, which reduces the optical bandgap to a so called mobility gap. Band tails are evidenced by the fact that the maximum of the peak of photoluminescence measurements of kesterite samples is usually noticeable red-shifted compared to the optical bandgap which can be explained by band tails, as band-tail to band-tail transition are observed.[119,122,128] Furthermore, a slow decay of the IQE signal below bandgap which is frequently observed in kesterite devices is another indication for sub-bandgap absorption.[103,119] Electrostatic potential fluctuations or bandgap fluctuations are proposed to be responsible for this non zero density of states within the bandgap.[119] In Figure 3.7. the effect of potential fluctuation (a) as well as band gap fluctuations (b) on the band structure are shown, where one can see that both effects create states within the bandgap. The origins of electrostatic potential fluctuation are charged defects whereas bandgap fluctuations can be explained by local in homogeneities in the absorber layer, like non-uniform composition, ordered/disordered domains or secondary phases.[49,119] Tail states can be quantified by the Urbach Energy E_u because sub-bandgap absorption can be described by $\alpha \propto \exp\left(-\frac{E_g-E}{E_u}\right)$.[129] De Wolf et al.[130] showed for different photovoltaic materials a linear relationship between Urbach energy and V_{oc} deficit, where lowest E_u resulted in lowest V_{oc} deficit. Cu/Zn disorder in the kesterite lattice was suspected to be responsible for tail states, however recent studies show that up to now no clear correlation between Cu/Zn ordering, tail states, and further V_{oc} deficit could be found and the origins of the large tails are still not totally clear.[49,50] On the whole in current kesterite device most likely several of the proposed V_{oc} limiting mechanism are present and responsible for the still low device performance and current research tries intensively to further investigate its origins and to find solutions to overcome them and solve the V_{oc} deficit of this promising earth abundant absorber material.

Goal of this thesis was to investigate efficiency limiting issues of CZTSe solar cells related especially to the front interface, i.e. buffer layer and absorber surface, as well as the absorber bulk itself. In Chapter 4.1 the importance of the surface chemistry on device performance is demonstrated. A low temperature annealing which leads to a Cu/Zn reordering of the absorber surface and grain boundaries after a necessary oxidizing etching to remove unwanted secondary phases is presented. In Chapter 4.2 an optimization of the CdS buffer layer is shown, which reduces losses due to interface especially if light active defect states are present in the buffer layer. In Chapter 4.3 this optimization was extended to Cd-free ZnS(O,OH) buffer layer. Finally, in Chapter 5.1 and 5.2 of this thesis it will be shown that by controlled doping with Ge the formation of deep defect related to Sn antisites/vacancies can be avoided and device performance, especially V_{oc} improved.

4 FRONT INTERFACE OPTIMIZATION

4.1 Complex Surface Chemistry of Kesterites: Cu/Zn Reordering after Low Temperature Postdeposition Annealing and Its Role in High Performance Devices

The work presented in the following was published in the journal Chemistry of Materials: *Chemistry of Materials 2015 27 (15), 5279-5287 DOI: 10.1021/acs.chemmater.5b01473*

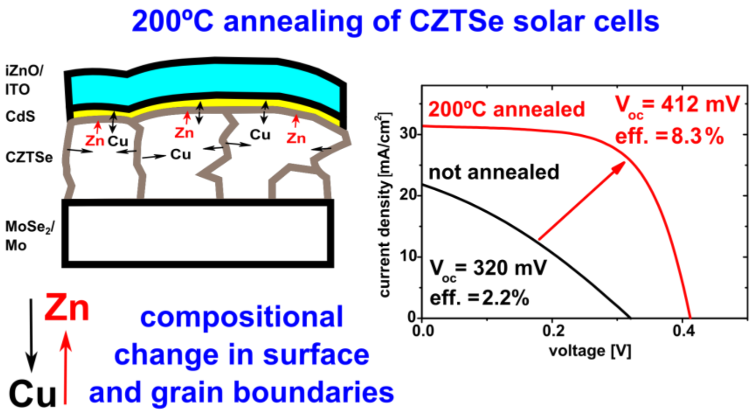

Figure 4.1. Table of content graphic showing the effects of low temperature post deposition annealing.

CHEMISTRY OF MATERIALS
Article
pubs.acs.org/cm

Complex Surface Chemistry of Kesterites: Cu/Zn Reordering after Low Temperature Postdeposition Annealing and Its Role in High Performance Devices

Markus Neuschitzer,*[‡,†] Yudania Sanchez,[‡,†] Tetiana Olar,[§] Thomas Thersleff,[∥] Simon Lopez-Marino,[†] Florian Oliva,[†] Moises Espindola-Rodriguez,[†] Haibing Xie,[†] Marcel Placidi,[†] Victor Izquierdo-Roca,[†] Iver Lauermann,[§] Klaus Leifer,[∥] Alejandro Pérez-Rodriguez,[†,⊥] and Edgardo Saucedo[†]

[†]Catalonia Institute for Energy Research- IREC, Jadins de les Dones de Negre 1, 08930 Sant Adrià de Besòs, Barcelona, Spain
[§]Helmholtz-Zentrum Berlin für Materialien und Energie GmbH, Institute for Heterogeneous Materials, 14109 Berlin, Germany
[∥]The Ångström Laboratory, Department of Engineering Sciences, Uppsala University, Box 534, 75121 Uppsala, Sweden
[⊥]IN2UB, Departament d'Electrònica, Universitat de Barcelona, C. Martí i Franquès 1, 08028 Barcelona, Barcelona, Spain

Ⓢ *Supporting Information*

ABSTRACT: A detailed study explaining the beneficial effects of low temperature postdeposition annealing combined with selective surface etchings for $Cu_2ZnSnSe_4$ (CZTSe) based solar cells is presented. After performing a selective oxidizing surface etching to remove ZnSe secondary phases typically formed during the synthesis processes an additional 200 °C annealing step is necessary to increase device performance from below 3% power conversion efficiency up to 8.3% for the best case. This significant increase in efficiency can be explained by changes in the surface chemistry which results in strong improvement of the CdS/CZTSe heterojunction commonly used in this kind of absorber/buffer/window heterojunction solar cells. XPS measurements reveal that the 200 °C annealing promotes a Cu depletion and Zn enrichment of the etched CZTSe absorber surface relative to the CZTSe bulk. Raman measurements confirm a change in Cu/Zn ordering and an increase in defect density. Furthermore, TEM microstructural investigations indicate a change of grain boundaries composition by a reduction of their Cu content after the 200 °C annealing treatment. Additionally, insights in the CdS/CZTSe interface are gained showing a significant amount of Cu in the CdS buffer layer which further helps the formation of a Cu-depleted surface and seems to play an important role in the formation of the pn-heterojunction.

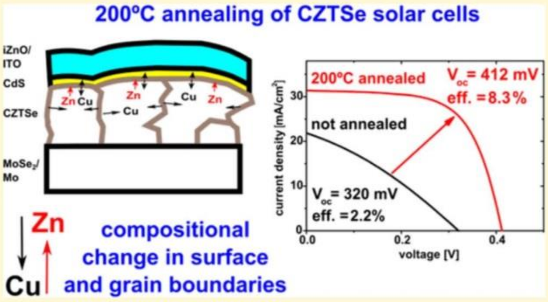

1. INTRODUCTION

Kesterite $Cu_2ZnSn(S_{1-x}Se_x)_4$ (CZTSSe) has attracted much attention in the past years as a possible replacement for chalcopyrites (CIGS = $CuIn_{1-x}Ga_xSe_2$) as an absorber layer in thin film solar cells because of its composition of more earth abundant materials. Although there are many similarities between kesterites and CIGS, there is still a large gap between record efficiencies of chalcopyrites, which are currently exceeding 21% in comparison to 12.6% for CZTSSe.[1,2] The main difference in device performance is a much higher open circuit voltage deficit (V_{oc}-deficit: E_g/q-V_{oc}; E_g is bandgap of the absorber and q is the electron charge) for CZTSSe based solar cells than for CIGS. For record CZTSSe cells the V_{oc}-deficit is around 0.6 eV, whereas record CIGS cells obtain V_{oc} deficits of 0.4 eV.[1−3] Thus, experimentally obtained V_{oc} values for kesterite based solar cells are still much lower than theoretically possible, which is currently the main efficiency limiting factor of this technology. The reasons for this high V_{oc}-deficit are not totally clear yet. Enhanced band tailing, due to electrostatic potential fluctuations induced by charged antisite defects pairs like $[Cu_{Zn}^- + Zn_{Cu}^+]$ could be one of the reasons.[4,5] Furthermore, J. Kim et al. showed that by applying a double In_2S_3/CdS buffer layer combined with a short postdeposition annealing at 250 °C to diffuse In into CdS and CZTSSe layers the V_{oc} deficit could be improved to below 0.6 eV because of an enhanced doping due to In incorporation.[6] In general, several groups report beneficial effects of low temperature post-deposition annealing either in air or inert atmosphere for kesterite based solar cells.[7−9] Already in CIGS, short air annealing is reported to improve solar cell performances due to oxygen related defect passivation and is used in devices with over 20% efficiency.[10,11] For kesterite, the aspect of low temperature annealing is especially interesting since recently an order−disorder transition was observed after low-temperature

Received: April 21, 2015
Revised: July 16, 2015

DOI: 10.1021/acs.chemmater.5b01473
Chem. Mater. XXXX, XXX, XXX−XXX

annealing at around 260 or 200 °C for the pure sulfide (CZTS) or selenide (CZTSe) compound, respectively.[12,13] Disorder at the Cu and Zn sites increases strongly above this temperature, whereas annealing below it can increase the order. NMR measurements show that [V_{Cu}+Zn_{Cu}] complexes control the random disorder created by Cu_{Zn} and Zn_{Cu} interstitial defects.[14] However, the relationship of order−disorder with point defects and their influence on device performance is not yet clearly understood. In this work, we study the complex surface chemistry of $Cu_2ZnSnSe_4$ before and after a soft postgrowth annealing and its impact on the optoelectronic parameters of the solar cells.

In the first part of this work we present the optimization of different postdeposition annealing treatments for either the CZTSe absorber, CZTSe/CdS heterojunction, or full CZTS/CdS/iZnO+ITO heterojunction solar cells and its strong impact on device performance. By applying an optimal postdeposition treatment, efficiencies could be increased from below 2% to over 8%. In the second part we reveal the influences of this annealing on the absorber, the CdS buffer layer, and especially on the CZTSe absorber surface which can explain the observed beneficial effects.

2. EXPERIMENTAL SECTION

Pure selenide kesterite absorbers (CZTSe) were grown by a two stage process. First metallic stacks of Cu/Sn/Cu/Zn were sputtered by direct current (DC) magnetron sputtering onto ZnO(10 nm)/Mo(800 nm) coated soda lime glass substrates as described in more detail in S. Lopez-Marino et al.[15] These precursor stacks (5 × 5 cm^2) are further reactively annealed in a graphite box containing elemental Se and Sn powders (100 mg Se and 5 mg Sn) inside of a conventional 3 zone tube furnace under argon atmosphere. A two-step temperature profile is used for annealing. First a selenization at 400 °C for 30 min under argon flow, keeping the pressure at 1.5 mbar, is carried out followed by a second shorter annealing at 550 °C for 15 min under static 1000 mbar argon pressure to improve crystallinity. Cooling is allowed naturally to room temperature which normally takes about 1.5 h. The final metallic composition of the CZTSe absorbers was Cu poor and Zn rich, as reported to yield highest device performance,[16] with metallic ratios of $[Cu]/([Zn]+[Sn]) = 0.80 \pm 0.02$ and $[Zn]/[Sn] = 1.18 \pm 0.07$ as measured by X-ray florescence spectroscopy (XRF). To complete solar cells a CdS buffer layer is deposited by chemical bath deposition as described elsewhere.[17] Before buffer layer deposition different chemical etchings are employed. To remove possible unwanted ZnSe secondary phases formed on the absorber surface under Zn-rich and Cu-poor growth conditions a combined $KMnO_4$ (0.01M) + H_2SO_4 (0.1 M) and Na_2S (1 M) etching was used for 40 and 60 s, respectively.[18] Solar cells are finished by depositing DC-pulsed sputtered ZnO (50 nm) and In_2O_3:SnO_2 (ITO; 90/10 wt %; 350 nm, $R_\square = 50\ \Omega cm^{-1}$) window layer. 3 × 3 mm^2 cells are separated by mechanical scribing using a manual microdiamond scriber MR200 OEG and contacted directly on the ITO for electrical characterization, without the use of metal grids and antireflective coatings.

Illuminated current density voltage (JV) curves are recorded using a Sun 3000 class AAA solar simulator from ABET technologies which is calibrated with a Si reference cell to 1 sun.

External quantum efficiencies (EQE) are measured using a Bentham PVE300 system. Reversed voltage biased EQE curves were collected by connecting a Keithley 2400 source meter directly to the primary coil of the transformer biasing the device at the desired voltage.

Raman scattering measurements were made using a Raman probe developed at IREC coupled with optical fiber to an iHR320 Horiba Jobin Yvon spectrometer. The measurements were made in back-scattering configuration focusing the excitation laser spot directly on the surface of the samples (diameter 50 μm, excitation power density <1 kW/cm^2) with an excitation wavelength of 633 nm.

Raman spectra were calibrated using a monocrystal Si reference sample before each measurement by imposing the position of the dominant Si peak at 520 cm^{-1}.

Photoluminescence (PL) measurements were made using a Horiba Jobin Yvon LabRam HR 800 −UV system coupled to a metallurgical microscope under 325 nm excitation wavelength. The measurements were performed using 2 μm diameter laser spot size and power density was kept below to 1 kW/cm^2 in order to avoid thermal effects. To perform measurements with a similar area to the Raman measurements, an area of 30 × 30 μm^2 was integrated using a scanning probe stage. Intensity and frequency calibration were performed using calibrated halogen and He lamps, respectively.

Transmission electron microscopy (TEM) analysis were carried out using a Tecnai F30 from FEI company operated at 300 kV and equipped with a Tridiem image filter from Gatan, Inc. for Electron Energy-Loss Spectrometry (EELS) measurements. The lamellae were prepared for TEM investigation using the Focused Ion Beam (FIB) in situ lift-out method and thinned to a final thickness of approximately 80 nm using a 5 kV Ga^+ beam.

X-ray photoelectron spectroscopy (XPS) measurements were performed using an Al Kα X-ray source and a CLAM4 electron spectrometer (Thermo VG Scientific). The electron spectrometer was calibrated according to D. Briggs and M. P. Seah[19] using XPS and Auger line positions of different metals (Cu 3p, Au 4f7/2, Cu L3MM, and Cu 2p3/2).

3. RESULTS

Here, first the effects of different postdeposition annealing treatments on device performance are presented. The following treatments are employed:

i) annealing of CZTSe/CdS heterojunction
ii) annealing of bare CZTSe absorber
iii) annealing of CZTSe/CdS/iZnO+ITO heterostructure (full cell)

In the second part of results, the effects of postdeposition annealing on the different layers of CZTSe/CdS/iZnO+ITO heterostructure are investigated to shed light on its beneficial effects.

3.1. Effects of Postdeposition Annealing on Device Performance.

First, a short 5 min air annealing at different temperatures directly after CdS deposition and its influence on device parameters was studied. Annealing was carried out directly after CdS buffer layer deposition on a hot plate in air hereafter called CZTSe/CdS annealing. This kind of annealing has already been reported in solar cell processing of high performance CIGS and recently in CZTSSe; however, its effects are not well understood for kesterite-based solar cells.[9,11] Prior to the CdS deposition and annealing the CZTSe absorber was etched using a combined etching of $KMnO_4$ + H_2SO_4 and Na_2S to remove possible formed ZnSe secondary phases as described elsewhere in more detail.[18] This etching was employed for all device presented in this work. The impact of this selective chemical etching in combination with postdeposition annealing on the surface chemistry will be discussed later in this work. In Figure 1 (a) the influence of 5 min CZTSe/CdS air annealing at different temperatures on the device parameters are shown. It can clearly be seen that there is a significant increase in device efficiency from below 2% to above 5% after annealing at 200 °C compared to the not annealed reference. All device parameters are improved. Annealing at a lower temperature of 150 °C increases performance as well, however less pronounced. Annealing at 250 °C is detrimental for the solar cell, due to a deterioration of the CdS layer as will be shown later. In the next step the influence of annealing time was investigated. In Figure 1 (b) the

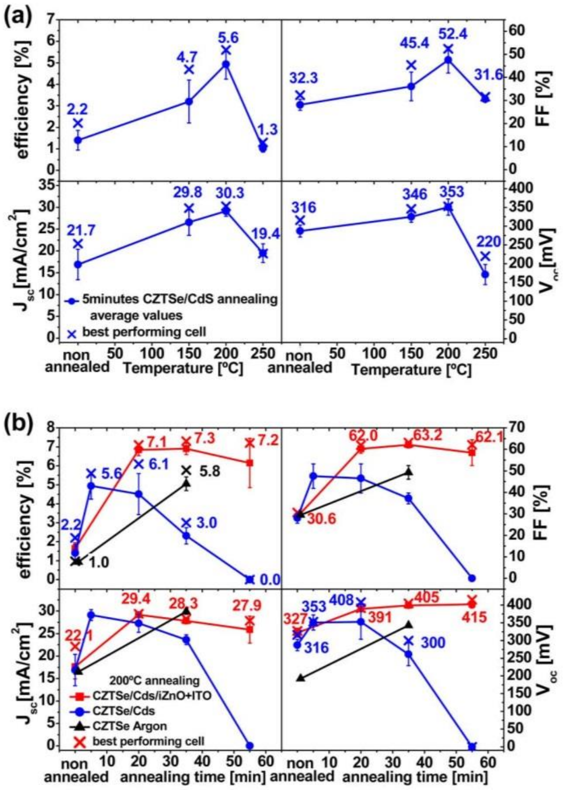

Figure 1. (a) Comparison of solar cell device performance after 5 min air annealing of CZTSe/CdS heterostructures after CdS deposition at different temperatures. A clear improvement of all device parameters after annealing at 200 °C is observed. Average values of at least 9 individual solar cells per sample and the values corresponding to the maximal efficient cell are indicated. (b) Influence of annealing time and different annealing conditions on device parameters. Full finished solar cell CZTSe/CdS/i-ZnO+ITO (red line-square symbols), CZTSe/CdS heterostructure (blue line), and CZTSe absorber in argon (black line) annealings are compared. Annealing temperature was fixed at 200 °C.

evolution of device parameters with annealing time at 200 °C which as shown before was identified as the most promising temperature for different annealing conditions is shown. For the case of CZTSe/CdS heterostructure annealing in air (blue curve) a strong increase in performance after 5 min from below 2% to above 5% is observed which starts to decrease after 20 min until the cells are completely deteriorated after 55 min. Although a decrease in average efficiency is observed after 20 min annealing, the maximum cell efficiency was achieved in this sample batch (6.1%). The further increase in V_{oc} from 353 mV to 408 mV of the best performing cells by increasing the annealing time from 5 to 20 min is remarkable. However, the standard deviation of device parameters (error bars) also increase for 20 min annealing time which can be explained by a start of deterioration of the thin CdS layer which is unprotected during annealing. To protect the CdS layer the i-ZnO+ITO window layer was deposited and full solar cell (CZTSe/CdS/i-ZnO+ITO heterostructure) air annealing at 200 °C was investigated for different times (red line). By annealing the full cell the device efficiency could be further increased from below 2% to above 7%. The best performing cell was achieved after 35 min of annealing with an efficiency of 7.3%, V_{oc} = 406 mV, J_{sc} = 28.3 mA/cm^2, and a FF of 63.2%.

For longer annealing times the average efficiency decreases again with an increasing error bars, which indicates the beginning of cell deterioration. However, V_{oc} increases slightly further after 55 min, whereas J_{sc} decreases.

To investigate if the improvement is due to annealing of the CdS layer, one bare CZTSe absorber was annealed at 200 °C for 35 min after surface etching but before CdS deposition. Here again an increase in device performance from around 1% to 5% is observed after annealing, which is however less pronounced than for full cell annealing. This strongly indicates that the beneficial effects of postdeposition annealing treatment are also due to changes in the CZTSe absorber itself and not only due to improvements of the CdS. The annealing of the bare CZTSe absorber alone was carried out in argon atmosphere instead of air because total cell deterioration was observed after air annealing for 35 min (results not shown here). Shorter annealing carried out in air led to improved device efficiencies as well but still lower than in argon atmosphere (see Supporting Information Figure S1). Thus, it cannot be concluded that the annealing must be necessarily carried out in air, although oxygen can still play an important role since the samples are exposed to air in between different processing steps.

In Figure 2 (a) the illuminated current density voltage (JV)-curves are shown for exactly the same cell before and after the optimal annealing treatment of 35 min full cell air annealing at 200 °C. Comparing the two curves before and after annealing one can clearly see that before annealing the shape of the curve looks much more distorted. Both curves start approximately at similar values at a reverse bias of −0.5 V; however, the photogenerated current gets blocked as the bias voltage is increased in the forward direction. Therefore, J_{sc} is much lower (19.0 mA/cm^2 compared to 28.3 mA/cm^2) and series resistance is elevated (8.1 Ω.cm^{-2} compared to 0.7 Ω.cm^{-2}) as expected if a barrier for electron transport is present. The existence of a barrier for photogenerated electrons, thus a problem in minority carrier (electron) collection, is confirmed by biased external quantum efficiency (EQE) measurements. In Figure 2 (b) unbiased, −0.5 V reverse voltage biased EQE and the ratio between biased and unbiased curves are shown before and after annealing. Before annealing a strong increase of the biased EQE signal is observed at a wavelength higher than 520 nm, thus as soon as absorption, i.e. creation of photogenerated charge carries inside the CZTSe layer starts. By applying a reverse bias photogenerated electrons can overcome the barrier resulting in an increased EQE signal. After annealing the unbiased EQE signal is enhanced over the full wavelength region, and no difference between biased and unbiased EQE is observed, indicating no problem with minority carrier collection. From the inflection point in the long wavelength region a bandgap of 1.02 eV was determined, in agreement with values reported for CZTSe.[20] The same value is obtained from the biased EQE before annealing. Determination of the bandgap from the unbiased EQE before annealing is difficult due to the low signal in the long wavelength region. After annealing also the short wavelength part below 520 nm of the EQE is increased indicating an improvement in the CdS buffer layer and increased transparency of the i-ZnO/ITO window layer as generally observed for transparent conductive oxides after air annealing.[21]

DOI: 10.1021/acs.chemmater.5b01473
Chem. Mater. XXXX, XXX, XXX−XXX

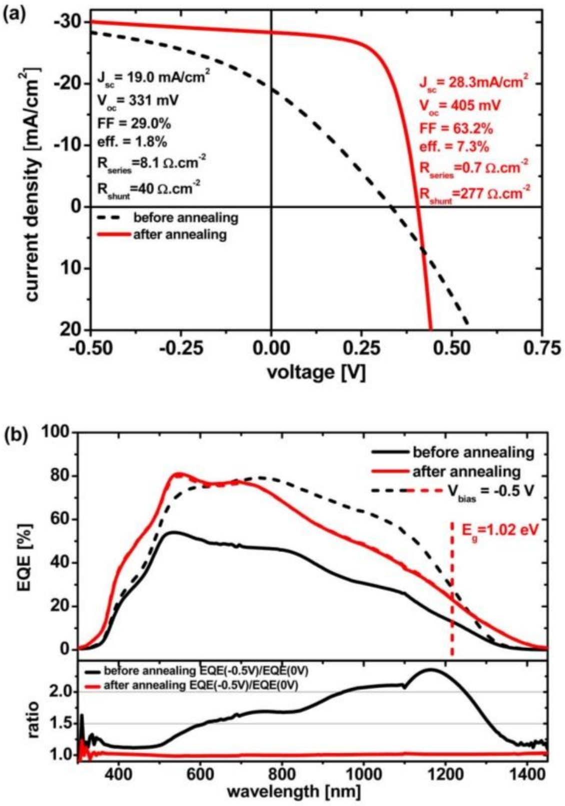

Figure 2. (a) Comparison of 1 Sun illuminated JV-curves and device paramteres of the same cell before and after 35 min full cell annealing at 200 °C. (b) Unbiased and −0.5 V reversed biased EQE measurements of the same cell before and after annealing, as well as the ratios between bias and unbiased EQE signal (−0.5 V biased and unbiased curve almost overlap over the whole wavelength range).

3.2. Influence of Annealing Treatment on CZTSe/CdS/iZnO+ITO Heterojunction.

To reveal the origins of the beneficial effects of low temperature postdeposition annealing on the device performance, possible changes in the different layers of the CZTSe/CdS/i-ZnO+ITO heterojunction solar cell were investigated after the prior presented postdeposition annealing treatments.

3.2.1. Influence of Annealing Treatment on the CdS Buffer Layer and the CZTSe/CdS Interface. In Figure 3 (a) room temperature photoluminescence (PL) spectra of the CdS layer on CZTSe after the same annealing treatments as reported before are shown. PL was measured on CZTSe/CdS samples annealed at different temperatures and times, thus the changes observed here can be directly related to changes on device performance observed for the CZTSe/CdS annealing case in Figure 1. The as grown CdS shows a very weak PL emission which slightly increases after 150 °C annealing typically for nanocrystalline CdS.[22] After 200 °C annealing the PL signal increases strongly indicating an improvement of the crystalline quality. With increasing annealing time at 200 °C the PL signal increases first but decreases again for 55 min marking the starting of CdS layer deterioration. The same is the case for annealing at 250 °C. The maxima of the PL emission shift monotonically toward lower energies with increasing annealing temperature, with a jump of 0.17 eV (from 2.46 to 2.29 eV) as soon as crystalline quality increases at 200 °C.

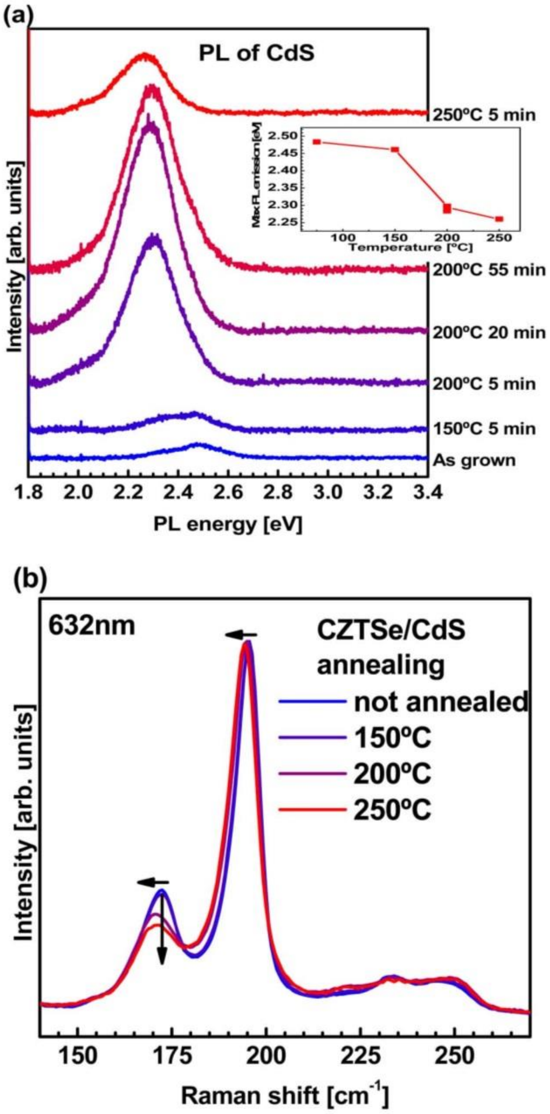

Figure 3. (a) Room temperature photoluminescence spectra of CdS grown onto CZTSe and annealed at different temperatures and times in air. The inset shows the evolution of maximum Pl peak position with annealing temperature. (b) Raman spectra of CZTSe after annealing at different temperatures. A red shift of the two most intense peaks, as well as a decrease in relative intensity is observed after annealing temperature is 200 °C.

Taking the maximum PL emission as an indication for the band gap, this means a decrease of the CdS bandgap with annealing temperature. For CZTSe and CdS a spike-like conduction band alignment between $\Delta E_c = 0.33$ eV and $\Delta E_c = 0.48$ eV is reported.[23,24] That means that the minimum of the conduction band of the CdS buffer layer is ΔE_c higher than the one of the CZTSe absorbers, whereas the valence band maximum is lower. This spike-like alignment is reported to be beneficial for solar cells performance as it prevents a loss in V_{oc}

DOI: 10.1021/acs.chemmater.5b01473
Chem. Mater. XXXX, XXX, XXX−XXX

due to decreased interface recombination.[25−27] Ideal spike-like alignments are below 0.5 eV, and a too high spike can act like a barrier in the conduction band and block minority carriers. Assuming that the annealing treatment does not change the valence band offset between CdS and CZTSe the observed band gap decrease after annealing could result in a reduction of the spike-like conduction band alignment. Since the reported ΔE_c values are in the upper limit for an ideal band alignment, a small change could have a large influence on the minority carrier transport and explain the current blocking behavior observed in the JV curves before annealing.

TEM investigations of the CdS/CZTSe interface after postdeposition thermal treatment of the full cell show that CdS defect structures extend in some regions into the i-ZnO +ITO window layer (see Figure 4). More remarkable is the high overall Cu concentration inside the CdS layer which is enhanced in the region where the defect evolves as can be seen from EELS elemental maps. Although Cu out diffusion is reported as an artifact from FIB sample preparation for the $MoSe_2$/CZTSe interface,[28] the enhancement of it in defect regions as seen here strongly indicates the observation of a real feature. In contrast no significant amount of Cd is evidenced in the CZTSe bulk, as opposed to pronounced Cd diffusion observed for CIGS/CdS heterojunctions.[29,30] From theoretical calculations it is reported that Cu is favorably incorporated on the cation site in the CdS layers, thus replacing Cd or filling Cd vacancies (V_{Cd}).[31] Cu incorporated on Cd sites (Cu_{Cd}) compensates the n-type CdS layer because Cu_{Cd} acts as a deep acceptor defect.[31,32] The possible effects of a highly compensated CdS will be discussed later.

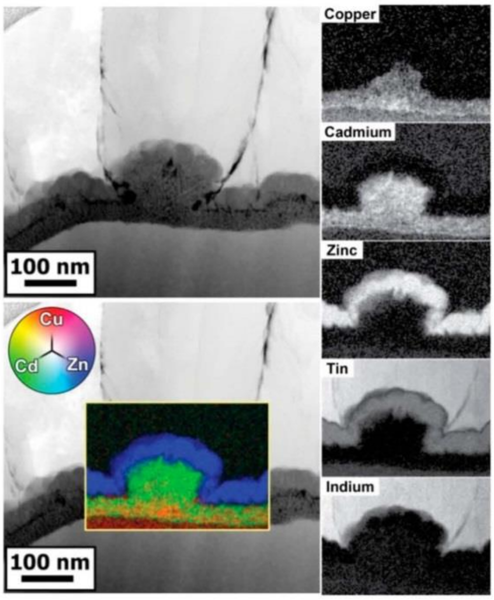

Figure 4. TEM overview image and zoom with elemental maps using EELS of CZTSe/CdS/i-ZnO/ITO solar cell after 200 °C postdeposition annealing treatment. A defect in the CdS layer is observed which extends into the i-ZnO+ITO window layer. Remarkable is the significant amount of Cu present in the CdS layer.

3.2.2. Influence of Annealing Treatment on the CZTSe Surface. Since an improvement of the device performance was also observed for a bare absorber annealed prior to CdS deposition (see Figure 1(b)) the beneficial effects cannot fully be attributed to improvements in the CdS. Raman measurements on absorbers annealed at different temperatures show interesting changes in peak position and intensity (see Figure 3b). The annealing was applied to the CZTSe/CdS heterostructure (without iZNO+ITO), and Raman measurements were carried out on full devices, i.e. the same devices presented in Figure 1. This is possible due to the fact that the iZnO+ITO and CdS layers are almost transparent for the 632 nm laser used. To ensure that the changes visible are not due to the influence of the CdS layer or iZnO+ITO window, bare absorbers were annealed at different temperatures and measured showing the same trends (see Supporting Information Figure S2). After annealing at 200 °C and above, a redshift in the main A-mode (at around 197 cm^{-1}) and the second most intense peak at around 170 cm^{-1}, peak broadenings, as well as a large decrease in intensity of the peak at around 170 cm^{-1} are present. This indicates a decrease in crystal domain size related to changes in Cu/Zn-ordering, since the peak at 170 cm^{-1} is composed of several modes sensitive to Cu-vibrations.[33,34] This decrease in relative peak intensities of the two main CZTSe Raman peaks is also observed for samples with decreasing the relative Cu content.[35] Cu, Zn, and Sn enriched surfaces show the same Raman behavior as can be seen in the Supporting Information Figure S3. Furthermore, a decrease in the relative peak intensity of the peak at 170 cm^{-1} accompanied by an increase of peak width of the main A mode is reported for an increase of disorder in the Zn and Cu sites.[13] Raman measurements mainly probe the surface near region of the CZTSe absorber (100−150 nm),[36] which is one of the most crucial zones for solar cell devices.

To further investigate specifically a possible change in the surface chemistry after annealing, XPS measurements were carried out combined with in situ annealing inside the XPS chamber (see Supporting Information Figure S4). Here 200 °C was used as the annealing temperature because the best performance was obtained for this annealing temperature as shown before. First the CZTSe absorber layer was etched as it is the case for all devices presented in this work using a combined $KMnO_4 + H_2SO_4$ and Na_2S etching, which removes effectively possible ZnSe secondary phases and is used as our standard etching for Zn-rich Cu-poor absorbers. Different combinations of surface etching reported for kesterites like KCN and a combination of KCN and $KMnO_4 + H_2SO_4$ and Na_2S and its influence on device performance were studied as well and are presented in the Supporting Information.[37] In Figure 5 the evolution of the relative cation composition extracted from XPS data with annealing time at 200 °C is shown. A clear decrease of Cu and increase of Zn concentration in the CZTSe absorber surface is revealed, whereas the Sn surface concentration stays almost constant.

3.2.3. Influence of Annealing Treatment on CZTSe Bulk. TEM microstructural analyses were carried out to further investigate possible changes inside the CZTSe bulk as shown in Figure 6. Here, solar cells from the same batch are compared, one with a postdeposition annealing step at 200 °C of the full device (eff. = 6.7%, V_{oc} = 395 mV, J_{sc} = 30.2 mA/cm2, FF = 55.8%; with efficiency below 2% before annealing) and one without this step (eff. = 1.8%, V_{oc} = 240 mV, J_{sc} = 22.4 mA/cm2, FF = 32.7%). EELS elemental maps reveal that for nonannealed devices a significant amount of Cu is found in the grain boundaries which is not obvious for the postdeposition

DOI: 10.1021/acs.chemmater.5b01473
Chem. Mater. XXXX, XXX, XXX−XXX

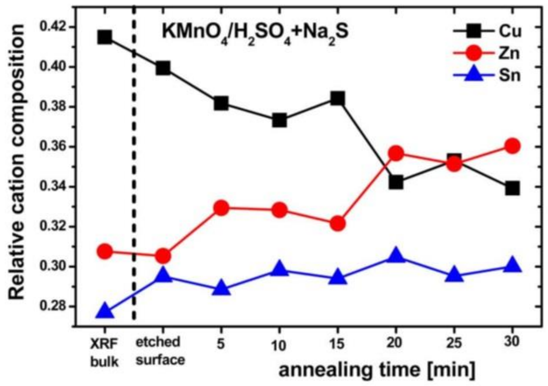

Figure 5. . Evolution of relative cation composition after different annealing times at 200 °C extracted from XPS data and comparison with XRF bulk composition for KMnO$_4$/H$_2$SO$_4$+Na$_2$S etched CZTSe absorbers.

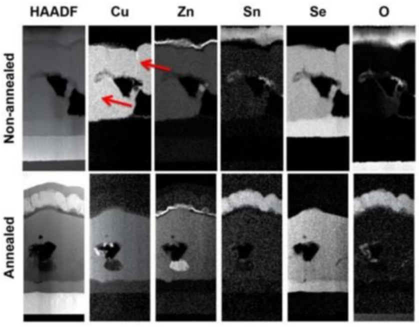

Figure 6. High angle annular dark field image (HAADF) TEM image and EELS maps of CZTSe/CdS/i-ZnO/ITO solar cell before and after 200 °C postdeposition annealing treatment. For the nonannealed sample a clear segregation of Cu in the grain boundaries is visible (highlighted with red arrows) which is not obvious for an annealed one.

annealed case as shown in Figure 6. Therefore, TEM measurements suggest that not only the Cu surface composition is changing after annealing treatments but also the grain boundaries. Furthermore, it can be seen in Figure 6 that voids are present in the CZTSe layer, and Cu and Zn rich secondary phases, possibly ZnSe and Cu$_x$Se$_y$, are segregated inside them as commonly observed.[6,38] In both nonannealed as well as annealed samples there is evidence for regions with enhanced Sn and O signal near the voids, suggesting the presence of SnOx; however, different than recent auger nanoprobe studies of air annealed CZTSSe absorbers no SnOx is found in the grain boundaries.[9]

The highest cell efficency achieved with the combination of KMnO$_4$ + H$_2$SO$_4$ and Na$_2$S etching together with an optimal full cell postdeposition annealing treatment of 35 min at 200 °C is 8.3% as shown in Figure 7 which was below 3% before postdeposition annealing. The improvement of approximately 1% in comparison to the other reported cells in the study is related to improvements in the CdS buffer layer deposition as described elsewhere.[17]

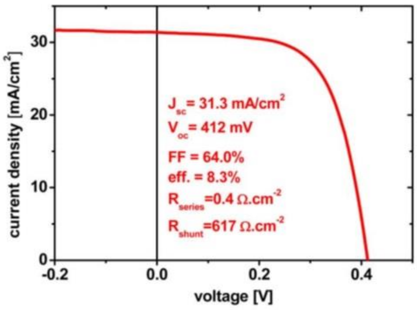

Figure 7. Best performing cell after optimized full cell postdeposition annealing treatment. Average device parameters obtained of 6 3 × 3 mm individual scribed solar cells of the sample are J_{sc} = (30.5 ± 1) mA/cm^2, V_{oc} = (414 ± 6) mV, FF = 61 ± 2%, and eff. = (7.7 ± 0.5)%.

4. DISCUSSION

One part of the improved device efficiency after full cell postdeposition thermal annealing can be attributed to improvements in the CdS buffer layer as evidenced by PL and EQE measurements. However, since the KMnO$_4$/H$_2$SO$_4$ and Na$_2$S etched and prior to CdS deposition postannealed absorber showed strong efficiency improvements, the main changes are likely due to the change in the CZTSe absorber and especially the absorber surface itself. There is an increase in defect density after annealing treatments evidenced by Raman spectroscopy; however, the more crucial changes are observed in the absorber surface. Here, especially the specific etching to remove unwanted ZnSe secondary phases plays an important role. After employing this oxidizing etching (KMnO$_4$ + H$_2$SO$_4$ and Na$_2$S), the surface composition measured by XPS is similar to the bulk composition measured by XRF (see Figure 5). However, device performance is low. Only after an annealing treatment high efficient devices can be obtained. The annealing treatment leads to a Cu depletion and Zn enrichment of the CZTSe surface which seems to be crucial for high device performance. We found a temperature around 200 °C as the optimal temperature for full cell annealing, since it is low enough not to deteriorate the CdS layer as evidenced by PL but high enough to promote cation diffusion.

Haight et al. show that for kesterites using the same solution based hydrazine process as for the current world record efficient kesterite solar cells, the kesterite surface is Cu depleted and Zn rich relative to the bulk composition, which confirms our findings that the Cu-poor Zn-rich surface is essential for high devices performance.[39] There it is also shown that this Cu depletion and Zn enrichment of the surface can be increased by air annealing as we observe in this work. However, no conclusions about the influence on device performance are made. Furthermore, theoretical calculations for pure sulfide nonstoichiometric kesterite (Cu-poor, Zn-rich) show that a Cu depleted surface termination is energetically favorable and that this surface termination does not show any deep gap state which could be detrimental to solar cell performance, whereas a Cu-rich surface produces detrimental states in the bandgap.[40] We propose that after the necessary oxidizing etching used to remove ZnSe from the surface of the CZTSe layer synthesized using this 2 stage approach (sputtering of metal precursors and selenization) also the kesterite surface gets partly etched.[18] This destroys the Cu-poor Zn-rich favorable surface termination. A thermal annealing afterward promotes the Cu and Zn diffusion

DOI: 10.1021/acs.chemmater.5b01473
Chem. Mater. XXXX, XXX, XXX−XXX

and restores low energy Cu-poor and Zn-rich surface termination. All investigated CZTSe absorbers here are so-called A-type kesterite (Cu-poor, Zn-rich, Sn-stoichiometric), for which the formation of the $[V_{Cu}+Zn_{Cu}]$ defect cluster is most likely.[41] After low temperature thermal annealing the disorder in Zn and Cu sites increases as evidenced by Raman measurements. We suggest an increase of $[V_{Cu}+Zn_{Cu}]$ cluster density in the surface near region due to Cu^{1+} diffusion toward the bulk compensated with a Zn^{2+} enrichment of the surface. Additionally, as evidenced by TEM, Cu diffuses into the CdS buffer layer which can further increase the Cu depletion of the CZTSe surface. $[V_{Cu}+Zn_{Cu}]$ clusters increase the band bending that facilitates the separation of photogenerated charge carries which is in agreement with the observed improved minority carrier collection after thermal annealing.[5] Furthermore, TEM measurements indicate a change in grain boundary composition. Prior to the postdeposition annealing treatment grain boundaries are Cu rich. Several microstructural investigations report Cu rich grain boundaries in kesterite absorber material and list it as a possible reason for low obtained V_{oc} values.[42,43] After annealing treatment, no Cu rich grain boundaries are observed, thus annealing does not only change the CZTSe surface but also promotes a change in grain boundary composition. This could be a further reason for the observed V_{oc} increase because Cu rich grain boundaries can decrease the bandgap of CZTSe locally which is reported to be detrimental to device performance (V_{oc}) due to enhanced recombination, as theoretical simulations suggest.[44] This is in line with recent nanoscale investigations of grain boundaries in the high performance CZTSSe device where Cu poor grain boundaries are observed after air annealing.[9] However, different than the findings of K. Sardashti et al.[9] for CZTSSe absorbers no SnO_x could be evidenced in the grain boundaries. Only small nanoclusters in the vicinity of voids in the CZTSe bulk seems to be Sn and O rich. Contrary to CIGS no evidence in favor of Cd diffusion into the CZTSe bulk was observed in these experiments. Similar results were reported in recent atom probe tomography studies of annealed CdS/CZTS interfaces for annealing temperature of 200 °C.[45] This is in contrast to the proposed junction formation in CIGS/CdS heterojunction devices where V_{Cu} at the surface region is reported to be beneficial, as it allows Cd diffusion into V_{Cu}.[46,47] Thus, in the kesterites, a different mechanism for the formation of an optimal CdS/CZTSe heterojunction should be considered. Remarkable is the high Cu concentration in the CdS layer revealed by TEM. Enhanced Cu diffusion into the CdS layer from the underlying CTZS absorber was also observed by Hiroi et al. and linked to an enhanced V_{oc} obtained for this sample.[48] Cu is known to act as an acceptor defect when incorporated on cation sites in CdS.[32] A highly compensated CdS could imply totally different junction properties as for CdS/CIGSe where Cd diffusion into the Cu-poor CIGS surface is crucial. A strong compensated CdS layer in the ITO+iZnO/CdS/CZTSe heterojunction could lead to the formation of a metal–insulator-semiconductor (MIS)-like structure.

5. CONCLUSION

In this work we presented a systematic study of the strong influences of surface etching combined with postdeposition low temperature annealings on the CZTSe absorber surface, the CdS buffer layer, and the CdS/CZTSe interface and further on device performance. We showed that if an oxidizing etching route consisting of $KMnO_4/H_2SO_4$ and Na_2S is used to remove ZnSe secondary phases from the surface the resulting surface composition is close to the XRF bulk composition. A thermal annealing changes the surface composition to a Cu poorer and Zn richer configuration. This change in surface composition led to improvement of device efficiencies from below 3% to up to 8.3%. Additionally to changes in the Cu surface concentration, TEM EELS mapping shows a reduction of Cu in the grain boundaries after annealing treatment. This annealing induced change toward a more benign composition of the GB can further explain the gain in V_{oc} compared to nonannealed devices.

A second result of this work is an improved understanding of the CdS/CZTSe heterojunction. TEM EELS maps detect a large amount of Cu inside of the CdS layer. It is known that Cu as dopant in CdS can strongly compensate the n-type CdS, thus the formation of a metal–insulator-semiconductor junction becomes plausible. In conclusion, we revealed that a Cu-poor Zn-rich surface composition is mandatory for high device performance in CZTSe based solar cells. Beneficial surface passivation and grain boundary composition can be achieved by tailored chemical surface treatments combined with annealing. Getting insights in the complex surface chemistry of CZTSe absorbers and its strong influences on solar cells performance opens up new ways to further optimize kesterite based solar cells by developing processing routes (e.g., postdeposition annealings, surface modifications by chemical and/or physical ways) for a better and easier control of the surface composition.

■ ASSOCIATED CONTENT

Ⓢ Supporting Information

Influence of annealing atmosphere during CZTSe absorber annealing on device efficiency (Figure S1), Raman spectra of bare CZTSe absorber annealing and of Cu, Zn, and Sn enriched CZTSe surfaces and their device performance (Figure S2 and S3), and XPS measurements on CZTSe absorbers etched with different solutions in dependence of annealing time and the influence of different surface etchings and annealing on device performance (Figures S4–S7). The Supporting Information is available free of charge on the ACS Publications website at DOI: 10.1021/acs.chemmater.5b01473.

■ AUTHOR INFORMATION

Corresponding Author

*E-mail: mneuschitzer@irec.cat.

Author Contributions

‡These authors contributed equally.

Notes

The authors declare no competing financial interest.

■ ACKNOWLEDGMENTS

This research was supported by the Framework 7 program under the project KESTCELLS (FP7-PEOPLE-2012-ITN-316488), by the European Regional Development Founds (ERDF, FEDER Programa Competitivitat de Catalunya 2007–2013), and by MINECO (Ministerio de Economía y Competitividad de España) under the NOVACOST project (PCIN-2013-128-C02-01, Solar-ERA.NET) and SUNBEAM project (ENE2013-49136-C4-1-R). Authors from IREC and the University of Barcelona belong to the M-2E (Electronic Materials for Energy) Consolidated Research Group and the XaRMAE Network of Excellence on Materials for Energy of the "Generalitat de Catalunya". E.S. thanks the Government of

Spain for the "Ramon y Cajal" fellowship (RYC-2011-09212), Y.S. for the PTA fellowship (PTA2012-7852-A), M.E.-R. for the FPI-MINECO (BES-2011-045774), M.P. for MINECO postdoctoral fellow (FPDI-2013-18968), and H.X. thanks the "China Scholarship Council" fellowship (CSC No. 201206340113).

■ REFERENCES

(1) Jackson, P.; Hariskos, D.; Wuerz, R.; Wischmann, W.; Powalla, M. Compositional Investigation of Potassium Doped Cu(In,Ga)Se_2 Solar Cells with Efficiencies up to 20.8%: Compositional Investigation of Potassium Doped Cu(In,Ga)Se_2 Solar Cells with Efficiencies up to 20.8%. *Phys. Status Solidi RRL* **2014**, *8*, 219–222.

(2) Wang, W.; Winkler, M. T.; Gunawan, O.; Gokmen, T.; Todorov, T. K.; Zhu, Y.; Mitzi, D. B. Device Characteristics of CZTSSe Thin-Film Solar Cells with 12.6% Efficiency. *Adv. Energy Mater.* **2014**, *4*, 1301465.

(3) Lee, Y. S.; Gershon, T.; Gunawan, O.; Todorov, T. K.; Gokmen, T.; Virgus, Y.; Guha, S. $Cu_2ZnSnSe_4$ Thin-Film Solar Cells by Thermal Co-Evaporation with 11.6% Efficiency and Improved Minority Carrier Diffusion Length. *Adv. Energy Mater.* **2015**, *5*, doi: 10.1002/aenm.201401372.

(4) Gokmen, T.; Gunawan, O.; Todorov, T. K.; Mitzi, D. B. Band Tailing and Efficiency Limitation in Kesterite Solar Cells. *Appl. Phys. Lett.* **2013**, *103*, 103506.

(5) Chen, S.; Walsh, A.; Gong, X.-G.; Wei, S.-H. Classification of Lattice Defects in the Kesterite Cu_2ZnSnS_4 and Cu_2 $ZnSnSe_4$ Earth-Abundant Solar Cell Absorbers. *Adv. Mater.* **2013**, *25*, 1522–1539.

(6) Kim, J.; Hiroi, H.; Todorov, T. K.; Gunawan, O.; Kuwahara, M.; Gokmen, T.; Nair, D.; Hopstaken, M.; Shin, B.; Lee, Y. S.; et al. High Efficiency $Cu_2ZnSn(S,Se)_4$ Solar Cells by Applying a Double In_2S_3/CdS Emitter. *Adv. Mater.* **2014**, *26*, 7427–7431.

(7) Hironiwa, D.; Sakai, N.; Kato, T.; Sugimoto, H.; Tang, Z.; Chantana, J.; Minemoto, T. Impact of Annealing Treatment before Buffer Layer Deposition on $Cu_2ZnSn(S,Se)_4$ Solar Cells. *Thin Solid Films* **2015**, *582*, 151–153.

(8) Repins, I.; Beall, C.; Vora, N.; DeHart, C.; Kuciauskas, D.; Dippo, P.; To, B.; Mann, J.; Hsu, W.-C.; Goodrich, A.; et al. Co-Evaporated $Cu_2ZnSnSe_4$ Films and Devices. *Sol. Energy Mater. Sol. Cells* **2012**, *101*, 154–159.

(9) Sardashti, K.; Haight, R.; Gokmen, T.; Wang, W.; Chang, L.-Y.; Mitzi, D. B.; Kummel, A. C. Impact of Nanoscale Elemental Distribution in High-Performance Kesterite Solar Cells. *Adv. Energy Mater.* **2015**, *5*, doi: 10.1002/aenm.201402180.

(10) Rau, U.; Braunger, D.; Herberholz, R.; Schock, H. W.; Guillemoles, J.-F.; Kronik, L.; Cahen, D. Oxygenation and Air-Annealing Effects on the Electronic Properties of Cu(In,Ga)Se_2 Films and Devices. *J. Appl. Phys.* **1999**, *86*, 497.

(11) Chirilă, A.; Reinhard, P.; Pianezzi, F.; Bloesch, P.; Uhl, A. R.; Fella, C.; Kranz, L.; Keller, D.; Gretener, C.; Hagendorfer, H.; et al. Potassium-Induced Surface Modification of Cu(In,Ga)Se2 Thin Films for High-Efficiency Solar Cells. *Nat. Mater.* **2013**, *12*, 1107–1111.

(12) Scragg, J. J. S.; Choubrac, L.; Lafond, A.; Ericson, T.; Platzer-Björkman, C. A Low-Temperature Order-Disorder Transition in Cu_2ZnSnS_4 Thin Films. *Appl. Phys. Lett.* **2014**, *104*, 041911.

(13) Rey, G.; Redinger, A.; Sendler, J.; Weiss, T. P.; Thevenin, M.; Guennou, M.; El Adib, B.; Siebentritt, S. The Band Gap of $Cu_2ZnSnSe_4$: Effect of Order-Disorder. *Appl. Phys. Lett.* **2014**, *105*, 112106.

(14) Paris, M.; Choubrac, L.; Lafond, A.; Guillot-Deudon, C.; Jobic, S. Solid-State NMR and Raman Spectroscopy To Address the Local Structure of Defects and the Tricky Issue of the Cu/Zn Disorder in Cu-Poor, Zn-Rich CZTS Materials. *Inorg. Chem.* **2014**, *53*, 8646–8653.

(15) López-Marino, S.; Placidi, M.; Pérez-Tomás, A.; Llobet, J.; Izquierdo-Roca, V.; Fontané, X.; Fairbrother, A.; Espíndola-Rodríguez, M.; Sylla, D.; Pérez-Rodríguez, A.; et al. Inhibiting the absorber/Mo-Back Contact Decomposition Reaction in $Cu_2ZnSnSe_4$ Solar Cells: The Role of a ZnO Intermediate Nanolayer. *J. Mater. Chem. A* **2013**, *1*, 8338–8343.

(16) Polizzotti, A.; Repins, I. L.; Noufi, R.; Wei, S.-H.; Mitzi, D. B. The State and Future Prospects of Kesterite Photovoltaics. *Energy Environ. Sci.* **2013**, *6*, 3171–3182.

(17) Neuschitzer, M.; Sanchez, Y.; López-Marino, S.; Xie, H.; Fairbrother, A.; Placidi, M.; Haass, S.; Izquierdo-Roca, V.; Perez-Rodriguez, A.; Saucedo, E. Optimization of CdS Buffer Layer for High-Performance $Cu_2ZnSnSe_4$ Solar Cells and the Effects of Light Soaking: Elimination of Crossover and Red Kink: CdS and Effects of Light Soaking: Elimination of Crossover and Red Kink. *Prog. Photovoltaics* **2015**, DOI: 10.1002/pip.2589.

(18) López-Marino, S.; Sánchez, Y.; Placidi, M.; Fairbrother, A.; Espindola-Rodríguez, M.; Fontané, X.; Izquierdo-Roca, V.; López-García, J.; Calvo-Barrio, L.; Pérez-Rodríguez, A.; et al. ZnSe Etching of Zn-Rich $Cu_2ZnSnSe_4$: An Oxidation Route for Improved Solar-Cell Efficiency. *Chem. - Eur. J.* **2013**, *19*, 14814–14822.

(19) Briggs, D.; Seah, M. P. *Practical Surface Analysis*, 2nd ed.; Wiley; Salle + Sauerländer: Chichester; New York, Aarau, 1990.

(20) Ahn, S.; Jung, S.; Gwak, J.; Cho, A.; Shin, K.; Yoon, K.; Park, D.; Cheong, H.; Yun, J. H. Determination of Band Gap Energy (E_G) of $Cu_2ZnSnSe_4$ Thin Films: On the Discrepancies of Reported Band Gap Values. *Appl. Phys. Lett.* **2010**, *97*, 021905.

(21) Gonçalves, G.; Elangovan, E.; Barquinha, P.; Pereira, L.; Martins, R.; Fortunato, E. Influence of Post-Annealing Temperature on the Properties Exhibited by ITO, IZO and GZO Thin Films. *Thin Solid Films* **2007**, *515*, 8562–8566.

(22) Park, K.; Yu, H. J.; Chung, W. K.; Kim, B.-J.; Kim, S. H. Effect of Heat-Treatment on CdS and CdS/ZnS Nanoparticles. *J. Mater. Sci.* **2009**, *44*, 4315–4320.

(23) Haight, R.; Barkhouse, A.; Gunawan, O.; Shin, B.; Copel, M.; Hopstaken, M.; Mitzi, D. B. Band Alignment at the Cu2ZnSn-$(S_xSe_{1-x})_4$/CdS Interface. *Appl. Phys. Lett.* **2011**, *98*, 253502.

(24) Li, J.; Wei, M.; Du, Q.; Liu, W.; Jiang, G.; Zhu, C. The Band Alignment at CdS/$Cu_2ZnSnSe_4$ Heterojunction Interface. *Surf. Interface Anal.* **2013**, *45*, 682–684.

(25) Scheer, R.; Schock, H. W. *Chalcogenide Photovoltaics Physics, Technologies, and Thin Film Devices*; Wiley-VCH; John Wiley: Weinheim; Chichester, 2011.

(26) Gloeckler, M.; Sites, J. R. Efficiency Limitations for Wide-Band-Gap Chalcopyrite Solar Cells. *Thin Solid Films* **2005**, *480–481*, 241–245.

(27) Minemoto, T.; Matsui, T.; Takakura, H.; Hamakawa, Y.; Negami, T.; Hashimoto, Y.; Uenoyama, T.; Kitagawa, M. Theoretical Analysis of the Effect of Conduction Band Offset of window/CIS Layers on Performance of CIS Solar Cells Using Device Simulation. *Sol. Energy Mater. Sol. Cells* **2001**, *67*, 83–88.

(28) Timo Wätjen, J.; Scragg, J. J.; Edoff, M.; Rubino, S.; Platzer-Björkman, C. Cu out-Diffusion in kesterites—A Transmission Electron Microscopy Specimen Preparation Artifact. *Appl. Phys. Lett.* **2013**, *102*, 051902.

(29) Rusu, M.; Bär, M.; Lehmann, S.; Sadewasser, S.; Weinhardt, L.; Kaufmann, C. A.; Strub, E.; Röhrich, J.; Bohne, W.; Lauermann, I.; et al. Three-Dimensional Structure of the Buffer/absorber Interface in CdS/$CuGaSe_2$ Based Thin Film Solar Cells. *Appl. Phys. Lett.* **2009**, *95*, 173502.

(30) Hiepko, K.; Bastek, J.; Schlesiger, R.; Schmitz, G.; Wuerz, R.; Stolwijk, N. A. Diffusion and Incorporation of Cd in Solar-Grade Cu(In,Ga)Se_2 Layers. *Appl. Phys. Lett.* **2011**, *99*, 234101.

(31) Varley, J. B.; Lordi, V. Intermixing at the Absorber-Buffer Layer Interface in Thin-Film Solar Cells: The Electronic Effects of Point Defects in Cu(In,Ga)$(Se,S)_2$ and $Cu_2ZnSn(Se,S)_4$ Devices. *J. Appl. Phys.* **2014**, *116*, 063505.

(32) Nishidate, K.; Sato, T.; Matsukura, Y.; Baba, M.; Hasegawa, M.; Sasaki, T. Density-Functional Electronic Structure Calculations for Native Defects and Cu Impurities in CdS. *Phys. Rev. B: Condens. Matter Mater. Phys.* **2006**, *74*, 035210.

(33) Mortazavi Amiri, N. B.; Postnikov, A. Electronic Structure and Lattice Dynamics in Kesterite-Type $Cu_2ZnSnSe_4$ from First-Principles

Calculations. *Phys. Rev. B: Condens. Matter Mater. Phys.* **2010**, *82*, 205204.

(34) Dimitrievska, M.; Fairbrother, A.; Saucedo, E.; Pérez-Rodríguez, A.; Izquierdo-Roca, V. Influence of Compositionally Induced Defects on the Vibrational Properties of Device Grade Cu2ZnSnSe4 Absorbers for Kesterite Based Solar Cells. *Appl. Phys. Lett.* **2015**, *106*, 073903.

(35) Márquez-Prieto, J.; Ren, Y.; Miles, R. W.; Pearsall, N.; Forbes, I. The Influence of Precursor Cu Content and Two-Stage Processing Conditions on the Microstructure of $Cu_2ZnSnSe_4$. *Thin Solid Films* **2015**, *582*, 220−223.

(36) Salomé, P. M. P.; Fernandes, P. A.; Leitão, J. P.; Sousa, M. G.; Teixeira, J. P.; da Cunha, A. F. Secondary Crystalline Phases Identification in $Cu_2ZnSnSe_4$ Thin Films: Contributions from Raman Scattering and Photoluminescence. *J. Mater. Sci.* **2014**, *49*, 7425−7436.

(37) Tanaka, T.; Sueishi, T.; Saito, K.; Guo, Q.; Nishio, M.; Yu, K. M.; Walukiewicz, W. Existence and Removal of Cu2Se Second Phase in Coevaporated $Cu_2ZnSnSe_4$ Thin Films. *J. Appl. Phys.* **2012**, *111*, 053522.

(38) Buffière, M.; Brammertz, G.; Batuk, M.; Verbist, C.; Mangin, D.; Koble, C.; Hadermann, J.; Meuris, M.; Poortmans, J. Microstructural Analysis of 9.7% Efficient $Cu_2ZnSnSe_4$ Thin Film Solar Cells. *Appl. Phys. Lett.* **2014**, *105*, 183903.

(39) Haight, R.; Shao, X.; Wang, W.; Mitzi, D. B. Electronic and Elemental Properties of the $Cu_2ZnSn(S,Se)_4$ Surface and Grain Boundaries. *Appl. Phys. Lett.* **2014**, *104*, 033902.

(40) Xu, P.; Chen, S.; Huang, B.; Xiang, H. J.; Gong, X.-G.; Wei, S.-H. Stability and Electronic Structure of Cu_2ZnSnS_4 Surfaces: First-Principles Study. *Phys. Rev. B: Condens. Matter Mater. Phys.* **2013**, *88*, 045427.

(41) Lafond, A.; Choubrac, L.; Guillot-Deudon, C.; Deniard, P.; Jobic, S. Crystal Structures of Photovoltaic Chalcogenides, an Intricate Puzzle to Solve: The Cases of CIGSe and CZTS Materials. *Z. Anorg. Allg. Chem.* **2012**, *638*, 2571−2577.

(42) Wang, K.; Shin, B.; Reuter, K. B.; Todorov, T.; Mitzi, D. B.; Guha, S. Structural and Elemental Characterization of High Efficiency Cu_2ZnSnS_4 Solar Cells. *Appl. Phys. Lett.* **2011**, *98*, 051912.

(43) Bag, S.; Gunawan, O.; Gokmen, T.; Zhu, Y.; Todorov, T. K.; Mitzi, D. B. Low Band Gap Liquid-Processed CZTSe Solar Cell with 10.1% Efficiency. *Energy Environ. Sci.* **2012**, *5* (5), 7060−7065.

(44) Kanevce, A.; Repins, I.; Wei, S.-H. Impact of Bulk Properties and Local Secondary Phases on the $Cu_2(Zn,Sn)Se_4$ Solar Cells Open-Circuit Voltage. *Sol. Energy Mater. Sol. Cells* **2015**, *133*, 119−125.

(45) Tajima, S.; Asahi, R.; Isheim, D.; Seidman, D. N.; Itoh, T.; Hasegawa, M.; Ohishi, K. Atom-Probe Tomographic Study of Interfaces of Cu2ZnSnS4 Photovoltaic Cells. *Appl. Phys. Lett.* **2014**, *105*, 093901.

(46) Nakada, T.; Kunioka, A. Direct Evidence of Cd Diffusion into $Cu(In, Ga)Se_2$ Thin Films during Chemical-Bath Deposition Process of CdS Films. *Appl. Phys. Lett.* **1999**, *74*, 2444.

(47) Kiss, J.; Gruhn, T.; Roma, G.; Felser, C. Theoretical Study on the Structure and Energetics of Cd Insertion and Cu Depletion of $CuIn_5Se_8$. *J. Phys. Chem. C* **2013**, *117*, 10892−10900.

(48) Hiroi, H.; Sakai, N.; Kato, T.; Sugimoto, H. High Voltage Cu_2ZnSnS_4 Submodules by Hybrid Buffer Layer. *Photovoltaic Specialists Conference (PVSC), 2013 IEEE 39th*, 2013, 0863−0866.

Supporting information

The complex surface chemistry of kesterites: Cu/Zn re-ordering after low temperature post deposition annealing and its role in high performance devices

Markus Neuschitzer[†], Yudania Sánchez[†], Tetiana Olar[§], Thomas Thersleff[¤], Simon López-Marino[†], Florian Oliva[†], Moises Espindola-Rodriguez[†], Haibing Xie[†], Marcel Placidi[†], Victor Izquierdo-Roca[†], Iver Lauermann[§], Klaus Leifer[¤], Alejandro Perez-Rodriguez[†,Δ], and Edgardo Saucedo[†]

[†]Catalonia Institute for Energy Research- IREC, Jadins de les Dones de Negre 1, 08930 Sant Adrià de Besòs (Barcelona), Spain

[§]Helmholtz-Zentrum Berlin für Materialien und Energie GmbH, Institute for Heterogeneous Materials, Berlin, Germany

[¤]The Ångström Laboratory, Department of Engineering Sciences, Uppsala University, Box 534, Uppsala, Sweden

ΔIN2UB, Departament d'Electrònica, Universitat de Barcelona, C. Martí i Franquès 1, 08028 Barcelona, Spain.

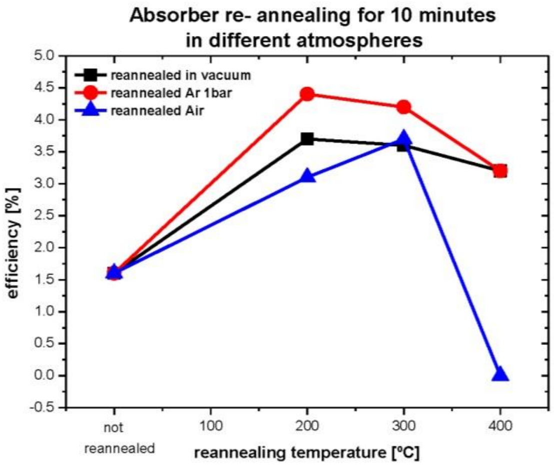

Figure S1. Maximal devices efficiencies of bare absorbers reannealed in diffenert atmospheres and temperatures.

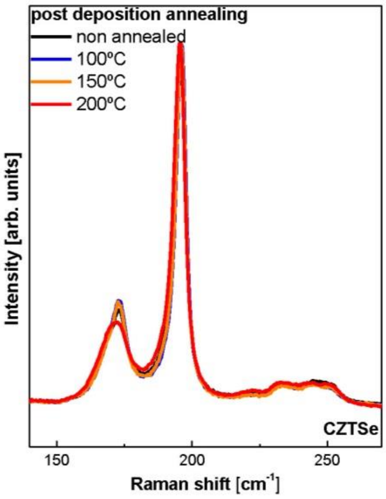

Figure S2. Raman spectra of bare CZTSe absorber annealed in argon at different temperatures. There is a clear decrease in the ratio of ratio of the main Raman peak at 197 cm^{-1} and second most intens peak at at around 170 cm^{-1} as well as a red shift of the main peak visible for annealing temperature of 200ºC. Here the annealing was carried out on bare CZTSe absorber layers and the same features as in the main manuscript are observed. Thus an influence of CdS and iZnO+ITO window layer on this measurments can be excluded.

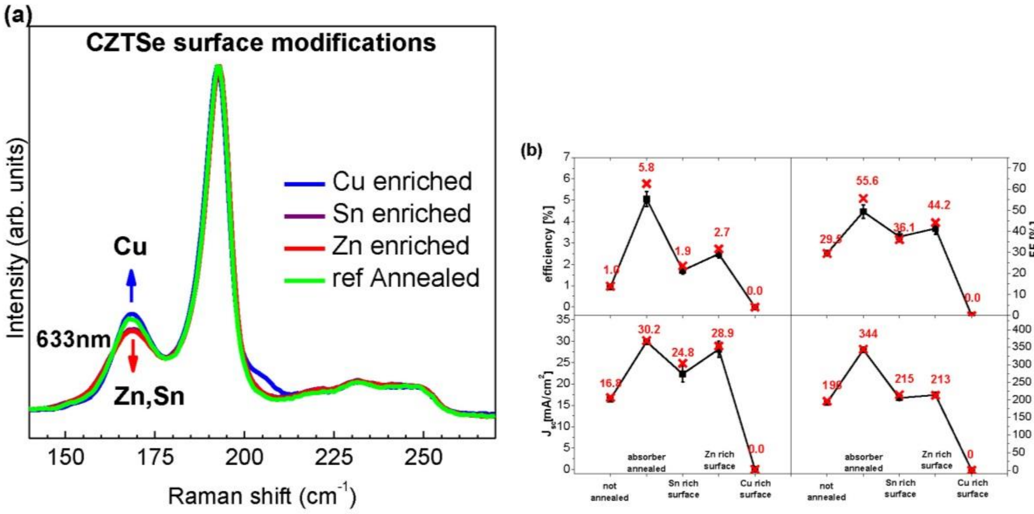

Figure S3. (a) Raman spectra of CZTSe absorber with artificially Cu, Zn, Sn enriched 5 nm surfaces. Cu, Zn, Sn enriched surface were prepared by evaporating 5nm of elemental Cu, Zn or Sn ontop of CZTSe absorber and further annealing at 200ºC for 30 minutes in argon atmosphere. (b) device performance of absorbers with artificially Cu, Zn or Sn enriched surfaces showing that Cu rich surface is detrimental.

XPS analysis and influence of different surface etchings on device performance.

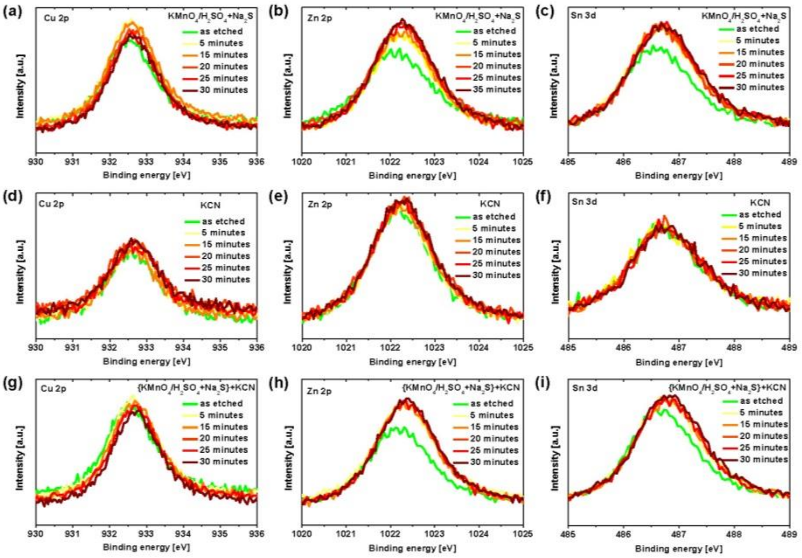

Figure S4. XPS peaks of Cu 2p, Zn 2p, and Sn 3d from CZTSe absorber surface after (a)-(c) $KMnO_4/H_2SO_4+Na_2S$, (d)-(f) KCN only, and (g)-(i) $KMnO_4/H_2SO_4+Na_2S+KCN$ etchings and different times of in-situ annealing at 200°C.

In Figure S4 XPS peaks of Cu 2p, Zn 2p and Sn 3d are shown after different surface etching and annealing times at 200°C. First of all the effect of a combined $KMnO_4+H_2SO_4$ and Na_2S etching, which removes effectively possible ZnSe secondary phases and is used as our standard etching for Zn-rich Cu-poor absorbers was investigated. Furthermore, KCN only etching (10 wt. % for 30 seconds), which is widely reported as standard etching in CIGS and CZTSSe for the removal of Cu rich secondary phases and oxides and the combination of $KMnO_4+H_2SO_4$ and Na_2S with KCN are studied.[1] For the case of $KMnO_4+H_2SO_4$ and Na_2S etching (Figure S4 (a)-(c)) after 5 minutes annealing first an increase in all peak intensities is observed. This can be explained by evaporation of a monolayer of OH- radicals which is present after wet chemical etchings and attenuate the XPS signal (see Figure S5). Then, with increasing annealing time a decrease of Cu 2p peak and increase of Zn 2p are observed, whereas the Sn 3d peak stays almost constant. Thus, a decrease of Cu and increase of Zn concentration in the CZTSe absorber surface is revealed. From fitting the spectra of Figure S4 the relative cation composition for each etching case are extracted in dependance of the annealing time and compared to XRF bulk composition (see Figure S6). For the KCN only etched case no pronounced changes are observed (Figure S6 (a)). In general the relative Zn concentration is much higher than the bulk composition measured by XRF. This can be explained by possible presence of ZnSe secondary phases on the absorber surface which cannot be removed by KCN.[2] The case of the combined etching of $KMnO_4+H_2SO_4$ and Na_2S with KCN shows again the same behavior as for the $KMnO_4+H_2SO_4$ and Na_2S etching, with the sole difference that the Cu-concentration is already lower before annealing than for the non KCN case (Figure 6 (b)). A further decrease in Cu concentration and increase in Zn concentration with increased annealing time at 200 °C is observed.

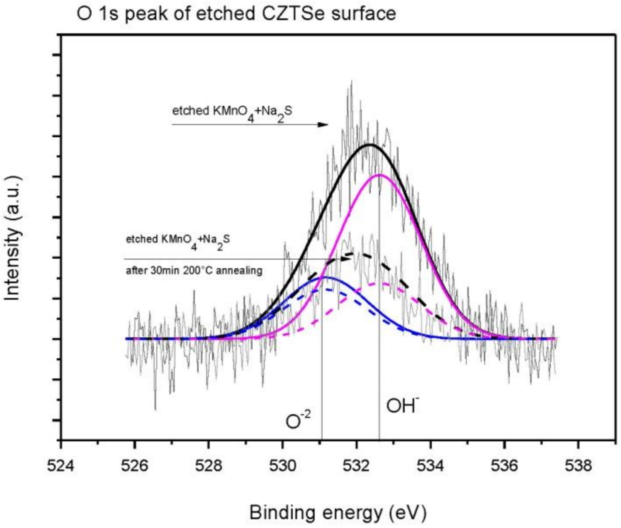

Figure S5. XPS peaks and fitting of O^{-2} and OH$^-$ contributions of etched CZTSe surface before and after 30 minutes annealing showing evaporation of OH monolayer which is present after wet chemical etching. After annealing the shoulder corresponding to the OH$^-$ peak is reduced.

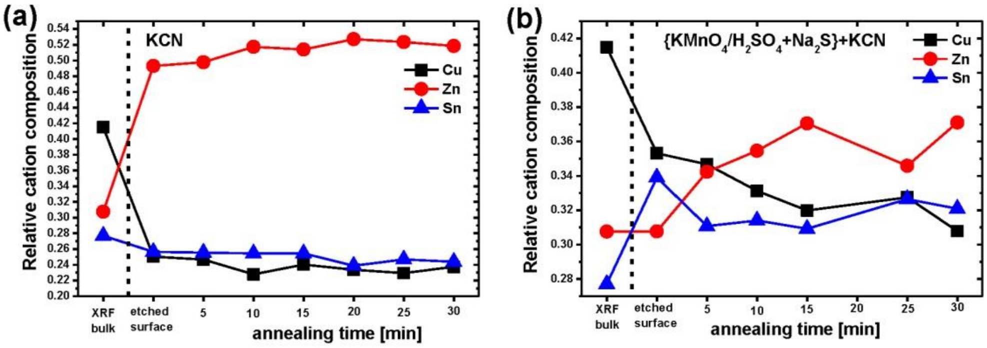

Figure S6. Evolution of relative cation composition after different annealing times at 200°C extracted from XPS data and comparison with XRF bulk composition for (a) KCN only, and (b) KMnO$_4$/H$_2$SO$_4$+Na$_2$S+KCN etched CZTSe absorbers for comparision with Figure 5 in the original manuscript.

To study the influence of this chemical and thermal induced surface modifications on device performance, solar cells using the 3 different etching routines where produced from the same absorber batch (see Figure S7 (a)). For as prepared devices again low efficient devices around 2% where obtained if KMnO$_4$+H$_2$SO$_4$ and Na$_2$S or KMnO$_4$+H$_2$SO$_4$ and Na$_2$S and KCN etchings where used. However, after an annealing treatment at 200°C of the full cell efficiency increased to above 6%, 7.3% for the best case. The difference between KMnO$_4$+H$_2$SO$_4$ and Na$_2$S and KMnO$_4$+H$_2$SO$_4$ and Na$_2$S combined with KCN etched devices are minimal. In contrary, as prepared devices produced from KCN only etched absorbers shows efficiencies around 5% and did not increase after annealing. Efficiency even decreased slightly. Raman measurements of these devices before and after annealing indicate a decrease in intensity of the peak at 170 cm^{-1} together with a red shift of the two main peaks. However, there are no differences in Raman for different surface etchings observed. This further confirms that the improvement after annealing treatment is mainly due to changes in the CZTSe absorber surface layer itself. The lower performance of KCN only etched devices could be explained by the possible presence of ZnSe secondary phases on the surface as observed under Zn-rich Cu-poor growth conditions for this synthesis method, which could not be removed by using KCN etchings.[2,3]

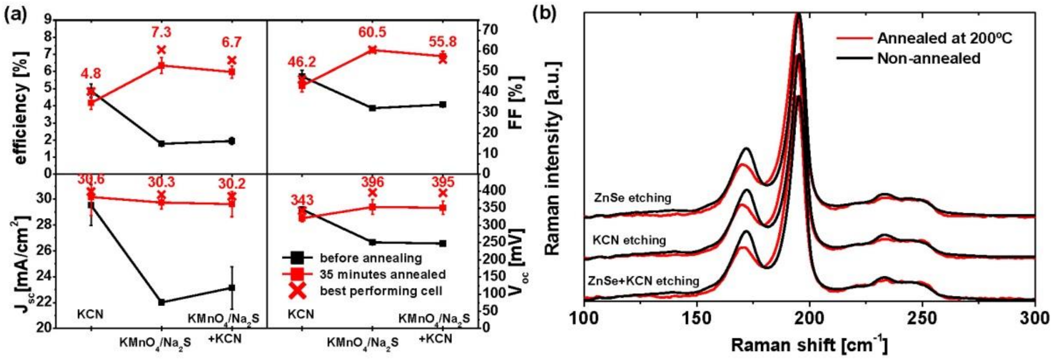

Figure S7. (a) Influence of different CZTSe absorber sur-face etchings before CdS deposition on device perfor-mance and its change after 200ºC annealing of the full cell. (b) Raman spectra of the best cells before and after annealing for different surface etchings (ZnSe etching = $KMnO_4/H_2SO_4 + Na_2S$).

Improvements of device performance after post deposition annealing is only observed when the oxidizing ZnSe etching route ($KMnO_4/H_2SO_4 + Na_2S$) is used. Therefore, the main focus on understanding this beneficial effect has to be on changes of the absorber surface properties.

Although recently an order-disorder transition was reported at around 200ºC for selenium pure CZTSe[4], the beneficial effects on device performance observed in this work cannot fully be related to this phenomena because devices etched with KCN and annealed did not show changes in device efficiency, however the same changes in the Raman spectra as for annealed $KMnO_4/H_2SO_4 + Na_2S$ etched samples are present.

Since KCN only etched samples show medium device performance (5%) without any annealing and also a very low Cu concentration in the XPS surface composition it could be argued that first of all the Cu poor surface is mandatory. Cu poor surfaces can be achieved not only by the KCN etch, but also, as we demonstrate, by thermal annealing after $KMnO_4+H_2SO_4$ and Na_2S etchings. However, the Cu-poor surface is not enough for good device performance. Certain Zn enrichment is also necessary as can be seen in the non-annealed device which was etched with $KMnO_4+H_2SO_4$ and Na_2S and subsequently with KCN. Here, the Cu surface concentration is lower than for the $KMnO_4+H_2SO_4$ and Na_2S only etched case, subsequently requiring an annealing treatment, which induces a Zn enrichment and further Cu depletion, to achieve high device performance.

Additional References

(1) Tanaka, T.; Sueishi, T.; Saito, K.; Guo, Q.; Nishio, M.; Yu, K. M.; Walukiewicz, W. Existence and Removal of Cu2Se Second Phase in Coevaporated Cu2ZnSnSe4 Thin Films. *J. Appl. Phys.* **2012**, *111* (5), 053522.

(2) López-Marino, S.; Sánchez, Y.; Placidi, M.; Fairbrother, A.; Espindola-Rodríguez, M.; Fontané, X.; Izquierdo-Roca, V.; López-García, J.; Calvo-Barrio, L.; Pérez-Rodríguez, A.; et al. ZnSe Etching of Zn-Rich Cu2ZnSnSe4: An Oxidation Route for Improved Solar-Cell Efficiency. *Chem. – Eur. J.* **2013**, *19* (44), 14814–14822.

(3) Xie, H.; Sánchez, Y.; López-Marino, S.; Espíndola-Rodríguez, M.; Neuschitzer, M.; Sylla, D.; Fairbrother, A.; Izquierdo-Roca, V.; Pérez-Rodríguez, A.; Saucedo, E. Impact of Sn(S,Se) Secondary Phases in Cu $_2$ ZnSn(S,Se) $_4$ Solar Cells: A Chemical Route for Their Selective Removal and Absorber Surface Passivation. *ACS Appl. Mater. Interfaces* **2014**, *6* (15), 12744–12751.

(4) Rey, G.; Redinger, A.; Sendler, J.; Weiss, T. P.; Thevenin, M.; Guennou, M.; Adib, B. El; Siebentritt, S. The Band Gap of Cu2ZnSnSe4: Effect of Order-Disorder. *Appl. Phys. Lett.* **2014**, *105* (11), 112106.

4.2 Optimization of CdS Buffer Layer for High-Performance Cu2ZnSnSe4 Solar Cells and the Effects of Light Soaking: Elimination of Crossover and Red Kink.

The work presented in the following was published in the journal Progress in Photovoltaics: Research and Applications:
Prog. Photovolt: Res. Appl., 23: 1660–1667. doi:10.1002/pip.2589.

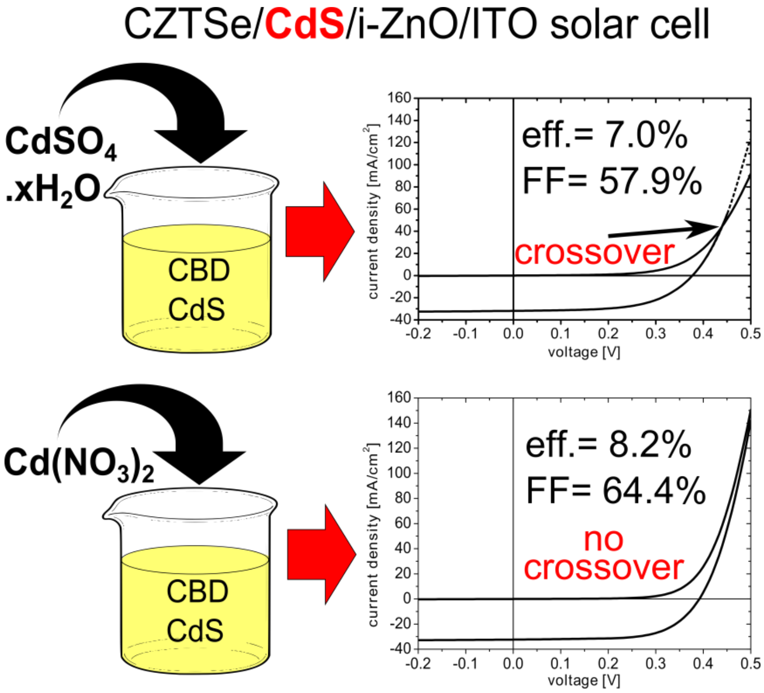

Figure 4.2. Table of content graphic showing the effects of optimizing the CdS buffer layer by changing the precursor salt for the chemical bath deposited CdS.

Progress in
PHOTOVOLTAICS

PROGRESS IN PHOTOVOLTAICS: RESEARCH AND APPLICATIONS
Prog. Photovolt: Res. Appl. (2015)

DOI: 10.1002/pip.2589

SHORT COMMUNICATION

Optimization of CdS buffer layer for high-performance $Cu_2ZnSnSe_4$ solar cells and the effects of light soaking: elimination of crossover and red kink

Markus Neuschitzer[1], Yudania Sanchez[1], Simon López-Marino[1], Haibing Xie[1],
Andrew Fairbrother[1], Marcel Placidi[1], Stefan Haass[2], Victor Izquierdo-Roca[1],
Alejandro Perez-Rodriguez[1,3] and Edgardo Saucedo[1]*

[1] Catalonia Institute for Energy Research—IREC, Jardins de les Dones de Negre 1, 08930 Sant Adrià de Besòs (Barcelona), Spain
[2] Empa—Swiss Federal Laboratories for Materials Science and Technology, Laboratory for Thin Films and Photovoltaics, 8600 Dübendorf, Switzerland
[3] IN2UB, Departament d'Electrònica, Universitat de Barcelona, C. Martí i Franquès 1, 08028 Barcelona, Spain

ABSTRACT

A spike-like conduction band alignment of kesterite absorbers with a CdS buffer layer is one of the key factors for high-performance solar cells using this buffer/absorber heterojunction combination. However, it can also be the origin of fill factor and current-reducing distortions in current–voltage curves, such as light/dark curve crossover, or an s-like curve shape for long wavelength monochromatic illumination (red kink) if light-dependent defect states are present in the buffer layer. In this work, we show that by changing the cadmium precursor source from sulfate to nitrate salts for the chemical bath deposited cadmium sulfide for $Cu_2ZnSnSnSe_4$/CdS heterojunction solar cells red kink can be eliminated, and crossover greatly improved (and eliminated entirely after light soaking). These improvements lead to a decrease in series resistance and an increase in fill factor and increase power conversion efficiency from 7.0% to 8.2%. We attribute this improvement to a reduction of deep level acceptor-like traps states inside the CdS layer, which are responsible for an increase of the conduction band spike up to a current blocking value for the sulfate precursor case. Furthermore, the effects of light soaking will be discussed. Copyright © 2015 John Wiley & Sons, Ltd.

KEYWORDS
thin film solar cells; buffer layer; crossover; light soaking; chalcogenides

***Correspondence**
Edgardo Saucedo, Catalonia Institute for Energy Research—IREC, Jardins de les Dones de Negre 1, 08930 Sant Adrià de Besòs (Barcelona), Spain.
E-mail: esaucedo@irec.cat

Received 27 June 2014; Revised 5 November 2014; Accepted 3 December 2014

1. INTRODUCTION

Kesterite $Cu_2ZnSn(S_{1-x}Se_x)_4$ (CZTSSe) is a promising candidate to replace chalcopyrites ($CuIn_{1-x}Ga_xSe_2$ - CIGS) as an absorber layer in thin-film solar cells due to its composition of more earth-abundant materials. Although in addition to a high-quality bulk absorber material, an optimal band alignment and optical architecture of the absorber/buffer/window heterostructure is crucial for high-performance solar cells, as highlighted in the results published by Wang et al. on the world record 12.6% efficient CZTSSe solar cell [1]. Regarding the optimal band alignment of the absorber/buffer interface, a so-called spike-like alignment is favorable [2–4]. In this kind of alignment, the conduction band minimum of the buffer layer has a slightly higher value (positive offset ΔE_c), and the buffer valence band maximum has a lower value than the corresponding bands of the absorber. This prevents a loss in open circuit voltage (V_{oc}) because of a reduction of buffer/absorber interface recombination of majority carriers, whereas the absence of a spike-like alignment, or even a negative ΔE_c, leads to a drop in V_{oc} as theoretical simulations show for the CIGS/window heterostructure [3,4]. For kesterites solar cells, such detailed theoretical studies are still pending, however, similar trends can be expected as M. Gloeckler *et al.* performed simulations starting from a CIGS baseline but extending it to a larger range of bandgap energies, which allows more general conclusions to be drawn [3]. The ideal conduction band offset ΔE_c is reported to be between 0.0 and 0.5 eV and has no negative influence on the electron transport, as can be shown by theoretical calculations assuming thermionic emission across the junction [5]. However, too high of a spike in the band alignment leads to a drastic reduction in short circuit current (J_{sc}) and efficiency, because it acts as a barrier for electrons. Up to now, the highest cell efficiencies for CZTSSe are achieved with a CdS buffer layer [1,6]. From ultraviolet spectroscopy measurements, a spike-like conduction band offset of the kesterite absorber and CdS between 0.33 and 0.48 eV is reported depending on the bandgap (sulfur/selenium content) and CdS deposition method [7,8]. For sulfur pure kesterites, a cliff-like alignment of −0.33 eV has been even observed [9]. The values of these offsets are still under discussion and could strongly depend on the growth condition of absorber and buffer layer [10]. For Se pure CZTSe, the experimentally reported values from 0.33 eV to 0.48 eV are in the upper limit for an ideal conduction band offset as mentioned earlier. Additional factors that can influence the buffer/absorber band alignment are photo-induced defect states in the buffer, buffer/absorber or buffer/ZnO window interfaces [11]. The occupation of these deep defect states depends on illumination and modifies the height of the spike barrier. This result in a crossover of dark and illuminated current–voltage (JV) curves and a distortion of the JV curve measured with red light only, the so-called red kink [12–15]. In literature, JV characteristics of many high-performance kesterite devices show crossover between dark and illuminated measurements, which can be linked to a current blocking back contact, or recently to the buffer layer, and a trend of improved efficiency due to reduced crossover is observed [16–18]. In this communication, we present an optimization of the CdS buffer layer preparation by chemical bath deposition for Se pure CZTSe absorbers, focusing on changing the cadmium source. The main objective of changing the cadmium source is to study the impact on the p–n junction of fast chemical bath deposition (CBD) processes (like those based on $CdSO_4$, where the average growth rate is estimated at 10 ± 2 nm/min), and slow CBD processes (like those based on $Cd(NO_3)_2$, where the average growth rate is estimated at 0.9 ± 0.2 nm/min). This last process could be better adapted to the higher surface roughness of CZTSe films when compared with CIGS.

We show that an optimized CBD process can eliminate red kink and dark and illuminated JV curve crossover, leading to overall improved device efficiencies with high fill factor (FF) and lower series resistance. Furthermore, the influence of the buffer layer on high series resistance and the origin of the beneficial effect of light soaking on the device performance are discussed.

2. EXPERIMENTAL

CZTSe absorbers were produced by reactive thermal annealing of metallic precursor stacks. For this purpose, a Cu/Sn/Cu/Zn metallic stack was deposited by direct current (DC) magnetron sputtering onto a soda-lime-glass/Mo/ZnO substrate (the purpose of this 10 nm ZnO interlayer is described elsewhere in more detail [19]). The metallic precursor sample ($5 \times 5\,cm^2$ area) was reactively annealed in a three-zone tubular furnace using a two-step process. The sample was placed in a graphite box that contained 100 mg Se and 5 mg Sn powder to provide a Se + Sn atmosphere during annealing. The first annealing step was carried out at 450 °C for 30 min in vacuum under an argon flow, with pressure maintained at 1.5 mbar, followed by a second annealing step at 550 °C for 15 min under a static Ar pressure of 1 bar. The heating rate was 20 °C/min and cooling was allowed to occur naturally down to room temperature (approximately 1.5 h to cool down to below 100 °C). The precursor composition was Cu-poor and Zn-rich, in order to obtain metallic ratios in the final CZTSe absorber of $[Cu]/([Zn] + [Sn]) = 0.77 \pm 0.05$ and $[Zn]/[Sn] = 1.21 \pm 0.08$ (measured by X-ray fluorescence). These values are in the same range as those of the best-performing kesterite devices reported in literature ($[Cu]/([Zn] + [Sn]) = 0.8–0.9$ and $[Zn]/[Sn] = 1.2–1.3$) [10,16].

The CZTSe absorber was split into two parts to investigate the influence of two different CdS buffer layers deposited by chemical bath deposition, using two different cadmium precursor sources, namely cadmium sulfate ($CdSO_4.H_2O$) and cadmium nitrate ($Cd(NO_3)_2$). This was done with a process previously reported ($[CdSO_4]$ or $[Cd(NO_3)_2] = 0.12$ M, [Thiourea] 0.3 M, pH = 9.5, T = 70 °C), and keeping the same Cd and S concentration in both solutions [20]. Prior to the deposition of the buffer layer, the CZTSe absorber is etched using $KMnO_4$ in a H_2SO_4-based medium, followed by subsequent etching in Na_2S to remove potential ZnSe secondary phases formed during the annealing process [20].

In the first CBD process (subsequently referred to as CdS1), cadmium sulfate ($CdSO_4.H_2O$) is used as the Cd source. The process takes 5 min to deposit a CdS layer with an estimated thickness of 50 ± 8 nm (calibrated by X-ray fluorescence (XRF) on CdS samples deposited on glass).

In the second CBD process (hereafter CdS2), cadmium nitrate ($Cd(NO_3)_2$) is used as the Cd source. The process takes 40 min to reach an estimated CdS thickness of 35 ± 7 nm. The use of $Cd(NO_3)_2$ results in a much slower growth kinetic of CdS, allowing the preparation of thinner layers with higher quality (see Supporting Information for a direct comparison of the fast and slow CBD processes based on $CdSO_4$ and $Cd(NO_3)_2$, respectively). Additionally, S is more effectively incorporated into the CdS layer because of the better control of the CdS precipitation.

Devices were annealed for a short time at 200 °C in air after CdS buffer layer deposition to improve the junction quality and completed by DC-pulsed sputtering deposition of 50 nm i-ZnO and 350 nm of DC-pulsed $In_2O_3:SnO_2$ (90/10 wt.%) ($R_\square = 35\ \Omega\square^{-1}$) as a transparent conductive window layer. The influence of low-temperature post-deposition annealing is currently under investigation, but widely reported to be beneficial for kesterite and chalcopyrites solar cell devices [21,22]. Individual solar cells of $3\times3\ mm^2$ were isolated using a manual microdiamond scriber MR200 OEG (OEG Gesellschaft für Optik, Elektronik & Gerätetechnik mbH, Frankfurt, Germany) with a scribed line width of 20 µm.

Dark and illuminated JV curves were measured using a Sun 3000 class AAA solar simulator (Abet Technologies Inc., Milford, Connecticut, USA; uniform illumination area of $15x15\ cm^2$), starting from negative to positive voltages (no hysteresis is observed using a reverse voltage ramp). Measurements were carried out at 25 °C, and before measuring the irradiance, intensity of the solar simulator was calibrated to 1 sun AM 1.5 by using a Si reference cell. To obtain red light JV curves, a 550-nm long pass filter was used, which has over 90% transmittance for wavelengths above 550 nm and 0% for lower wavelengths (see Supporting Information, Figure S2). Spectral response/external quantum efficiency (EQE) measurements were made using a Bentham PVE300 system (Bentham Instruments Ltd, Berkshire, U.K.) calibrated with a Si and Ge photodiode. Reversed voltage-biased EQE curves were collected by connecting a Keithley 2400 source meter (Keithley Instruments Inc., Cleveland, Ohio, USA) directly to the primary coil of the transformer and biasing the device at the desired voltage.

For temperature-dependent V_{OC} measurements, a liquid-nitrogen-cooled cryostat was used. The illumination source was a 100-W halogen lamp, and data was acquired by a Keithley 2400 source meter.

3. RESULTS AND DISCUSSION

Figure 1(a) shows the dark, red light illuminated and 1 sun illuminated JV curves for the CZTSe device with the CdS1 buffer layer (prepared using cadmium sulfate in the CBD process). These measurements were made after keeping the sample in dark for several days to relax all potential light-sensitive defects states. The first measurement, before exposing the cell to any light source, a dark JV curve was recorded, followed by a red light illuminated JV curve, (1.5 AM spectrum filtered by a 550 nm long pass filter), a 1 sun 1.5 AM illuminated curve, and then again a dark JV curve. A pronounced kink in the forward bias direction is observed for the red light illuminated curve. At about 0.3 V, the current is totally blocked and the curve approximately follows the dark curve. The 1 sun white light illuminated JV curve (approximately 5 s illumination) measured afterwards does not show any distortions. The dark curve measured directly afterwards is shifted compared to the initial dark curve. The dark and illuminated curve shows a crossover already at very low current value of $J_{cross} = 6.0\ mA/cm^2$. The same CZTSe absorber used for this device was split into two halves after synthesis, and a second device was fabricated with a CdS buffer layer using cadmium nitrate in the CBD process

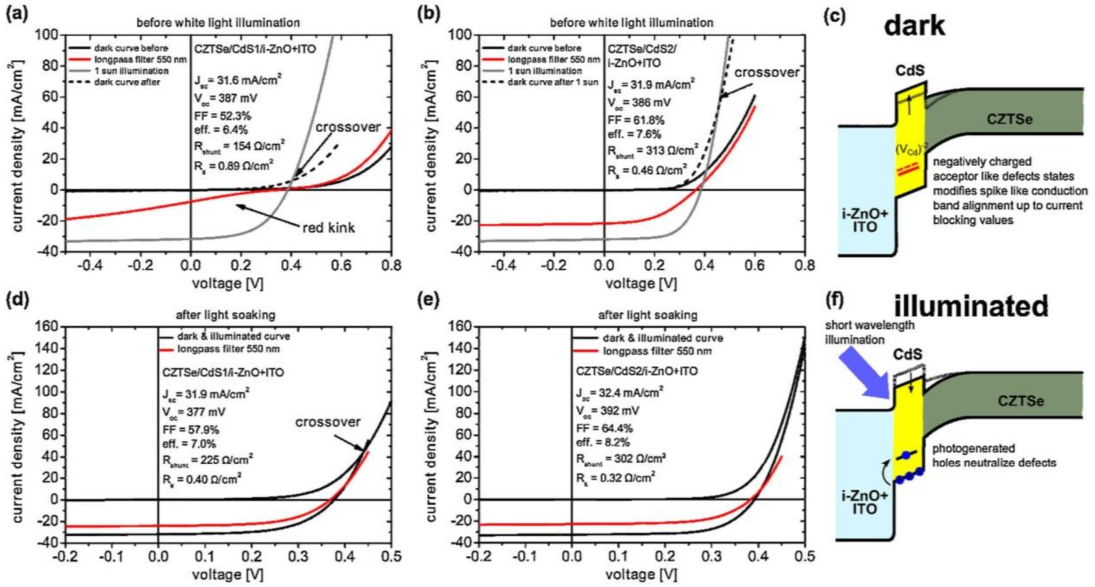

Figure 1. Dark, illuminated and filtered JV characteristics for cells with unoptimized (CdS1) and optimized CdS (CdS2) buffer layers before and after light soaking. A pronounced red kink is observed for sample with CdS1 buffer layer (a) which is removed after light soaking (d), although the crossover between dark and illuminated curve is still present. For CdS2 samples, no red kink is observed (b). Crossover between dark and illuminated curves could be improved and totally eliminated after light soaking (e). (c), (f) Schematic band diagram for CZTSe/CdS/i-ZnO + ITO heterostructure with light-sensitive defects in the CdS buffer. FF, fill factor.

(CdS2). The same measurements as for sample CdS1 were carried out for CdS2 after storing it under the same dark conditions CdS1 (Figure 1(b)). It can clearly be seen that no red kink is observed. The dark curve measured after white light illumination still shifts further to the left compared to the initial one; however, the shift is much less pronounced than for the CdS1 case. A crossover is still present, but the crossover point is significantly improved and increases up to $J_{cross} = 53.1\,mA/cm^2$. V_{oc} and J_{sc} for both samples are comparable ($J_{sc} = 31.6\,mA/cm^2$ and $V_{oc} = 387\,mV$, and $J_{sc} = 31.9\,mA/cm^2$ and $V_{oc} = 386\,mV$ for CdS1 and CdS2, respectively). However, the main difference is FF, and thus series and shunt resistance, resulting in an improved power conversion efficiency of 7.6% for CdS2 (with an average efficiency of 7.0 ± 0.5% for 13 $3 \times 3mm^2$ measured cells) compared to 6.4% for CdS1 (with an average efficiency of 5.8 ± 0.6% for 12 $3 \times 3mm^2$ measured cells). Both samples were light soaked (LS) for 40 min in open circuit conditions while keeping them at 25 °C and then remeasured (Figure 1 (d) and (e)). After LS, the red kink disappears for the CdS1 sample and the crossover point increases to $J_{cross} = 43.6\,mA/cm^2$. For the CdS2 sample, crossover could be totally eliminated after LS. In both samples, the main improvement after LS is the FF, which increases from 52.3% to 57.9% for CdS1 and from 61.8% to 64.4% for CdS2, leading to improved efficiencies of 7.0% and 8.2%, respectively. Because both samples are from the same CZTSe absorber and were finished in the same i-ZnO + ITO window layer deposition run, all changes can be directly correlated to differences in the CdS buffer layer. In Table I, device characteristics extracted from dark and illuminated JV curves before and after LS are summarized for both samples. Here, it can clearly be seen that the main parameter affected by light and the change of buffer layer is the series resistance. Before LS, the series resistance of dark and light JV curve vary largely for the CdS1 case ($2.09\,\Omega.cm^{-2}$ and $0.89\,\Omega.cm^{-2}$ for dark and light, respectively), whereas for sample CdS2, the difference is less drastic ($0.83\,\Omega.cm^{-2}$ and $0.46\,\Omega.cm^{-2}$, respectively). After LS, the series resistance extracted from dark and light JV curves has very similar values ($0.47\,\Omega.cm^{-2}$ and $0.40\,\Omega.cm^{-2}$, respectively, for CdS1 and $0.31\,\Omega.cm^{-2}$ and $0.32\,\Omega.cm^{-2}$ for CdS2), and series resistances could largely be improved for the CdS1 case compared to before LS values. The shunt resistance is less affected by LS, although there is a difference between dark and illuminated case.

The illumination-dependent series resistance and the red kink observed for CdS1 can be explained by deep acceptor-like traps in the CdS modifying the conduction band alignment as widely reported in literature [12–15]. In dark, the acceptor-like traps are ionized, compensating the natural n-type doping of the CdS because no photogenerated holes in the CdS layer are available to neutralize these acceptor states. Therefore, a more negative space charge is created inside the buffer layer, which decreases the conduction band bending, that is, increase of the spike as illustrated in Figure 1(c). Under white light illumination, photons absorbed in the buffer layer create electron hole pairs. The photogenerated holes from the CdS valence band are captured by the acceptor traps and neutralize them. Subsequently, the downward band bending of the absorber conduction band is enhanced, thus decreasing the spike (Figure 1(f)). A high spike acts as a barrier for photogenerated electrons like a second diode. Thus, for the case of a buffer layer with light active defects, JV curves measured with only red light will show current blocking at a certain forward bias voltage, that is, a distortion (kink) of the JV curve and a high series resistance. The n-type nature of CdS is related to doping by intrinsic defects. Theoretical calculations suggest that sulfur vacancies are the dominant donor defect as they have the lowest formation energies [23]. On the other hand, in an n-type environment, the formation energy for Cd vacancies (V_{Cd}), which act as acceptor, is the lowest, followed by sulfur on cadmium positions, which also acts as deeper acceptor defects. We propose that the optimization of the CdS growth process by slowing down the growth dynamic during chemical bath

Table I. Comparison of light and dark device characteristics of CZTSe/CdS/i-ZnO + ITO heterojunction solar cells using different CdS buffer deposition processes before and after light soaking (LS) for approximately 1 h.

Sample		Efficiency [%]	FF [%]	J_{sc} [mA/cm^2]	V_{oc} [mV]	R_{series} [Ω.cm^{-2}]	R_{shunt} [Ω.cm^{-2}]	A	J_0 [mA.cm^{-2}]	E_g [eV]	E_g/q-V_{oc} [V]
CdS1 before LS	Light	6.4	52.3	31.6	387	0.89	154	2.38	8.2×10^{-2}	1.01	0.623
	Dark					2.09	525	3.02	4.0×10^{-2}		
CdS1 after LS	Light	7.0	57.9	31.9	377	0.40	225	2.02	2.2×10^{-2}	1.01	0.633
	Dark					0.47	497	1.95	1.1×10^{-2}		
CdS2 before LS	Light	7.6	61.8	31.9	386	0.46	313	1.66	4.9×10^{-3}	1.02	0.634
	Dark					0.83	1202	1.48	1.3×10^{-3}		
CdS2 after LS	Light	8.2	64.4	32.4	392	0.32	302	1.52	2.1×10^{-3}	1.02	0.628
	Dark					0.31	792	1.36	2.4×10^{-4}		

FF, fill factor; CdS1, first CBD process; CdS2, second CBD process.

R_{series}, R_{shunt}, diode quality factor A and reverse-saturation current J_0 were extracted using the method described by Sites *et al.*[24] for illuminated as well as for dark curves.

Dark curves were measured immediately after measuring the illuminated curves.

Bandgap values were extracted from external quantum efficiency curves.

deposition of CdS using $Cd(NO_3)_2$ as a cadmium precursor improves the cadmium incorporation in the film, thus reducing the formation of Cd vacancies for the sample with CdS2. For the fast growth process of CdS1, which employs $CdSO_4$ as a cadmium source, V_{Cd} defects are more likely formed. In fact, X-ray fluorescence measurements (calibrated using standards measured by inductively coupled plasma mass spectroscopy) show a higher [Cd]/[S] ratio for layer CdS2 ($[Cd]/[S]_{CdS1} = 1.22$ and $[Cd]/[S]_{CdS2} = 1.50$), in close agreement with the results presented before. V_{Cd} acceptor-like defects have a negative stable charge state, thus pushing the CdS buffer to a more negative charge and modifying the conduction band bending, that is, increasing the conduction band spike up to a current blocking value in dark conditions. After white light illumination, and especially after longer light soakings, holes generated by short wavelength photons absorbed in the CdS get trapped in these states, neutralizing them and thus decreasing the spike again. The relaxation of these defects is slow, therefore, after LS soaking the red kink disappears, the crossover improves and the series resistances of dark as well as illuminated curves are decreased. To investigate the dynamics of this defect relaxation, the evolution of the dark curve over time in dark was measured after 40 min of LS (see Supplementary Information, Figure S3). From these dark curves obtained after LS and remeasuring after a certain time in dark, the series resistance and diode quality factor was extracted using the method described by Sites *et al.* [24], as shown in Figure 2. Here, an exponential increase of the dark curve series resistance over time in dark is observed for CdS1, whereas for sample CdS2 only a minor increase is observed. The diode factor is not affected. This confirms the presence of light-sensitive defects states in the CdS1 buffer layer, which relaxes in dark modifying the CZTSe/CdS conduction band spike to a high value that negatively influences the charge transport. Furthermore, the diode quality factors and reverse saturation currents extracted from dark as well as for illuminated curves after LS of CdS2 are lower than for CdS1, indicating an improvement of the interface. The optimization of CdS deposition allows growing thinner and at the same time homogeneous films, which explains the improved current collection in the short wavelength region of the EQE in Figure 3(b) for sample CdS2, without affecting the device performance (V_{oc}) as observed for thin buffer layer in CIGS [25]. To verify that the elimination of red kink and crossover is not only an effect of thickness reduction, devices with thinner CdS buffer layer were grown on a piece of the same CZTSe absorber using half of the time of the CdS1 process. This device shows worse cell performance and pronounced crossover (see Supplementary Information, Figure S4). From the inflection point of the EQE in the long wavelength region, the bandgaps for both samples were determined (1.01 eV and 1.02 eV for CdS1 and CdS2, respectively) in agreement with the bandgap reported for Se pure kesterite [26]. The less pronounced decrease of the EQE signal for a wavelength range higher than E_g for CdS1 can be attributed to stronger band tailing due to less passivated interface defects, which is also the most probable reason for a lower V_{oc} in the CdS1 device [27]. To further investigate interface-related problems, the activation energy of the recombination process (E_a) is extracted from the intercept at 0 K of V_{oc} versus T plots, as shown in Figure 3(a). For CdS1, E_a of 0.87 eV was found, which is much lower than the extracted bandgap ($E_g = 1.01$ eV), confirming an increased interface recombination, thus explaining a lower V_{oc}. For the CdS2, device E_a is much closer to the determined bandgap value (0.96 eV compared to $E_g = 1.02$ eV), indicating that the optimized CdS2 largely improves the buffer/absorber interface [16]. Reverse-biased EQE measurement further indicate problems with minority charge carrier (electrons) collection from the absorber bulk for the CdS1 sample as the ratio of reversed-biased to unbiased EQE signal increases at higher wavelengths region. Here, what is especially remarkable is the first jump in the ratio of reversed-biased to unbiased EQE signal at approximately 515 nm (2.4 eV), which corresponds to the beginning of photogeneration of charge carriers in the CZTSe absorber. This is in agreement with a high barrier in the conduction band, which can be overcome by applying a reverse-bias voltage. The further slow linear increase of the ratio toward longer wavelengths can be explained by a more compensated CdS1, thus lower doping concentration and smaller depletion width inside the CZTSe absorber. By applying a reverse-bias voltage the depletion width increases and therefore improves the collection of minority charge carries generated deeper inside the bulk of the absorber. Sample CdS2 does not show problems with minority carrier collection as the ratio stays constant around unity for the whole wavelength range.

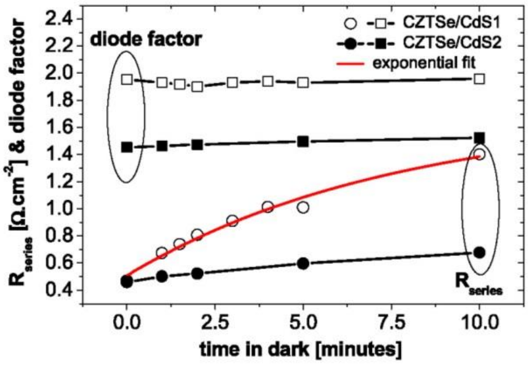

Figure 2. Evolution of series resistance and diode factor extracted from the dark curves after 40 min light soaking and with increasing time in dark. For the CdS1 sample, an exponential increase in series resistance in observed. This figure is available in colour online at wileyonlinelibrary.com/journal/pip

$E_g/q\text{-}V_{oc}$ values of the devices are comparable with current kesterite champion devices, and only the J_{sc} is lower, which could be improved by employing metal

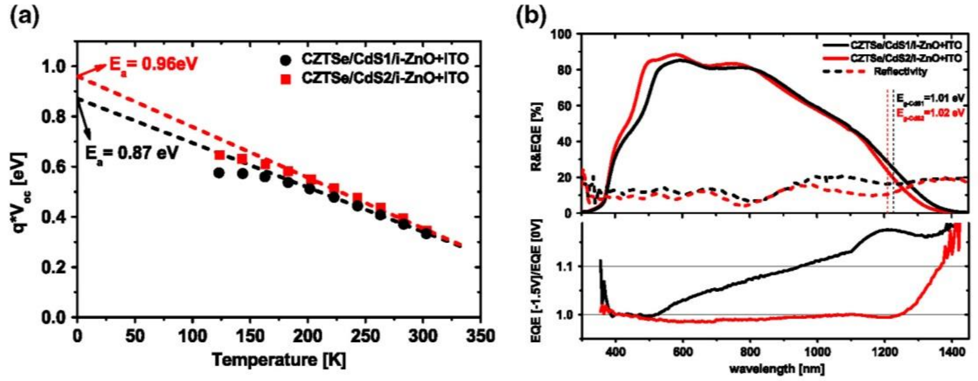

Figure 3. (a) Temperature dependence of the V_{OC} and linear extrapolation to T = 0 K to extract the activation energy (E_a) of the recombination process. (b) Unbiased external quantum efficiency (EQE) curves, reflectivity and the ratios between voltage biased (−1.5 V) and unbiased EQE for solar cells with CdS1 and CdS2. Bandgaps are extracted from the inflection point of the EQE signal in the long wavelength range. This figure is available in colour online at wileyonlinelibrary.com/journal/pip

grids and anti-reflective coatings as the reflectivity of the cells is especially high in the long wavelength range (above 15%, Figure 3).

4. CONCLUSION

In summary, we have demonstrated the importance of optimized buffer layer deposition for high-performance kesterite solar cell devices, and we could clearly show that an unoptimized buffer layer is the cause of dark and illuminated JV crossover and high series resistance. The reduction of light-sensitive defect states inside the CdS buffer that modified the buffer/absorber spike-like band alignment to an unfavorably high current blocking value can be eliminated by optimizing the CBD process. A fast CdS layer growth (CdS1) favors the formation of compensating defects states. V_{Cd} seems to be the most obvious candidate as an acceptor-like defect compensating the n-type CdS, which is further responsible for high series resistance and low FF. Light soaking can temporarily improve device performance by neutralizing these defects in the buffer layer by photogenerated holes and leads to a reduction of series resistance and improvement of FF. Understanding the origins of this current and FF-limiting JV curve distortions opens new perspectives to optimizing solar cell performance. A slower growth process definitely reduces the amount of light-sensitive defects resulting in an elimination of crossover and red kink and a reduction of series resistance, which is considered as one of the main efficiency-limiting problems in kesterite-based solar cells among with the V_{oc} deficit. This buffer layer optimization allowed obtaining an 8.2% efficient CZTSe/CdS/i-ZnO/ITO heterostructure solar cell with low series resistance and an FF value of 64.4%, which is among the highest FF values so far reported for Se pure kesterite absorbers.

ACKNOWLEDGEMENTS

This research was supported by the Framework 7 program under the project KESTCELLS (FP7-PEOPLE-2012-ITN-316488) and by the European Regional Development Funds (ERDF, FEDER Programa Competitivitat de Catalunya 2007–2013). Authors from IREC and the University of Barcelona belong to the M-2E (Electronic Materials for Energy) Consolidated Research Group and the XaRMAE Network of Excellence on Materials for Energy of the "Generalitat de Catalunya." E. S. thanks the Government of Spain for the "Ramon y Cajal" fellowship (RYC-2011-09212), V. I. for the "Juan de la Cierva" fellowship (JCI-2011-10782), A. F. for the FPU Fellowship (FPU12/05508), Y. S. for the PTA fellowship (PTA2012-7852-A), and H. X. thanks the "China Scholarship Council" fellowship (CSC N° 201206340113).

REFERENCES

1. Wang W, Winkler MT, Gunawan O, Gokmen T, Todorov TK, Zhu Y, Mitzi DB. Device characteristics of CZTSSe thin-film solar cells with 12.6% efficiency. *Advanced Energy Materials* 2013 n/a–n/a. DOI:10.1002/aenm.201301465
2. Scheer R, Schock HW. *Wiley InterScience (Online Service), Chalcogenide Photovoltaics Physics, Technologies, and Thin Film Devices, Wiley-VCH*. John Wiley [distributor]: Weinheim; Chichester, 2011; http://public.eblib.com/EBLPublic/PublicView.do?ptiID=700838 (accessed February 5, 2014).
3. Gloeckler M, Sites JR. Efficiency limitations for wide-band-gap chalcopyrite solar cells. *Thin Solid Films* 2005; **480–481**: 241–245. DOI: 10.1016/j.tsf.2004.11.018

4. Minemoto T, Matsui T, Takakura H, Hamakawa Y, Negami T, Hashimoto Y, Uenoyama T, Kitagawa M. Theoretical analysis of the effect of conduction band offset of window/CIS layers on performance of CIS solar cells using device simulation. *Solar Energy Materials & Solar Cells* 2001; **67**: 83–88. DOI: 10.1016/S0927-0248(00)00266-X
5. Niemegeers A, Burgelman M, Vos AD. On the CdS/CuInSe$_2$ conduction band discontinuity. *Applied Physics Letters* 1995; **67**: 843–845. DOI: 10.1063/1.115523
6. Brammertz G, Buffière M, Oueslati S, ElAnzeery H, Messaoud KB, Sahayaraj S, Köble C, Meuris M, Poortmans J. Characterization of defects in 9.7% efficient Cu$_2$ZnSnSe$_4$-CdS-ZnO solar cells. *Applied Physics Letters* 2013; **103**: 163904. DOI: 10.1063/1.4826448
7. Haight R, Barkhouse A, Gunawan O, Shin B, Copel M, Hopstaken M, Mitzi DB. Band alignment at the Cu$_2$ZnSn(S$_x$Se$_{1-x}$)$_4$/CdS interface. *Applied Physics Letters* 2011; **98**: 253502. DOI: 10.1063/1.3600776
8. Li J, Wei M, Du Q, Liu W, Jiang G, Zhu C. The band alignment at CdS/Cu$_2$ZnSnSe$_4$ heterojunction interface. *Surface and Interface Analysis* 2013; **45**: 682–684. DOI: 10.1002/sia.5095
9. Bär M, Schubert B-A, Marsen B, Wilks RG, Pookpanratana S, Blum M, Krause S, Unold T, Yang W, Weinhardt L, Heske C, Schock H-W. Cliff-like conduction band offset and KCN-induced recombination barrier enhancement at the CdS/Cu$_2$ZnSnS$_4$ thin-film solar cell heterojunction. *Applied Physics Letters* 2011; **99**: 222105. DOI: 10.1063/1.3663327
10. Polizzotti A, Repins IL, Noufi R, Wei S-H, Mitzi DB. The state and future prospects of kesterite photovoltaics. *Energy & Environmental Science* 2013. DOI: 10.1039/c3ee41781f
11. Nichterwitz M, Caballero R, Kaufmann CA, Schock H-W, Unold T. Generation-dependent charge carrier transport in Cu(In,Ga)Se$_2$/CdS/ZnO thin-film solar-cells. *Journal of Applied Physics* 2013; **113**: 044515. DOI: 10.1063/1.4788827
12. Eisgruber I, Granata J, Sites J, Hou J, Kessler J. Blue-photon modification of nonstandard diode barrier in CuInSe$_2$ solar cells. *Solar Energy Materials & Solar Cells* 1998; **53**: 367–377. DOI: 10.1016/S0927-0248(98)00035-X
13. Köntges M, Reineke-Koch R, Nollet P, Beier J, Schäffler R, Parisi J. Light induced changes in the electrical behavior of CdTe and Cu(In, Ga)Se$_2$ solar cells. *Thin Solid Films* 2002; **403**: 280–286.
14. Gloeckler M, Jenkins CR, Sites JR. Explanation of light/dark superposition failure in CIGS solar cells, in: MRS Proc., 2003; http://journals.cambridge.org/abstract_S194642740013338X (accessed January 8, 2014).
15. Pudov AO, Sites JR, Contreras MA, Nakada T, Schock H-W. CIGS J–V distortion in the absence of blue photons. *Thin Solid Films* 2005; **480-481**: 273–278. DOI: 10.1016/j.tsf.2004.11.099
16. Mitzi DB, Gunawan O, Todorov TK, Wang K, Guha S. The path towards a high-performance solution-processed kesterite solar cell. *Solar Energy Materials & Solar Cells* 2011; **95**: 1421–1436. DOI: 10.1016/j.solmat.2010.11.028
17. Todorov TK, Tang J, Bag S, Gunawan O, Gokmen T, Zhu Y, Mitzi DB. Beyond 11% efficiency: characteristics of state-of-the-art Cu$_2$ZnSn(S,Se)$_4$ solar cells. *Advanced Energy Materials* 2013; **3**: 34–38. DOI: 10.1002/aenm.201200348
18. Buffière M, Brammertz G, Oueslati S, Anzeery HE, Bekaert J, Messaoud KB, Köble C, Khelifi M, Meuris M, Poortmans J. Spectral current–voltage analysis of kesterite solar cells. *Journal of Physics D: Applied Physics* 2014; **47**: 175101. DOI: 10.1088/0022-3727/47/17/175101
19. López-Marino S, Placidi M, Pérez-Tomás A, Llobet J, Izquierdo-Roca V, Fontané X, Fairbrother A, Espíndola-Rodríguez M, Sylla D, Pérez-Rodríguez A, Saucedo E. Inhibiting the absorber/Mo-back contact decomposition reaction in Cu$_2$ZnSnSe$_4$ solar cells: the role of a ZnO intermediate nanolayer. *Journal of Materials Chemistry A* 2013; **1**: 8338–8343. DOI: 10.1039/C3TA11419H
20. López-Marino S, Sánchez Y, Placidi M, Fairbrother A, Espindola-Rodríguez M, Fontané X, Izquierdo-Roca V, López-García J, Calvo-Barrio L, Pérez-Rodríguez A, Saucedo E. ZnSe etching of Zn-rich Cu$_2$ZnSnSe$_4$: an oxidation route for improved solar-cell efficiency. *Chemistry – A European Journal* 2013; **19**: 14814–14822. DOI: 10.1002/chem.201302589
21. Repins I, Beall C, Vora N, DeHart C, Kuciauskas D, Dippo P, To B, Mann J, Hsu W-C, Goodrich A, Nouf R. Co-evaporated Cu$_2$ZnSnSe$_4$ films and devices. *Solar Energy Materials & Solar Cells* 2012; **101**: 154–159. DOI: 10.1016/j.solmat.2012.01.008
22. Chirilă A, Reinhard P, Pianezzi F, Bloesch P, Uhl AR, Fella C, Kranz L, Keller D, Gretener C, Hagendorfer H, Jaeger D, Erni R, Nishiwaki S, Buecheler S, Tiwari AN. Potassium-induced surface modification of Cu(In,Ga)Se$_2$ thin films for high-efficiency solar cells. *Nature Materials* 2013; **12**: 1107–1111. DOI: 10.1038/nmat3789
23. Nishidate K, Sato T, Matsukura Y, Baba M, Hasegawa M, Sasaki T. Density-functional electronic structure calculations for native defects and Cu impurities in

CdS. *Physical Review B* 2006; **74**. DOI: 10.1103/PhysRevB.74.035210

24. Sites JR, Mauk PH. Diode quality factor determination for thin-film solar cells. *Solar Cells* 1989; **27**: 411–417.
25. Contreras MA, Romero MJ, To B, Hasoon F, Noufi R, Ward S, Ramanathan K. Optimization of CBD CdS process in high-efficiency Cu(In,Ga)Se_2-based solar cells. *Thin Solid Films* 2002; **403–404**: 204–211. DOI: 10.1016/S0040-6090(01)01538-3
26. Ahn S, Jung S, Gwak J, Cho A, Shin K, Yoon K, Park D, Cheong H, Yun JH. Determination of band gap energy (E_g) of $Cu_2ZnSnSe_4$ thin films: on the discrepancies of reported band gap values. *Applied Physics Letters* 2010; **97**: 021905. DOI: 10.1063/1.3457172
27. Gokmen T, Gunawan O, Todorov TK, Mitzi DB. Band tailing and efficiency limitation in kesterite solar cells. *Applied Physics Letters* 2013; **103**: 103506. DOI: 10.1063/1.4820250

SUPPORTING INFORMATION

Additional supporting information may be found in the online version of this article at the publisher's website.

Supporting Information

Optimization of CdS Buffer Layer for High Performance $Cu_2ZnSnSe_4$ Solar Cells and the Effects of Light Soaking: Elimination of Crossover and Red Kink

Markus Neuschitzer, Yudania Sanchez, Simon López-Marino, Haibing Xie, Andrew Fairbrother, Marcel Placidi, Stefan Haass, Victor Izquierdo-Roca, Alejandro Perez-Rodriguez, and Edgardo Saucedo

1. Supplementary measurements

The main objective of this paper is to adapt the CdS buffer layer to the intrinsic characteristics of CZTSe absorbers by using different Cd sources. In Figure S1 we show a comparison of the CBD process using $CdSO_4$ and $Cd(NO_3)_2$ as Cd sources. It is clear that using $CdSO_4$ leads to the precipitation of a large density of CdS aggregates, characteristic of a fast formation reaction. Conversely, when $Cd(NO_3)_2$ is used, the solution is more transparent and the formation of aggregates is not evident until the final stages of the growth process.

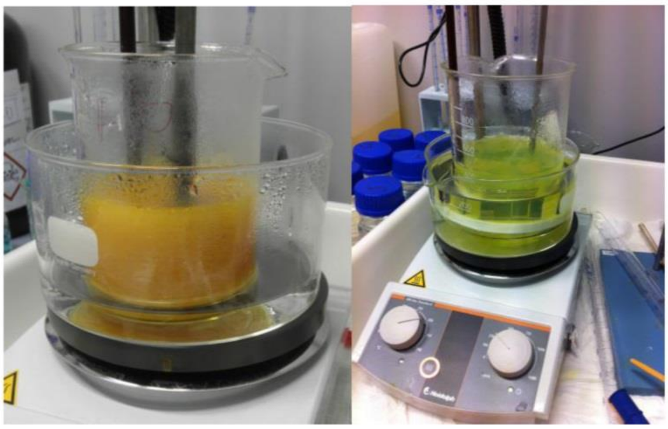

Figure S1. Images showing the aspect of the two different baths used in this study (CdS1 (left) and CdS2 (right)). Both pictures were taken after 5 min of the reaction starts.

In Figure S2 the transmittance of a 550 nm longpass filter measured with a PerkinElmer Lambda 950 UV/VIS Spectrometer is shown. The filter blocks light with wavelengths below 550 nm and has over 90% transmittance for wavelengths above 550 nm. Using this filter in combination with a solar simulator allows measurement of JV curves illuminated with the long wavelength portion of the AM 1.5 spectrum, as shown in Figure S1. Using the long wavelength part of the solar spectrum avoids absorption inside the buffer/window layer, and thus allows studying possible light sensitive meta-stabilities induced by these layers.

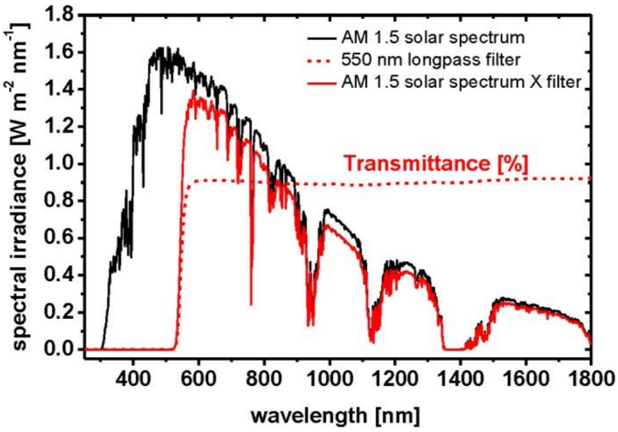

Figure S2. AM 1.5 solar spectrum and AM 1.5 solar spectrum filtered with a 550 nm longpass filter.

In Figure S3 the relaxation of the dark curves of the set of samples used in the main text after 40 minutes light soaking is shown. For the sample with the unoptimized CdS deposition (CdS1) it can clearly be seen that the part of the JV at higher currents, which is more influenced by the series resistance, changes drastically. For the optimized CdS (CdS2) a less pronounced change is observed.

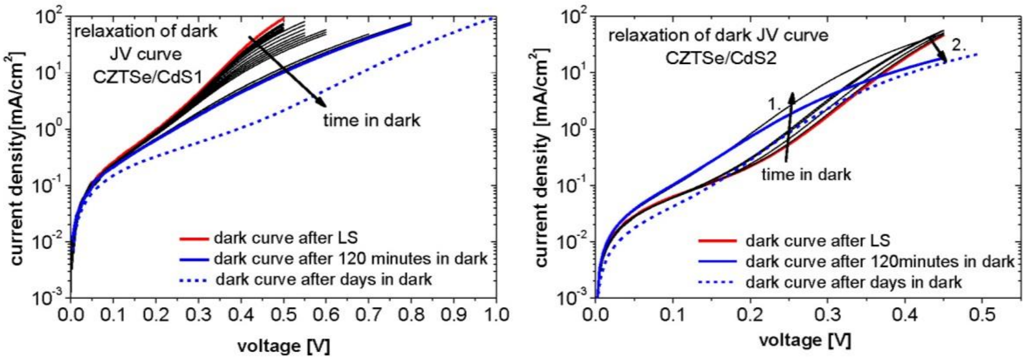

Figure S3. Relaxation of dark curves after approximately 40 minutes of light soaking.

To ensure that the improvement of cross-over and red kink are not only due to the reduced thickness of the optimized buffer layer deposition for CdS2, on one piece of the same absorber a CdS buffer layer was deposited using the CdS1 process and half of the time normally used (3 minutes - to achieve an estimated thickness of around 25nm). The i-ZnO/ITO layer was deposited in the same run as all other samples used in this study. In Figure S4 the dark and illuminated JV curves before and after light soaking of this device are shown. The overall device performance is worse than for the optimized deposition time using process CdS1 presented in the main part of this study (5 minutes - to achieve an estimated thickness of around 50 nm measured by XRF on glass). It can clearly been seen that cross over between the dark and illuminated curve is very pronounced and can be improved after light soaking showing that the improved device performance, elimination of red kink and crossover is not only due to an decrease of buffer layer thickness, but due to an improvement in the buffer layer growth itself.

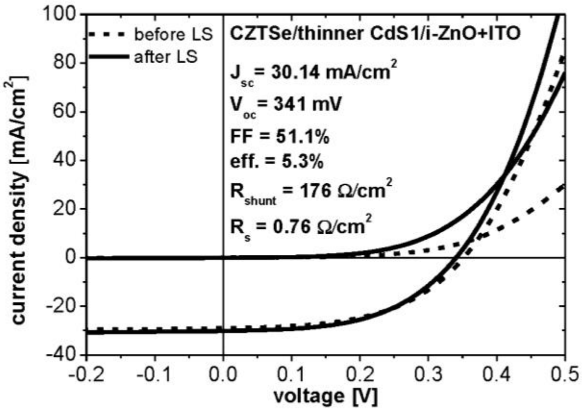

Figure S4. Dark and illuminated JV characteristics with unoptimized CdS1 buffer layer deposited with half of optimal time to before and after light soaking (LS)

2. Extended study on additional CZTSe devices with CdS1 and CdS2 buffer layer

In addition to the set of samples presented in the main part of the study different other samples were investigated to confirm the beneficial effect of the optimized CdS deposition. In Figure S5 monochromatic JV curves of a CZTSe/**CdS1**/i-ZnO/ITO heterosturcture is shown. Monochromatic JV curves were obtained by illuminating the device with different monochromatic LEDs (in contrast to the main text where a longpass filter was used for long wavelength illuminated JV curves). The CZTSe absorber was synthesized in a different run under same conditions as described in the main text and solar cells were finished using CdS1 process for buffer layer deposition. Strong kinks in the infrared (850 nm) and red light (660 nm) illuminated curves are observed, which disappears as soon as green light (505 nm) is used. This further confirms problems with CdS buffer layers deposited by the CdS1 process because 505 nm corresponds to 2.46 eV, which is above the bandgap of CdS (2.4 eV). This indicates that the kink disappears as soon as charge carries are created in the CdS buffer layer as discussed in the main text. The 1 sun illuminated and dark JV curve show a strong crossover. After light soaking the crossover is reduced and device performance increases. The main improvement is FF related due to a decrease in series resistance consistent with the observation and explanations given in the main text.

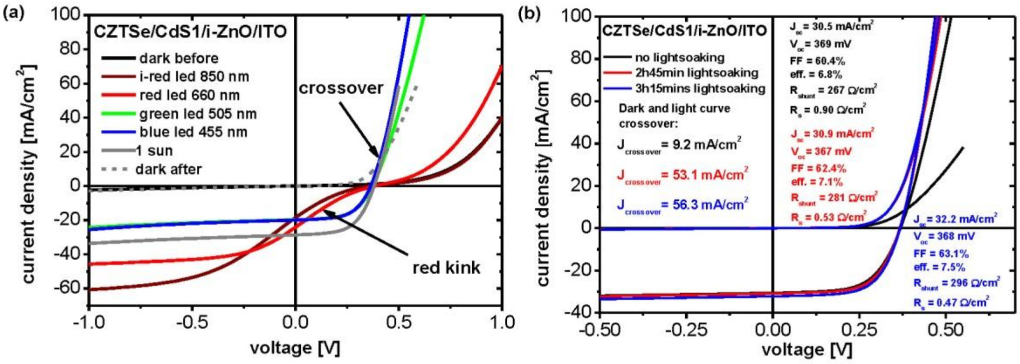

Figure S5. (a) dark, monochromatic LED illuminated and one sun illuminated JV curves of CZTSe/CdS1/i-ZnO/ITO heterostructure solar cell. Before short wavelength illumination a strong red kink is observed. Dark and 1 sun illuminated JV curves show strong crossover. (b) Same sample measured before and after different times of 1 sun light soaking.

A further set of samples comparing the two different CdS depositions processes (CdS1 using cadmium sulfates and CdS2 using nitrates as Cd-source, respectively) were investigated using monochromatic JV curves as shown in Figure S6. Here the device efficiencies are lower than of devices presented in the main part, mostly due to a lower Jsc. However, the same effects as presented in the main part of this paper are observed. For the device with CdS buffer layer deposited using the CdS1 process a strong kink is observed for long wavelength illuminated curves which disappears as soon as light is absorbed inside the CdS buffer layer (green LED). After short wavelength illumination the kink disappears also in the long wavelength illuminated curves, however a strong crossover between dark and illuminated curve is still present. For the device finished using the optimized CdS2 process no kink is observed for long wavelength illumination and further crossover is largely improved. Although, device efficiencies are lower for this set of devices still the device with CdS2 process yields power conversion efficiencies of 1% higher than for the CdS1 samples showing no red kink, and a largely improved crossover which further confirms the beneficial effect of our CdS deposition optimization.

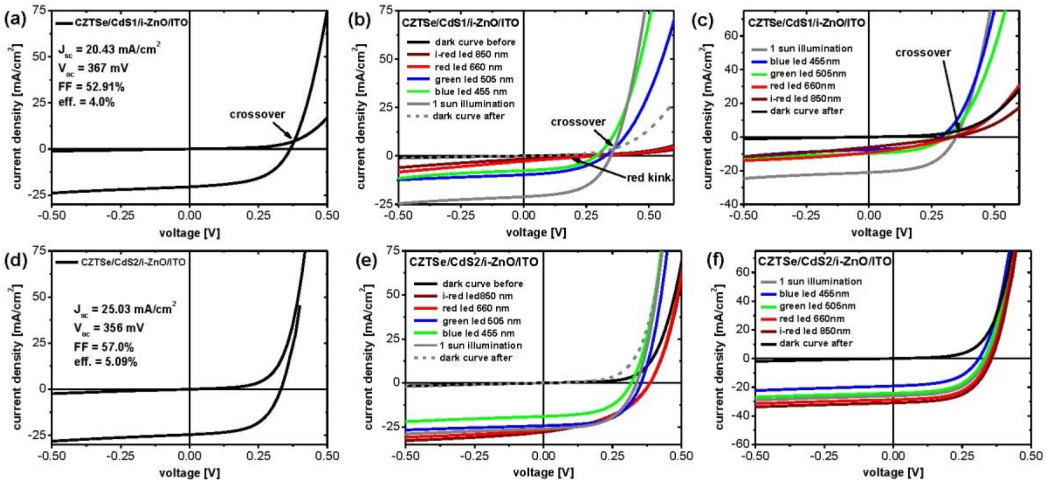

Figure S6. Dark, illuminated and monochromatic J-V characteristics for cells with CdS1 and CdS2 buffer layer ((a), (b), (c) CdS1; (d), (e), (f) CdS2. (b) and (e) monochromatic J-V curves before white light illumination starting with long wavelength illumination. A red kink is observed for CdS1 (b) which is removed after white light illumination(c). The crossover between dark and illuminated curve is still present. For CdS2 no red kink is observed (e), however a shift of the red and i-red Voc value can be seen after white light exposure (f). Crossover between dark and illuminated curves is almost eliminated.

4.3 Towards high performance Cd-free CZTSe solar cells with a ZnS(O,OH) buffer layer: the influence of thiourea concentration on chemical bath deposition

The work presented in the following was published in the Journal of Physics D: Applied Physics:
J. Phys. D: Appl. Phys. 49, 125602 DOI:10.1088/0022-3727/49/12/125602

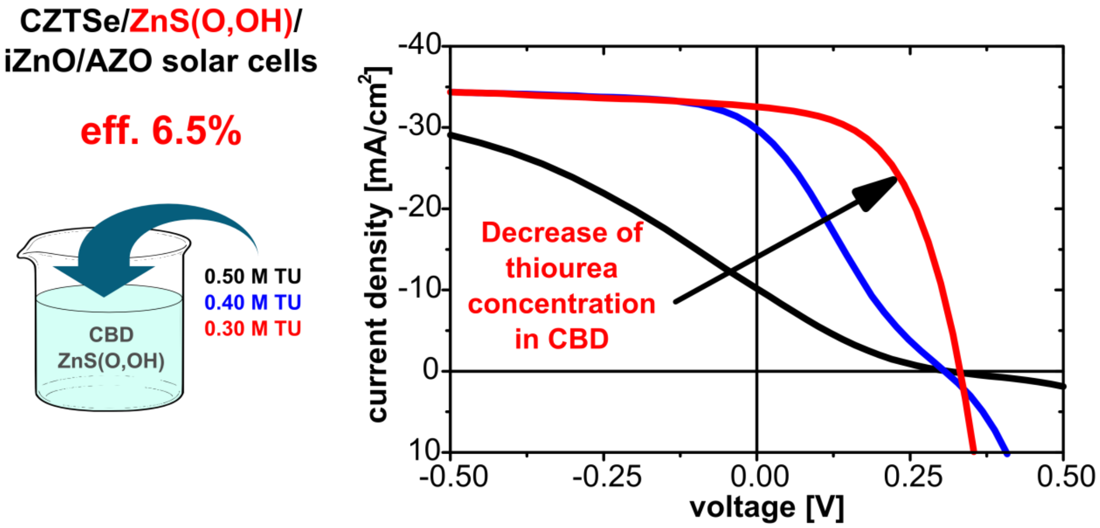

Figure 4.3. Illustration of the effect on device performance of optimizing ZnS(O,OH) buffer layers by adjusting the thiourea concertation in the chemical bath deposition process.

IOP Publishing Journal of Physics D: Applied Physics
J. Phys. D: Appl. Phys. **49** (2016) 125602 (9pp) doi:10.1088/0022-3727/49/12/125602

Towards high performance Cd-free CZTSe solar cells with a ZnS(O,OH) buffer layer: the influence of thiourea concentration on chemical bath deposition

Markus Neuschitzer[1], Karla Lienau[2], Maxim Guc[1], Lorenzo Calvo Barrio[3], Stefan Haass[2], Jose Marquez Prieto[4], Yudania Sanchez[1], Moises Espindola-Rodriguez[1], Yaroslav Romanyuk[2], Alejandro Perez-Rodriguez[1,5], Victor Izquierdo-Roca[1] and Edgardo Saucedo[1]

[1] Catalonia Institute for Energy Research- IREC, Jadins de les Dones de Negre 1, 08930 Sant Adrià de Besòs (Barcelona), Spain
[2] Empa—Swiss Federal Laboratories for Materials Science and Technology, Laboratory for Thin Films and Photovoltaics, 8600 Dübendorf, Switzerland
[3] Centres Científics i Tecnològics CCiTUB, Universitat de Barcelona, C. Lluis Solé i Sabarés 1, 08028 Barcelona, Spain
[4] Northumbria Photovoltaic Applications Group, Department of Physics and Electrical Engineering, Northumbria University, Newcastle upon Tyne NE1 8ST, UK
[5] IN2UB, Departament d'Electrònica, Universitat de Barcelona, C. Martí i Franquès 1, 08028 Barcelona, Spain

E-mail: mneuschitzer@irec.cat

Received 22 October 2015, revised 28 December 2015
Accepted for publication 18 January 2016
Published 23 February 2016

Abstract

High-performance kesterite- (CZTSe-)based solar cell devices usually employ an absorber/buffer heterostructure using toxic CdS deposited by chemical bath deposition (CBD) as a buffer layer. This is due to the favourable spike-like conduction band alignment of the CdS buffer and CZTSe absorber. ZnS(O,OH) buffer layers provide a promising nontoxic alternative. Here, variation of the thiourea concentration in the CBD of ZnS(O,OH) buffer layers and its influence on device performances of pure selenide CZTSe heterostructure solar cells is presented. Furthermore, the influence of buffer layer deposition conditions on light-induced metastabilities is discussed. A ZnS(O,OH) buffer layer deposited with a high thiourea concentration leads to distorted illuminated *J*–*V* curves as expected for devices with unfavourably high spike-like conduction band alignment between the buffer and CZTSe absorber. By adjusting the thiourea concentration *J*–*V* curve distortions can be reduced. An optimized CBD process leads to a device efficiency of up to 6.5% after light soaking, which is comparable to the efficiency of a reference device that employs CdS as the buffer layer (6.9%).

Keywords: thin-film solar cell, buffer layer, chalcogenides, CZTSe, Cd-free, ZnS(O,OH), light soaking

(Some figures may appear in colour only in the online journal)

0022-3727/16/125602+9$33.00

1. Introduction

In recent years $Cu_2ZnSn(S_{1-x}Se_x)_4$ (CZTSSe) has attracted much attention as a possible alternative to more mature chalcopyrite ($CuIn_{1-x}Ga_xSe_2$; CIGS) p-type absorber materials for thin-film solar cells due to its composition of more abundant elements [1]. Different from most silicon solar cells where a homojunction is created by doping of the Si, chalcogenide thin-film solar cells use a heterojunction architecture to create the p–n junction for the separation of light-generated electron–hole pairs [2]. This heterostructure consists of a polycrystalline semiconducting absorber material and some kind of transparent emitter, completed with front and back contacts. In a heterostructure, the electric properties of the junction strongly depend on the energy band alignment at the interface of the two different semiconducting materials. CZTSe-based solar cell devices employ a p-type absorber/n-type buffer/window heterostructure to form the p–n junction [1]. The role of the buffer layer is to provide a conduction band alignment of absorber/buffer/window heterostructure that is optimal for high device performance, and a so-called spike-like band alignment is favourable [2, 3]. In a spike-like alignment the conduction band minimum of the n-type buffer layer has a higher value (positive offset ΔE_c) than the conduction band minimum of the p-type absorber,whereas the opposite occurs for the corresponding valence band maxima, as shown in figure 1. Theoretical calculations for CIGS/window heterostructures show that a slightly positive spike between 0.0–0.5 eV prevents losses in open circuit voltage (V_{oc}) due to a reduction of buffer/absorber interface recombination. Furthermore, this small spike has no negative influence on electron transport as shown by theoretical calculations assuming thermionic emission across the junction [3–5]. In contrast, too high a spike in the conduction band will act as barrier for electrons, and therefore drastically reduce the short-circuit current (J_{sc}). The absence of a spike, i.e. a negative conduction band offset, called a cliff (see figure 1), leads to a drastic reduction of V_{oc} due to a reduction of the interface bandgap [3].

The highest efficiency reported so far for CZTSSe solar cells with CdS buffer layer grown by CBD is 12.6% [6]. For CZTSSe absorber and CdS buffer positive conduction band offsets between 0.34 eV to 0.48 eV are reported, depending on the sulphur to selenium ratio (bandgap of absorber) and CdS deposition methods [7, 8]. Owing to the high toxicity of cadmium and the low bandgap of CdS of 2.4 eV there is an incentive to replace this buffer layer with a more environmentally friendly material that is more transparent in the short-wavelength region of the visible solar spectrum to avoid absorption losses.

ZnS(O,OH) is a promising alternative due to its low toxicity, higher bandgap and the possibility of tuning the band alignment depending on the sulphur to oxygen ratio [9]. In addition, this material has demonstrated very encouraging results as a buffer layer in CIGS technology, suggesting a good potentiality for being applied in CZTSe-based solar cells [10]. For CZTSSe ([S]/([S] + [Se]) = 0.4, $E_g = 1.2$ eV) and ZnS deposited by CBD a high spike-like conduction band offset of 1.1 eV is reported [11]. For the same CZTSSe absorber and ZnO deposited by atomic layer deposition (ALD) a slight cliff-like offset is observed [11]. Devices prepared with this buffer layer show zero and 2.46% efficiencies for ZnS and ZnO, respectively, whereas the CdS reference device yield a 7.75% power conversion efficiency [11]. In figure 2 the approximated band alignment of ZnS and ZnO with a pure selenide CZTSe ($E_g = 1.0$ eV) absorber is shown. A high spike- and cliff-like alignment is expected for ZnS and ZnO, respectively. Thus, the optimal band alignment necessary for high device performance could be adjusted by changing the ratio of oxygen to sulphur.

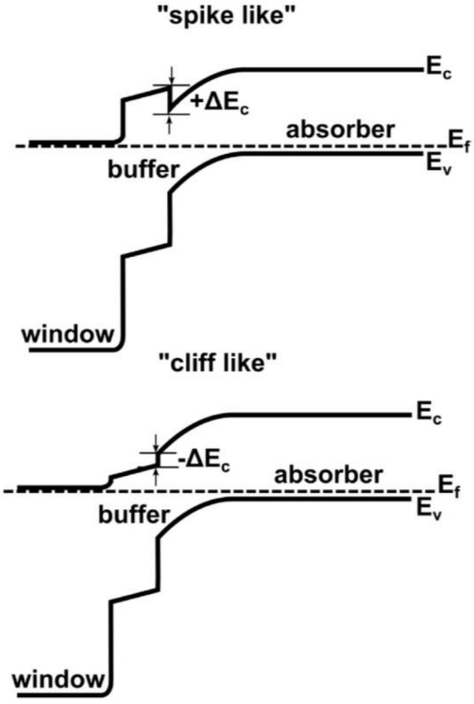

Figure 1. Schematics of the band diagrams of window/buffer/absorber heterostructures for spike- and cliff-like conduction band alignments.

For pure sulphide CZTS Ericson *et al* [12] showed that the sulphur ratios in an ALD-grown Zn(O,S) buffer layer have a large influence on solar cell device performance, resulting in devices with a 4.6% efficiency for an optimized composition compared with 7.3% for a reference CZTS/CdS device. Nguyen *et al* [13] showed that a thin 10–25 nm ZnS buffer layer grown by CBD for monograin CZTSSe ([S]/([S] + [Se]) = 0.8) solar cells yields efficiencies up to 4.5% compared with a 4.8% CdS reference cell. Grenet *et al* [14] report power conversion efficiency of 5.8% for CZTSSe ([S]/([S] + [Se]) = 0.15) devices with a ZnS(O,OH) buffer deposited by CBD compared with 7.0% for a CdS buffer device. However, a 24 h light soaking (LS) was necessary to increase the power conversion efficiency from almost zero to a higher value due to metastabilities. In CIGS/ZnS(O,OH)-based devices metastabilities are commonly observed and strongly

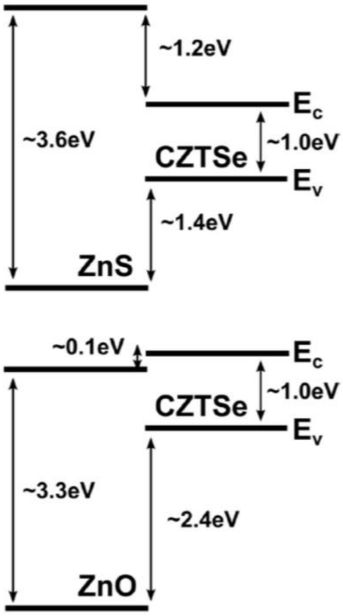

Figure 2. Approximation of band alignment of CZTSe absorber with ZnS (spike-like) and ZnO (cliff-like). Band offsets were taken from Barkhouse *et al* [11] and adjusted to the CZTSe absorber by shifting the valence band minimum according to theoretical calculations [17]. A small spike-like conduction band alignment ($\Delta E_c < 0.5\,\text{eV}$) would be preferable and could be achieved by tailoring the S/O ratio in Zn(O,S) [9].

depend on the absorber surface composition [15]. In CIGS it is reported that these can be reduced by increasing the buffer layer thickness, using a highly resistive subsequently deposited i-ZnO layer or by heat and LS treatments [15, 16].

In this study we present for the first time the variation of the thiourea (TU) concentration, i.e. the sulphur source, in the chemical bath of CBD-grown ZnS(O,OH) buffer layer and its strong influence on the device performances and stability of pure selenide CZTSe/ZnS(O,OH)/i-ZnO/ZnO:Al heterostructure solar cells.

2. Experimental methods

2.1. Absorber synthesis

CZTSe absorbers were synthesized by a two-stage approach. First Cu/Sn/Cu/Zn metal stacks were sputtered onto Mo-coated soda lime glass followed by a reactive annealing in a graphite box under a selenium and tin atmosphere as described in more detail in [18, 19]. The synthesized absorber was split into equal pieces to investigate different buffer layers.

2.2. Buffer layer deposition

Prior to the deposition of the buffer layer, the absorbers were etched using KCN (10wt%) for 30 s for surface cleaning. The ZnS(O,OH) buffer layers were grown by CBD using a $ZnSO_4$ (0.15 M)/ammonia (4.9 M)/TU aqueous solution. The CBD process is adapted from recipes reported in the literature for high-efficiency chalcopyrite/ZnS(O,OH) heterostructure solar cells [16, 20, 21]. The ammonia acts as complexing agent for the Zn^{+2} cations and TU is used as the sulphur source. Four different TU concentrations were investigated, namely 0.50 M, 0.40 M, 0.35 M and 0.30 M. The bath temperature was kept at 85 °C and the total duration of each of the runs was kept constant at 12 min for all samples. The CBD process can be described by following three simplified reaction equations

$$Zn(NH_3)_x^{2+} + S^{2-} \rightleftharpoons ZnS \downarrow + NH_3 \uparrow \qquad (1)$$

$$Zn(NH_3)_x^{2+} + 2OH^- \rightleftharpoons ZnO \downarrow + H_2O + NH_3 \uparrow \qquad (2)$$

$$Zn(NH_3)_x^{2+} + 2OH^- \rightleftharpoons Zn(OH)_2 \downarrow + NH_3 \uparrow \qquad (3)$$

Reactions (2) and (3) compete due to their similar solubility product, whereas the solubility product of ZnS (reaction (1)) is higher [22]. Reducing the sulphur concentration, i.e. TU concentration, in the bath led to decreased growth of ZnS. Reactions (2) and (3) are not affected, thus an increased oxygen content in the final ZnS(O,OH) films can be expected.

Immediately after the CBD process, samples were rinsed with 1.5 M ammonia aqueous solution and air annealed for 10 min at 200 °C as this was found to be beneficial for device performance [23]. A reference cell with a standard CdS buffer layer was also grown. Solar cells were completed with an i-ZnO/ZnO:Al bilayer (80 nm/600 nm) by RF magnetron sputtering. Individual cells with an area of $3 \times 3\,\text{mm}^2$ were defined by mechanical scribing.

2.3. *J–V* curves and external quantum efficiency (EQE)

Solar cells were characterized by *J–V* curves under 100 mW cm^{-2} simulated AM1.5 solar illumination calibrated with an Si reference cell.

EQE was measured using a lock-in amplifier and a chopped white light source (900 W, halogen lamp, 360 Hz) combined with a dual grating monochromator that was calibrated using an Si reference cell.

Temperature dependent *J–V* curves were recorded using a closed-cycle He cryostat and a Oriel small-area solar simulator calibrated to 1 sun with an Si reference cell.

2.4. Raman spectroscopy

ZnS(O,OH) layers were characterized by resonant Raman spectroscopy using a Horiba Jovin Yvon LabRam HR 800-UV system coupled to an Olympus metallurgical microscope under a 325 nm excitation wavelength, scanned over an area of $30 \times 30\ \mu\text{m}^2$ using a DuoScan accessory. In order to avoid the thermal effect the power density was kept below 0.4 mW in a spot of about 1 μm in diameter. All spectra were calibrated imposing the main peak of monocrystalline silicon at $520\,\text{cm}^{-1}$.

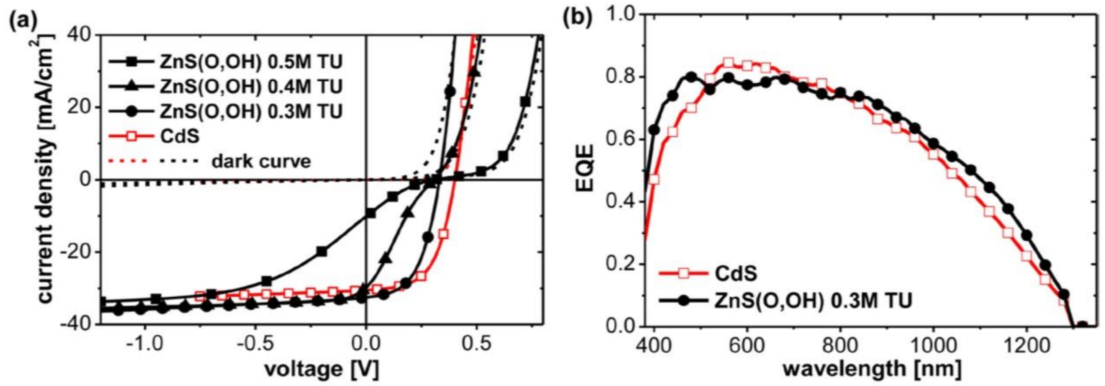

Figure 3. (a) Illuminated and dark *J–V* curves of devices with ZnS(O,OH) buffer layers deposited with different TU concentrations during the CBD process and CdS as a reference buffer layer. (b) EQE of a device with 0.3 M TU ZnS(O,OH) buffer and a CdS buffer.

2.5. X-ray photoelectron spectroscopy (XPS)

XPS experiments were performed in a PHI 5500 Multitechnique System (from Physical Electronics) with a monochromatic x-ray source (aluminium Kα line of 1486.6 eV energy and 350 W) placed perpendicular to the analyser axis and calibrated using the 3*d*5/2 line of Ag with a full width at half maximum (FWHM) of 0.8 eV.

3. Results and discussion

Figure 3 shows illuminated and dark *J–V* curves of the CZTSe absorbers with a CdS reference and the ZnS(O,OH) buffer layer deposited using three different TU concentrations in the bath. It can clearly be seen that for the sample with the highest TU concentration during CBD (0.50 M TU) the photocurrent (i.e. the difference between the current values of dark and illuminated *J–V* curves) starts to become blocked at a reverse bias of −1.0 V. Then the *J–V* curve shows a kink-like shape and follows the dark *J–V* curve in the forward bias direction. The solar cell device shows a low efficiency with poor J_{sc} and FF (see table 1). This behaviour is expected for a solar cell with a conduction band alignment with a too high spike, as this high spike acts as a barrier for photogenerated electrons, like a second diode. For the sample with ZnS(O,OH) 0.40 M TU concentration this current blocking occurs at a higher voltage and the distortion of the illuminated *J–V* curve is less pronounced, indicating a reduction of the still too-high barrier in the conduction band. This suggests less incorporation of sulphur into the ZnS(O,OH) film during the CBD process as discussed in the experimental section. However, the current blocking still starts at negative voltage (−0.1 V), which explains the lower J_{sc} value and FF obtained in comparison to the 0.30 M sample. For the sample of ZnS(O,OH) 0.30 M TU no current blocking, i.e. distortion of the curve, is observed. Comparing the device parameters of ZnS(O,OH) 0.30 M samples with the CdS reference cell (see table 1) one can clearly see that the J_{sc} is around 2 mA cm^{-2} higher, however the V_{oc} is still lower (332 mV compared with 401 mV, for ZnS(O,OH) 0.30 M and CdS respectively).

Table 1. Performance of devices with ZnS(O,OH) buffer layer deposited with different TU concentrations in the CBD process and CdS reference. R_{series}, R_{shunt} and A were extracted from illuminated *J–V* curves using the method described by Sites *et al* [25].

Buffer	CdS	ZnS(O,OH) 0.3 M TU	ZnS(O,OH) 0.4 M TU	ZnS(O,OH) 0.5 M TU
Efficiency (%)	6.9	5.6	2.1	0.6
FF (%)	56.3	51.8	22.9	17.9
J_{sc} (mA cm^{-2})	30.5	32.6	30.5	10.1
V_{oc} (mV)	401	332	306	311
R_{series} (Ω cm^2)	0.85	0.72	—	—
R_{shunt} (Ω cm^2)	235	131	—	—
A	2.14	2.02	—	—

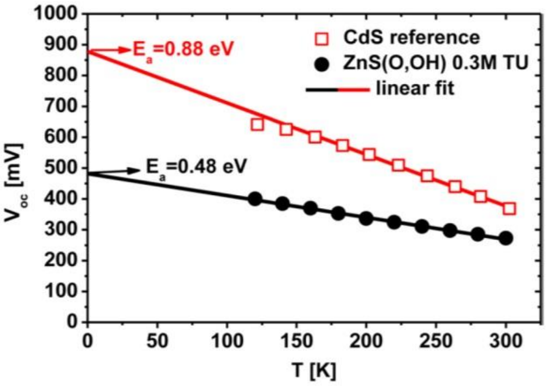

Figure 4. Temperature dependence of V_{oc} and linear extrapolation to $T = 0$ K to extract the E_a of the recombination process for solar cells with ZnS(O,OH) 0.3 M TU and CdS buffer layers.

The J_{sc} increase is expected because ZnS(O,OH) has a higher band gap than CdS, which increases its transparency, i.e. increases the absorption of short-wavelength photons in the CZTSe absorber. EQE measurements, as shown in figure 2(b), confirm an increased charge carrier generation in the short-wavelength region below 500 nm. The loss in

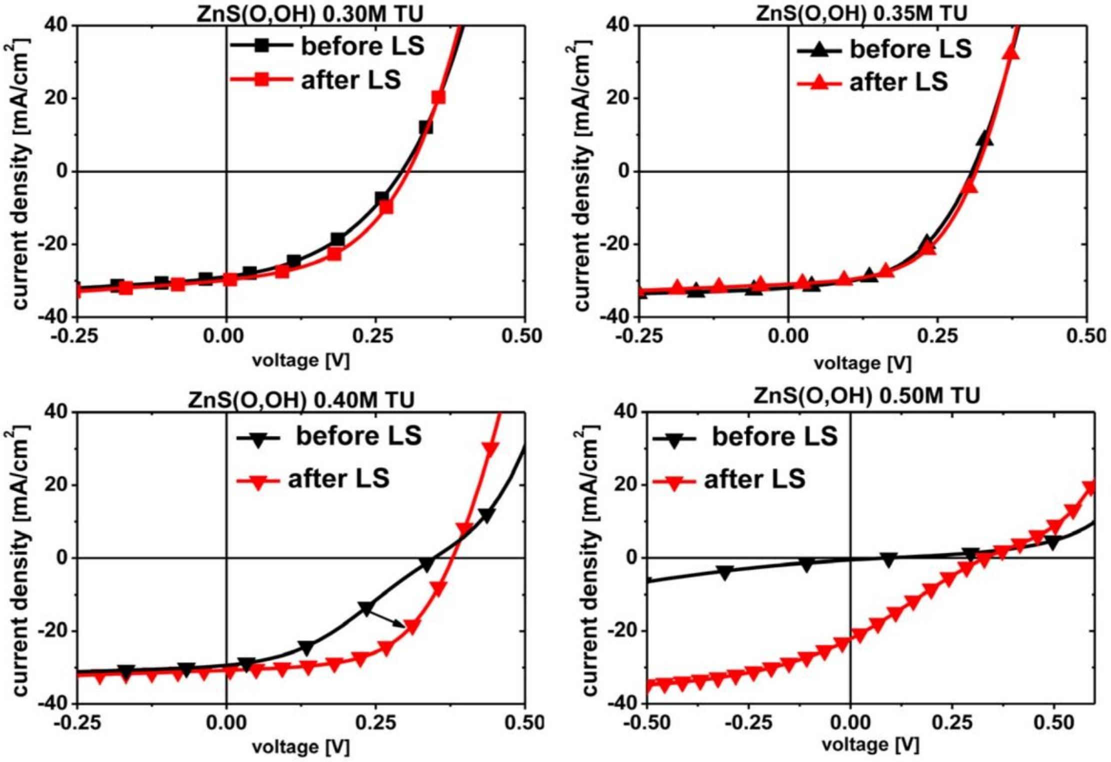

Figure 5. Illuminated *J–V* curves of devices with ZnS(O,OH) buffer layers deposited with different TU concentrations during the CBD process before and after LS for 260 min.

Table 2. Performance of devices with a ZnS(O,OH) buffer layer deposited with different TU concentrations during the CBD process before and after LS for 260 min. R_{series}, R_{shunt} and A were extracted from illuminated *J–V* curves using the method described by Sites *et al* [25].

	ZnS(O,OH) 0.30 M TU		ZnS(O,OH) 0.35 M TU		ZnS(O,OH) 0.40 M TU		ZnS(O,OH) 0.50 M TU	
Buffer	Before	After LS	Before	After LS	Before	After LS	Before	After LS
Efficiency (%)	3.5	4.2	4.8	5.1	3.6	6.5	0.01	1.8
FF (%)	41.1	45.7	49.2	52.5	35.3	55.9	24.1	24.7
J_{sc} (mA cm^{-2})	28.9	29.8	32.0	30.9	29.4	30.7	0.6	22.2
V_{oc} (mV)	294	304	308	311	348	379	96	330
R_{series} (Ω cm^2)	0.38	0.50	0.64	0.55	—	0.55	—	—
R_{shunt} (Ω cm^2)	48	59	97	114	143	174	—	—
A	3.3	2.6	2.3	2.1	—	2.1	—	—

V_{oc} for the ZnS(O,OH) 0.30 M TU sample can be explained by a lower sulphur content in the buffer layer and therefore a transition from a spike-like alignment to a cliff, as is also observed for CIGS with an ALD-grown Zn(O,S) buffer layer with low sulphur content [9]. A very low sulphur contents in the ZnS(O,OH) 0.30 M TU buffer layer a value $S/(S + O) < 0.04$ was confirmed by Raman measurement, as will be discussed later. Therefore, it is reasonable to assume a cliff-like conduction band alignment as it is the case for pure ZnO (see figure 2). For both devices, the CdS reference and ZnS(O,OH) 0.30 M TU, the diode ideality factor A is around 2, suggesting the main recombination paths limiting V_{oc} are trap states in the space charge region or the interface [24]. To determine if V_{oc} limitations are due to interface recombination temperature-dependent *J–V* curves were recorded. In figure 4 the temperature dependence of the V_{oc} for the ZnS(O,OH) 0.30 M TU and CdS reference devices are shown. From a linear extrapolation of V_{oc} to 0 K the activation energy (E_{a}) of recombination can be calculated ($E_{\text{a}} = V_{\text{oc}}\, q$; where $q$is the elementary charge). A clear difference between ZnS(O,OH) 0.30 M TU and the CdS reference can be seen. For the CdS reference $E_{\text{a}} = 0.88$ eV was extracted, which is close to the fundamental bandgap of CZTSe of 1.0 eV. For ZnS(O,OH) 0.30 M TU the activation energy is clearly lower, at a value of 0.48 eV. Thus, an increased interface recombination due to the presence of a cliff-like conduction band alignment reduces the V_{oc} of the 0.30 M TU device as discussed earlier.

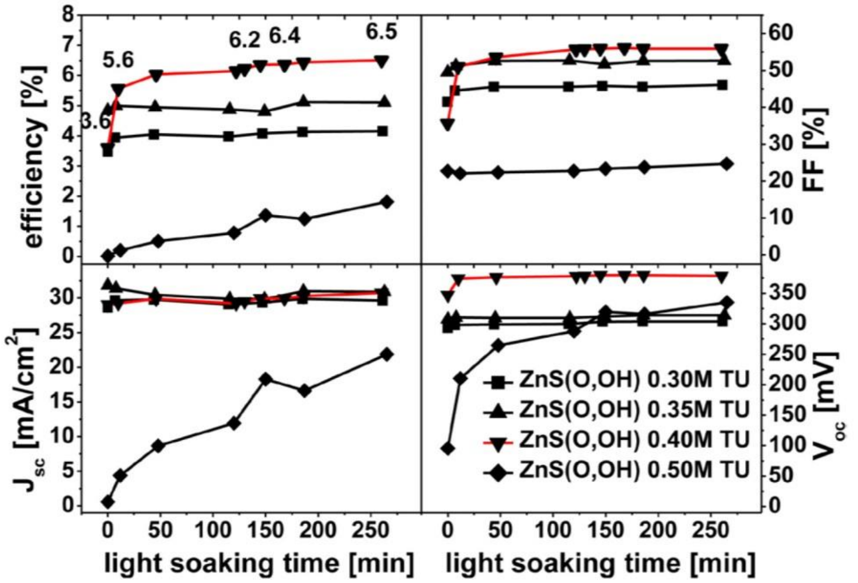

Figure 6. Evolution of device parameters with 1 sun LS time for devices with ZnS(O,OH) buffer layers deposited with different TU concentrations during the CBD process.

Although at first sight the efficiency of the ZnS(O,OH) 0.30 M TU sample seems better than the 0.40 M TU sample, a cliff-like band alignment is a clear limitation for device performance. As will be shown in the following, LS treatments can largely improve the performance of devices with ZnS(O,OH) buffer layers with higher sulfur contents, i.e. with a spike-like band alignment.

To characterize the ZnS(O,OH) layers grown onto CZTSe absorber and prove the reproducibility of the process a new set of samples was prepared using four different TU concentrations (0.30 M, 0.35 M, 0.40 M and 0.50 M). One part of each sample was included in solar cells and one was kept for characterization of the buffer layer itself.

In figure 5 *J–V* curves of these devices are shown and the device parameters are summarized in table 2. All devices show same behaviour as for the first set of samples, with non-distorted curves for low-TU deposited buffers and kinks for 0.40 M and 0.50 M samples. Furthermore, for this set of samples the effects of LS were studied in detail. As all CZTSe absorber layer used were produced in the same synthesis run, all observed differences in LS behaviour can be attributed to the properties of the different ZnS(O,OH) buffer layers. In figure 6 the evolution of device parameters depending on one sun white LS time are presented and the device parameters before and after LS are summarized in table 2. It can clearly be seen that 0.30 M and 0.35 M sample are almost unaffected by LS. However, LS has a large influence on the 0.40 M and 0.50 M sample. After the first 10 min of LS a large increase in device performance is observed for the 0.40 M sample from 3.5 % to 5.8% efficiency, which further stabilizes at 6.5% after 250 min. Comparing the *J–V* curves before and after LS in figure 5 one can see that LS eliminates the *J–V* curve distortion, leading to a strong increase in V_{oc}, J_{sc}, and FF. Also for the 0.50 M device a strong improvement in device performance is observed. With increasing LS time *J–V* distortion is reduced allowing collection of photogenerated charge carriers. This indicates a reduction of the barrier to photogenerated electrons, i.e. a reduction of the spike in the

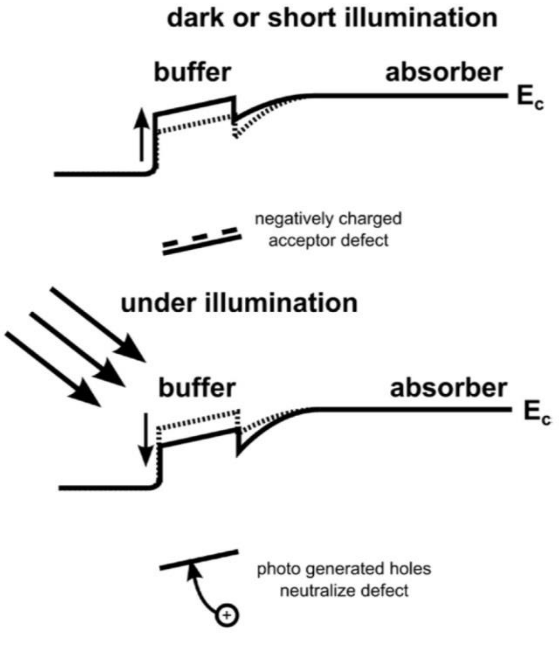

Figure 7. Schematic of the conduction band alignment in the presence of acceptor-like deep defect states. In the dark these defects are negatively charged due to trapping of electrons contributed from the donors of the buffer layer. This negative space charge decreases the band bending and increases the spike in the conduction band. Under illumination photogenerated holes can neutralize the defects resulting in a decrease of the spike.

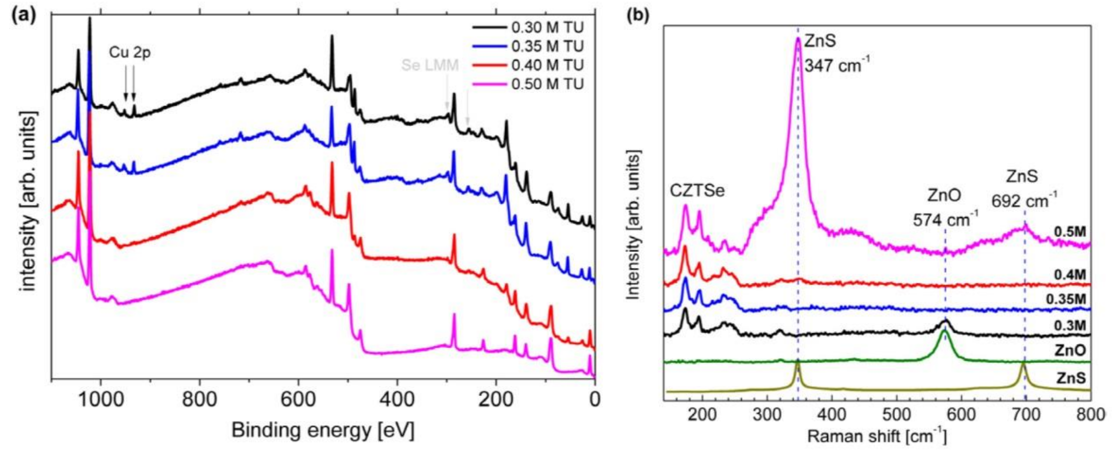

Figure 8. X-ray photoelectron spectroscopy (a) and UV-Raman (b) spectra of ZnS(O,OH) buffer layers on CZTSe absorbers deposited with different TU concentrations during the CBD process; ZnO and ZnS reference spectra were added for convenience.

conduction band due to photodoping of ZnS(O,OH) [26]. The beneficial effect of LS can be explained by the presence of acceptor-like deep states in the buffer layer, buffer/absorber or buffer/window interface, which is widely reported in literature [26–28]. In the dark or after only a short illumination period these acceptor-like states are ionized by trapping electrons contributed by the donors of the n-type buffer layer, thus compensating it. A more negative space charge is created inside the buffer layer that results in a decrease in band bending and increase of the conduction band spike as illustrated in figure 7. During white light illumination photogenerated holes in the buffer layer get trapped by the acceptor defects, neutralizing them and reducing the spike further (see figure 7). This is due to the fact that negatively charged acceptor-like defects have larger capture cross-section for holes than when they are neutral for electrons [26]. As electron–hole pairs are created inside the buffer during illumination a large amount of free holes is present, which can be captured and neutralize the defect. Therefore, white LS can reduce the conduction band spike slightly. Thus the small influence of LS and lower V_{oc} of the 0.30 M and 0.35 M devices further suggest a cliff-like conduction band alignment in contrast to the 0.40 M and 0.50 M devices [29]. After 150 min of LS the V_{oc} of the 0.50 M device overtakes the values of the 0.30 M and 0.35 M devices.

To characterize the ZnS(O,OH) layer itself, XPS measurements were carried out on sister pieces of the Mo/CZTSe/ZnS(O,OH) layers that were finished to solar cells (see figure 8(a)). XPS shows that all four ZnS(O,OH) layers are thinner than 10 nm, with estimated thicknesses of less than 2 nm for the 0.30 M and 0.35 M case, 6 nm for 0.40 M and around 9 nm for the 0.50 M case, calculated by using a multipack fit program and the NIST database for the estimation of the electron inelastic mean free path. For the 0.30 M and 0.35 M samples even the Cu and Se peaks of the CZTSe layer beneath are visible, confirming a thickness of around 2 nm. Full coverage of all layers is assumed, as no sever shunting of the devices is observed even after applying high reverse bias voltages (see figures 3 and 5). Other direct or indirect thickness measurements of these nanometric buffer layers on top of absorbers are challenging as the CZTSe absorber surface is quite rough, making the use of optical-based measurements impossible. The use of other smoother substrates would greatly influence the growth conditions, which could lead to misinterpretations when comparing with ZnS(O,OH) grown onto CZTSe absorbers. This fact and the small thickness make further advanced electrical, optical or compositional characterization of the exactly same buffer layers as used in solar cell devices a difficult task. To determine S/(S + O) ratios a carbon surface layer had to be removed by argon sputtering, unfortunately leading to the removal of the full layer for 0.30 M, 0.35 M and 0.40 M samples due to their nanometre thicknesses. For the 0.50 M sample an S/(S + O) ratio of 0.63 was calculated. The ZnS(O,OH) layers were further investigated by resonant Raman measurements, which are very sensitive to the bandgap modifications of materials that originate from composition change or nanotexturization [30–32]. In the measured spectra a ZnO-like LO Raman peak was found for the 0.30 M sample and a ZnS-like LO Raman peak for the 0.50 M sample (see figure 8(b)). This fact indicates a different incorporation of sulphur and oxygen due to changes in the TU concentration during CBD as already suggested by the observed solar cell device performance. For the 0.30 M sample the frequency of the ZnO-like LO peak is very close to that from the measured pure ZnO reference. This indicates that this layer has a very low S content, with a value of $S/(S + O) < 0.04$ according to the dependence of the frequency of this peak on the S/(S + O) content reported in Polity *et al* [33]. In the spectra from the 0.35 M and 0.40 M samples only Raman peaks characteristic of CZTSe were observed [34, 35]. This could be related to a loss of the resonant Raman excitation conditions when using the UV excitation line in these very thin layers because of the strong bandgap bowing that takes place in Zn(O,S) alloys with S/(S + O) relative content close to 0.5 [33]. In the case of the 0.50 M sample the ratio of first- (at 347 cm^{-1}) and second-

(at 692 cm^{-1}) order ZnS-like Raman peaks allows estimation of the grain size in layers thinner than 10 nm that is in agreement with the XPS-estimated thicknesses below 9 nm [30].

4. Conclusion

In conclusion, this work shows that CBD-grown ZnS(O,OH) buffer layers show promising results for cadmium-free CZTSe-based solar cells with power conversion efficiencies of up to 6.5% after LS, a value comparable to that of the CdS reference case. Variation of the TU concentration in the CBD shows a strong impact on device performance. A strong distortion (kink) in illuminated *J–V* curves is observed for high TU concentration samples (0.5 − 0.4 M) indicating a barrier for photogenerated electrons as expected for ZnS as the buffer layer due to a spike in the conduction band alignment that is too high[11]. No distortions but lower V_{oc} values are obtained for 0.35 and 0.30 M TU devices. Furthermore, 0.35 M and 0.30 M samples are less affected by LS, whereas 0.40 M and 0.50 M devices show strong improvements after LS. XPS and Raman spectroscopy indicate layer thicknesses of less than 10 nm for all cases, and a decrease in thickness with decreasing TU concentration. Variations of S/(S + O) ratios are not evident from XPS due to carbon surface contamination and the low layer thickness. However, Raman scattering spectra exhibited a ZnO-like peak for the 0.30 M sample and ZnS-like peaks for the 0.50 M sample. The observed decrease in thickness with decreasing TU concentration together with a strong reduction of metastable behaviour is another indication for changes in S/(S + O) ratio, i.e. band alignment, as in CIGS the opposite thickness related trend is observed [15]. However, for CIGS it is shown that metastable effects can be reduced by reducing the conduction band offset towards a cliff [29]. On the whole, insights into the strong influence of TU concentration in CBD of ZnS(O,OH) buffer layers on device performance opens up new and easy ways to further increase the efficiencies of environmentally friendly cadmium-free element- abundant solar cells.

Acknowledgments

This research was supported by the Seventh Framework Programme (FP7) under the project KESTCELLS (FP7-PEOPLE-2012-ITN-316488), by the NOVAZOLAR project from the SOLARERANET International program (subproject ref. PCIN-2013-193 funded by Spanish MINECO) and by European Regional Development Founds (ERDF, FEDER Programa Competitivitat de Catalunya 2007–2013). Authors from IREC and the University of Barcelona belong to the M-2E (Electronic Materials for Energy) Consolidated Research Group and the XaRMAE Network of Excellence on materials for Energy of the 'Generalitat de Catalunya; ES thanks the Government of Spain for the 'Ramon y Cajal' fellowship (RYC-2011–09212) and Y S thanks for the PTA fellowship (PTA2012-7852-A).

References

[1] Polizzotti A, Repins I L, Noufi R, Wei S-H and Mitzi D B 2013 *Energy Environ. Sci.* **6** 3171
[2] Scheer R and Schock H W 2011 *Chalcogenide Photovoltaics Physics, Technologies, and Thin Film Devices* (New York: Wiley)
[3] Minemoto T, Matsui T, Takakura H, Hamakawa Y, Negami T, Hashimoto Y, Uenoyama T and Kitagawa M 2001 *Sol. Energy Mater. Sol. Cells* **67** 83
[4] Gloeckler M and Sites J R 2005 *Thin Solid Films* **480–1** 241
[5] Niemegeers A, Burgelman M and Vos A D 1995 *Appl. Phys. Lett.* **67** 843
[6] Wang W, Winkler M T, Gunawan O, Gokmen T, Todorov T K, Zhu Y and Mitzi D B 2013 *Adv. Energy Mater.* **4** 1301465
[7] Haight R, Barkhouse A, Gunawan O, Shin B, Copel M, Hopstaken M and Mitzi D B 2011 *Appl. Phys. Lett.* **98** 253502
[8] Li J, Wei M, Du Q, Liu W, Jiang G and Zhu C 2013 *Surf. Interface Anal.* **45** 682
[9] Platzer-Björkman C, Törndahl T, Abou-Ras D, Malmström J, Kessler J and Stolt L 2006 *J. Appl. Phys.* **100** 044506
[10] Nakamura M, Yoneyama N, Horiguchi K, Iwata Y, Yamaguchi K, Sugimoto H and Kato T 2014 *Proc. IEEE 40th Photovolt. Spec. Conf.* (Piscataway, NJ: IEEE) pp 0107–10
[11] Barkhouse D A R, Haight R, Sakai N, Hiroi H, Sugimoto H and Mitzi D B 2012 *Appl. Phys. Lett.* **100** 193904
[12] Ericson T, Scragg J J, Hultqvist A, Watjen J T, Szaniawski P, Torndahl T and Platzer-Björkman C 2014 *IEEE J. Photovolt.* **4** 465
[13] Nguyen M *et al* 2015 *Sol. Energy* **111** 344
[14] Grenet L *et al* 2014 *Thin Solid Films* **564** 375
[15] Buffière M, Barreau N, Arzel L, Zabierowski P and Kessler J 2014 *Prog. Photovolt. Res. Appl.* **23** 462
[16] Kobayashi T, Yamaguchi H and Nakada T 2014 *Prog. Photovolt. Res. Appl.* **22** 115
[17] Walsh A, Chen S, Wei S-H and Gong X-G 2012 *Adv. Energy Mater.* **2** 400
[18] López-Marino S *et al* 2013 *J. Mater. Chem.* A **1** 8338
[19] Neuschitzer M, Sanchez Y, López-Marino S, Xie H, Fairbrother A, Placidi M, Haass S, Izquierdo-Roca V, Perez-Rodriguez A and Saucedo E 2015 *Prog. Photovolt. Res. Appl.* **23** 1660
[20] Ennaoui A, Bär M, Klaer J, Kropp T, Sáez-Araoz R and Lux-Steiner M C 2006 *Prog. Photovolt. Res. Appl.* **14** 499
[21] Nakada T, Mizutani M, Hagiwara Y and Kunioka A 2001 *Sol. Energy Mater. Sol. Cells* **67** 260
[22] Hubert C, Naghavi N, Canava B, Etcheberry A and Lincot D 2007 *Thin Solid Films* **515** 6032
[23] Neuschitzer M *et al* 2015 *Chem. Mater.* **27** 5279–87
[24] Hegedus S S and Shafarman W N 2004 *Prog. Photovolt. Res. Appl.* **12** 155
[25] Sites J R and Mauk P H 1989 *Sol. Cells* **27** 411
[26] Eisgruber I, Granata J, Sites J, Hou J and Kessler J 1998 *Sol. Energy Mater. Sol. Cells* **53** 367
[27] Pudov A O, Sites J R, Contreras M A, Nakada T and Schock H-W 2005 *Thin Solid Films* **480–1** 273
[28] Nichterwitz M, Caballero R, Kaufmann C A, Schock H-W and Unold T 2013 *J. Appl. Phys.* **113** 044515
[29] Hori H, Minemoto T and Takakura H 2010 *Curr. Appl. Phys.* **10** S150
[30] Fairbrother A, Izquierdo-Roca V, Fontané X, Ibáñez M, Cabot A, Saucedo E and Pérez-Rodríguez A 2014 *CrystEngComm* **16** 4120
[31] Dimitrievska M, Xie H, Fairbrother A, Fontané X, Gurieva G, Saucedo E, Pérez-Rodríguez A, Schorr S and Izquierdo-Roca V 2014 *Appl. Phys. Lett.* **105** 031913

[32] Izquierdo-Roca V, Fontané X, Saucedo E, Jaime-Ferrer J S, Álvarez-García J, Pérez-Rodríguez A, Bermudez V and Morante J R 2011 *New J. Chem.* **35** 453

[33] Polity A, Meyer B K, Krämer T, Wang C, Haboeck U and Hoffmann A 2006 *Phys. Status Solidi* a **203** 2867

[34] Guc M, Levcenko S, Izquierdo-Roca V, Fontane X, Valakh M Y, Arushanov E and Pérez-Rodríguez A 2013 *J. Appl. Phys.* **114** 173507

[35] Dimitrievska M, Fairbrother A, Saucedo E, Pérez-Rodríguez A and Izquierdo-Roca V 2015 *Appl. Phys. Lett.* **106** 073903

5 GE-DOPING OF CZTSE PHOTOVOLTAIC ABSORBERS

5.1 V_{oc} boosting and grain growth enhancing Ge-doping strategy for $Cu_2ZnSnSe_4$ photovoltaic absorbers

The work presented in the following was published in The Journal of Physical Chemistry C:

The Journal of Physical Chemistry C 2016 120 (18), 9661-9670
DOI:10.1021/acs.jpcc.6b02315

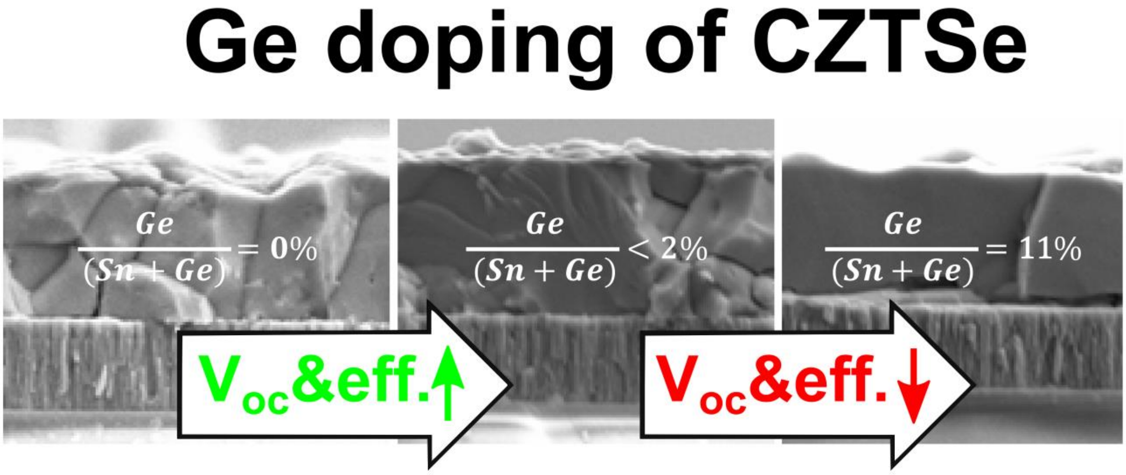

Figure 5.1. Table of content graphic showing the effects of Ge doping on grain growth and indicating its influence on device performance.

THE JOURNAL OF PHYSICAL CHEMISTRY C
Article
pubs.acs.org/JPCC

V_{oc} Boosting and Grain Growth Enhancing Ge-Doping Strategy for $Cu_2ZnSnSe_4$ Photovoltaic Absorbers

Markus Neuschitzer,*,[†] Jose Marquez,[‡] Sergio Giraldo,[†] Mirjana Dimitrievska,[†] Marcel Placidi,[†] Ian Forbes,[‡] Victor Izquierdo-Roca,[†] Alejandro Pérez-Rodriguez,[†,§] and Edgardo Saucedo[†]

[†]Catalonia Institute for Energy Research-IREC, Jadins de les Dones de Negre 1, 08930 Sant Adrià de Besòs (Barcelona), Spain
[‡]Northumbria Photovoltaic Applications Group, Department of Physics and Electrical Engineering, Northumbria University, Newcastle upon Tyne, U.K.
[§]IN2UB, Departament d'Electrònica, Universitat de Barcelona, C. Martí i Franquès 1, 08028 Barcelona, Spain

Supporting Information

ABSTRACT: $Cu_2ZnSnSe_4$ (CZTSe) is a promising thin film photovoltaic absorber material. However, up to now its main problem is the low open circuit voltage (V_{oc}) compared to more mature thin film photovoltaic technologies. Most kesterite synthesis routes employ a two-step approach consisting of precursor deposition followed by a crystallization step. In this study, a Ge-assisted crystallization process for nanocrystalline CZTSe precursors is presented. This process shows a strong beneficial influence on crystal growth and further solar cell device performance, especially the open circuit voltage. Detailed morphological and structural analyses as well as in depth solar cell device characterization are presented for different Ge doping. For low Ge doping an increase in charge carrier density is observed, resulting in devices with 8.5% efficiencies without antireflective coating and V_{oc} of over 470 mV, which corresponds to V_{oc} deficits ($E_g/q - V_{oc}$) below 580 mV, a value comparable to current record devices. High Ge amounts, despite enhancing grain growth, deteriorate cell performance. Admittance spectroscopy measurements identified the appearance of a deep defect for high Ge doping, and this may be the cause for this deterioration. These results indicate that an accurate control of group IV (Ge, Sn) elemental composition during crystallization may be mandatory for high device performance. In view of that we propose a defect model based in the interaction of group IV elements with Cu, giving important insights into the understanding of fundamental limitations of current kesterite device performances.

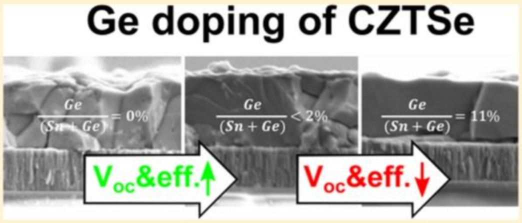

1. INTRODUCTION

$Cu_2ZnSn(S_{1-x}Se_x)_4$ (CZTSSe), in the literature often referred to as kesterite due to its crystal structure,[1] is a promising candidate to replace chalcopyrites ($CuIn_{1-x}Ga_xSe_2$, CIGS) as absorber layer in thin film solar cells due its composition of more earth abundant materials. However, one of the main challenges so far for kesterite-based solar cells is the low open circuit voltage (V_{oc}) compared to more mature thin film solar cell technologies like CIGS and CdTe. V_{oc} deficits (i.e., $\Delta V_{oc\text{-}def} = E_g/q - V_{oc}$) for CZTSSe-based solar cells have not achieved values significantly less than 0.6 V, whereas for record CIGS devices V_{oc} deficits of 0.44 V are obtained.[2,3] The origins for this low V_{oc} are being intensively investigated. Interface recombination, low minority carrier lifetime, electrostatic potential fluctuations, and tail states are proposed as possible reasons.[4−6] Recently, a novel sintering approach using a nanometric Ge layer deposited onto metallic precursor stacks prior to a reactive annealing in Se and Sn atmosphere showed a large increase in device performance and especially in V_{oc}.[7] The role of the Ge during the sintering process is not yet fully understood; however, different than Ge alloying in kesterites reported previously,[8,9] minimal quantities of Ge are observed in the final CZTSe absorber, still ensuring the abundance of all elements of the final thin film absorber material.[7] In previous reported improvements of device performance due to Ge alloying, large amounts of Sn are substituted by Ge in final CZTSe films, resulting in ratios of Ge/(Ge + Sn) = 0.4[8] and Ge/(Ge + Sn) = 0.3.[9] The substitution of Sn by Ge in the CZTSe lattice increases the bandgap of the material from 1.0 eV for Sn pure CZTSe to around 1.36 eV for Ge pure CZGSe.[10,11] Thus, although for the latter cases of Ge alloying an improvement in device performance (from 9.07% to 9.14%[8] and from 8.4% to 9.4%[9]) and V_{oc} was observed, the V_{oc} deficit could not be reduced due to an increase of the bandgap with increased Ge content alloyed in the CZTSe absorber. In contrast to the Ge-assisted selenization process of metallic precursor stacks,[7] in this current work the possibility of Ge doping for already synthesized pure selenide kesterite (CZTSe)

Received: March 4, 2016
Revised: April 21, 2016
Published: April 22, 2016

DOI: 10.1021/acs.jpcc.6b02315
J. Phys. Chem. C 2016, 120, 9661−9670

absorbers are investigated. The work shows that there is a beneficial effect of the Ge-doping approach for CZTSe absorbers in general. Initial experiments trying to incorporate Ge directly into already highly crystalline absorber materials, i.e., develop a postdeposition Ge-doping step, did not lead to satisfactory results as demonstrated in the Supporting Information (Figures S1 and S2). However, as will be shown in this work nanocrystalline CZTSe as precursor material allows a successful Ge doping with beneficial effects on device performance resulting in V_{oc} higher than 470 mV and a reduction of V_{oc} deficit to $V_{oc\text{-def}} = 0.576$ V for the best case, while keeping the Ge/(Ge + Sn) ratio of the film below 2%. For higher Ge amounts, despite enhancing grain growth, lower devices performance is achieved as will be shown for the first time and can be explained by the appearance of a deep defect. Thus, this work emphasizes the importance of group IV elemental composition during crystallization. Furthermore, all kesterite absorber synthesis routes of high performance solar cells use a two-step approach consisting of a precursor deposition followed by reactive annealing in chalcogen atmosphere for crystallization and grain growth.[3,7,12−14] Therefore, the beneficial Ge-assisted crystallization presented here might also be applicable for different chalcogen-containing precursors which consist of nanocrystalline CZTSSe obtained via chemical-based routes, nanocrystal synthesis, or vacuum processes.[12−15]

In a first and second part a Ge-assisted crystallization process of nanocrystalline CZTSe material and the influence of Ge content on the composition, morphology, and structural properties of the absorber layer are presented. The third part focuses on the influence of this Ge doping on solar cell device performance and gives more insights into possible origins for the beneficial effects of Ge doping, proposing a dynamic defect model that can shed light on the current efficiency limitations of kesterite-based solar cells.

2. EXPERIMENTAL SECTION

2.1. Metal Stack Deposition and Annealing Treatments. Molybdenum and Cu/Sn/Cu/Zn stacks were deposited using dc magnetron sputtering (Alliance Ac450). Cu-poor, Zn-rich compositions with ratios of Cu/(Zn + Sn) = 0.8 and Zn/Sn = 1.2 were targeted in the metal stack layers and controlled by a calibrated X-ray fluorescence (XRF, Fischerscope XVD) measurements. Ge nanolayers were deposited by thermal evaporation using an Oerlikon Univex 250 evaporator.

All annealing treatments were carried out in a conventional tube furnace using a graphite box (69 cm^3 in volume) and are described in more detail in each part. Se and Sn−Se atmospheres are created inside of the graphite box by the addition of elemental Se and Sn (100 mg Se and 5 mg Sn). A heating rate of 20 °C/min is used for all treatments, and cooling is allowed naturally.

2.2. Material and Device Characterization. Scanning electron microscopy (SEM) images were obtained using a ZEISS Series Auriga microscope and 5 kV acceleration voltage.

Raman scattering measurements were obtained in backscattering configuration using a homemade Raman system coupled with an iHR320 Horiba Jobin Yvon spectrometer and a gas HeCd laser with 442 nm and solid state lasers with 532 nm as well as 785 nm excitation wavelengths. Excitation and light collection were made through an Olympus metallographic microscope, with a laser spot size diameter of approximately 100 μm (depending on the excitation wavelength). In all cases, in order to avoid the presence of thermal effects in the spectra, the power excitation density was kept below 50 W/cm^2. The first-order Raman spectrum of monocrystalline Si was measured as a reference before and after acquisition of each Raman spectrum, and the spectra were corrected with respect to the Si line at 520 cm^{-1}.

X-ray diffraction (XRD) measurements were carried out in Bragg−Brentano geometry using a Bruker D8 discover diffractometer equipped with a Cu tube. For the suppression of Kβ radiation a nickel filter was used.

2.3. Solar Cell Processing. Solar cells are completed by depositing a CdS buffer layer (50 nm) by chemical bath deposition followed by a iZnO/ITO (50 nm/350 nm) window layer by dc pulsed sputtering (CT100 Alliance Concepts) as described elsewhere in more detail.[16] Prior to the CdS deposition the absorber layers are etched using $KMnO_4$ + H_2SO_4 solution (40 s), followed by a chemical etching in $(NH_4)_2S$ solution (2 min), and finally 2% KCN aqueous solution (2 min).[17,18] Individual solar cell of 3 × 3 mm^2 are defined by mechanical scribing. No antireflective coating or metallic grids were used, and solar cells were electrically contacted directly on the ITO window layer for characterization. A low temperature (<250 °C) postdeposition air annealing was carried out on full devices to improve solar cell performance as described elsewhere in more detail.[19] In a recent work GeO_x nanoinclusions were found in absorbers synthesized by a Ge-assisted selenization process of metallic precursor stacks.[7] The role of these GeO_x nanoinclusions is still under investigation. Here in this work different to Ge-assisted selenization process of metallic precursor stacks nanocrystalline precursor are used, and although air annealings of final devices were carried out to improve device performance, no new evidence of GeO_x formation was found with the methods used in this work; however, its presence in the final absorbers cannot be excluded.

2.4. Solar Cell Device Characterization. Illuminated current−voltage (J−V) curves were recorded using Keithley source meter and a Sun 3000 class AAA solar simulator (Abet Technologies, 25 °C, AM1.5G illumination) calibrated with Si reference cell. External quantum efficiency (EQE) characterization was carried out using a Bentham PVE300 system calibrated with Si and Ge photodiodes. To obtain internal quantum efficiency (IQE), the reflectance (R) of the solar cell was measured using the same Bentham PVE300 system as light source and an integrating sphere as detector. IQE was calculated as IQE = EQE/(1 − R). Capacitance voltage measurements (CV) were carried out using an impedance analyzer from Novocontrol Technologies. A parallel circuit model was assumed to derive the device capacitance. From CV measurements doping profiles were calculated using the formalism of Miller[20] and a relative dielectric permittivity of $\varepsilon = 8.5$ for CZTSe.[21] Admittance spectroscopy (capacitance versus frequency: C−f) measurements at different temperatures (from 100 to 325 K) were carried out using a liquid nitrogen cryostat from SemiMetrics Ltd. and an Agilent E4980A LCR meter employing a parallel circuit model to extract the capacitance of the device.

3. RESULTS AND DISCUSSION

3.1. Characterization of Nanocrystalline Precursor Layer. Nanocrystalline CZTSe precursor layers on glass/Mo substrates were obtained by low-temperature reactive annealing of glass/Mo/Cu/Sn/Cu/Zn metallic stacks in a graphite box

DOI: 10.1021/acs.jpcc.6b02315
J. Phys. Chem. C 2016, 120, 9661−9670

under Se and Sn atmosphere using a conventional tube furnace. Two different sample series were produced. One was annealed at 350 °C and the other at 400 °C, each set for 30 min under argon flow keeping the pressure at 1.5 mbar. In the following sections, just results of the sample series obtained at 400 °C are shown. Nevertheless, all Ge-assisted crystallization experiments presented in this work were carried out on two sample sets to demonstrate the reproducibility of the obtained results for nanocrystalline precursors of different crystalline quality. All related results to the 350 °C sample set can be found in the Supporting Information. In Figure 1, SEM top views as well as cross sections of the sample obtained after 400 °C selenization can be seen. The film shows densely packed nanocrystalline grains, with grain sizes well below 100 nm. To determine the phase composition of this nanocrystalline layer, multiwavelength Raman measurements[22] were carried out. In Figure 2 the Raman spectra for different wavelengths can be seen. The sample mainly consists of CZTSe phase with some $SnSe_2$ secondary phases as well as small amounts of ZnSe.[23,24] A large full width half-maximum (fwhm) value of the main CZTSe peak is observed, indicating a small average domain size.[25] From XRD measurements the same secondary phases could be identified, and no other phases were observed (see Figure S4). Both Raman and SEM confirm a dense nanocrystalline CZTSe film, making it a perfect precursor layer for Ge-assisted crystallization experiments.

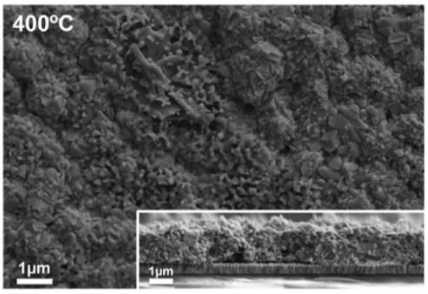

Figure 1. SEM top view and cross section of Cu/Sn/Cu/Zn stack selenized at 400 °C. Nanocrystalline CZTSe grains are visible.

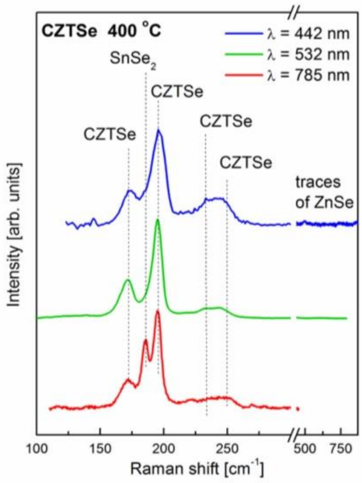

Figure 2. Multiwavelength Raman spectra of Cu/Sn/Cu/Zn stack selenized at 400 °C. CZTSe can be identified as main phase with $SnSe_2$ and traces of ZnSe secondary phases.

3.2. Ge-Assisted Crystallization of Nanocrystalline CZTSe Precursor: Influence on the Composition, Morphology, and Structural Properties of the Absorber Layers. The influence of Ge addition during the crystallization process of nanocrystalline CZTSe precursors was studied. For this purpose different thicknesses of Ge, nominally 5, 10, 15, 25, and 50 nm, were thermally evaporated onto the two different sets of nanocrystalline CZTSe precursor layers. Here in the following just the results regarding the 400 °C precursor are presented. The results obtained with the 350 °C precursor are identical confirming the reproducibility of the presented Ge-assisted crystallization and can be found in the Supporting Information. After the Ge evaporation on top of the precursor the samples were annealed in a graphite box containing elemental Se (100 mg) to provide a selenium-rich atmosphere inside of the box using a conventional tube furnace with argon atmosphere and a two-step annealing profile. The first step was carried out at 400 °C for 15 min at a low pressure of 1.5 mbar followed by a higher temperature step of 550 °C and 1000 mbar argon pressure for 15 min. The first step allows the formation of a Ge_3Se_7 phase which at 385 °C melts incongruently to volatile $GeSe_2$ and a liquid with composition of around 85 at. % Se.[26] This selenium-rich liquid phase assists grain growth and promotes the substitution of Sn for Ge in the CZTSe phase during the second high temperature step at 550 °C and high pressure of 1000 mbar.[7] Additionally to the Ge capped precursor layers one sample without Ge capping was added as well to the crystallization process. In Figure 3, SEM top views and cross section of the 400 °C nanocrystalline precursor crystallized using different thicknesses of Ge capping are shown. Comparing the sample without Ge addition and the one of 50 nm, one can clearly see a largely increased grain size for the latter case. All grains of the 50 nm Ge sample extend from the Mo back contact to the front surface and reach lateral sizes of over 5 μm. For samples with lower Ge content an

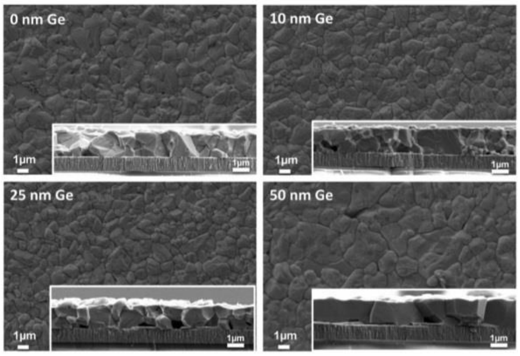

Figure 3. SEM top view and cross section of 400 °C CZTSe precursor crystallized using different Ge quantities evaporated on top of the nanocrystalline CZTSe precursor layer. An increased grain size with increased Ge quantity can be observed especially for the 50 nm case.

DOI: 10.1021/acs.jpcc.6b02315
J. Phys. Chem. C 2016, 120, 9661−9670

increased grain size is not evident, different than a previous study where nanometric Ge layers were evaporated prior to selenization directly onto metal precursor stacks instead of CZTSe nanocrystals, and an increased grain size is observed already for low Ge capping layer thicknesses (<15 nm).[7] Nevertheless, all these samples show grain sizes already above 1 μm with several grains extending from the back contact to the front surface.

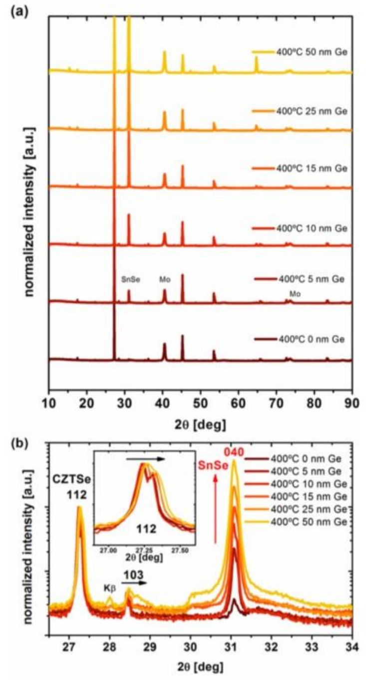

Figure 4. (a) XRD patterns of 400 °C CZTSe precursor crystallized using different Ge quantities evaporated on top of the CZTSe precursor layer. Intensities are normalized to the 112 kesterite peak, and curves are shifted vertically for the sake of clarity. (b) Zoom of XRD patterns on logarithmic scale. A shift of the main 112 kesterite type structure peak (see inset) as well as an increased formation of SnSe can be observed with increasing Ge thickness used.

XRD patterns for all crystallized samples were recorded as can be seen in Figure 4a and indicating that all the CZTSe and Ge-doped absorbers are crystallizing in a tetragonal structure.[27] Interestingly, an increase of the intensity of SnSe secondary phase peak is observed with increasing Ge amount used during the crystallization process (see Figure 4b). This indicates that the extra Sn present in the absorber layer due to the substitution of Sn by Ge leads to the formation of SnSe secondary phase. SEM EDS analysis found that the SnSe phases are mostly segregated on the absorber surface as plate-like crystallites whereas no indication for Ge-related secondary phases was found (see Supporting Information Figure S8).

Furthermore, the substitution of Sn by the smaller ion Ge results in crystal lattice shrinkage which is evidenced by a peak shift of all kesterite related peaks toward higher angles. This peak shift becomes clearer for Ge amounts above 15 nm. Below this value almost no change in peak position is observed, indicating a very low Ge incorporation in agreement with compositional measurements by XRF (see Table 1). From the diffraction patterns the lattice parameters were determined using LeBail analysis.[28] Figure 5a,b shows the obtained lattice parameters (a, c) as well as the tetragonal deformation ($c/2a$) in dependence of the Ge amount used during crystallization. Below 15 nm almost no change is observed, however, for 25 and 50 nm a decrease in both lattice parameters a and c can be seen as expected for the substitution of Sn by the smaller Ge ion.[10,11] The tetragonal distortion ($1 - c/2a$, i.e., the shift of $c/2a$ from the ideal value of 1) increases as the Ge content increases as it has been observed experimentally.[10,11]

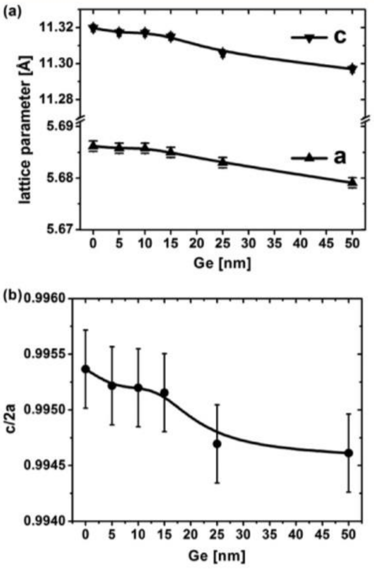

Figure 5. (a) Lattice parameters and (b) tetragonal deformation ($c/2a$) in dependence of the Ge quantity used during the crystallization of the 400 °C nanocrystalline CZTSe precursor layers.

Table 1. Cationic Composition and Cation Ratios of Ge-Doped CZTSe after Etching Measured by XRF

Ge	Cu [%]	Zn [%]	Sn [%]	Ge [%]	Ge/(Ge + Sn)	Zn/(Sn + Ge)	Cu/(Zn + Sn + Ge)
0 nm	44.22 ± 0.2	31.05 ± 0.2	24.73 ± 0.2	0.0 ± 0.1	0.00 ± 0.01	1.26 ± 0.05	0.79 ± 0.01
5 nm	44.43 ± 0.2	31.33 ± 0.2	24.19 ± 0.2	0.05 ± 0.1	0.00 ± 0.01	1.29 ± 0.04	0.80 ± 0.03
10 nm	44.33 ± 0.3	31.12 ± 0.2	24.34 ± 0.4	0.21 ± 0.1	0.01 ± 0.02	1.27 ± 0.04	0.80 ± 0.02
15 nm	44.31 ± 0.2	31.20 ± 0.2	24.03 ± 0.3	0.46 ± 0.1	0.02 ± 0.02	1.27 ± 0.03	0.80 ± 0.02
25 nm	44.45 ± 0.2	31.17 ± 0.2	23.10 ± 0.2	1.28 ± 0.2	0.05 ± 0.02	1.28 ± 0.03	0.80 ± 0.01
50 nm	44.35 ± 0.3	31.07 ± 0.2	21.77 ± 0.5	2.81 ± 0.2	0.11 ± 0.01	1.26 ± 0.02	0.80 ± 0.02

The material characterization showed a largely increased grain size for absorber layer crystallized in assistance of a large amount of Ge; however, a large segregation of SnSe secondary phases is observed. Secondary phases are known to harm solar cell device performance;[29] however, since most secondary phases were detected on the absorber surface, selective etching routes can effectively remove all unwanted phases and further passivate the absorber surface.[17,18] Prior to the CdS buffer layer and iZnO/ITO window deposition, the absorber layers were etched using a combined etching to remove possible formed ZnSe and SnSe secondary phases. This etching consisted of an oxidizing $KMnO_4$ + H_2SO_4 etching for ZnSe removal[17] followed by $(NH_4)_2S$ to remove SnSe phases.[18] The effectiveness of this etching can be seen in Figure 6a where the XRD pattern of the same samples as in Figure 4b are shown, however, after etching. Here only for the 50 nm Ge sample small traces of SnSe are detected. For all other samples no more SnSe is evidenced in the CZTSe absorber layer, though before etching XRD measurements indicate large SnSe amounts (see Figure 4b). Furthermore, Raman measurements on etched absorbers confirm highly crystalline CZTSe absorbers with no secondary phases (see Figure 6b). Only a peak shift for higher Ge amounts is observed as expected for higher incorporation of Ge into the CZTSe lattice.[10] Therefore, we can in principle exclude influences of secondary phases on the device performance of the different set of samples and can relate changes in device performance to the Ge amount used during crystallization. XRF measurements of the etched samples show that the Cu and Zn atomic compositions are only changing within the error of the measurements, whereas the Sn content decreases and Ge increases with increased Ge amount used during crystallization, which is in agreement with the Raman and XRD measurements. It further confirms the replacement of Sn by Ge in the CZTSe films. For Ge amounts of up to 15 nm the Ge/(Ge + Sn) ratio is below 2%, which is in the same range of low Ge incorporation observed for metallic precursor stacks selenized with similar Ge capping layers.[7] Since Cu and Zn atomic compositions are not changing, this means that although the samples crystallized with thick Ge capping layers, i.e., are crystallized in group IV (Ge, Sn) element rich conditions, the final films are not group IV (Ge, Sn) element rich. This can also be seen in the Zn/(Sn + Ge) and Cu/(Zn + Sn + Ge) ratios which just vary in between the error of the measurement. The excess of Sn segregates as SnSe secondary phase and is removed by a chemical etching and Ge excess most probably evaporates as volatile $GeSe_2$ phase.[26] Nevertheless, even if the final CZTSe film is not group IV element rich, the growth of the CZTSe absorber in Cu poor and group IV element rich condition could favor the formation of detrimental antisites defects like Sn_{Cu} or Ge_{Cu} as will be discussed in the following in more detail.

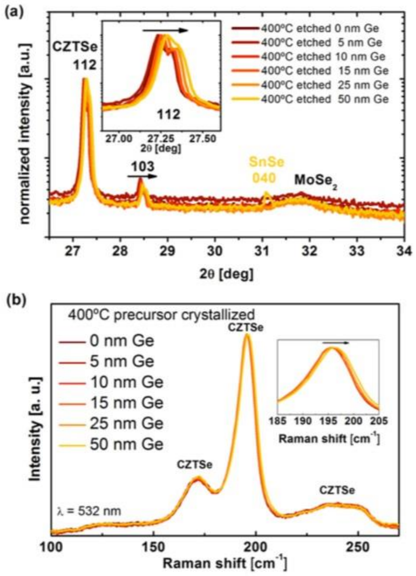

Figure 6. (a) XRD pattern of 400 °C CZTSe precursor crystallized using different Ge quantities evaporated on top of the CZTSe precursor layer after chemical etching to remove unwanted secondary phases as it used in solar cell processing. Only small rest of SnSe was found for the 50 nm sample in (a) (note the logarithmic scale). (b) Raman spectra of the same CZTSe absorbers. A small peak shift is observed for high Ge content (see inset).

3.3. Influence of Ge Doping on Solar Cell Performance.

In Figure 7a, the device parameters of the best cell for each sample are shown (see Supporting Information Figure S13 for JV curves and Figure S14 for sample statistics). A clear increase in V_{oc} is observed as the Ge layer thickness used during crystallization increases from 0 to 15 nm. The maximum V_{oc} of the device employing an absorber which was crystallized without the addition of Ge is 431 mV. V_{oc} increases to up 472 mV for the 10−15 nm Ge devices. A larger increase of Ge causes V_{oc} to decrease again to below 420 mV for the sample obtained using the 50 nm Ge layer. The efficiency follows the same trend and a maximum of 8.5% is obtained for the samples processed using the 10−15 nm Ge layers. The short circuit current (J_{sc}) behaves differently, decreasing slightly for low Ge content, followed by an increase for the 25 and 50 nm Ge layer based devices. The fill factor (FF) decreases slightly with increasing the Ge content up to the sample based on the 15 nm Ge layer and drops below 60% for those based on the 25 and 50 nm Ge capped-layer devices. To obtain a greater insight into the possible reasons for this optimum range of Ge capping of between 10 and 15 nm, IQE and CV measurements were performed. In Figure 8a the IQE curves of all devices are shown. The increase of the IQE signal in the long wavelength region is remarkable for the 25−50 nm Ge-capped samples. This increase indicates that there is better collection of photogenerated charge carrier in the CZTSe absorber and is in agreement with a higher J_{sc} of these devices. To estimate bandgap (E_g) values from IQE the absorption function ($\alpha \propto (h\nu - E_g)^{1/2}$) can be approximated by $\alpha \propto \ln(1 - \mathrm{IQE})$ if collection in the space charge region is assumed.[31,32] Thus, the bandgap can be calculated from intercept with the *x*-axis of a plot of hυ vs $(\ln(1 - \mathrm{IQE}))^2$, as shown in Figure S12. An error of the extracted bandgap values of about 0.04 eV has been obtained from linear fits of the hυ vs $(\ln(1 - \mathrm{IQE}))^2$ plots (see Figure S12). As it can be seen in Figure 7a, the bandgap of the absorbers stays constant around a value of 1.05 eV for the samples with Ge additions of 15 nm and below (see also Figures S11 and S12 for the comparison of *hυ* vs $(\ln(1 - \mathrm{IQE}))^2$ plots of the different devices). For higher Ge content, based on the 25 and 50 nm Ge capping layers, a monotonic increase in bandgap is observed up to 1.07 and 1.08 eV, respectively. This is in agreement with low Ge incorporation as

DOI: 10.1021/acs.jpcc.6b02315
J. Phys. Chem. C 2016, 120, 9661−9670

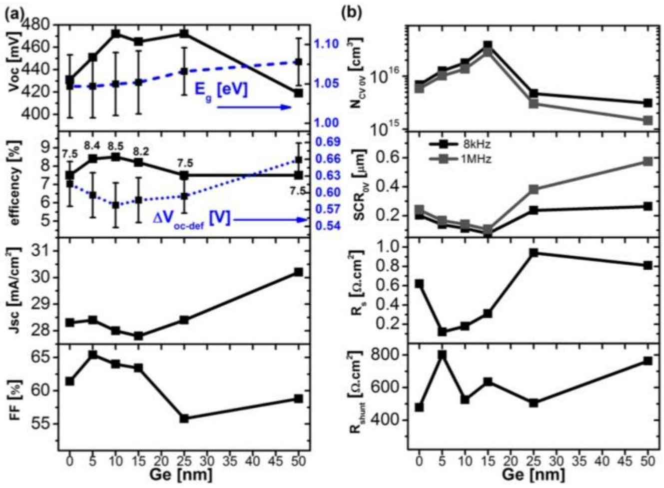

Figure 7. (a, b) Device parameters of best solar cells in dependence of the Ge quantity used during crystallization of CTZSe precursors. The band gap (E_g) extracted from IQE as well as the V_{oc} deficit ($\Delta V_{oc\text{-}def} = E_g/q - V_{oc}$) are indicated as well. Shunt resistance (R_{shunt}) and series resistance (R_s) are extracted from the illuminated curve using the method described by Sites et al.[30]

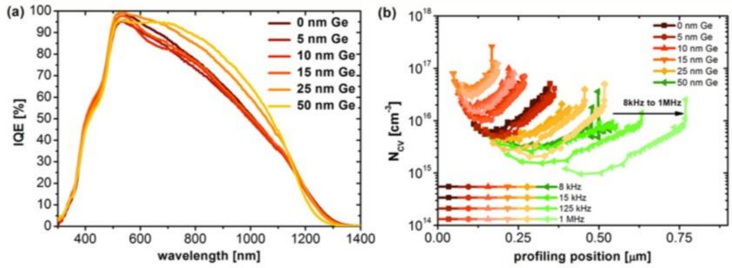

Figure 8. (a) IQE and (b) doping profiles as obtained from CV measurements for different frequencies of best solar cells of the different samples used in this study.

evidenced by XRD and XRF for the absorbers that were crystallized with 5−15 nm Ge layer, whereas for higher Ge quantities (based on the 25 and 50 nm Ge capping layers) Ge is incorporated into the CZTSe absorber and increases the bandgap.[10,11] An increased V_{oc} would be expected for devices with higher bandgap. However, this is not the case here as can be seen in Figure 7a, where the V_{oc} actually decreases for the devices based on 50 nm Ge capping layers although the bandgap increases. Whereas, the increase of V_{oc} occurs while the bandgap remains constant for devices that incorporated capping layers up to 15 nm in thickness. The V_{oc} deficit is reduced, and therefore a maximum device performance is observed (see Figure 7a). For devices with higher Ge content based on incorporation of the 25 and 50 nm Ge layers, the V_{oc} deficit increases again because although the bandgap starts to increase significantly for these samples, the V_{oc} values are not improving. Therefore, the V_{oc} improvements observed in this work for the devices based on 5−15 nm Ge capping layers are not related to a Ge-induced increase in bandgap as for other Ge alloyed CZTSe absorbers reported in the literature.[8,9] For example, Hages et al.[9] observe a monotonic increase in V_{oc} and bandgap with increasing Ge content in the film. However, the V_{oc} deficit increases with increased Ge content because bandgap and V_{oc} do not increase at the same rate. In their work highest device performance was obtained for a CZTGSe device with 30% at. Ge incorporated due to an improvement in carrier collection.[9] Similarly, Bag et al. observed an increase in V_{oc} and bandgap. However, an increase in V_{oc} deficit with increasing Ge content was observed in their devices.[8] The IQE spectra of Figure 8a show no significant increase in bandgap for devices based on Ge capping layers up to a thickness of 15 nm. Therefore, the observed V_{oc} improvement for this Ge range has to have different origins than an increased bandgap.

Doping profiles derived from CV measurements show an increase of charge carrier concentration from the reference sample (0 nm Ge) up to the sample that incorporated the 15 nm Ge layer and then a decrease for higher Ge amounts (see Figure 8b). The charge carrier concentrations (N_{CV}) as well as the space charge region (SCR) widths extracted at 0 V bias voltage from the doping profiles are shown in Figure 7b. For the samples that incorporated the 50 nm Ge layer the space charge region widths increase with decreasing charge carrier concentrations. This increase in SCR width can explain the improved collection of photogenerated charge carriers in the long wavelength range as observed in EQE measurements because a higher SCR width facilitates the collection of charge

DOI: 10.1021/acs.jpcc.6b02315
J. Phys. Chem. C 2016, 120, 9661−9670

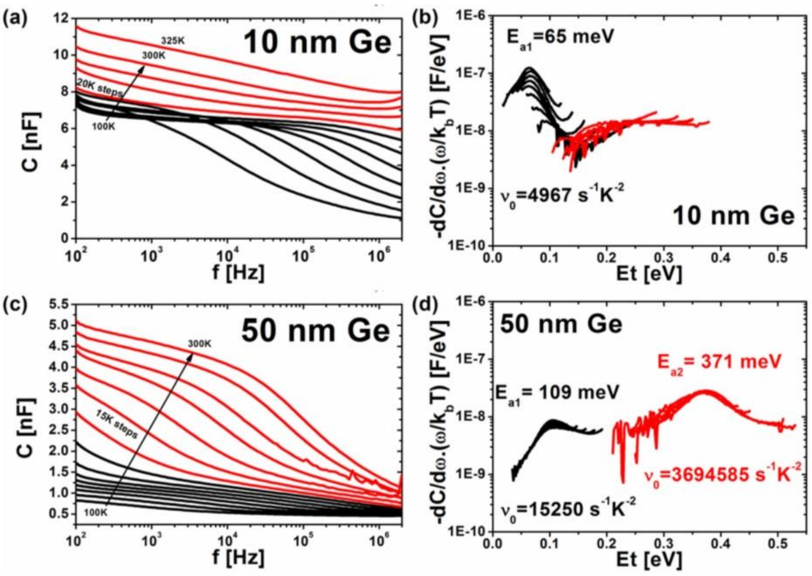

Figure 9. (a , c) $C-f$ spectra as well as the from it derived (b, d) defect spectra for 10 and 50 nm Ge device.

carriers created deeper inside the bulk of the absorber material, i.e., the region corresponding to the long wavelength part of the IQE. Furthermore, the decrease in V_{oc} with increased SCR is a strong indication for trap assisted tunneling recombination which was recently identified as one of the most probable causes for V_{oc} loss in kesterite-based solar cells.[31,33] In general, polycrystalline kesterite films show low mobility values;[34] thus, together with lower doping density this translates into lower bulk conductivity and as a result higher series resistance (R_s) which can explain the lower FF observed for the 50 nm Ge device (see Figure 7a). The shunt resistance (R_{shunt}) vary as well with Ge content, with a maximum for the best devices; however, the trend is not so clear.

For absorbers limited by recombination in the neutral zone the V_{oc} can be expressed by[35]

$$\Delta V_{oc} = \frac{E_g}{q} - \frac{k_b T}{q} \ln\left(\frac{q D_n N_C N_V}{J_{sc} N_A L_D}\right) \tag{1}$$

where k_b is the Boltzmann constant, T the temperature, q the elementary charge, D_n the diffusion constant for electrons, $N_{C/V}$ the effective density of states in the conduction/valence band, L_D the diffusion length of electrons, and N_A the acceptor density of the absorber. A comparable expression can be derived for V_{oc} limited by recombination in the SCR.[35] Assuming absorber layers with the same bandgap and L_D, the expected change in V_{oc} due to different doping levels (N) can be estimated by[36]

$$\Delta V_{oc} = \frac{k_b T}{q} \ln\left(\frac{N_1}{N_2}\right) \tag{2}$$

The observed increase of doping density from around 4×10^{15} to 3×10^{16} cm^{-3} for device without Ge and with the optimal range of 10−15 nm of Ge, respectively, would result in a V_{oc} increase of 50 mV. This is in good agreement with the V_{oc} increase from 431 to 473 mV obtained for these cases, indicating that the V_{oc} increase can be explained by a favorable doping level. The reasons for this increase in doping density by Ge doping are not clear yet. A possible interaction of Ge and alkali (Na, K) dopants diffusing from the soda lime glass substrate is suspected, as recently the beneficial effects of Ge doping for CZTSe solar cells on Na free substrates are especially observed in the presence of additional Na.[37] Interestingly the charge carrier density decreases again significantly for the device crystallized with high Ge amount (>25 nm Ge). This may indicate the presence of two competing effects because the lower V_{oc} of the 50 nm devices cannot only be explained by a unfavorable low doping level since these devices have a 30 meV higher bandgap which should increase V_{oc}. It is remarkable that for the 50 nm devices the CV profiles are strongly frequency dependent (see Figure 8b), which is a strong indication of the presence of deep defects.[38] To get further insights into electronic defect levels, admittance spectroscopy measurements were carried out. In Figure 9a,c the $C-f$ curves of a device with optimal Ge amount (400 °C precursor crystallized with 10 nm thick Ge layer) and a high Ge amount (400 °C precursor crystallized with 50 nm thick Ge layer) are shown for a temperature range of 100−325 K. There is a clear difference between the two devices visible. For the 10 nm Ge device a capacitance step is visible only for low temperatures (100−200 K; indicated as black curves), whereas for the 50 nm Ge also a pronounced high temperature step appears. The activation energies (E_a) and corresponding attempt to escape frequencies (ν_0) of each capacitance step can be determined via an Arrhenius plot of the inflection frequencies in the Cf curves versus $1/T$ and related to dominant defect bands that occur between Fermi energy and midgap.[38] These defect energies can be illustrated by plotting the scaled derivative $-dC/d\omega(\omega/k_bT)$ against the energy axis $E_t = k_bT \ln(\nu_0 T^2/\omega)$ as shown in Figure 9b,d.[39] For the 10 nm Ge device only a low temperature step with activation energy of

DOI: 10.1021/acs.jpcc.6b02315
J. Phys. Chem. C 2016, 120, 9661−9670

65 meV appears (see Figure 9b). For the 50 nm Ge device besides the low temperature step which activation energy shift to higher energies of 109 meV, a high temperature step with activation energy of 371 meV is detected. The energy level of the shallower defect is in the same range as previous reported for kesterite devices, where also an increase of energy with increasing absorber bandgap is observed.[12,14,21,40−42] Interesting is the appearance of a deep defect of 371 meV for devices based on a absorber using large amount of Ge (50 nm) during crystallization. Recently, Larramona et al.[14] showed that by fine-tuning of the Sn composition in CZTSSe absorber layer the formation of a deep defect at around 600 meV could be avoided and device performance increased to over 11% power conversion efficiency. There the deep defect is attributed to Cu_{Sn} antisites or V_{Sn} vacancy acceptor defects formed if Sn loss occurs during the synthesis process. In general, theoretical calculations show that Sn-related lattice defects create deep levels inside the bandgap and act as electron−hole recombination centers which could limit solar cell performance.[43]

Assuming that Sn and Ge have similar properties, this could be extended to group IV elements in general. Since all samples presented here have Cu-poor and Zn-rich composition with constant Cu and Zn atomic content (see Table 1), it is more likely to assume to formation of Sn_{Cu} or Ge_{Cu} antisite donor defects if samples are grown in excess of group IV elements like it is the case for the 50 nm Ge device. We propose following mechanism for samples grown in Cu-poor and very Ge-rich conditions:

$$V_{Cu} + Sn_{Sn} + Ge \rightarrow Ge_{Sn} + Sn_{Cu} \quad (3)$$

or

$$V_{Cu} + Ge \rightarrow Ge_{Cu} \quad (4)$$

Ge replaces Sn, and the excess Sn/Ge can either occupy Cu vacancies (V_{Cu}) forming Sn_{Cu}/Ge_{Cu} antisites or segregates as SnSe secondary phase as evidenced by XRD. Sn_{Cu} antisites creates a deep donor level[43] which acts as electron−hole recombination centers deteriorating the solar cell performance. This would further explain the lower doping observed for high Ge (50 nm) devices due to compensation. On the other hand, for lower Ge quantities, like 10 nm, the Ge could actually prevent the formation of deep defects like Cu_{Sn} or V_{Sn} formed due to Sn loss as proposed by Larramona et al.[14] The optimal Ge amount compensates possible Sn loss and the formation of deep Cu_{Sn} antisites or V_{Sn} vacancy defects as can be illustrated by

$$V_{Cu} + Cu_{Sn} + Ge \rightarrow Ge_{Sn} + Cu_{Cu} \quad (5)$$

or

$$V_{Sn} + Ge \rightarrow Ge_{Sn} \quad (6)$$

From admittance spectroscopy it is unfortunately not possible to attribute the defect levels to either donor or acceptor like traps; thus, more advanced characterizations are necessary to determine clearly the origin of this deep defect level observed.

4. CONCLUSION

In this work a beneficial Ge doping strategy for nanocrystalline CZTSe precursor layer is presented. By adding small amounts of Ge during the crystallization process, the device performance, particularly V_{oc}, was increased. An optimal range of 10−15 nm of Ge addition during the crystallization process of nanocrystalline CZTSe in selenium atmosphere led to an increase of charge carrier density and V_{oc} compared to the non-Ge-doped reference cells. XRF, XRD, and Raman evidenced a low level of Ge incorporation into the kesterite-type structure for this low range (10−15 nm Ge), keeping the Ge/(Sn + Ge) below 2%. Higher Ge quantities added during the crystallization process result in a large increase of grain size of the CZTSe absorber layers and significant replacement of Sn by Ge in the final films. Despite the largely increased grain size and bandgap widening due to Ge incorporation, the device performance and V_{oc} are not further improved compared to the lower Ge-doped devices. Admittance spectroscopy shows the presence of a shallow defect for optimal and high Ge doping. This defect becomes deeper as the amount of Ge incorporation increases. In addition to this shallow defect, a deep defect appears for the highest Ge-content sample. This deep, midgap, defect may be assigned to Sn_{Cu} or Ge_{Cu} antisites donor defects, formed under Cu-poor and group IV element-rich growth condition, and it is likely to act as an electron−hole recombination center which could explain the deterioration of the solar cell performance. Therefore, a careful control of the composition of the group IV elements seems to be critical to obtain high performance kesterite devices. The tuning of the element IV composition during crystallization of nanocrystalline precursors by Ge doping has shown to be an efficient way to avoid the formation of this deep defect and enabled devices with efficiencies of up to 8.5% to be produced (without antireflective coating). These devices show V_{oc} values above 470 mV and a V_{oc} deficit of 578 mV, which is comparable to current record devices.[12−14]

■ ASSOCIATED CONTENT

Supporting Information

The Supporting Information is available free of charge on the ACS Publications website at DOI: 10.1021/acs.jpcc.6b02315.

> Assessment of effects of postdeposition Ge doping on crystalline CZTSe absorbers (Figures S1 and S2), results of Ge-assisted crystallization of 350 °C precursor (Figures S3−S7 and S9−S15) as well as SEM top view with EDX phase map of 50 nm Ge sample (Figure S8), EQE and reflectance measurement and bandgap extraction from IQE (Figures S10−S12), *J*−*V* curves (Figure S13), and statistic of device performance of each sample (Figure S14) (PDF)

■ AUTHOR INFORMATION

Corresponding Author

*E-mail mneuschitzer@irec.cat; Ph +34-933-562-615 (M.N.).

Notes

The authors declare no competing financial interest.

■ ACKNOWLEDGMENTS

This research was supported by the Framework 7 program under the project KESTCELLS (FP7-PEOPLE-2012-ITN-316488) and by European Regional Development Founds (ERDF, FEDER Programa Competitivitat de Catalunya 2007−2013). Authors from IREC and the University of Barcelona belong to the M-2E (Electronic Materials for Energy) Consolidated Research Group and the XaRMAE Network of Excellence on Materials for Energy of the "Generalitat de Catalunya". E.S. thanks the Government of Spain for the "Ramon y Cajal" fellowship (RYC-2011-09212), S.G. for the FPI fellowship (BES-2014-068533), and M.P. for the MINECO postdoctoral fellowship (FPDI-2013-18968). Many thanks to

Eric Don from SemiMetrics Ltd. for help with the cryostat and admittance measurement setup.

■ REFERENCES

(1) Siebentritt, S.; Schorr, S. Kesterites-a Challenging Material for Solar Cells: Kesterites-a Challenging Material for Solar Cells. *Prog. Photovoltaics* **2012**, *20*, 512−519.

(2) Jackson, P.; Hariskos, D.; Wuerz, R.; Kiowski, O.; Bauer, A.; Friedlmeier, T. M.; Powalla, M. Properties of Cu(In,Ga)Se_2 Solar Cells with New Record Efficiencies up to 21.7%. *Phys. Status Solidi RRL* **2015**, *9*, 28−31.

(3) Wang, W.; Winkler, M. T.; Gunawan, O.; Gokmen, T.; Todorov, T. K.; Zhu, Y.; Mitzi, D. B. Device Characteristics of CZTSSe Thin-Film Solar Cells with 12.6% Efficiency. *Adv. Energy Mater.* **2014**, *4*, 1614−6840.

(4) Gunawan, O.; Todorov, T. K.; Mitzi, D. B. Loss Mechanisms in Hydrazine-Processed $Cu_2ZnSn(Se,S)_4$ Solar Cells. *Appl. Phys. Lett.* **2010**, *97*, 233506.

(5) Repins, I. L.; Moutinho, H.; Choi, S. G.; Kanevce, A.; Kuciauskas, D.; Dippo, P.; Beall, C. L.; Carapella, J.; DeHart, C.; Huang, B.; Wei, S. H. Indications of Short Minority-Carrier Lifetime in Kesterite Solar Cells. *J. Appl. Phys.* **2013**, *114*, 084507.

(6) Gokmen, T.; Gunawan, O.; Todorov, T. K.; Mitzi, D. B. Band Tailing and Efficiency Limitation in Kesterite Solar Cells. *Appl. Phys. Lett.* **2013**, *103*, 103506.

(7) Giraldo, S.; Neuschitzer, M.; Thersleff, T.; López-Marino, S.; Sánchez, Y.; Xie, H.; Colina, M.; Placidi, M.; Pistor, P.; Izquierdo-Roca, V.; et al. Large Efficiency Improvement in $Cu_2ZnSnSe_4$ Solar Cells by Introducing a Superficial Ge Nanolayer. *Adv. Energy Mater.* **2015**, *5*, 1501070.

(8) Bag, S.; Gunawan, O.; Gokmen, T.; Zhu, Y.; Mitzi, D. B. Hydrazine-Processed Ge-Substituted CZTSe Solar Cells. *Chem. Mater.* **2012**, *24*, 4588−4593.

(9) Hages, C. J.; Levcenco, S.; Miskin, C. K.; Alsmeier, J. H.; Abou-Ras, D.; Wilks, R. G.; Bär, M.; Unold, T.; Agrawal, R. Improved Performance of Ge-Alloyed CZTGeSSe Thin-Film Solar Cells through Control of Elemental Losses. *Prog. Photovoltaics* **2015**, *23*, 376−384.

(10) Grossberg, M.; Timmo, K.; Raadik, T.; Kärber, E.; Mikli, V.; Krustok, J. Study of Structural and Optoelectronic Properties of $Cu_2Zn(Sn_{1-x}Ge_x)Se_4$ (x = 0 to 1) Alloy Compounds. *Thin Solid Films* **2015**, *582*, 176−179.

(11) Khadka, D. B.; Kim, J. Band Gap Engineering of Alloyed $Cu_2ZnGe_xSn_{1-x}$ Q_4 (Q = S,Se) Films for Solar Cell. *J. Phys. Chem. C* **2015**, *119*, 1706−1713.

(12) Haass, S. G.; Diethelm, M.; Werner, M.; Bissig, B.; Romanyuk, Y. E.; Tiwari, A. N. 11.2% Efficient Solution Processed Kesterite Solar Cell with a Low Voltage Deficit. *Adv. Energy Mater.* **2015**, *5*, 1500712.

(13) Lee, Y. S.; Gershon, T.; Gunawan, O.; Todorov, T. K.; Gokmen, T.; Virgus, Y.; Guha, S. $Cu_2ZnSnSe_4$ Thin-Film Solar Cells by Thermal Co-Evaporation with 11.6% Efficiency and Improved Minority Carrier Diffusion Length. *Adv. Energy Mater.* **2015**, *5*, 1401372.

(14) Larramona, G.; Levcenko, S.; Bourdais, S.; Jacob, A.; Choné, C.; Delatouche, B.; Moisan, C.; Just, J.; Unold, T.; Dennler, G. Fine-Tuning the Sn Content in CZTSSe Thin Films to Achieve 10.8% Solar Cell Efficiency from Spray-Deposited Water-Ethanol-Based Colloidal Inks. *Adv. Energy Mater.* **2015**, *5*, 1501404.

(15) Guo, Q.; Ford, G. M.; Yang, W.-C.; Walker, B. C.; Stach, E. A.; Hillhouse, H. W.; Agrawal, R. Fabrication of 7.2% Efficient CZTSSe Solar Cells Using CZTS Nanocrystals. *J. Am. Chem. Soc.* **2010**, *132*, 17384−17386.

(16) Neuschitzer, M.; Sanchez, Y.; López-Marino, S.; Xie, H.; Fairbrother, A.; Placidi, M.; Haass, S.; Izquierdo-Roca, V.; Perez-Rodriguez, A.; Saucedo, E. Optimization of CdS Buffer Layer for High-Performance $Cu_2ZnSnSe_4$ Solar Cells and the Effects of Light Soaking. *Prog. Photovoltaics* **2015**, *23*, 1660−1667.

(17) López-Marino, S.; Sánchez, Y.; Placidi, M.; Fairbrother, A.; Espindola-Rodríguez, M.; Fontané, X.; Izquierdo-Roca, V.; López-García, J.; Calvo-Barrio, L.; Pérez-Rodríguez, A.; et al. ZnSe Etching of Zn-Rich $Cu_2ZnSnSe_4$: An Oxidation Route for Improved Solar-Cell Efficiency. *Chem. - Eur. J.* **2013**, *19*, 14814−14822.

(18) Xie, H.; Sánchez, Y.; López-Marino, S.; Espíndola-Rodríguez, M.; Neuschitzer, M.; Sylla, D.; Fairbrother, A.; Izquierdo-Roca, V.; Pérez-Rodríguez, A.; Saucedo, E. Impact of Sn(S,Se) Secondary Phases in $Cu_2ZnSn(S,Se)_4$ Solar Cells: A Chemical Route for Their Selective Removal and Absorber Surface Passivation. *ACS Appl. Mater. Interfaces* **2014**, *6*, 12744−12751.

(19) Neuschitzer, M.; Sanchez, Y.; Olar, T.; Thersleff, T.; Lopez-Marino, S.; Oliva, F.; Espindola-Rodriguez, M.; Xie, H.; Placidi, M.; Izquierdo-Roca, V.; et al. cComplex Surface Chemistry of Kesterites: Cu/Zn Reordering after Low Temperature Postdeposition Annealing and Its Role in High Performance Devices. *Chem. Mater.* **2015**, *27*, 5279−5287.

(20) Miller, G. L. A Feedback Method for Investigating Carrier Distributions in Semiconductors. *IEEE Trans. Electron Devices* **1972**, *19*, 1103−1108.

(21) Gunawan, O.; Gokmen, T.; Warren, C. W.; Cohen, J. D.; Todorov, T. K.; Barkhouse, D. A. R.; Bag, S.; Tang, J.; Shin, B.; Mitzi, D. B. Electronic Properties of the $Cu_2ZnSn(Se,S)_4$ Absorber Layer in Solar Cells as Revealed by Admittance Spectroscopy and Related Methods. *Appl. Phys. Lett.* **2012**, *100*, 253905.

(22) Dimitrievska, M.; Fairbrother, A.; Fontané, X.; Jawhari, T.; Izquierdo-Roca, V.; Saucedo, E.; Pérez-Rodríguez, A. Multiwavelength Excitation Raman Scattering Study of Polycrystalline Kesterite Cu_2ZnSnS_4 Thin Films. *Appl. Phys. Lett.* **2014**, *104*, 021901.

(23) Dimitrievska, M.; Xie, H.; Jackson, A. J.; Fontané, X.; Espíndola-Rodríguez, M.; Saucedo, E.; Pérez-Rodríguez, A.; Walsh, A.; Izquierdo-Roca, V. Resonant Raman Scattering of ZnS_xSe_{1-x} Solid Solutions: The Role of S and Se Electronic States. *Phys. Chem. Chem. Phys.* **2016**, *18*, 7632−7640.

(24) Márquez, J.; Neuschitzer, M.; Dimitrievska, M.; Gunder, R.; Haass, S.; Werner, M.; Romanyuk, Y. E.; Schorr, S.; Pearsall, N. M.; Forbes, I. Systematic Compositional Changes and Their Influence on Lattice and Optoelectronic Properties of $Cu_2ZnSnSe_4$ Kesterite Solar Cells. *Sol. Energy Mater. Sol. Cells* **2016**, *144*, 579−585.

(25) Dimitrievska, M.; Fairbrother, A.; Pérez-Rodríguez, A.; Saucedo, E.; Izquierdo-Roca, V. Raman Scattering Crystalline Assessment of Polycrystalline Cu_2ZnSnS_4 Thin Films for Sustainable Photovoltaic Technologies: Phonon Confinement Model. *Acta Mater.* **2014**, *70*, 272−280.

(26) Stølen, S.; Johnsen, H. B.; Bøe, C. S.; Karlsen, O. B.; Grande, T. Stable and Metastable Phase Equilibria in the GeSe2-Se System. *J. Phase Equilib.* **1999**, *20* (1), 17−28.

(27) Schorr, S. The Crystal Structure of Kesterite Type Compounds: A Neutron and X-Ray Diffraction Study. *Sol. Energy Mater. Sol. Cells* **2011**, *95*, 1482−1488.

(28) Le Bail, A.; Duroy, H.; Fourquet, J. L. Ab-Initio Structure Determination of LiSbWO6 by X-Ray Powder Diffraction. *Mater. Res. Bull.* **1988**, *23*, 447−452.

(29) Xie, H.; Dimitrievska, M.; Fontané, X.; Sánchez, Y.; López-Marino, S.; Izquierdo-Roca, V.; Bermúdez, V.; Pérez-Rodríguez, A.; Saucedo, E. Formation and Impact of Secondary Phases in Cu-Poor Zn-Rich $Cu_2ZnSn(S_{1-y}Se_y)4$ $(0 \leq y \leq 1)$ Based Solar Cells. *Sol. Energy Mater. Sol. Cells* **2015**, *140*, 289−298.

(30) Sites, J. R.; Mauk, P. H. Diode Quality Factor Determination for Thin-Film Solar Cells. *Sol. Cells* **1989**, *27*, 411−417.

(31) Hages, C. J.; Carter, N. J.; Agrawal, R. Generalized Quantum Efficiency Analysis for Non-Ideal Solar Cells: Case of $Cu_2ZnSnSe_4$. *J. Appl. Phys.* **2016**, *119*, 014505.

(32) Hegedus, S. S.; Shafarman, W. N. Thin-Film Solar Cells: Device Measurements and Analysis. *Prog. Photovoltaics* **2004**, *12*, 155−176.

(33) Courel, M.; Pulgarín-Agudelo, F. A.; Andrade-Arvizu, J. A.; Vigil-Galán, O. Open-Circuit Voltage Enhancement in CdS/$Cu_2ZnSnSe_4$-Based Thin Film Solar Cells: A Metal−insulator−semiconductor (MIS) Performance. *Sol. Energy Mater. Sol. Cells* **2016**, *149*, 204−212.

(34) Gunawan, O.; Gokmen, T.; Mitzi, D. B. Suns-VOC Characteristics of High Performance Kesterite Solar Cells. *J. Appl. Phys.* **2014**, *116*, 084504.

(35) Rau, U.; Schock, H.-W. Electronic Properties of Cu(In,Ga)Se_2 Heterojunction Solar Cells—recent Achievements, Current Understanding, and Future Challenges. *Appl. Phys. A: Mater. Sci. Process.* **1999**, *69*, 131−147.

(36) Pianezzi, F.; Reinhard, P.; Chirilă, A.; Bissig, B.; Nishiwaki, S.; Buecheler, S.; Tiwari, A. N. Unveiling the Effects of Post-Deposition Treatment with Different Alkaline Elements on the Electronic Properties of CIGS Thin Film Solar Cells. *Phys. Chem. Chem. Phys.* **2014**, *16*, 8843.

(37) López-Marino, S.; Sánchez, Y.; Espíndola-Rodríguez, M.; Alcobé, X.; Xie, H.; Neuschitzer, M.; Becerril, I.; Giraldo, S.; Dimitrievska, M.; Placidi, M.; et al. Alkali Doping Strategies for Flexible and Light-Weight $Cu_2ZnSnSe_4$ Solar Cells. *J. Mater. Chem. A* **2016**, *4*, 1895−1907.

(38) *Advanced Characterization Techniques for Thin Film Solar Cells*; Rau, U., Abou-Ras, D., Kirchartz, T., Eds.; Wiley-VCH: Weinheim, Germany, 2011.

(39) Walter, T.; Herberholz, R.; Müller, C.; Schock, H. W. Determination of Defect Distributions from Admittance Measurements and Application to Cu(In,Ga)Se_2 Based Heterojunctions. *J. Appl. Phys.* **1996**, *80*, 4411.

(40) Kask, E.; Grossberg, M.; Josepson, R.; Salu, P.; Timmo, K.; Krustok, J. Defect Studies in $Cu_2ZnSnSe_4$ and $Cu_2ZnSn(Se_{0.75}S_{0.25})_4$ by Admittance and Photoluminescence Spectroscopy. *Mater. Sci. Semicond. Process.* **2013**, *16*, 992−996.

(41) Weiss, P. T.; Redinger, A.; Luckas, J.; Mousel, M.; Siebentritt, S. Admittance Spectroscopy in Kesterite Solar Cells: Defect Signal or Circuit Response. *Appl. Phys. Lett.* **2013**, *102*, 202105.

(42) Moore, J.; Hages, C.; Lundstrom, M.; Agrawa, R. Influence of Ge Doping on Defect Distributions of $Cu_2Zn(Sn_xGe_{1-x})(S_ySe_{1-y})$ Fabricated by Nanocrystal Ink Deposition with Selenization. Photovoltaic Specialists Conference (PVSC), 2012 38th IEEE, 2012; pp 1475−1480.

(43) Chen, S.; Walsh, A.; Gong, X.-G.; Wei, S.-H. Classification of Lattice Defects in the Kesterite Cu_2ZnSnS_4 and $Cu_2ZnSnSe_4$ Earth-Abundant Solar Cell Absorbers. *Adv. Mater.* **2013**, *25*, 1522−1539.

Supporting information

V_{OC} Boosting and Grain Growth Enhancing Ge-Doping Strategy for $Cu_2ZnSnSe_4$ Photovoltaic Absorbers

Markus Neuschitzer[a]*, Jose Marquez[b], Sergio Giraldo[a], Mirjana Dimitrievska[a], Marcel Placidi[a], Ian Forbes[b], Victor Izquierdo-Roca[a], Alejandro Pérez-Rodriguez[a,c], Edgardo Saucedo[a]

[a] Catalonia Institute for Energy Research- IREC, Jadins de les Dones de Negre 1, 08930 Sant Adrià de Besòs (Barcelona), Spain
[b] Northumbria Photovoltaic Applications Group, Department of Physics and Electrical Engineering, Northumbria University, Newcastle upon Tyne, UK
[c] IN2UB, Departament d'Electrònica, Universitat de Barcelona, C. Martí i Franquès 1, 08028 Barcelona, Spain
E-mail: mneuschitzer@irec.cat

1. Assessment of effects of post deposition Ge doping on crystalline CZTSe absorbers

Different conditions for a post deposition Ge doping of already crystalline CZTSe material and its influence on device performance were investigated. The CZTSe absorbers were synthesized using a two-step approach which consists of the deposition of metallic Cu/Sn/Cu/Zn precursor stacks followed by a reactive thermal annealing in Se and Sn atmosphere as described in more detail in Refs. S1 an S2. [S1,S2]. After the synthesis different Ge doping strategies were tested. For this purpose, nanometric layers of 1- 10 nm were thermally evaporated onto the crystalline CZTSe absorbers. To promote a possible diffusion of the Ge into the CZTSe different annealings were carried out. First annealings at different temperatures in a conventional tube furnace under argon atmosphere were investigated. Furthermore, a rapid thermal processing furnace with argon atmosphere was used to employ higher ramping rates (3°C/s). All treatments led to solar cell devices with lower device performance than untreated CZTSe reference solar cell as can be seen in Figure S1 indicating a non-favourable effect of Ge post deposition treatments on already crystalline CZTSe absorbers.

In a previous work we reported the beneficial effects of a nanometric Ge layer deposited onto Cu/Sn/Cu/Zn metallic precursor stacks prior to a reactive annealing in selenium atmosphere to form CZTSe absorber.[S3] There, the formation of a Ge_3Se_7 liquid phase was supposed that assists the crystallization of the material. Therefore, a possible Ge post deposition treatment in selenium atmosphere for already crystalline CZTSe absorber was studied as well. In Figure S2

SEM top-views of CZTSe absorbers which were annealed a second time in selenium atmosphere after the deposition of thin Ge layers are shown. A strong change of the CZTSe surface is observed. With increasing Ge thickness the crystalline CZTSe surface gets more and more deteriorated indicating the formation of a Ge-selenium liquid phases which reacts with the crystalline CZTSe surface. Solar cell device made from this absorbers show low performance.

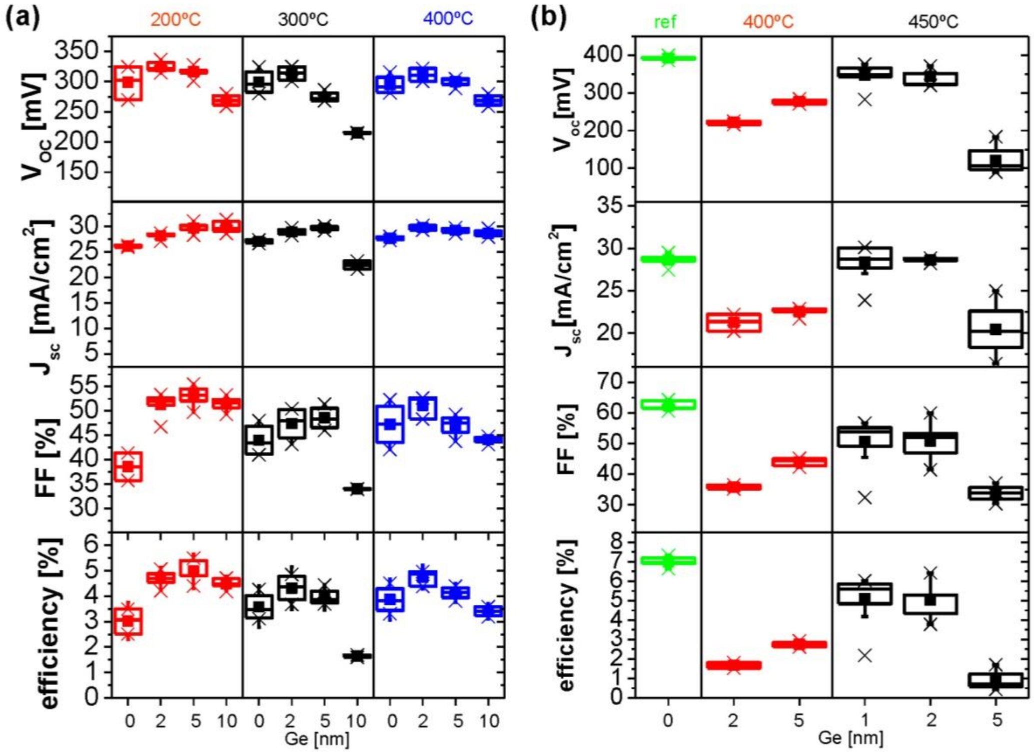

Figure S1. Box plots of device parameters for different post deposition Ge doping approaches on already highly crystalline CZTSe absorbers: (a) Evaporation of different Ge thicknesses from 0-10 nm on top of crystalline CZTSe absorber followed by an annealing under argon atmosphere in a conventional tube furnace in argon atmosphere for 30 minutes at 200ºC, 300ºC and 400ºC to promote a possible Ge diffusion into the CZTSe absorber. (b) Evaporation of different Ge thicknesses on top of crystalline CZTSe absorber followed by rapid thermal annealing (3ºC/s of heating rate) at 400ºC and 450ºC for 5 minutes. All Ge doping approaches for already highly crystalline material results in lower performance than a non-doped reference cell (see box plots in (b) named ref).

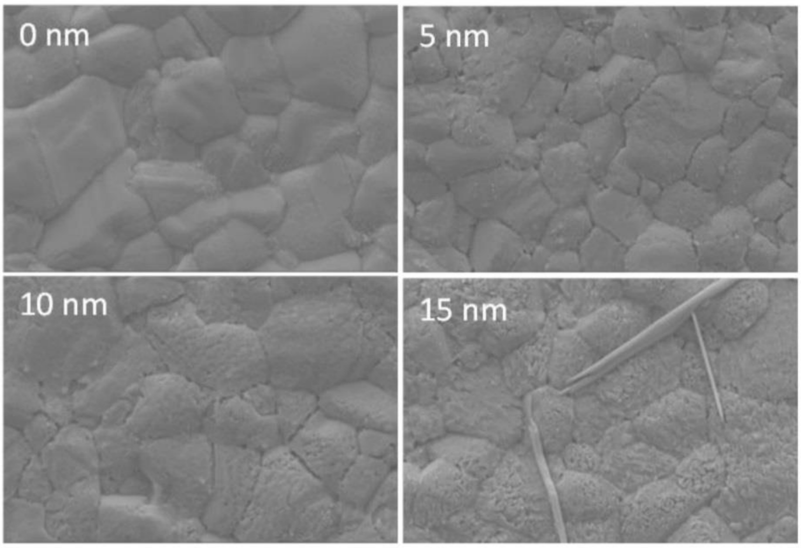

Figure S2. SEM topview of CZTSe absorbers which were re-selenized at 400°C with different Ge quantities prior evaporated on top of the crystalline CZTSe layers. Before the re-selenization the CZTSe layers showed already a high crystalline quality as seen for the 0 nm case. The Ge assisted re-selenization (,i.e. annealing in selenium atmosphere) affected largely the CZTSe surface with increasing Ge thickness. Solar cell devices made with this absorbers showed low performance compared to the not re-selenized reference. Therefore, a Ge treatment on already crystalline CZTSe layers was found to be detrimental to device performance.

2. Ge assisted crystallization of nanocrystalline CZTSe

Here all results related to the second precursor sample set are presented, which was obtained by selenization of a metal stack at 350°C and additional data from the 400°C series is shown. The same Ge assisted crystallization experiments as for the 400°C samples from the main manuscript were carried to demonstrate the reproducibility of the presented Ge beneficial Ge assisted crystallization.

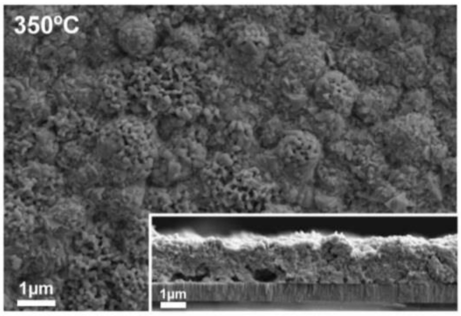

Figure S3. SEM top view and crosssection of Cu/Sn/Cu/Zn stack selenized at 350°C. Nanocrystalline CZTSe grains are visible.

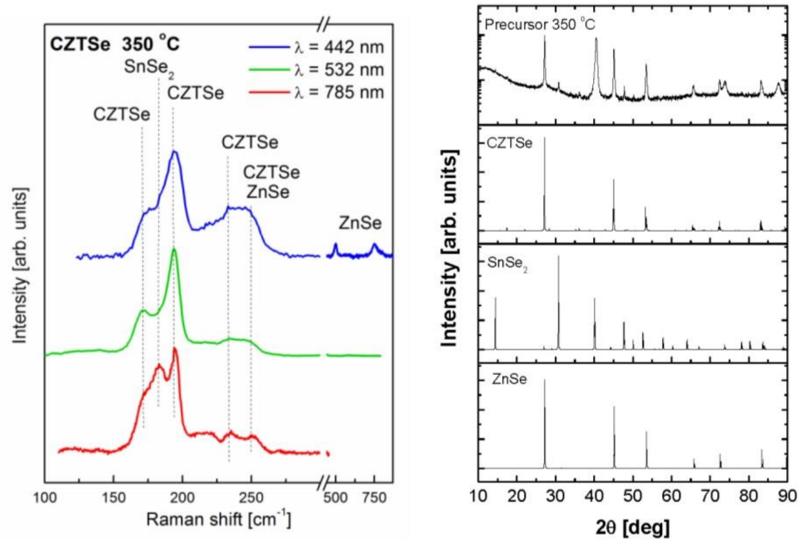

Figure S4. Multiwavelength Raman spectra of Cu/Sn/Cu/Zn stack selenized at 350ºC. CZTSe can be identified as main phase with SnSe2 and traces of ZnSe secondary phases. XRD confirms this finding and shows no traces of metal phases, indicating a full selenization of the stack.

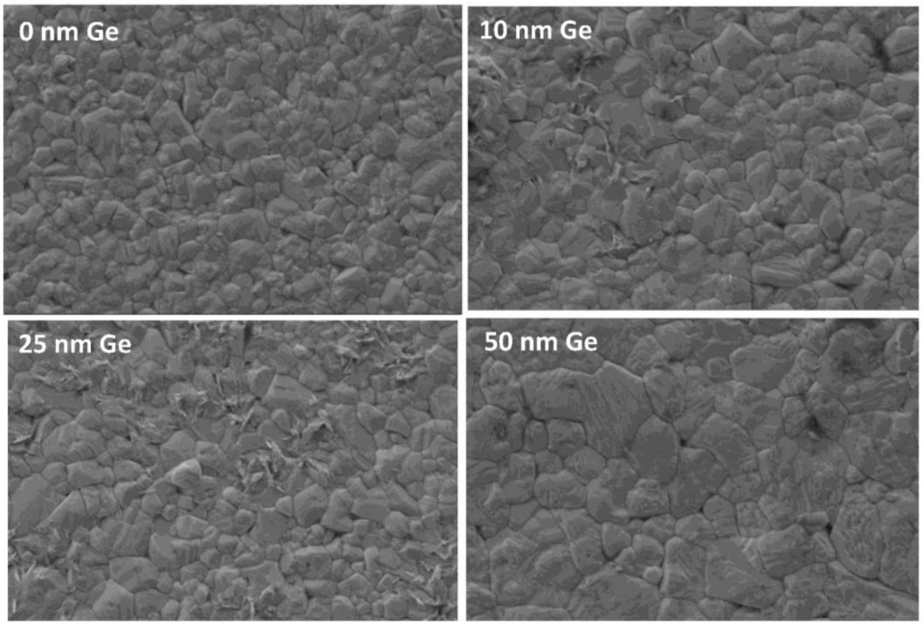

Figure S5. SEM top-view of 350ºC CZTSe precursor crystallized using different Ge quantities evaporated on top of the CZTSe precursor layer. An increased grain size with increased Ge quantity can be observed especially for the 50 nm case.

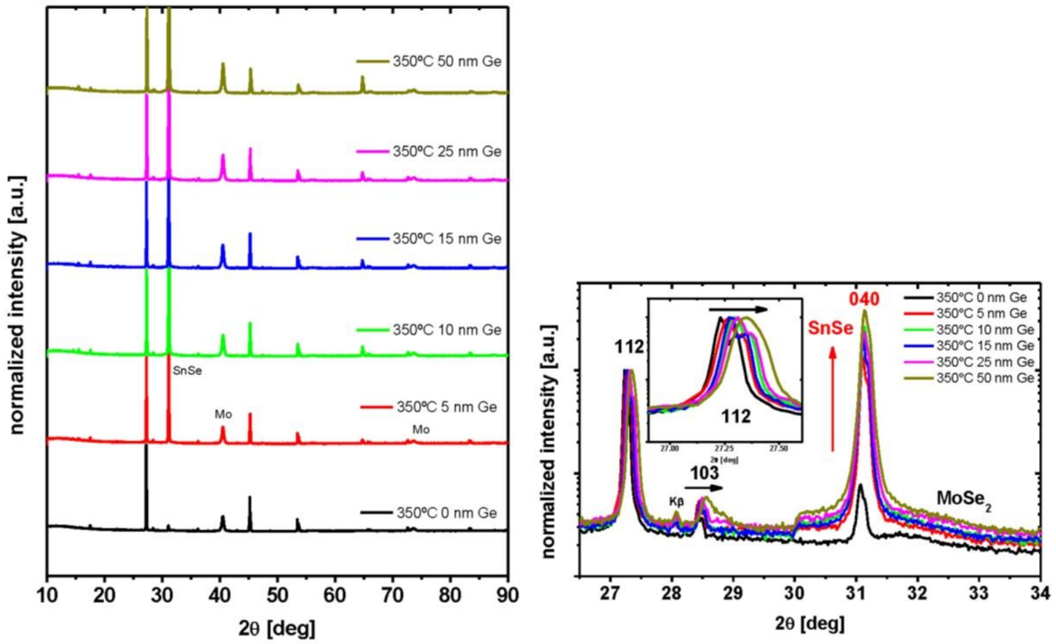

Figure S6. (a) XRD patterns of 350ºC CZTSe precursor crystalized using different Ge quantities evaporated on top of the nanocrystalline CZTSe precursor layer. (b) Zoom of XRD patterns on logarithmic scale. A shift of the main 112 kesterite peak as well as an increase formation of SnSe can be observed with increasing Ge thickness.

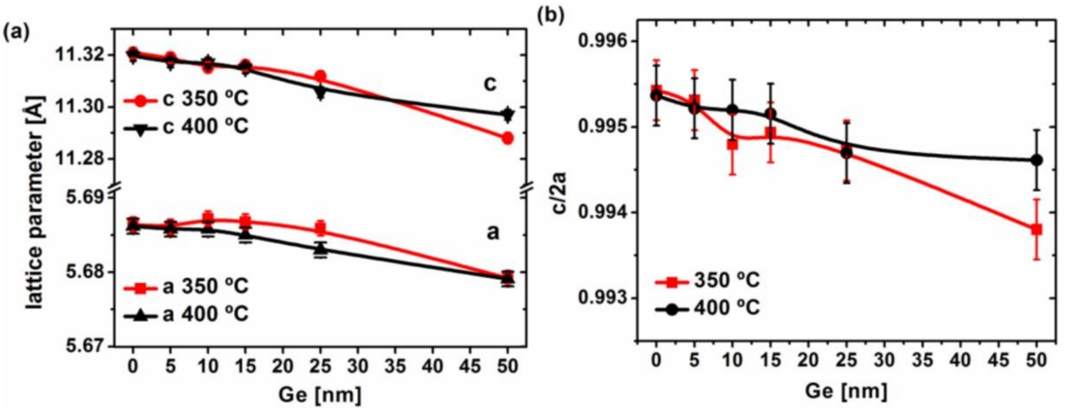

Figure S7. (a) Lattice parameters and (b) tetragonal distortion parameter (c/2a) in dependence of the Ge quantity used during the crystallization of the 350ºC and 400ºC CZTSe precursor layers. As shown in the original manuscript for the 400ºC series, there is almost no change observed for Ge quantities below 15 nm indicating very low Ge incorporation into the lattice.

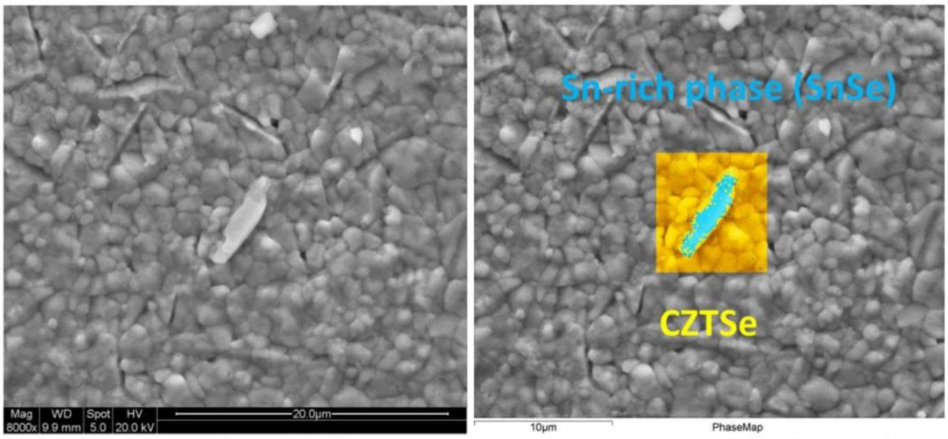

Figure S8. In SEM top-view plate like secondary phases were detected for the sample recrystallized with 50 nm Ge. EDX phase mapping identify these as SnSe.

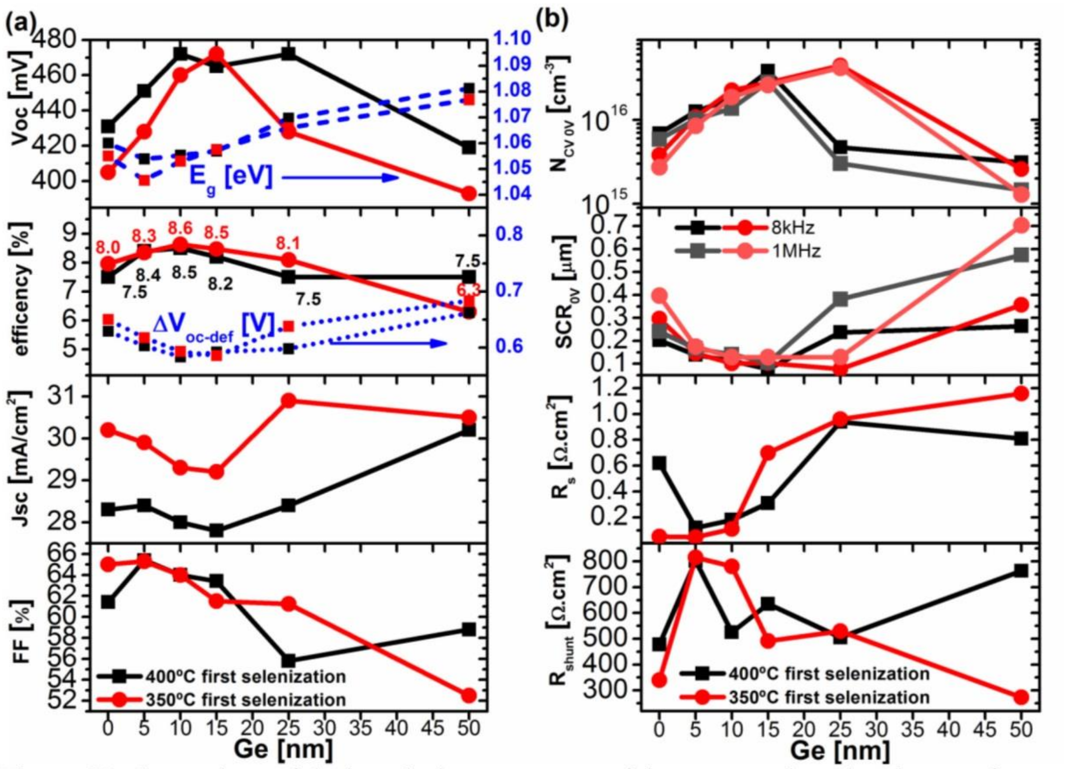

Figure S9. Comparison of the best device parameters of the two sample series show perfect reproducibility of the beneficial effects of the Ge assisted crystallization process presented in the main manuscript. (a),(b) device parameters of best solar cells in dependence of the Ge quantity used during crystallization of CTZSe precursors. The band gap (Eg) extracted from EQE as well as the Voc deficit (ΔVoc-def =Eg/q-Voc) are indicated as well. Shunt resistance (Rshunt) and series resistance (Rs) are extracted from the illuminated curve using the method described by Sites et al.

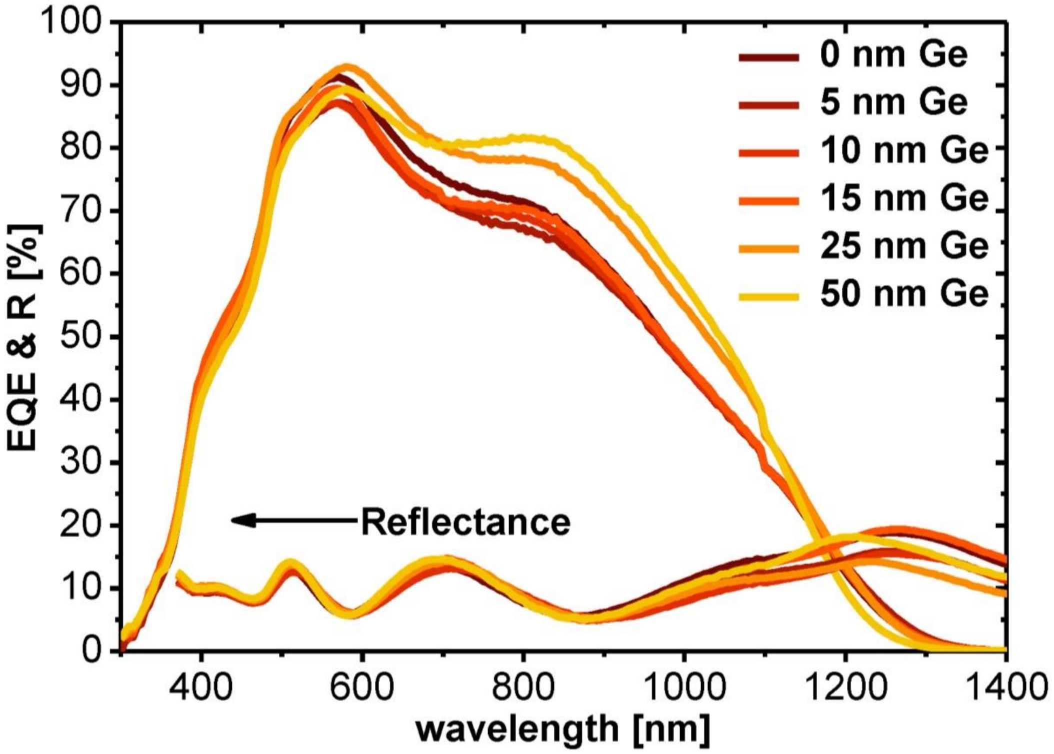

Figure S10. EQE and and reflectance of best solar cells of the 400ºC sample series. The Reflectance is between 5 to almost 20%, thus a significant improvement in Jsc is expected if an antireflective coating is employed.

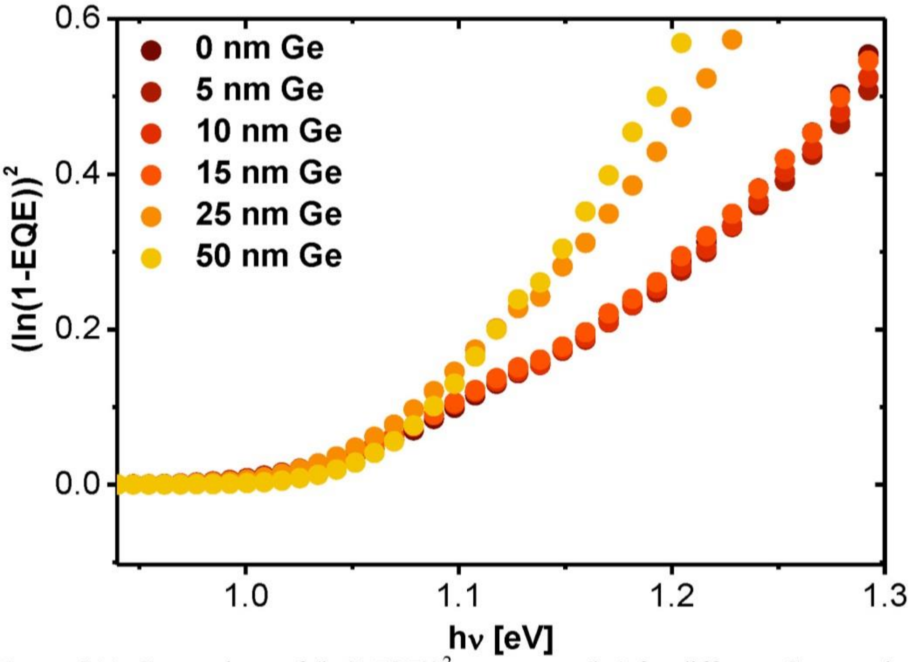

Figure S11. Comparison of $(\ln(1\text{-IQE}))^2$ vs. energy (hν) for different Ge quantity used during crystallization of nanocrystalline CTZSe precursors at 400ºC. Up to 15 nm almost no change is observed.

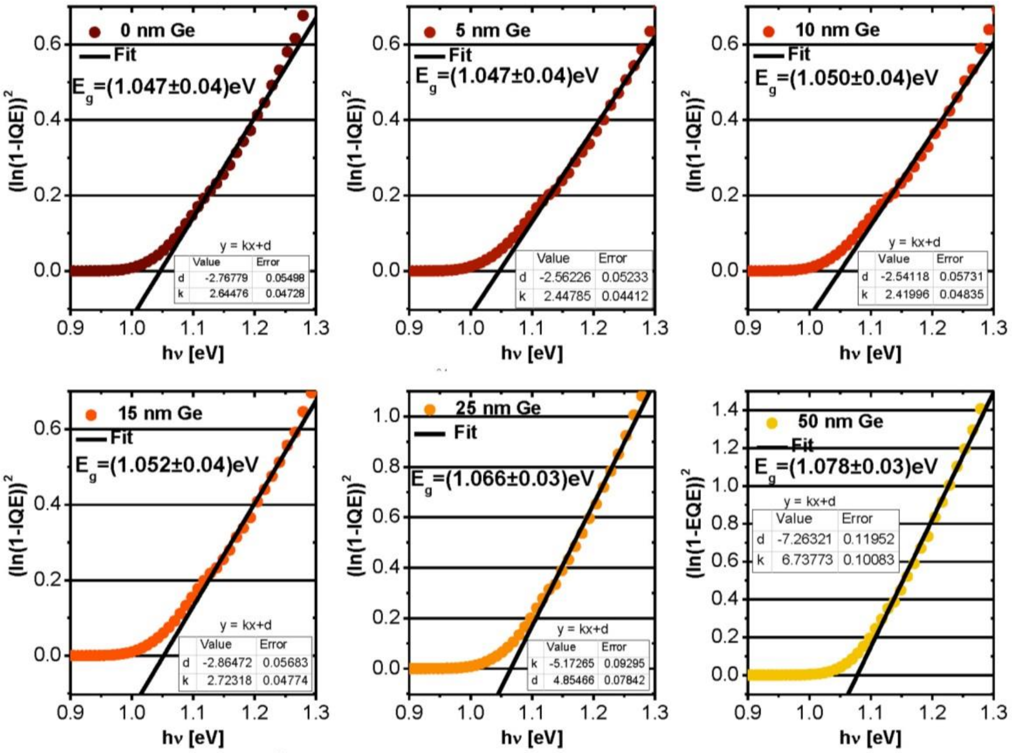

Figure S12. (ln(1-IQE))^2 vs. energy (hν) for different Ge quantity used during crystallization of nanocrystalline CTZSe precursors at 400ºC. From a linear fit the bandgap of the absorber can be estimated. Up to a Ge quantity of 15 nm almost no change in bandgap is observed. Errors are calculated from the errors obtained from the linear fit and using error propagation.

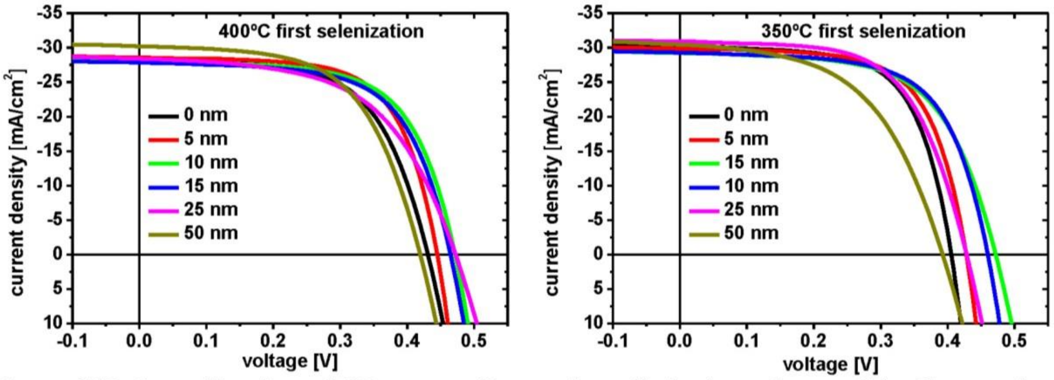

Figure S13. 1 sun illuminated JV curves of best solar cells in dependence of the Ge quantity used during crystallization of nanocrystalline CTZSe precursors obtained at 350ºC and 400ºC.

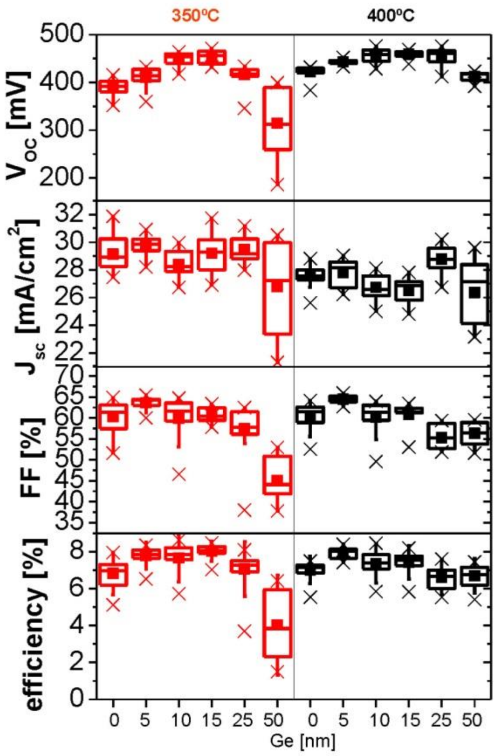

Figure S14. Box plots of device parameters in dependence of the Ge quantity used during crystallization of nanocrystalline CTZSe precursors obtained at 350ºC and 400ºC. Minimum 9 individual 3x3 mm^2 solar cells devices were investigated for each sample.

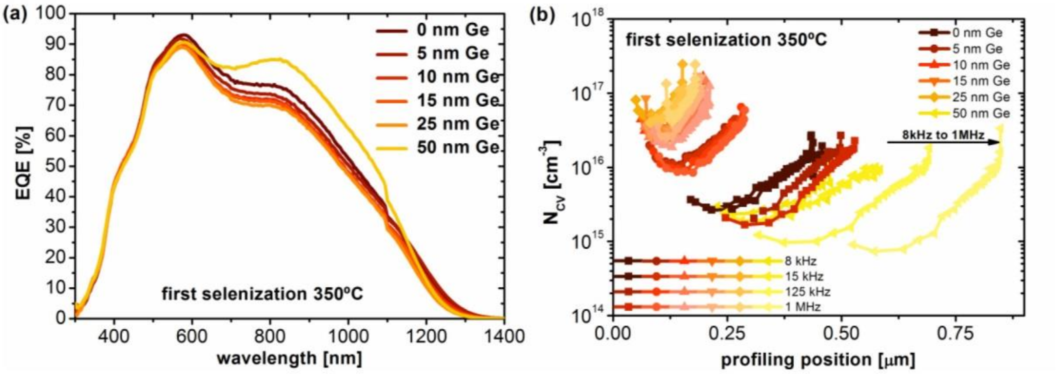

Figure S15. (a) EQE and (b) doping profiles as obtained from CV measurements for different frequencies of best solar cells of the 350ºC sample series.

Additional References

[S1] Neuschitzer, M.; Sanchez, Y.; López-Marino, S.; Xie, H.; Fairbrother, A.; Placidi, M.; Haass, S.; Izquierdo-Roca, V.; Perez-Rodriguez, A.; Saucedo, E. Optimization of CdS Buffer Layer for High-Performance $Cu_2ZnSnSe_4$ Solar Cells and the Effects of Light Soaking: Elimination of Crossover and Red Kink. *Prog. Photovolt. Res. Appl.* **2015**, *23*, 1660–1667.

[S2] Neuschitzer, M.; Sanchez, Y.; Olar, T.; Thersleff, T.; Lopez-Marino, S.; Oliva, F.; Espindola-Rodriguez, M.; Xie, H.; Placidi, M.; Izquierdo-Roca, V., et al.cComplex Surface Chemistry of Kesterites: Cu/Zn Reordering after Low Temperature Postdeposition Annealing and Its Role in High Performance Devices. *Chem. Mater.* **2015**, *27*, 5279–5287.

[S3] Giraldo, S.; Neuschitzer, M.; Thersleff, T.; López-Marino, S.; Sánchez, Y.; Xie, H.; Colina, M.; Placidi, M.; Pistor, P.; Izquierdo-Roca, V., et al. Large Efficiency Improvement in $Cu_2ZnSnSe_4$ Solar Cells by Introducing a Superficial Ge Nanolayer. *Adv. Energy Mater.* **2015**, *5*, 1501070.

5.2 Revealing the beneficial effects of Ge doping on $Cu_2ZnSnSe_4$ thin film solar cells

Goal of this chapter is to get a deeper insight into the beneficial effects of Ge doping on device performance. It is surprising that there is an optimum amount of Ge in the range of 5-15 nm that has to be added during synthesis of either metal stacks[67] or nanocrystalline precursors as shown in Chapter 5.1 to improve device performance and that higher Ge amounts added despite enhance grain growth significantly are detrimental for cell performance. The purpose of this study is to shed light on the beneficial effects of Ge doping by in-depth solar cell device characterization. Three different solar cells devices out of a series with different Ge-doping, as it was introduced in Chapter 5.1 are presented here in detail. The first one was synthesized without Ge addition (0 nm Ge), the second was synthesized with 10 nm Ge evaporated on top of the nanocrystalline precursor before a crystallization step, which corresponds to the range of optimal Ge doping. The third was obtained employing high Ge addition (50 nm Ge) during crystallization step under selenium atmosphere. Furthermore, the strong interaction of Ge and Na is demonstrated by investigating Ge and additionally Na doped absorbers. Solar cells fabricated from this different Ge and Ge+Na doped CZTSe absorbers were characterized using temperature dependent illuminated and dark JV curves, EQE as well as CV and admittance spectroscopy. Temperature dependent measurements were carried out with support of Dr. Moises Rodriguez at IREC and CV as well as admittance measurements were performed during an experimental stay at the group of Dr. Ian Forbes at Northumbria University with the support of Jose Marquez Prietro. Furthermore, temperature dependent PL and Raman were carried out on the Ge doped CZTSe absorbers. These measurements and it interpretations were done by Dr. Max Guc at IREC.

5.2.1 Experimental details

Ge doped CZTSe absorbers were grown using the same process as described in Chapter 5.1. First Cu/Sn/Cu/Zn metallic stacks deposited by DC magnetron sputtering onto Mo coated soda lime glass were selenized at low temperatures of 350ºC for 30 minutes under Ar flow keeping the pressure at 1.5 mbar to form a nanocrystalline precursor layer. On top of the precursors different thicknesses of Ge or Na+Ge where thermally evaporated. Then the precursors with the different capping layers were annealed under selenium atmosphere using a two-step profile, with a first step at 400ºC and Ar flux keeping the pressure at 1.5 mbar for 15 minutes, followed by a high temperature step at 550ºC and 1 bar for 15 minutes. Solar cell devices were finished by depositing CdS buffer and iZnO/ITO window layer as described in the previous Chapters.

Solar cells were characterized measuring JV curves under illumination of a 100 mW/cm^2 simulated solar spectrum by an Abet technology AAA solar simulator. Temperature dependent JV curves were recorded using a closed cycle He cryostat and a Oriel small area solar simulator calibrated to 1 sun with a Si reference cell.

External quantum efficiency (EQE) measurements were performed using a Bentham PVE300 system calibrated with Si and Ge photodiodes.

CV and Cf measurements at different temperatures (from 100K to 320K) were carried out using a liquid nitrogen cryostat from SemiMetrics Ltd and an Agilent E4980A LCR meter employing a parallel circuit model to extract the capacitance of the device.

Raman scattering (RS) and photoluminescence (PL) spectra were measured using the iHR320 Horiba Jobin Yvon spectrometer coupled with CCD and InGaAs detectors. The first detector was used for RS and second for PL spectra. Solid state laser with a 532 nm wavelength was used as excitation source for both methods. Spectra were measured in backscattering configuration through the Olympus metallographic objective and using the maximum laser power which ensured the absence of the thermal effects on the samples.

Laser power was changed by changing the current applied for the laser. Sample temperature was varied in the close-circle He cryostat and measured by Si-diode.

5.2.2 Results

5.2.2.1 Electrical and structural characterization

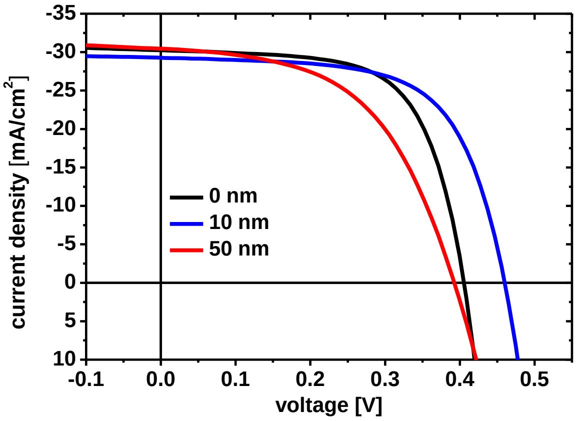

Figure 5.2. JV curves of solar cells doped with different amount of Ge during absorber synthesis.

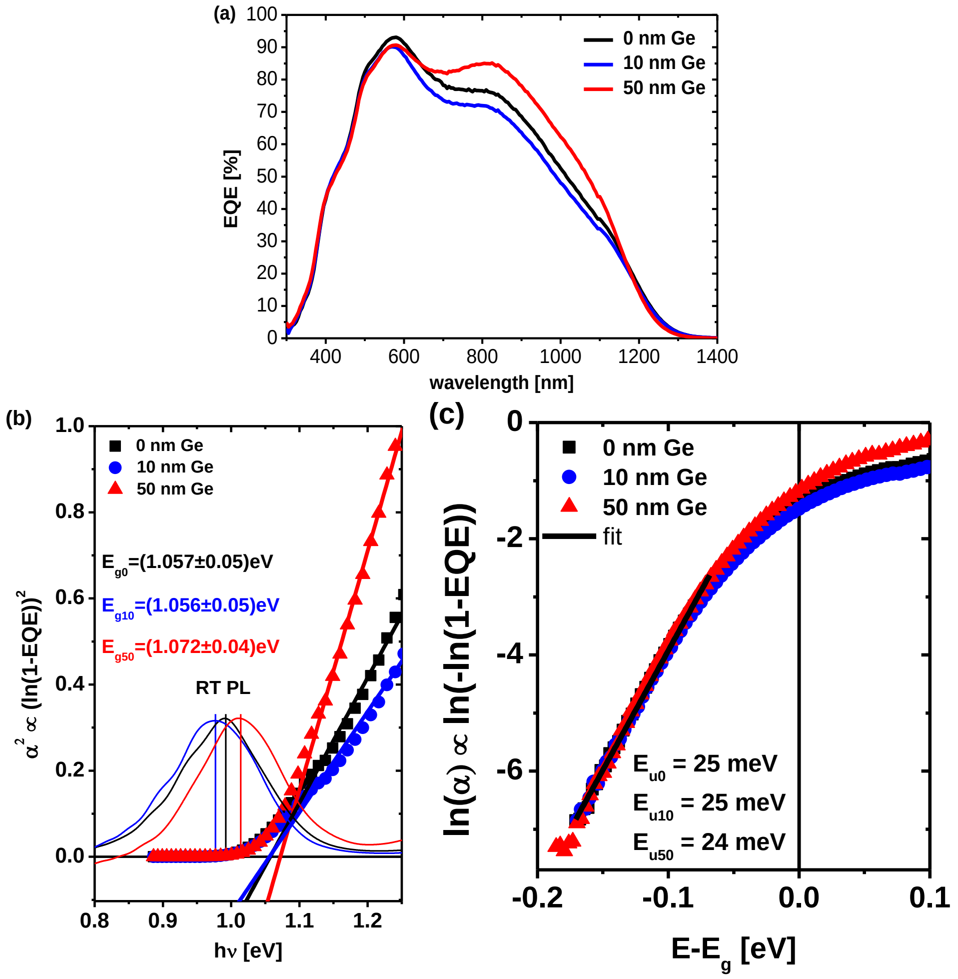

Figure 5.3. External quantum efficiency (a), bandgap extraction of EQE compared to RT PL (b), and extraction of Urbach energy from ln(-ln(1-EQE)) below the bandgap.

Table 5.1. Device parameters of solar cells with different Ge doping. N_{cv} and SCR are extracted at 132 kHz.

sample	Efficiency [%]	FF [%]	J_{sc} [mA/cm^2]	V_{oc} [mV]	R_{series} [Ω.cm^2]	R_{shunt} [Ω.cm^2]	A	J_0 [mA/cm^2]	E_g [eV]	$E_g/q-V_{oc}$ [V]	N_{cv} [cm^{-3}]	SCR [nm]
0 nm Ge	7.9	64.9	30.2	**405**	0.02	340	1.8	$5.1\text{x}10^{-3}$	1.057	**0.652**	$1.8\text{x}10^{15}$	317
10 nm Ge	8.6	64.1	29.3	**460**	0.27	780	1.9	$3.2\text{x}10^{-3}$	1.056	**0.596**	$1.5\text{x}10^{16}$	114
50 nm Ge	6.3	52.5	30.5	**393**	1.23	272	2.2	$7.1\text{x}10^{-2}$	1.072	**0.679**	$6.2\text{x}10^{14}$	622

In Figure 5.2 the JV curves of the three devices are shown as well as the device parameters are listed in Table 1. A clear improvement in V_{oc} is observed for the 10 nm Ge device compared to the 0 nm Ge reference. For the 50 nm Ge device a decrease in V_{oc} is observed. The bandgap was extracted from quantum efficiency (QE) measurements by assuming collection just in the space charge region (SCR, W), thus QE can be approximated by $QE \cong 1 - exp(-\alpha W)$, where α is the absorption coefficient.[101] The absorption coefficient is proportional to the bandgap of the absorber by[102] $\alpha(h\upsilon) \propto \sqrt{h\upsilon - E_g}$. Thus by plotting $(\ln(1 - QE))^2$ $vs.$ $h\upsilon$ and linear fitting of the long wavelength (low energy part) one can get the bandgap as the intercept with the $h\upsilon$-axis (see Figure 5.3 (b)). The bandgap stays constant around 1.05 eV up to a Ge amount of 10 nm and increases for the 50 nm Ge case. This is expected for higher Ge incorporation in the lattice.[131]

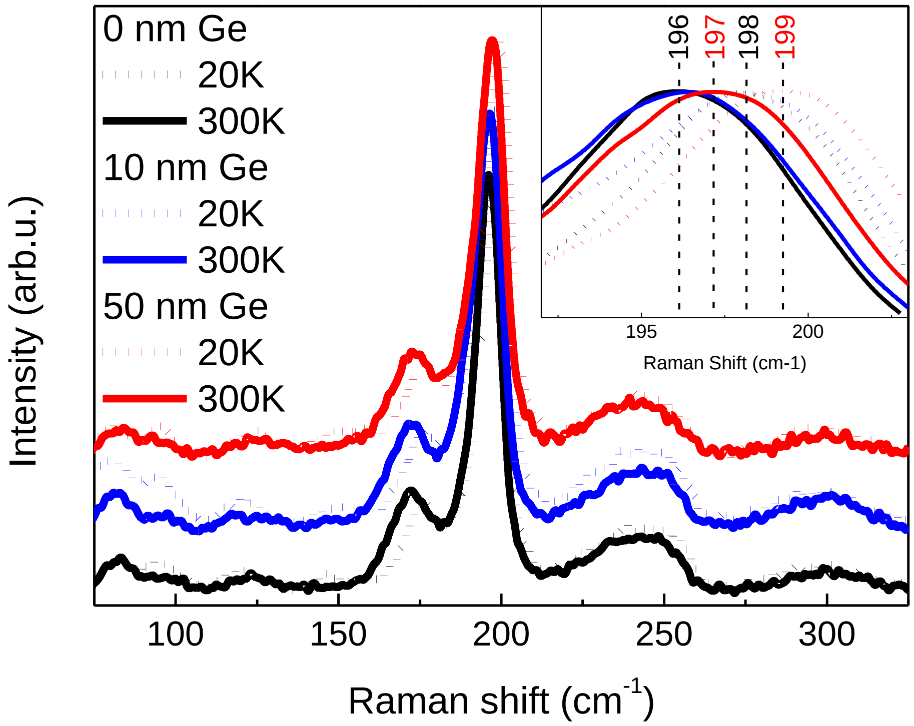

Figure 5.4. Raman scattering spectra of CZTSe layer with different thickness of Ge layer measured at different temperatures. The inset shows the enlarged region with the most intense peak.

Raman measurements confirm the low Ge incorporation into the CZTSe lattice for Ge amounts up to 10 nm, as is shown in Figure 5.4. In the 0 nm Ge sample the position of all Raman peaks at room temperature (RT) corresponds to the ones published previously for CZTSe compounds[132] and no peaks of secondary phases was found. The position of the most intense peaks of 0 nm Ge and the sample with 10 nm of Ge are similar, while the position of this peak in the 50 nm Ge sample shifts about 1 cm^{-1} to the higher wavenumbers. This indicates that in the last sample a $Cu_2ZnSn_xGe_{1-x}Se_4$ solid solution was formed with x ≈ 0.9[132], while in the sample with 10 nm of Ge almost no Ge was incorporated and Ge acts most possibly as a dopant. However, in the sample with 10 nm of Ge a small increase of the asymmetry of the most intense peak comparing to the reference sample was observed. According to Valakh et.al. is related to an increase of disorder in the samples.[133,134] With lowering the sample temperature a small blue shift of all Raman peaks was detected, which reached the 2 cm^{-1} at 20 K. Note that the shift was independent on the Ge content which indicates that it inclusion in the lattice do not create any additional strains and the change of lattice tensile with temperature, which is responsible for the shift of Raman peaks, is similar for all the samples.

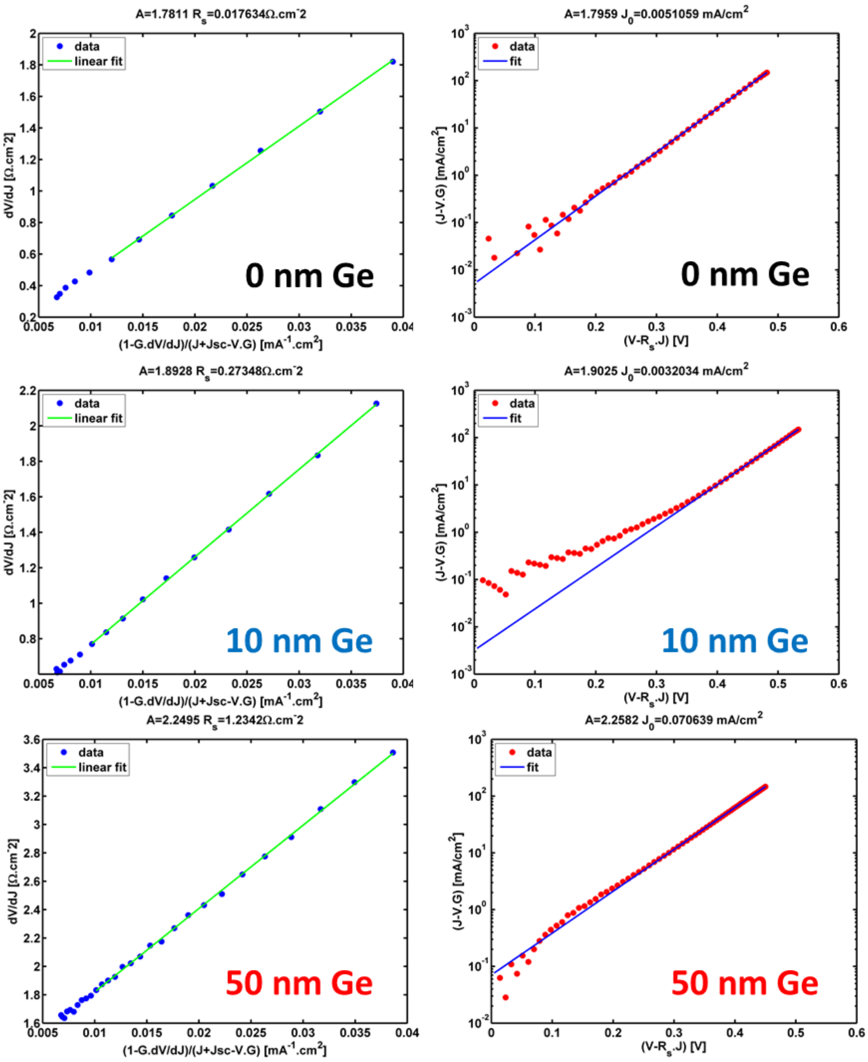

Figure 5.5. Extraction of series resistance, diode factor and J_0 using the method of Sites et al.[100,101]

Since the bandgap stays constant up to 10 nm Ge while the V_{oc} increases, the V_{oc} deficit can be reduced to below 600 mV. The increase in V_{oc} can therefore not be related to a bandgap increase due to Ge incorporation into the lattice[131] and has to have different origins as will be discussed in the following. The efficiency follows the same trend. The highest efficiency of 8.6% is obtained for the lowest V_{oc} deficit. In literature band tails were proposed as one of the main performance bottleneck in kesterite based solar cells causing low V_{oc} values.[48,119] One can characterize band tails which are responsible for sub-bandgap absorption by the Urbach energy E_u. Below the bandgap the absorption coefficient can be approximated by by $\alpha \propto \exp\left(-\frac{E_g-E}{E_u}\right)$ to extract E_u.[129] In Figure 5.3 (c) $\ln(\alpha) \propto x/E_u vs.(E-E_g)$ is shown for all devices and E_u extracted by linear fitting. A Urbach energy of around 25 meV is obtained with no significant difference between the different devices. Furthermore, this band tails are responsible for an unusual observed redshift of the main peak of room temperature (RT) photoluminescence (PL) measurements compared to the optical bandgap.[49,50,128] For all different Ge doped samples this red-shift is observed as can be seen in Figure 5.3 (b).Therefore, it can be concluded that Ge doping unfortunately does not modify band tails and reasons for efficiency improvements have to be different.

In Figure 5.5 the extraction of the diode parameters, like series resistance diode quality factor and saturation current density following procedure proposed by Sites et al. and Hegedus et al. is shown and all parameter are summarized in Table 5.1.[100,101] Diode quality factor for all three devices is close to 2, where for the 50 nm Ge devices it is slightly higher. This suggest that the main recombination path is recombination in the space charge region for all three samples.[73] The saturation current density of the 10 nm Ge devices is the lowest, whereas the one of the 50 nm Ge samples is one order of magnitude higher indicating an enhanced recombination as origin for the lower V_{oc} value obtained. To further investigate recombination mechanism in the devices temperature dependent JV measurements were carried out.

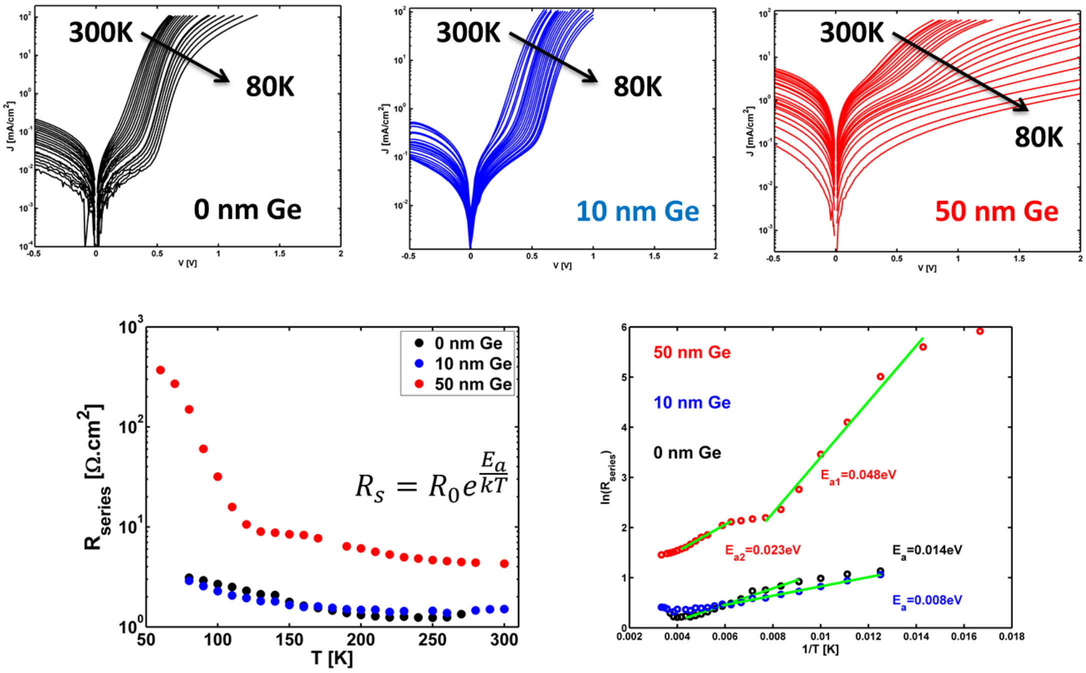

Figure 5.6. Temperature dependent dark JV curves and dark series resitance extracted for each temperature and exponential fits to extract activatioin energies.

In Figure 5.6 temperature dependent dark JV curves of all 3 devices are shown. Remarkable is the increase in series resistance at low temperature for the 50 nm Ge devices, as can be seen by the strong downward bending of the JV curves at higher forward bias. An exponential increase in series resistance is observed, where for the 50 nm Ge device one can distinguish two regions. The observed temperature dependence indicates a thermal activation of the carriers, thus the series resistance can be described by $R_s = R_0 \exp(\frac{E_a}{kT})$, where E_a is the activation energy.[135] In earlier studies this exponential increase in series resistance was related to an non-ohmic back contact of Kesterite and $MoS(e)_2$/Mo interface[28] however it is more likely that bulk conductivity itself limits the series resistance.[136] Gunawan et al. related the exponential increase in series resistance to a carrier freeze out due to the fact that the dominant acceptor defect is quiet deep, e.g. 0.13-0.2 eV above the valence band depending on the bandgap of the absorber.[136] In Figure 5.6 the extraction of the activation energies of the series resistances are shown for all three devices. For the 10 nm device the lowest activation energy of 8 meV was found.

For the 0 nm Ge devices it increases to 14 meV and for the 50 nm Ge device two regions have to be distinguished. For the first temperature range of 300-150 K an activation energy of 23 meV was found which increases to 48 meV for temperatures <130 K. Similar observations of two thermally activated processes are reported in literature, where the first activation energy is related to grain boundaries or shallow acceptor like defects and the second one at lower temperature to different processes like carrier localization in potential wells, radiative recombination or Mott's variable range hopping where holes occupy shallow states in the band gap and if a sufficient high concentration of this states is present the overlapping of their wave functions could form a impurity band.[135,137] Since the high temperature activation energy is the lowest for the 10 nm Ge device an reduction of grain boundary barrier height for the optimal Ge doping range of 10 nm could be speculated because in this temperature range thermionic emission across grain boundaries is typically the dominant conduction mechanism.[138] However, more detailed conductivity measurements of the thin films itself would be necessary to confirm it.

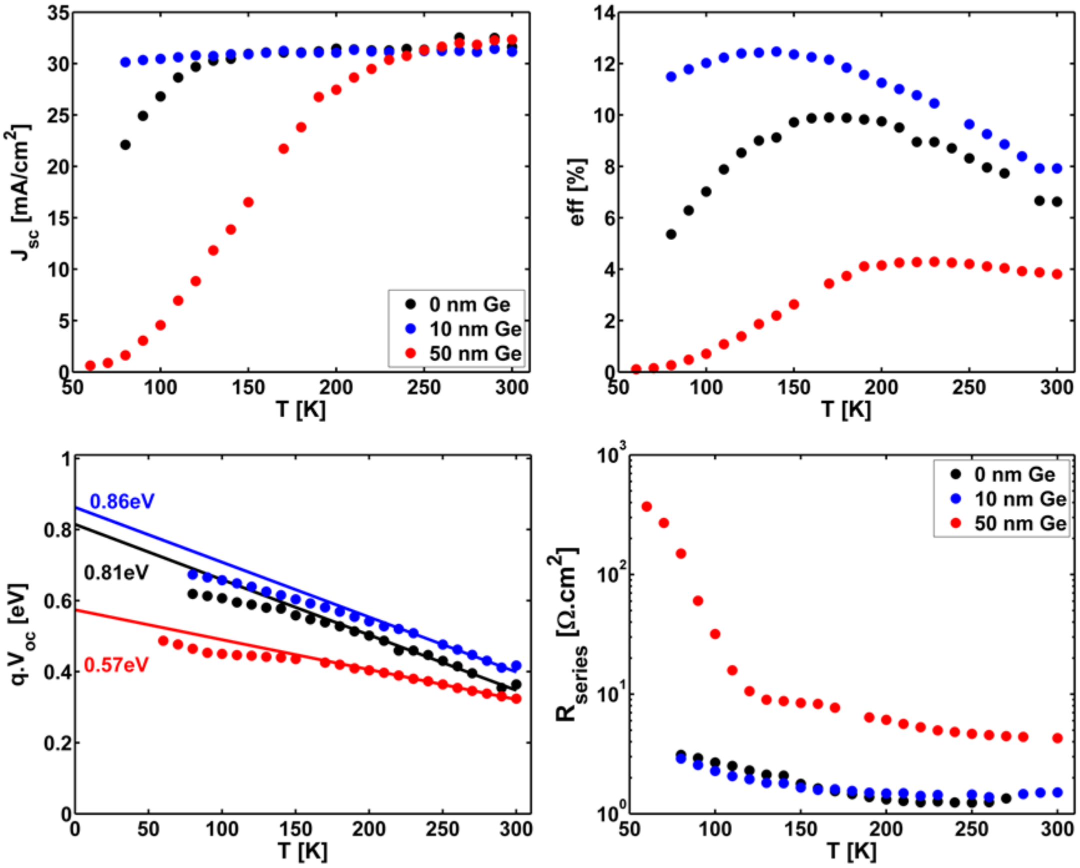

Figure 5.7. Temperature dependent solar cell device parameters and extraction of V_{oc} to 0K.

Besides dark JV-T analysis, the illuminated curves were recorded as well and device parameters extracted, In Figure 5.7. the J_{sc}, eff as well as V_{oc} for different temperatures is shown. From temperature dependent V_{oc} measurements the activation energy of the main recombination path can be determined by extrapolating the V_{oc} to 0K.[73] Comparing this value with the bandgap of the absorber allows conclusion about possible V_{oc} limitations due to the interface, i.e. unfavourable band alignment of absorber and buffer layer.[73] For the 0 nm Ge and 10 nm Ge values of 0.81 eV and 0.86 eV were obtained. These values are lower than the bandgap extracted from EQE, however since kesterite absorbers suffers from strong band tails the V_{oc} at 0 K should be compared to the energy of the radiative recombination in the bulk , i.e. to the maximum of the PL spectrum.[128] The values are similar to that of RT PL peaks (see Figure 5.3(b)) thus for 0 nm Ge and 10 nm Ge device

the main recombination is bulk recombination as commonly observed for selenium rich kesterite.[135] Surprisingly the V_{oc} at 0 K for the 50 nm Ge device is much lower, and an activation energy of 0.57 eV is obtained, This could be either related to a non-ideal diode like behaviour like a strong temperature dependent diode factor or voltage dependent carrier collection which makes the extraction of activation energy invalid[139] or a change of band alignment of the Ge containing kesterite with the CdS buffer to a cliff like alignment.
Furthermore, a strong decrease in J_{sc} for the 50 nm Ge device at low temperature is observed which is correlated with the strong increase of series resistance. For the 0 nm Ge device this decrease is less pronounced and for the 10 nm Ge devices almost no decrease is observed. The efficiency behaves the same way, a strong decrease for the 50 nm and 0 nm Ge device, whereas the 10 nm Ge devices continuously increases until almost 100 K. Quenching of efficiency at low temperature is commonly observed in kesterite devices and related to the carrier freeze out, i.e. strong increase of series resitance.[113] Kim et al. showed that by employing a In_2S_3/CdS double buffer layer the CZTSSe absorber doping level could be increased by In doping and the low temperature quenching eliminated, as well as the efficiency at room temperature improved.[113] In the following it will be shown that for the optimum Ge doping range of 10 nm also an increase in doping is observed which could explain that for the 10 nm Ge device no quenching at all is observed.
One interesting feature in the EQE measurements shown in Figure 5.3 that was not commented yet is the increased EQE signal in the long wavelength region for the 50 nm Ge device, which is in agreement with a higher J_{sc} obtained. Doping profiles derived from CV measurements (see Figure 5.8) show an increase in charge carrier density for the 10 nm Ge sample followed by a decrease for the 50 nm Ge device. The space charge region (SCR) extracted at 0 V from the profiles show the highest value for the 50 nm Ge case (see Table 5.1), which can explain the improved collection in the long wavelength region of the EQE. Assuming a change only in the absorber doping (N) one can estimate the change in V_{oc} by $\Delta V_{oc} = kT/qln(\frac{N_1}{N2})$.[99] The increase in doping of around one order of magnitude from 1.8×10^{15} cm^{-3} to 1.5×10^{16} as it is observed for the 0 nm Ge compared to the 10 nm Ge device would result in a V_{oc} improvement of 55 mV which corresponds perfectly to the observed V_{oc} improvements. The decrease of doping density for the 50 nm Ge is surprising and might be related to a different mechanism. As already observed in Chapter 5.1 there is high frequency dependence, for the 50 nm Ge device, of the doping profile observed. This is a strong indication for the presence of deep defects.[104]

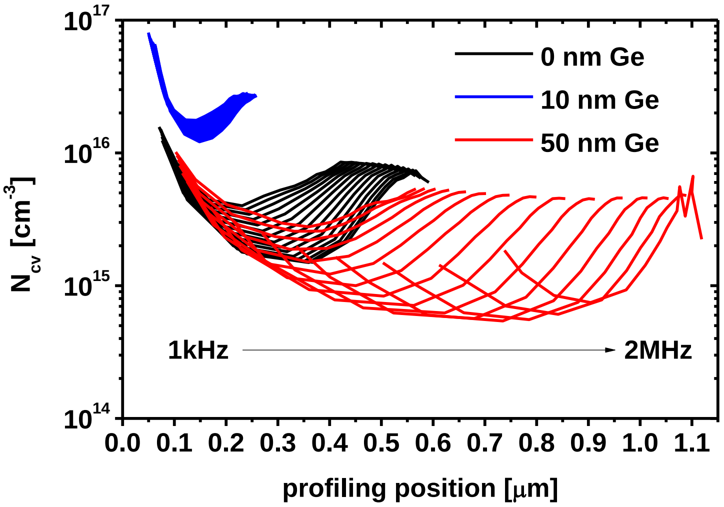

Figure 5.8. Doping profiles derived from CV measurements at different frequencies.

To further investigate defects in the three devices admittance spectroscopy measurements were carried out as shown in Figure 5.9. Two capacitance steps are present in the 50 nm Ge device, whereas for the 10 nm Ge device just one step is visible. Similar Cf spectra were obtained for the samples investigated in Chapter 5.1 confirming the reproducibility of the process and measurements. Here also the Cf spectrum of the 0 nm Ge reference device is shown, where also two steps are visible. The defect spectra derived from admittance spectroscopy measurements are shown in Figure 5.9 as well. For all cases a shallow defect around 100 mV is observed which gets shallower for the optimal Ge doping of 10 nm. Remarkable is the appearance of a deep defect for the 0 nm Ge as well as the 50 nm Ge device with activation energies above 400 meV. The values of activation energy extracted for this set of sample agree well with the once extracted from a different set investigated in Chapter 5.1 confirming the reproducibility of the processes. Recently Larramona et al. [65] showed that by fine tuning the Sn concentration the formation of a deep defect (600 meV), probably Cu_{Sn} antisites or V_{Cu} formed due to Sn loss, could be avoided and efficiency increased over 11%.

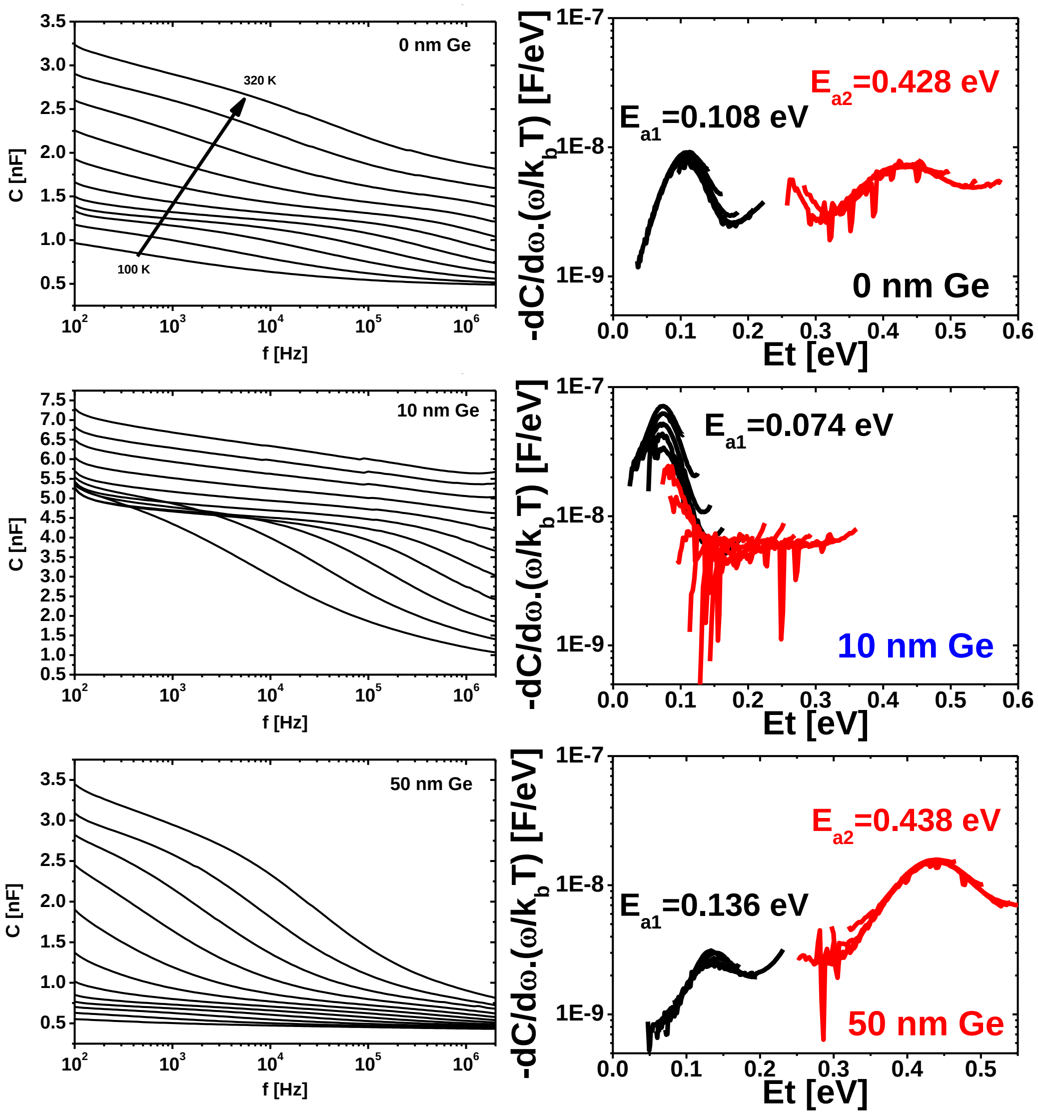

Figure 5.9. C-f spectra at different temperature and defect spectra derived from it.

This in in agreement with our observations for 10 nm Ge sample where Ge could compensate Sn loss and avoid a deep defect formation like Cu_{Sn} or V_{Sn} as already proposed in Chapter 5.1:

$$V_{Cu} + \boldsymbol{Cu_{Sn}} + Ge \rightarrow Ge_{Sn} + Cu_{Cu} \quad (5.1)$$

or

$$\boldsymbol{V_{Sn}} + Ge \rightarrow Ge_{Sn} \quad (5.2)$$

For high Ge content (i.e. 50 nm Ge) the formation of Cu_{Sn} is less likely because the CZTSe absorber are synthesized as Cu poor and in this case group IV element (Sn,Ge) rich. Thus the formation of Sn_{Cu} or Ge_{Cu} antisites donor defects which seems more likely under this growth conditions:

$$V_{Cu} + Sn_{Sn} + Ge \rightarrow Ge_{Sn} + \boldsymbol{Sn_{Cu}} \quad (5.3)$$

or

$$V_{Cu} + Ge \rightarrow \boldsymbol{Ge_{Cu}} \quad (5.4)$$

Ge replaces Sn and the excess Sn could led to the formation of Sn_{Cu} or Ge_{Cu} antisites defects. Sn_{Cu} creates a deep donor defect[44,52] which acts as electron-hole recombination centre deteriorating the solar cell performance. This would further explain the lower doping observed for high Ge (50 nm) devices due to compensation as already proposed in Chapter 5.1. Recently Wei et al. showed by admittance spectroscopy measurements and simulations that a deep n-type defect is present in a 10% CZTSSe solar cell, which could be a key limitations of the device performance and was possible assigned to Sn_{Cu} or Sn_{Zn} donor defects which is in line with our observations.[126] For the optimum Ge doping range of 10 nm Ge added during absorber synthesis the formation of deep defects either due to Sn loss or group IV elements antisites defects could be avoided and highest device performance is achieved. Still the reason for increased doping, which might be responsible for the increased V_{oc} besides the reduced recombination, due to the elimination of deep defects and as also evidenced by the lowest saturation current density (see Table 5.1) is not totally clear. A possible interaction of Na a well-known dopant in chalcogenide photovoltaic absorbers and Ge could be responsible for it as will be discussed later on in more detail.

5.2.2.2 Photoluminescence measurements

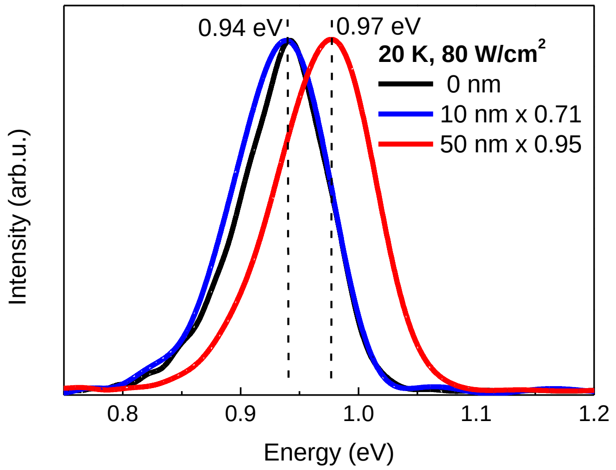

Figure 5.10. PL spectra of CZTSe layer with different thickness of Ge. The spectra were normalized to the PL intensity of the 0 nm Ge sample and numbers in the legend show the normalization coefficient

In the previous section a detailed electrical characterization is presented. To further investigate possible defects which are active in radiative processes photoluminescence (PL) measurements were carried out. Unfortunately due to detector limitations the PL spectra cannot assess midgap defects. Nevertheless valuable information about recombination processes and shallow defects can be obtained from temperature dependent PL spectra around the bandgap. In Figure 5.10 PL spectra of three analyzed samples measured at 20 K with highest excitation power are presented. The maximum peak position is not changed in the sample with 10 nm of Ge comparing to the 0 nm Ge one, while for the sample with 50 nm of Ge a shift to higher energy is observed. This correlates with Raman data which indicated the formation of new phase of $Cu_2ZnSn_xGe_{1-}$

$_x\text{Se}_4$ solid solution which has higher band gap than the pure CZTSe phase.[131] To determine the nature of the observed PL spectra an excitation power dependence study of PL spectra in all samples has been performed. Selected spectra of the sample with 10 nm of Ge are presented in Figure 5.11(a). Analysis of these spectra showed a strong blue shift of the peak maximum with excitation power. The increase is about 18 meV/decade (see Figure 5.11(b)). Additionally the analysis of the integrated PL intensity versus excitation power showed an exponential dependence in accordance with formulae $I_{PL} \sim I_{ex}^{k}$. The exponent k was found to be lower than 1 (see Figure 5.11(c)). This indicates the defect related nature of the observed PL spectra, while the strong blue shift of the maximum is an indication for a quasi-donor-acceptor pair (QDAP) recombination as radiative processes in the analyzed samples.[140] The QDAP recombination was previously found in pure CZTSe[141] and CZTS[142,143] compounds, as well as in their solid solutions.[141] It is characterized by a strong influence of the band bending due to a fluctuating potential of the PL band maximum, which could be described by [140]:

$$E_{PL} = E_g - (E_A + E_D) - 2\Gamma \qquad (5.5)$$

Here E_g is the band gap energy, E_A and E_D are the activation energies of the acceptor and donor, respectively, involved in the irradiative process and coefficient Γ is related with depth of the potential fluctuations. [140]

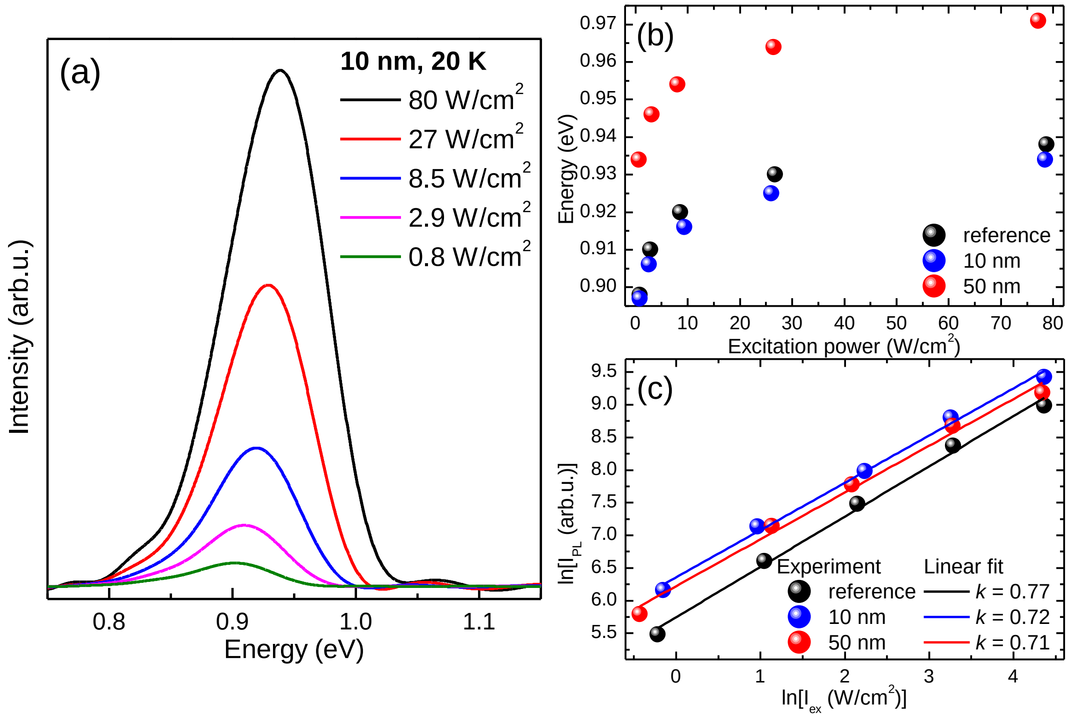

Figure 5.11. (a) Excitation power dependence of the PL spectra of CZTSe layer with 10 nm of Ge. (b) Maximum peak position vs. excitation power. (c) Integrated PL intensity vs. excitation power.

The analysis of temperature dependence of PL spectra (Figure 5.12(a)) showed a red shift of the band maximum up to ~ 100 K and blue shift at higher temperatures (Figure 5.12(b)). Similar dependencies was observed and in case of CZTSSe solid solutions for the QDAP emission[141,144]. A strong quenching of PL intensity of about 3 orders in the analyzed temperature range 20 – 300 K (Figure 5.12(a)) was found in the studied samples. This quenching could be described using the equation with two activation energies [145]:

$$I_{PL} = \frac{I_0}{1 + a_1 \exp(-E_1/k_b T) + a_2 \exp(-E_2/k_b T)} \qquad (5.6)$$

where a_1 and a_2 are the rate parameters of the non-irradiative process with activation energies E_1 and E_2. I_0 is PL intensity at lowest temperature and k_B is Boltzmann constant.

Both activation energies obtained from fitting of integrated PL intensity are almost constant in the 0 nm and 10 nm Ge samples and increase in case of sample with 50 nm of Ge (see Figure 5.12(c)). Note that in the framework of QDAP recombination model the lower E_1 energy is attributed to the average value of the valley depth, from which the carriers should be thermally activated for the subsequent recombination, rather than to the activation energy of some shallow defect level.[141] Obtained values of E_1, i.e. the depth valley in the analyzed samples showed only a slight change with Ge content used in agreement with a similar extracted Urbach energy from EQE for all samples (see Figure 5.3(a)).

The higher activation energy E_2 could be attributed to a deeper donor or acceptor level involved in the recombination process. At temperatures higher than 250 K the radiative mechanism of the observed PL spectra was found to be changed from QDAP to the band to impurity (BI) recombination, which is proven by the constant maximum position with excitation power change at 300 K. Since the CZTSe absorber has *p*-type conductivity the transitions acceptor-conduction band is more probable as origin for the observed PL band near room temperature. From the band gap energy found in EQE and the position of PL band maximum at 300 K the activation energy of the involved acceptor level (E_A) was roughly estimated to be in the range 58 – 79 meV for all the samples. This range is in agreement with the energy level found by admittance spectroscopy for the 10 nm Ge device. However, for 0 nm and 50 nm Ge device higher values are obtained which could be due to uncertainties of extraction of defect energies when two capacitance steps overlap or the increasing series resistance at low temperatures.[105,146] On the other hand, it is not possible to assign E_2 energy obtained from fitting the temperature dependence to the same acceptor level. This leads to conclusion that E_2 energy of 70-118 meV is attributed to a donor defect level (E_D) as proposed by Levcenco et al.[141]

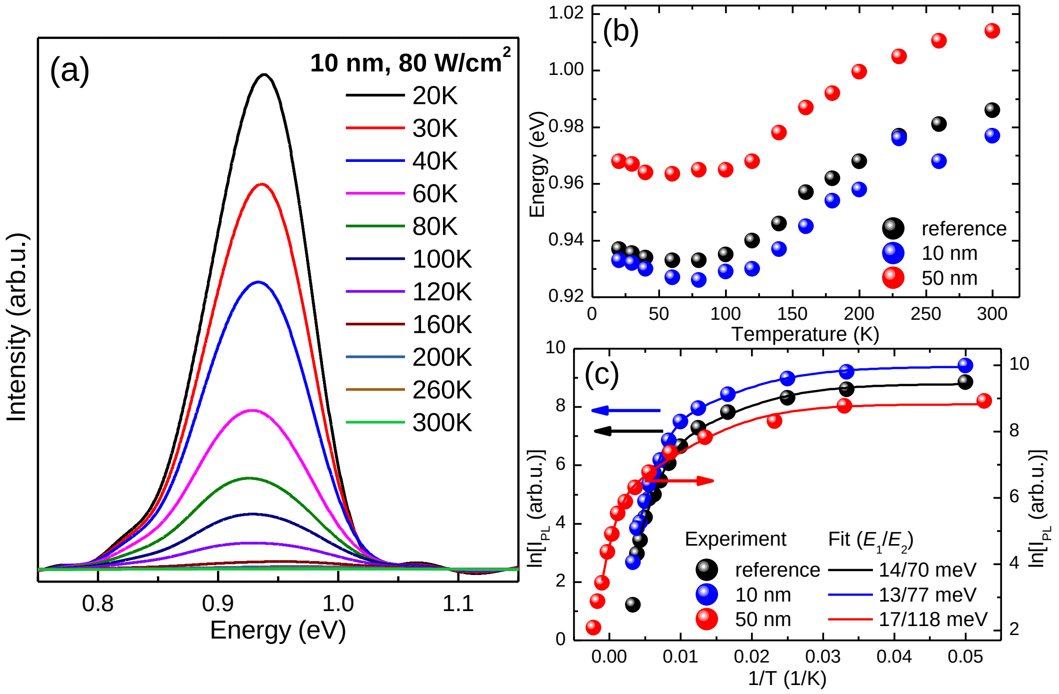

Figure 5.12. (a) Temperature dependence of the PL spectra of CZTSe layer with 10 nm of Ge. (b) Maximum peak position vs. sample temperature. (c) Integrated PL intensity vs. sample temperature.

5.2.2.3 Interaction of Ge and Na

The reasons for the increased charge carrier density for the optimum Ge doping of 10 nm, as observed by CV profiling (see Figure 5.8) is still not clear. Recently our group discovered a possible interaction of Ge and Na, a well-known dopant in kesterite based solar cells.[147] As shown in Giraldo et al. a higher amount of Na was found in the absorber layer synthesized using the optimum range of about 10 nm Ge during synthesis, whereas high Ge amounts used during synthesis led to a decrease in Na in the absorber. The Na amount found correlate well with the doping profiles obtained, where as it is shown in this study a higher doping level is obtained for 10 nm Ge devices whereas for higher Ge amounts (>25 nm) a decrease in doping density is observed.[147] In Giraldo et al. NaO_x crystals were found on top of absorbers synthesized under addition of high Ge quantities, thus an extraction of Na from the absorber towards the absorber surface was proposed due to the formation of a GeSe-liquid phases which can dissolve Na in large amounts. Furthermore, element IV (Sn,Ge) rich growth increase the probability of Ge_{Cu} and Sn_{Cu} anitistes and therefore hinder the incorporation of Na due to the fact that Na most likely occupies Cu vacancies (Na_{Cu}).[147] Furthermore, absorber synthesized on sodium free substrates like Si/SiO_2 showed that Ge assisted synthesis is only beneficial for device performance if additional Na is added by evaporation of a NaF layer. This fact was further confirmed by different Na free substrates like stainless steel.[90] To get more insights in the possible interaction between Na and Ge a sample series with optimum as well as high Ge range was prepared but with additional Na added by depositing NaF on top of nanocrystalline precursors before Ge deposition. Then these nanocrystalline precursors with Ge and NaF+Ge capping layer were annealed under selenium atmosphere as described in the experimental details and in Chapter 5.1. In Figure 5.13 box plots of the device parameters of the different samples are shown. For the optimum Ge amount of 10 nm the addition of Na has no significant influence on device performance. However, for the sample synthesized with large Ge amount of 25 nm additional Na clearly improve device performance especially V_{oc}. To probe if the additional NaF layer may change the Ge incorporation into the film, the bandgap values extracted from EQE (Figure 5.14(a)) measurements are compared in Figure 5.14(b) for the 25 nm Ge series. No significant difference is observed, indicating that the additional Na has no influence on Ge incorporation from the point of view of possible bandgap changes.

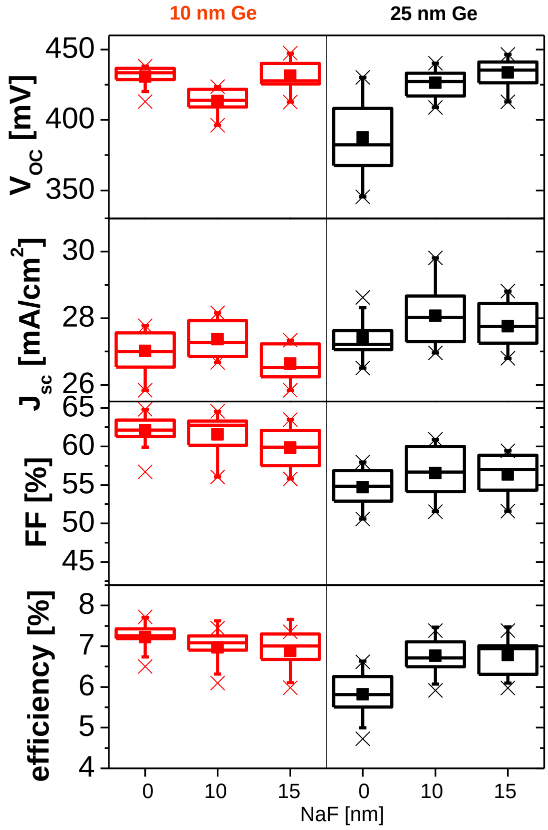

Figure 5.13. Box plot of device parameters of absorbers synthesized under the addition of Ge and NaF.

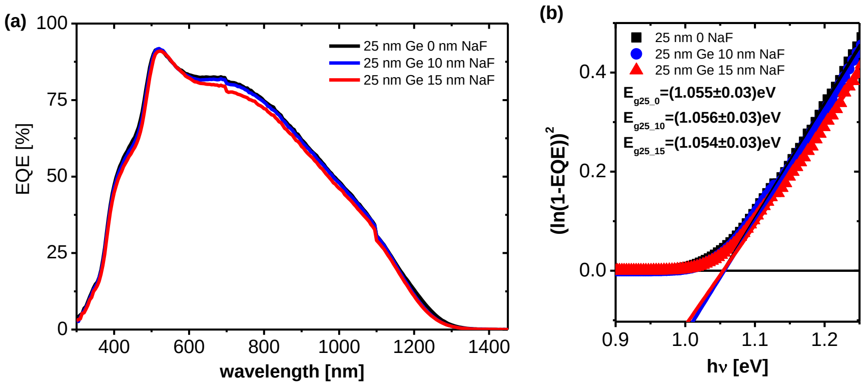

Figure 5.14. EQE as well as bandgap extraction from EQE.

Two different devices are investigated in more detail in the following. One which employs an absorber layer that was synthesized under Ge rich condition by adding 25 nm Ge on top of nanocrystalline precursor prior selenization and one which was synthesized using the same amount of Ge but additionally 15 nm NaF were evaporated on top before Ge evaporation. In Figure 5.15(b) the JV curve of the best cell of the two devices are shown. A clear improvement in V_{oc} is observed for the Ge+Na device and device performance could largely be improved as can be seen in Table 5.2.

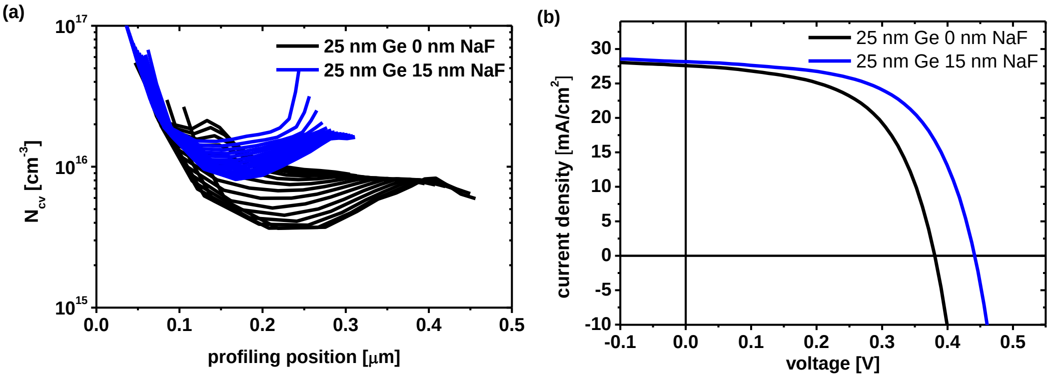

Figure 5.15. (a) Doping profiles extracted from CV measurements at different frequencies as well as the illuminated JV curves (b) for Ge and Ge+Na doped devices.

Doping profiles extracted from CV measurements of the two devices are shown in Figure 5.15(a). An increase in doping density for the Ge+Na device can be observed, as well as the frequency dependence of the doping profiles could be reduced.

Table 5.2. Device parameters of solar cells with Ge and Ge+Na doping. N_{cv} and SCR are extracted at 132 kHz.

Sample 25 nm Ge	Efficiency [%]	FF [%]	J_{sc} [mA/cm^2]	V_{oc} [mV]	R_{series} [Ω.cm^2]	R_{shunt} [Ω.cm^2]	A	J_0 [mA/cm^2]	E_g [eV]	E_g/q-V_{oc} [V]	N_{cv} [cm^{-3}]	SCR [nm]
+0 nm NaF	6.0	56.7	27.6	**381**	0.04	246	2.3	4.3×10^{-2}	1.055	**0.674**	5.7×10^{15}	161
+15 nm NaF	7.4	59.4	28.2	**441**	0.30	359	2.3	2.2×10^{-2}	1.054	**0.613**	1.1×10^{16}	118

Admittance spectroscopy measurements were carried out as well on the devices as can be seen in Figure 5.16. In the Cf spectrum of the device which absorber was synthesized just by 25 nm Ge addition and without additional Na (Figure 5.16 (a)) clearly two capacitance steps can be seen as it was observed for all absorbers synthesized using large amounts of Ge (>25 nm). The defect spectra extracted from the Cf measurements shows a shallower defect at around 163 meV, which for this device was found at higher activation energy compared to the devices investigated in Chapter 5.1 and before (see Figure 5.16(b) and compare to Figure 5.9 and Chapter 5.1). Additionally, a deep defect at 325 meV was found as it was detected for all devices with absorbers that were synthesized with thick Ge capping layers (>25 nm). Here this deep defect seems less pronounced which could be explained by the fact that less Ge (25 nm instead of 50 nm) was used during synthesis, thus less Ge_{Cu} or Sn_{Cu} antisites are probably formed. In the Cf spectrum of the 25 nm Ge + 15 nm NaF sample the high temperature capacitance step is not obvious anymore and only a step at low temperatures is clearly observed, which activation energy was found to be around 113 meV.

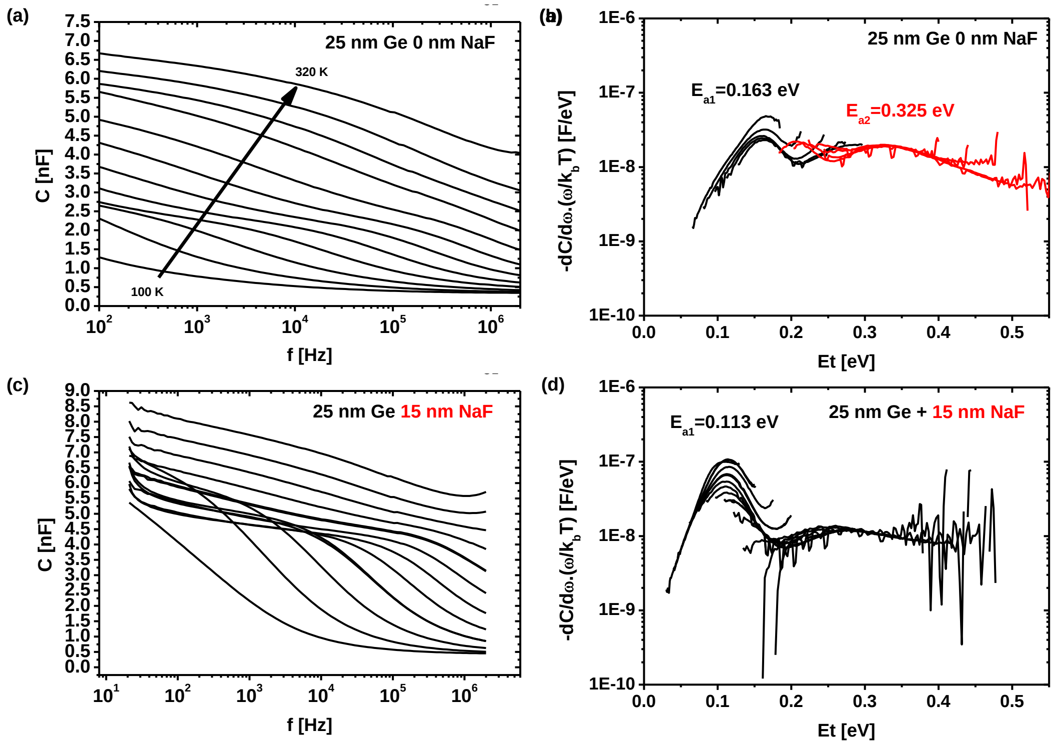

Figure 5.16. Cf spectra at different temperatures as well as from it derived defect spectra for Ge and Ge+Na doped devices.

The elimination of the deep defect by controlled Na addition confirms the suspected interaction between Ge and Na. As proposed in Giraldo et al. large amount of Ge used during synthesis, create an element IV (Sn,Ge) rich growth conditions, which could led to the release of Na out of the absorber.[147] The Ge-Na dynamics for this case can be illustrated by

$$Sn_{Sn} + Na_{Cu} + Ge \rightarrow Ge_{Sn} + \boldsymbol{Sn_{Cu}} + Na \quad (5.7)$$

or

$$Na_{Cu} + Ge \rightarrow \boldsymbol{Ge_{Cu}} + Na \quad (5.8)$$

Thus, large amounts of Ge supplied during a synthesis could led to the replacement of Na_{Cu}, releasing Na of the absorber and led to the formation of Sn_{Cu} or Ge_{Cu} antisites, which are deep donor defects as discussed earlier and deteriorate cell performance.[44,52] A sufficient high additionally supply of Na can avoid this process and therefore, no deep defects related to Ge_{Cu} or Sn_{Cu} and higher device performance is observed as could be illustrated by

$$V_{Cu} + Sn_{Sn} + Ge + \boldsymbol{Na} \rightarrow Ge_{Sn} + Sn_{sn} + \boldsymbol{Na_{Cu}} \quad (5.9)$$

or

$$V_{Cu} + Ge + \boldsymbol{Na} \rightarrow \boldsymbol{Na_{Cu}} + Ge \quad (5.10)$$

The observed increased doping density for the Ge+Na device can be explained by the reduced formation of compensating donor defects, and additional due to the expected higher Na amount in the absorber, which is known to increase doping of kesterite absorbers and as also observed here makes acceptor defects shallower.[87] Therefore, for the optimum Ge doping range of around 10 nm Ge, it is reasonable to assume that the right amount of Ge added during synthesis on one hand avoids the formation of V_{Sn} or Cu_{Sn} antisites which could form due to Sn loss and furthermore moderates the Na amount inside the final absorber layer.

5.2.3 Conclusions

A detailed study investigating the beneficial effects of Ge doping on device performance has been presented. For the optimal Ge amount provided during synthesis (i.e. around 10 nm), an large increase in V_{oc} is observed, which can be explained by an increase in doping density as well as a reduction of recombination due to the fact that the formation of deep defects is avoided as evidenced by admittance spectroscopy. For the device without Ge doping as well as for the one synthesized with the addition of a high Ge amount (50 nm) deep midgap defects have been found as possible reason for lower device performance and especially lower V_{oc} deficit. These defects could potentially be assigned to V_{Sn} or Cu_{Sn} antisites caused due to Sn loss, or Sn_{Cu} or Ge_{Cu} antisites formed due to element IV rich growth conditions. Controlled Ge addition in low quantities could avoid the formation of these defects by compensating possible Sn loss, besides the beneficial effects on grain growth due to the formation of liquid Ge-Se phase as discussed in Chapter 5.1 and shown in Giraldo et al.[67] Furthermore, the quenching of efficiency at low temperatures commonly reported in kesterite device is not observed for optimal range of Ge doping, thus the device behaviour gets more similar to that of high performance CIGS solar cells.[113]
PL of all three samples show similar behavior, with QDAP transition at low temperature up to 250 K and BI transitions at RT. The energy level of acceptor level involved in the BI transition of 58-79 meV agrees well with the values obtained from admittance spectroscopy of the 10 nm Ge sample. From fitting of the temperature dependent integrated PL intensity associated to the QDAP transition a donor level between 70-119 meV was found and the activation energy associated with the valley depth of potential fluctuations only changes slightly between the samples suggesting no significant influence of Ge doping on band tails as also observed from EQE measurements.
Furthermore, a clear interaction of Ge and Na has been demonstrated. Excessive Na addition to samples synthesized under Ge rich condition could avoid the formation of deep defects formed normally under this growth conditions. Therefore, Ge added during synthesis seems to moderate the Na content in the final absorber, which could explain the increase of doping observed for the optimal Ge range of 10 nm. In summary a careful control of group IV element content (Ge, Sn) is necessary during the growth of kesterite absorbers to avoid the formation of deep defects which are detrimental for device performance and especially V_{oc}. This could be either achieved by controlled Ge doping or by additionally supply of Na, which as has been demonstrated hinder the formation of detrimental deep defects.

6 CONCLUSIONS AND OUTLOOK

The main objective of this thesis was to develop strategies for the optimization of kesterite based heterostructure solar cells by PVD and chemical based processes. Special focus is put on an improved understanding of the influence of the surface properties of kesterite absorbers on device performance and furthermore to optimize the front interface, i.e. buffer layer as well as the kesterite absorber layer itself. Detailed device characterization is carried out to gain a deeper knowledge of the current bottlenecks of kesterite technology and to develop strategies and processing steps to eliminate possible efficiency limiting factors. The results obtain in this thesis have been published as articles in high impact peer-review journals.

First, a detailed study of the influence of surface chemistry on device performance is presented. After a chemical etching to remove unwanted ZnSe secondary phases formed during absorber synthesis, a low temperature post deposition annealing has to be carried out to increase solar cell performance from below 3% to over 8%. Different post deposition annealing conditions were investigated and an annealing of the full solar cell at 200ºC for around 30 minutes was found the best. The improved device performance could be attributed to changes in the different functional layers of the heterostructure solar cell. PL and EQE evidenced improvements in the CdS buffer as well as TCO window layer, however, main changes were found in the CZTSe absorber layer itself. Advanced characterization methods like XPS and TEM were used to gain information about possible changes in the absorber. An in-situ XPS annealing experiments revealed that after chemical etching the surface composition is similar to the one of the bulk, however, by performing a 200ºC annealing the surface gets Zn-richer and Cu-poorer. The necessity of a Cu-poor and Zn-enricher surface for high device performance was confirmed by investigating absorber layers with artificially Cu, Zn or Sn enriched surfaces and different chemical surface treatments. A Cu-poor Zn-rich surface favours the formation of $[V_{Cu}+Zn_{Cu}]$ defect clusters, which increase the band bending and facilitate the separation of light generated electron hole pairs. Furthermore, TEM investigation found a significant amount of Cu diffusing into the CdS layer, which further helps to create a Cu depleted absorber surface and TEM showed that grain boundaries tent to be Cu-rich prior to the annealing treatment which is not obvious after the annealing. Cu-rich grain boundaries are suspected to be detrimental because they can locally change the bandgap and increase recombination. On the whole this study demonstrated the importance of the absorber surface chemistry for device performance and how new processing routes like post

deposition annealings and surface etchings can be used to tailor the absorber surface and led to grain boundary passivation.
The second front interface optimization presented was focused on the CdS buffer layer. In-depth device characterization found problems related to the CdS buffer layer, like a pronounced dark light JV curve crossover and a JV curve distortion when illuminated with long wavelength photons (red kink), which could be related to charged defects in the CdS layer, most likely cadmium vacancies, which modify the band alignment. Light soaking can partly decrease these effects and improve efficiencies. Optimizing the CdS deposition process by changing the cadmium precursor salt which led to a more controlled and homogeneous growth largely improved the crossover and red kink. This optimized CdS buffer layer allowed to obtain devices with high FF and device performance could be improved by about 1% absolute compared to the former standard CdS deposition process.
However, the replacement of toxic components of solar cells like the CdS buffer layer is of utmost interest for the solar cell research, since the chances for commercialization are nowadays more and more linked to greener and sustainable products. In the last part of the front interface optimization a study of the potential use of non-toxic ZnS(O,OH) as buffer layers is presented. By changing the thiourea concentration, i.e. sulphur source, in the chemical bath deposition process of ZnS(O,OH) films, the S/O ratio of the final layers could be modified. Therefore, the band alignment of ZnS(O,OH) buffer and CZTSe absorber could be optimized. This allowed obtaining device efficiencies close to that of CdS reference cells.

Besides front interface optimization intensive work on improving the CZTSe absorber layer itself was carried out as well. A Ge assisted crystallization process for nanocrystalline precursor materials was developed which largely increase grain size as well as improved device performance and especially V_{oc}. In-depth device and defect characterization was carried out to get insights in the beneficial effects of this Ge assisted crystallization. On the one hand the Ge present during crystallization in selenium atmosphere forms a Ge-Se liquid phase which assists grain growth. Furthermore, small Ge amounts added avoid the formation of deep defects. These defects could be related to Sn antisites or vacancy defects formed due to Sn loss during crystallization. Ge can compensate Sn loss, however, if too large amounts of Ge/Sn are provided during crystallization other detrimental deep defect, most likely Ge_{Cu} or Sn_{Cu} antisites can form and decrease device performance. Additionally, a clear interaction of Na and Ge was evidenced. Ge seems to moderate the Na content in the absorber and by supplying excessive Na additionally to high Ge amounts during crystallization the formation of deep defects could be reduced. The Ge doping process developed allowed an accurate control of the group IV elemental (Ge/Sn) composition during crystallization and enabled to obtain device efficiencies of up to 8.6% with V_{oc} values over 470 mV that corresponds to V_{oc} deficits ($E_g/q - V_{oc}$) below 580 mV comparable to current record devices.

On the whole this thesis showed the importance of the absorber surface properties and that by optimizing the buffer layer - either CdS as well as Cd-free alternatives - to the kesterite absorber properties device performance could largely be improved. Furthermore, the importance of group IV elemental composition as well as Na content during crystallization was demonstrated to avoid the formation of deep detrimental defects. All this optimizations led to large improvements in device performance for solar cells, grown by two step process developed at IREC. Still the efficiency values obtained are lower than the current world record of 12.6% but V_{oc} values and V_{oc} deficits are close to that of current record devices. Nevertheless, there is still a large gap between kesterite and its already commercialized close cousin CIGS. Especially the high V_{oc} deficit is the main limitation of kesterite technology. One main reason for low V_{oc} values might be the presence of large band tails. Since defects related to Sn are mostly responsible for deep defects, Cu and Zn antisites and disorder might be one reason for tail states, as they could either led to bandgap or potential fluctuation that create a non-zero density of states in the bandgap which reduce V_{oc}. The partly replacement of one of this elements might be a future way to reduce this unfavourable tail states and improve device performance. Furthermore, a careful control of alkali elements is mandatory to accurately control the doping levels of the absorber as well as develop a reproducible process. Further improvements may be inspired from methods used in CIGS technology like bandgap gradients as well as the use of passivation layer in the front/back interface and selective contacts that show a more favourable band alignment which hopefully will help to increase solar cell performance of this promising earth abound photovoltaic absorber material in near future.

7 APPENDICES

MATERIAL REQUIREMENTS FOR DIFFERENT ABSORBER LAYER

CdTe:

Zinc blend crystal structure with lattice parameter a=6.48Å[148] and assuming stoichiometry 4 Cd and 4 Te atoms per unit cell.
Relative atomic weight:
ArCd = 112.41 u
ArTe = 127.6 u

Density:

$$\rho = \frac{(4 * 112.41 * u + 4 * 127.6 * u)}{a^3} = 5859\ kg/m^3$$

Contributions of each element:
Cd:

$$\frac{4 * 112.41 * u}{(4 * 112.41 * u + 4 * 127.6 * u)} = 46.8\%$$

Te:

$$\frac{4 * 112.41 * u}{(4 * 112.41 * u + 4 * 127.6 * u)} = 53.2\%$$

Assuming a absorber thickness of 2µm:
Material requirements of Cd:

$$5859 \frac{kg}{m^3} * 2.10^{-10} m * 0.468 = 0.00548 \frac{kg}{m^2} = 5.48\ \frac{g}{m^2}$$

Material requirements of Te:

$$5859 \frac{kg}{m^3} * 2.10^{-10} m * 0.532 = 0.00623 \frac{kg}{m^2} = 6.23 \frac{g}{m^2}$$

A 14% PV module corresponds to 140 W_p/m^2
For Cd:

$$\rightarrow \frac{0.00548\ \frac{kg}{m^2}}{140 * 10^{-9} \frac{GWp}{m^2}} = 39 \frac{t}{GWp}$$

For Te:

$$\rightarrow \frac{0.00623\ \frac{kg}{m^2}}{140 * 10^{-9} \frac{GWp}{m^2}} = 44 \frac{t}{GWp}$$

CIGS:

Tetragonal crystal structure with 4 Cu and 4 In/Ga and 8 Se atoms per unit cell.
Assuming a Ga/(Ga+In) ratio of 0.3, i.e. $CuIn_{0.7}Ga_{0.3}Se_2$ composition similar to record efficiency devices[88] and lattice parameters of[149]
a=5.74Å
c=11.35Å

Relative atomic weight:
ArCu = 63.546 u
ArIn = 114.814 u
ArGa = 69.723 u
ArSe= 78.97 u

Density:

$$\rho = \frac{(4 * \mathrm{ArCu} * u + 4 * 0.7 * \mathrm{ArIn} * u + 4 * 0.3 * \mathrm{ArGa} * u + 8 * \mathrm{ArSe} * u)}{a^2 * c} = 5733\ kg/m^3$$

Contributions of each element:
Cu=19.7%
In=24.9%
Ga=6.5%
Se=48.9%

Assuming a absorber thickness of 2µm the material requirements are the same as for CdTe case.

CZTSe:
Tetragonal crystal structure with 4 Cu, 2 Zn 2Sn and 8 Se atoms per unit cell for stoichiometric sample with lattice parameters[29].
a=5.695Å
c=11.345Å

Relative atomic weight:
ArZn = 65.38 u
ArSn = 118.71 u

Density:

$$\rho = \frac{(4 * \mathrm{ArCu} * u + 2 * \mathrm{ArZn} * u + 2 * \mathrm{ArSn} * u + 8 * \mathrm{ArSe} * u)}{a^2 * c} = 5660\ kg/m^3$$

Contributions of each element to density:
Cu=20.3%
Zn=10.4%
Sn=18.9%
Se=50.4%

REFERENCES

(1) Pachauri, R. K.; Allen, M. R.; Barros, V. R.; Broome, J.; Cramer, W.; Christ, R.; Church, J. A.; Clarke, L.; Dahe, Q.; Dasgupta, P.; others. Climate Change 2014: Synthesis Report. Contribution of Working Groups I, II and III to the Fifth Assessment Report of the Intergovernmental Panel on Climate Change. **2014**.

(2) *Energy and Climate Change*; World Energy Outlook Special Report; iea - International Energy Agency, 2015.

(3) OCDE, O. *World Energy Outlook 2015*; OECD Publishing, 2015.

(4) *Renewables 2015 Global Status Report*; REN21, 2015.

(5) Jäger-Waldau, A.; European Commission; Joint Research Centre; Institute for Energy and Transport. *PV Status Report 2014*; Publications Office: Luxembourg, 2014.

(6) Taylor, N.; Szabo, S.; Kona, A.; Melica, G.; Huld, T.; Jäger-Waldau, A.; Ossenbrink, H. DEPLOYMENT PATHWAYS FOR PHOTOVOLTAICS IN THE EU TOWARDS 2020: COMPARING ECONOMIC FACTORS WITH POLICIES AT MUNICIPAL LEVEL. **2015**.

(7) Ossenbrink, H.; Jäger-Waldau, A.; Taylor, A.; Szabo, S.; Huld, T.; Dunlop, E. TOWARDS A EUROPEAN UNION OF PHOTOVOLTAIC SOLAR ELECTRICITY. *31st EU-PVSEC* **2015**.

(8) Huld, T.; Waldau, A. J.; Ossenbrink, H.; Szabo, S.; Dunlop, E.; Taylor, N. Cost Maps for Unsubsidised Photovoltaic Electricity. *Eur. Comm.* **2014**.

(9) eurostat. *Electricity Price Statistics for 1 Semester 2015*; 2015.

(10) Jäger-Waldau, A. Does Europe Abandon Photovoltaics? *european energy innovation - autumn* **2015**, 59–62.

(11) Masuko, K.; Shigematsu, M.; Hashiguchi, T.; Fujishima, D.; Kai, M.; Yoshimura, N.; Yamaguchi, T.; Ichihashi, Y.; Mishima, T.; Matsubara, N.; Yamanishi, T.; Takahama, T.; Taguchi, M.; Maruyama, E.; Okamoto, S. Achievement of More Than 25&#x0025; Conversion Efficiency With Crystalline Silicon Heterojunction Solar Cell. *IEEE J. Photovolt.* **2014**, *4* (6), 1433–1435.

(12) Bhandari, K. P.; Collier, J. M.; Ellingson, R. J.; Apul, D. S. Energy Payback Time (EPBT) and Energy Return on Energy Invested (EROI) of Solar Photovoltaic Systems: A Systematic Review and Meta-Analysis. *Renew. Sustain. Energy Rev.* **2015**, *47*, 133–141.

(13) Green, M. A.; Emery, K.; Hishikawa, Y.; Warta, W.; Dunlop, E. D. Solar Cell Efficiency Tables (Version 47): Solar Cell Efficiency Tables. *Prog. Photovolt. Res. Appl.* **2016**, *24* (1), 3–11.

(14) Deng, W.; Chen, D.; Xiong, Z.; Verlinden, P. J.; Dong, J.; Ye, F.; Li, H.; Zhu, H.; Zhong, M.; Yang, Y.; Chen, Y.; Feng, Z.; Altermatt, P. 20.8&#x0025; PERC Solar Cell on 156 Mm &#x00D7; 156 Mm P-Type Multicrystalline Silicon Substrate. *IEEE J. Photovolt.* **2016**, *6* (1), 3–9.

(15) FirstSolar. *First Solar Achieves Yet Another Cell Conversion Efficiency World Record*; 2016.

(16) FirstSolar. *First Solar Achieves World Record 18.6 % Thin Film Module Conversion Efficiency*; 2015.

(17) Solar Frontier. *Solar Frontier Achieves World Record Thin-Film Solar Cell Efficiency: 22.3%*; 2015.

(18) Raugei, M.; Fullana-i-Palmer, P.; Fthenakis, V. The Energy Return on Energy Investment (EROI) of Photovoltaics: Methodology and Comparisons with Fossil Fuel Life Cycles. *Energy Policy* **2012**, *45*, 576–582.

(19) *Fraunhofer ISE: Photovoltaics Report, Updated: 11 March 2016*.

(20) WHITE PAPER FOR CIGS THIN FILM SOLAR CELL TECHNOLOGY. **2015**.

(21) Hans Wedepohl, K. The Composition of the Continental Crust. *Geochim. Cosmochim. Acta* **1995**, *59* (7), 1217–1232.

(22) Marwede, M.; Reller, A. Future Recycling Flows of Tellurium from Cadmium Telluride Photovoltaic Waste. *Resour. Conserv. Recycl.* **2012**, *69*, 35–49.

(23) Goldfarb, R. J. *Tellurium: The Bright Future of Solar Energy*; US Department of the Interior, US Geological Survey, 2014.

(24) *Mineral Commodities Summaries*; U.S. Geological Survey; 2016.

(25) Wang, W.; Winkler, M. T.; Gunawan, O.; Gokmen, T.; Todorov, T. K.; Zhu, Y.; Mitzi, D. B. Device Characteristics of CZTSSe Thin-Film Solar Cells with 12.6% Efficiency. *Adv. Energy Mater.* **2014**, *4* (7), n/a-n/a.

(26) Ito, K.; Nakazawa, T. Electrical and Optical Properties of Stannite-Type Quaternary Semiconductor Thin Films. *Jpn. J. Appl. Phys.* **1988**, *27* (Part 1, No. 11), 2094–2097.

(27) Katagiri, H.; Jimbo, K.; Yamada, S.; Kamimura, T.; Maw, W. S.; Fukano, T.; Ito, T.; Motohiro, T. Enhanced Conversion Efficiencies of Cu_2ZnSnS_4-Based Thin Film Solar Cells by Using Preferential Etching Technique. *Appl. Phys. Express* **2008**, *1*, 41201.

(28) Barkhouse, D. A. R.; Gunawan, O.; Gokmen, T.; Todorov, T. K.; Mitzi, D. B. Device Characteristics of a 10.1% Hydrazine-Processed Cu2ZnSn(Se,S)4 Solar Cell: Characteristics of a 10.1% Efficient Kesterite Solar Cell. *Prog. Photovolt. Res. Appl.* **2012**, *20* (1), 6–11.

(29) Siebentritt, S.; Schorr, S. Kesterites-a Challenging Material for Solar Cells: Kesterites-a Challenging Material for Solar Cells. *Prog. Photovolt. Res. Appl.* **2012**, *20* (5), 512–519.

(30) Hall, S. R.; Szymanski, J. T.; Stewart, J. M. Kesterite, Cu2(Zn,Fe)SnS4 , and Stannite, Cu2(Fe,Zn)SnS4 , Structurally Similar but Distinct Minerals. *Can. Mineral.* **1978**, *16* (2), 131–137.

(31) Schorr, S. The Crystal Structure of Kesterite Type Compounds: A Neutron and X-Ray Diffraction Study. *Sol. Energy Mater. Sol. Cells* **2011**, *95* (6), 1482–1488.

(32) Paris, M.; Choubrac, L.; Lafond, A.; Guillot-Deudon, C.; Jobic, S. Solid-State NMR and Raman Spectroscopy To Address the Local Structure of Defects and the Tricky Issue of the Cu/Zn Disorder in Cu-Poor, Zn-Rich CZTS Materials. *Inorg. Chem.* **2014**, *53* (16), 8646–8653.

(33) Scragg, J. J. S.; Choubrac, L.; Lafond, A.; Ericson, T.; Platzer-Björkman, C. A Low-Temperature Order-Disorder Transition in Cu2ZnSnS4 Thin Films. *Appl. Phys. Lett.* **2014**, *104* (4), 41911.

(34) Rey, G.; Redinger, A.; Sendler, J.; Weiss, T. P.; Thevenin, M.; Guennou, M.; El Adib, B.; Siebentritt, S. The Band Gap of Cu2ZnSnSe4: Effect of Order-Disorder. *Appl. Phys. Lett.* **2014**, *105* (11), 112106.

(35) Shockley, W.; Queisser, H. J. Detailed Balance Limit of Efficiency of P-N Junction Solar Cells. *J. Appl. Phys.* **1961**, *32* (3), 510.

(36) Xie, H.; Dimitrievska, M.; Fontané, X.; Sánchez, Y.; López-Marino, S.; Izquierdo-Roca, V.; Bermúdez, V.; Pérez-Rodríguez, A.; Saucedo, E. Formation and Impact of Secondary Phases in Cu-Poor Zn-Rich Cu2ZnSn(S1−ySey)4 (0≤y≤1) Based Solar Cells. *Sol. Energy Mater. Sol. Cells* **2015**, *140*, 289–298.

(37) Chen, S.; Walsh, A.; Yang, J.-H.; Gong, X. G.; Sun, L.; Yang, P.-X.; Chu, J.-H.; Wei, S.-H. Compositional Dependence of Structural and Electronic Properties of Cu 2 ZnSn(S,Se) 4 Alloys for Thin Film Solar Cells. *Phys. Rev. B* **2011**, *83* (12).

(38) Polizzotti, A.; Repins, I. L.; Noufi, R.; Wei, S.-H.; Mitzi, D. B. The State and Future Prospects of Kesterite Photovoltaics. *Energy Environ. Sci.* **2013**.

(39) Fairbrother, A.; Dimitrievska, M.; Sánchez, Y.; Izquierdo-Roca, V.; Pérez-Rodríguez, A.; Saucedo, E. Compositional Paradigms in Multinary Compound Systems for Photovoltaic Applications: A Case Study of Kesterites. *J Mater Chem A* **2015**, *3* (18), 9451–9455.

(40) Todorov, T.; Gunawan, O.; Chey, S. J.; de Monsabert, T. G.; Prabhakar, A.; Mitzi, D. B. Progress towards Marketable Earth-Abundant Chalcogenide Solar Cells. *Thin Solid Films* **2011**, *519* (21), 7378–7381.

(41) Valle Rios, L. E.; Neldner, K.; Gurieva, G.; Schorr, S. Existence of off-Stoichiometric Single Phase Kesterite. *J. Alloys Compd.* **2016**, *657*, 408–413.

(42) Lafond, A.; Choubrac, L.; Guillot-Deudon, C.; Deniard, P.; Jobic, S. Crystal Structures of Photovoltaic Chalcogenides, an Intricate Puzzle to Solve: The Cases of CIGSe and CZTS Materials. *Z. Für Anorg. Allg. Chem.* **2012**, *638* (15), 2571–2577.

(43) Choubrac, L.; Lafond, A.; Guillot-Deudon, C.; Moëlo, Y.; Jobic, S. Structure Flexibility of the Cu_2ZnSnS_4 Absorber in Low-Cost Photovoltaic Cells: From the Stoichiometric to the Copper-Poor Compounds. *Inorg. Chem.* **2012**, *51* (6), 3346–3348.

(44) Chen, S.; Walsh, A.; Gong, X.-G.; Wei, S.-H. Classification of Lattice Defects in the Kesterite Cu_2ZnSnS_4 and $Cu_2ZnSnSe_4$ Earth-Abundant Solar Cell Absorbers. *Adv. Mater.* **2013**, *25* (11), 1522–1539.

(45) Schorr, S.; Hoebler, H.-J.; Tovar, M. A Neutron Diffraction Study of the Stannite-Kesterite Solid Solution Series. *Eur. J. Mineral.* **2007**, *19* (1), 65–73.

(46) Choubrac, L.; Paris, M.; Lafond, A.; Guillot-Deudon, C.; Rocquefelte, X.; Jobic, S. Multinuclear (67Zn, 119Sn and 65Cu) NMR Spectroscopy – an Ideal Technique to Probe the Cationic Ordering in Cu2ZnSnS4 Photovoltaic Materials. *Phys. Chem. Chem. Phys.* **2013**, *15* (26), 10722.

(47) Scragg, J. J. S.; Larsen, J. K.; Kumar, M.; Persson, C.; Sendler, J.; Siebentritt, S.; Platzer Björkman, C. Cu-Zn Disorder and Band Gap Fluctuations in $Cu_2ZnSn(S,Se)_4$: Theoretical and Experimental Investigations: Cu-Zn Disorder and Band Gap Fluctuations in $Cu_2ZnSn(S,Se)_4$. *Phys. Status Solidi B* **2016**, *253* (2), 247–254.

(48) Gokmen, T.; Gunawan, O.; Mitzi, D. B. Semi-Empirical Device Model for Cu2ZnSn(S,Se)4 Solar Cells. *Appl. Phys. Lett.* **2014**, *105* (3), 33903.

(49) Bourdais, S.; Choné, C.; Delatouche, B.; Jacob, A.; Larramona, G.; Moisan, C.; Lafond, A.; Donatini, F.; Rey, G.; Siebentritt, S.; Walsh, A.; Dennler, G. Is the Cu/Zn Disorder the Main Culprit for the Voltage Deficit in Kesterite Solar Cells? *Adv. Energy Mater.* **2016**.

(50) Rey, G.; Weiss, T. P.; Sendler, J.; Finger, A.; Spindler, C.; Werner, F.; Melchiorre, M.; Hála, M.; Guennou, M.; Siebentritt, S. Ordering Kesterite Improves Solar Cells: A Low Temperature Post-Deposition Annealing Study. *Sol. Energy Mater. Sol. Cells* **2016**, *151*, 131–138.

(51) Huang, D.; Persson, C. Band Gap Change Induced by Defect Complexes in Cu2ZnSnS4. *Thin Solid Films* **2013**, *535*, 265–269.

(52) Yee, Y. S.; Magyari-Köpe, B.; Nishi, Y.; Bent, S. F.; Clemens, B. M. Deep Recombination Centers in C U 2 ZnSnS E 4 Revealed by Screened-Exchange Hybrid Density Functional Theory. *Phys. Rev. B* **2015**, *92* (19).

(53) Siebentritt, S. Why Are Kesterite Solar Cells Not 20% Efficient? *Thin Solid Films* **2013**, *535*, 1–4.

(54) Altamura, G.; Vidal, J. Impact of Minor Phases on the Performances of CZTSSe Thin Film Solar Cells. *Chem. Mater.* **2016**.

(55) Dimitrievska, M.; Fairbrother, A.; Saucedo, E.; Pérez-Rodríguez, A.; Izquierdo-Roca, V. Secondary Phase and Cu Substitutional Defect Dynamics in Kesterite Solar Cells: Impact on Optoelectronic Properties. *Sol. Energy Mater. Sol. Cells* **2016**, *149*, 304–309.

(56) López-Marino, S.; Sánchez, Y.; Placidi, M.; Fairbrother, A.; Espindola-Rodríguez, M.; Fontané, X.; Izquierdo-Roca, V.; López-García, J.; Calvo-Barrio, L.; Pérez-Rodríguez, A.; Saucedo, E. ZnSe Etching of Zn-Rich Cu2ZnSnSe4: An Oxidation Route for Improved Solar-Cell Efficiency. *Chem. – Eur. J.* **2013**, *19* (44), 14814–14822.

(57) Repins, I.; Beall, C.; Vora, N.; DeHart, C.; Kuciauskas, D.; Dippo, P.; To, B.; Mann, J.; Hsu, W.-C.; Goodrich, A.; Noufi, R. Co-Evaporated Cu2ZnSnSe4 Films and Devices. *Sol. Energy Mater. Sol. Cells* **2012**, *101*, 154–159.

(58) Fairbrother, A.; García-Hemme, E.; Izquierdo-Roca, V.; Fontané, X.; Pulgarín-Agudelo, F. A.; Vigil-Galán, O.; Pérez-Rodríguez, A.; Saucedo, E. Development of a

Selective Chemical Etch To Improve the Conversion Efficiency of Zn-Rich Cu $_2$ ZnSnS $_4$ Solar Cells. *J. Am. Chem. Soc.* **2012**, *134* (19), 8018–8021.

(59) Hsu, W.-C.; Repins, I.; Beall, C.; DeHart, C.; Teeter, G.; To, B.; Yang, Y.; Noufi, R. The Effect of Zn Excess on Kesterite Solar Cells. *Sol. Energy Mater. Sol. Cells* **2013**, *113*, 160–164.

(60) Xie, H.; Sánchez, Y.; López-Marino, S.; Espíndola-Rodríguez, M.; Neuschitzer, M.; Sylla, D.; Fairbrother, A.; Izquierdo-Roca, V.; Pérez-Rodríguez, A.; Saucedo, E. Impact of Sn(S,Se) Secondary Phases in Cu $_2$ ZnSn(S,Se) $_4$ Solar Cells: A Chemical Route for Their Selective Removal and Absorber Surface Passivation. *ACS Appl. Mater. Interfaces* **2014**, *6* (15), 12744–12751.

(61) Haass, S. G.; Diethelm, M.; Werner, M.; Bissig, B.; Romanyuk, Y. E.; Tiwari, A. N. 11.2% Efficient Solution Processed Kesterite Solar Cell with a Low Voltage Deficit. *Adv. Energy Mater.* **2015**, n/a-n/a.

(62) Schnabel, T.; Löw, M.; Ahlswede, E. Vacuum-Free Preparation of 7.5% Efficient $Cu_2ZnSn(S,Se)_4$ Solar Cells Based on Metal Salt Precursors. *Sol. Energy Mater. Sol. Cells* **2013**, *117*, 324–328.

(63) Guo, Q.; Ford, G. M.; Yang, W.-C.; Walker, B. C.; Stach, E. A.; Hillhouse, H. W.; Agrawal, R. Fabrication of 7.2% Efficient CZTSSe Solar Cells Using CZTS Nanocrystals. *J. Am. Chem. Soc.* **2010**, *132* (49), 17384–17386.

(64) Miskin, C. K.; Yang, W.-C.; Hages, C. J.; Carter, N. J.; Joglekar, C. S.; Stach, E. A.; Agrawal, R. 9.0% Efficient Cu $_2$ ZnSn(S,Se) $_4$ Solar Cells from Selenized Nanoparticle Inks: 9.2% Efficient Cu $_2$ ZnSn(S,Se) $_4$ Solar Cells. *Prog. Photovolt. Res. Appl.* **2015**, *23* (5), 654–659.

(65) Larramona, G.; Levcenko, S.; Bourdais, S.; Jacob, A.; Choné, C.; Delatouche, B.; Moisan, C.; Just, J.; Unold, T.; Dennler, G. Fine-Tuning the Sn Content in CZTSSe Thin Films to Achieve 10.8% Solar Cell Efficiency from Spray-Deposited Water-Ethanol-Based Colloidal Inks. *Adv. Energy Mater.* **2015**, *5* (24), n/a-n/a.

(66) Lee, Y. S.; Gershon, T.; Gunawan, O.; Todorov, T. K.; Gokmen, T.; Virgus, Y.; Guha, S. Cu $_2$ ZnSnSe $_4$ Thin-Film Solar Cells by Thermal Co-Evaporation with 11.6% Efficiency and Improved Minority Carrier Diffusion Length. *Adv. Energy Mater.* **2014**, n/a-n/a.

(67) Giraldo, S.; Neuschitzer, M.; Thersleff, T.; López-Marino, S.; Sánchez, Y.; Xie, H.; Colina, M.; Placidi, M.; Pistor, P.; Izquierdo-Roca, V.; Leifer, K.; Pérez-Rodríguez, A.; Saucedo, E. Large Efficiency Improvement in Cu $_2$ ZnSnSe $_4$ Solar Cells by Introducing a Superficial Ge Nanolayer. *Adv. Energy Mater.* **2015**, n/a-n/a.

(68) Brammertz, G.; Buffière, M.; Oueslati, S.; ElAnzeery, H.; Messaoud, K. B.; Sahayaraj, S.; Köble, C.; Meuris, M.; Poortmans, J. Characterization of Defects in 9.7% Efficient Cu2ZnSnSe4-CdS-ZnO Solar Cells. *Appl. Phys. Lett.* **2013**, *103* (16), 163904.

(69) Redinger, A.; Berg, D. M.; Dale, P. J.; Siebentritt, S. The Consequences of Kesterite Equilibria for Efficient Solar Cells. *J. Am. Chem. Soc.* **2011**, *133* (10), 3320–3323.

(70) Weber, A.; Mainz, R.; Schock, H. W. On the Sn Loss from Thin Films of the Material System Cu–Zn–Sn–S in High Vacuum. *J. Appl. Phys.* **2010**, *107* (1), 13516.

(71) Scragg, J. J.; Ericson, T.; Kubart, T.; Edoff, M.; Platzer-Björkman, C. Chemical Insights into the Instability of Cu2ZnSnS4 Films during Annealing. *Chem. Mater.* **2011**, *23* (20), 4625–4633.

(72) Würfel, P.; Würfel, U. *Physics of Solar Cells: From Basic Principles to Advanced Concepts*; Wiley-VCH: Weinheim, 2009.

(73) Scheer, R.; Schock, H. W.; Wiley InterScience (Online service). *Chalcogenide Photovoltaics Physics, Technologies, and Thin Film Devices*; Wiley-VCH ; John Wiley [distributor]: Weinheim; Chichester, 2011.

(74) *Copper Zinc Tin Sulphide-Based Thin Film Solar Cells*; Ito, K., Ed.; John Wiley & Sons Inc: Hoboken, 2014.

(75) Minemoto, T.; Matsui, T.; Takakura, H.; Hamakawa, Y.; Negami, T.; Hashimoto, Y.; Uenoyama, T.; Kitagawa, M. Theoretical Analysis of the Effect of Conduction Band

Offset of window/CIS Layers on Performance of CIS Solar Cells Using Device Simulation. *Sol. Energy Mater. Sol. Cells* **2001**, *67* (1–4), 83–88.

(76) Gloeckler, M.; Sites, J. R. Efficiency Limitations for Wide-Band-Gap Chalcopyrite Solar Cells. *Thin Solid Films* **2005**, *480–481*, 241–245.

(77) Niemegeers, A.; Burgelman, M.; Vos, A. D. On the CdS/CuInSe2 Conduction Band Discontinuity. *Appl. Phys. Lett.* **1995**, *67* (6), 843–845.

(78) Haight, R.; Barkhouse, A.; Gunawan, O.; Shin, B.; Copel, M.; Hopstaken, M.; Mitzi, D. B. Band Alignment at the Cu_2ZnSn(S[sub x]Se[sub 1−x])[sub 4]/CdS Interface. *Appl. Phys. Lett.* **2011**, *98* (25), 253502.

(79) Li, J.; Wei, M.; Du, Q.; Liu, W.; Jiang, G.; Zhu, C. The Band Alignment at CdS/Cu2ZnSnSe4 Heterojunction Interface. *Surf. Interface Anal.* **2013**, *45* (2), 682–684.

(80) Polity, A.; Meyer, B. K.; Krämer, T.; Wang, C.; Haboeck, U.; Hoffmann, A. ZnO Based Ternary Transparent Conductors. *Phys. Status Solidi A* **2006**, *203* (11), 2867–2872.

(81) Platzer-Björkman, C.; Törndahl, T.; Abou-Ras, D.; Malmström, J.; Kessler, J.; Stolt, L. Zn(O,S) Buffer Layers by Atomic Layer Deposition in Cu(In,Ga)Se[sub 2] Based Thin Film Solar Cells: Band Alignment and Sulfur Gradient. *J. Appl. Phys.* **2006**, *100* (4), 44506.

(82) Rau, U.; Schmidt, M. Electronic Properties of ZnO/CdS/Cu (In, Ga) Se 2 Solar Cells—aspects of Heterojunction Formation. *Thin Solid Films* **2001**, *387* (1), 141–146.

(83) Scheer, R.; Messmann-Vera, L.; Klenk, R.; Schock, H.-W. On the Role of Non-Doped ZnO in CIGSe Solar Cells: Non-Doped ZnO in CIGSe Solar Cells. *Prog. Photovolt. Res. Appl.* **2012**, *20* (6), 619–624.

(84) Niles, D. W. Na Impurity Chemistry in Photovoltaic CIGS Thin Films: Investigation with X-Ray Photoelectron Spectroscopy. *J. Vac. Sci. Technol. Vac. Surf. Films* **1997**, *15* (6), 3044.

(85) Xie, H.; Lopez-Marino, S.; Olar, T.; Sánchez González, Y.; Neuschitzer, M.; Oliva, F.; Giraldo, S.; Izquierdo-Roca, V.; Lauermann, I.; Pérez-Rodríguez, A.; Saucedo, E. On the Impact of Na Dynamics at the Cu2ZnSn(S,Se)4/CdS Interface During Post Low Temperature Treatment of Absorbers. *ACS Appl. Mater. Interfaces* **2016**, *8* (7), 5017–5024.

(86) Chirilă, A.; Reinhard, P.; Pianezzi, F.; Bloesch, P.; Uhl, A. R.; Fella, C.; Kranz, L.; Keller, D.; Gretener, C.; Hagendorfer, H.; Jaeger, D.; Erni, R.; Nishiwaki, S.; Buecheler, S.; Tiwari, A. N. Potassium-Induced Surface Modification of Cu(In,Ga)Se2 Thin Films for High-Efficiency Solar Cells. *Nat. Mater.* **2013**, *12* (12), 1107–1111.

(87) Li, J. V.; Kuciauskas, D.; Young, M. R.; Repins, I. L. Effects of Sodium Incorporation in Co-Evaporated Cu2ZnSnSe4 Thin-Film Solar Cells. *Appl. Phys. Lett.* **2013**, *102* (16), 163905.

(88) Jackson, P.; Hariskos, D.; Wuerz, R.; Kiowski, O.; Bauer, A.; Friedlmeier, T. M.; Powalla, M. Properties of Cu(In,Ga)Se $_2$ Solar Cells with New Record Efficiencies up to 21.7%: Properties of Cu(In,Ga)Se $_2$ Solar Cells with New Record Efficiencies up to 21.7%. *Phys. Status Solidi RRL - Rapid Res. Lett.* **2015**, *9* (1), 28–31.

(89) Ahmed, S.; Reuter, K. B.; Gunawan, O.; Guo, L.; Romankiw, L. T.; Deligianni, H. A High Efficiency Electrodeposited Cu2ZnSnS4 Solar Cell. *Adv. Energy Mater.* **2012**, *2* (2), 253–259.

(90) López-Marino, S.; Sánchez, Y.; Espíndola-Rodríguez, M.; Alcobé, X.; Xie, H.; Neuschitzer, M.; Becerril, I.; Giraldo, S.; Dimitrievska, M.; Placidi, M.; Fourdrinier, L.; Izquierdo-Roca, V.; Pérez-Rodríguez, A.; Saucedo, E. Alkali Doping Strategies for Flexible and Light-Weight Cu $_2$ ZnSnSe $_4$ Solar Cells. *J Mater Chem A* **2016**.

(91) Lopez-Marino, S.; Espíndola-Rodríguez, M.; Sánchez, Y.; Alcobé, X.; Oliva, F.; Xie, H.; Neuschitzer, M.; Giraldo, S.; Placidi, M.; Caballero, R.; Izquierdo-Roca, V.; Pérez-Rodríguez, A.; Saucedo, E. The Importance of Back Contact Modification in Cu2ZnSnSe4 Solar Cells: The Role of a Thin MoO2 Layer. *Nano Energy* **2016**.

(92) Scragg, J. J.; Wätjen, J. T.; Edoff, M.; Ericson, T.; Kubart, T.; Platzer-Björkman, C. A Detrimental Reaction at the Molybdenum Back Contact in Cu $_2$ ZnSn(S,Se) $_4$ Thin-Film Solar Cells. *J. Am. Chem. Soc.* **2012**, *134* (47), 19330–19333.

(93) Scragg, J. J.; Dale, P. J.; Colombara, D.; Peter, L. M. Thermodynamic Aspects of the Synthesis of Thin-Film Materials for Solar Cells. *ChemPhysChem* **2012**, *13* (12), 3035–3046.

(94) Huang, T. J.; Yin, X.; Qi, G.; Gong, H. CZTS-Based Materials and Interfaces and Their Effects on the Performance of Thin Film Solar Cells: CZTS-Based Materials and Interfaces and Their Effects on the Performance of Thin Film Solar Cells. *Phys. Status Solidi RRL - Rapid Res. Lett.* **2014**, *9999* (9999), n/a-n/a.

(95) Liu, X.; Feng, Y.; Cui, H.; Liu, F.; Hao, X.; Conibeer, G.; Mitzi, D. B.; Green, M. The Current Status and Future Prospects of Kesterite Solar Cells: A Brief Review: Kesterite Solar Cells. *Prog. Photovolt. Res. Appl.* **2016**, n/a-n/a.

(96) López-Marino, S.; Placidi, M.; Pérez-Tomás, A.; Llobet, J.; Izquierdo-Roca, V.; Fontané, X.; Fairbrother, A.; Espíndola-Rodríguez, M.; Sylla, D.; Pérez-Rodríguez, A.; Saucedo, E. Inhibiting the absorber/Mo-Back Contact Decomposition Reaction in Cu2ZnSnSe4 Solar Cells: The Role of a ZnO Intermediate Nanolayer. *J. Mater. Chem. A* **2013**, *1* (29), 8338–8343.

(97) Shin, B.; Zhu, Y.; Bojarczuk, N. A.; Jay Chey, S.; Guha, S. Control of an Interfacial MoSe2 Layer in Cu2ZnSnSe4 Thin Film Solar Cells: 8.9% Power Conversion Efficiency with a TiN Diffusion Barrier. *Appl. Phys. Lett.* **2012**, *101* (5), 53903.

(98) Liu, F.; Sun, K.; Li, W.; Yan, C.; Cui, H.; Jiang, L.; Hao, X.; Green, M. A. Enhancing the Cu2ZnSnS4 Solar Cell Efficiency by Back Contact Modification: Inserting a Thin TiB2 Intermediate Layer at Cu2ZnSnS4/Mo Interface. *Appl. Phys. Lett.* **2014**, *104* (5), 51105.

(99) Rau, U.; Schock, H.-W. Electronic Properties of Cu (In, Ga) Se2 Heterojunction Solar Cells–recent Achievements, Current Understanding, and Future Challenges. *Appl. Phys. A* **1999**, *69* (2), 131–147.

(100) Sites, J. R.; Mauk, P. H. Diode Quality Factor Determination for Thin-Film Solar Cells. *Sol. Cells* **1989**, *27* (1), 411–417.

(101) Hegedus, S. S.; Shafarman, W. N. Thin-Film Solar Cells: Device Measurements and Analysis. *Prog. Photovolt. Res. Appl.* **2004**, *12* (2–3), 155–176.

(102) Pankove, J. I. *Optical Processes in Semiconductors*, Unabridged republication, with slight corr.; Dover: Mineola [NY], 1975.

(103) Hages, C. J.; Carter, N. J.; Agrawal, R. Generalized Quantum Efficiency Analysis for Non-Ideal Solar Cells: Case of Cu2ZnSnSe4. *J. Appl. Phys.* **2016**, *119* (1), 14505.

(104) Rau, U.; Abou-Ras, D.; Kirchartz, T. *Advanced Characterization Techniques for Thin Film Solar Cells*; Wiley-VCH: Weinheim, Germany, 2011.

(105) Paul Weiss, T.; Redinger, A.; Luckas, J.; Mousel, M.; Siebentritt, S. Admittance Spectroscopy in Kesterite Solar Cells: Defect Signal or Circuit Response. *Appl. Phys. Lett.* **2013**, *102* (20), 202105.

(106) Lauwaert, J.; Decock, K.; Khelifi, S.; Burgelman, M. A Simple Correction Method for Series Resistance and Inductance on Solar Cell Admittance Spectroscopy. *Sol. Energy Mater. Sol. Cells* **2010**, *94* (6), 966–970.

(107) Miller, G. L. A Feedback Method for Investigating Carrier Distributions in Semiconductors. *Electron Devices IEEE Trans. On* **1972**, *19* (10), 1103–1108.

(108) Heath, J. T. Bulk and Metastable Defects in CuIn[sub 1−x]Ga[sub x]Se[sub 2] Thin Films Using Drive-Level Capacitance Profiling. *J. Appl. Phys.* **2004**, *95* (3), 1000.

(109) Walter, T.; Herberholz, R.; Müller, C.; Schock, H. W. Determination of Defect Distributions from Admittance Measurements and Application to Cu(In,Ga)Se2 Based Heterojunctions. *J. Appl. Phys.* **1996**, *80* (8), 4411.

(110) Jasenek, A.; Rau, U.; Nadenau, V.; Schock, H. W. Electronic Properties of CuGaSe[sub 2]-Based Heterojunction Solar Cells. Part II. Defect Spectroscopy. *J. Appl. Phys.* **2000**, *87* (1), 594.

(111) Le Bail, A.; Duroy, H.; Fourquet, J. L. Ab-Initio Structure Determination of LiSbWO6 by X-Ray Powder Diffraction. *Mater. Res. Bull.* **1988**, *23* (3), 447–452.

(112) Dimitrievska, M.; Fairbrother, A.; Saucedo, E.; Pérez-Rodríguez, A.; Izquierdo-Roca, V. Secondary Phase and Cu Substitutional Defect Dynamics in Kesterite Solar Cells: Impact on Optoelectronic Properties. *Sol. Energy Mater. Sol. Cells* **2016**, *149*, 304–309.

(113) Kim, J.; Hiroi, H.; Todorov, T. K.; Gunawan, O.; Kuwahara, M.; Gokmen, T.; Nair, D.; Hopstaken, M.; Shin, B.; Lee, Y. S.; Wang, W.; Sugimoto, H.; Mitzi, D. B. High Efficiency $Cu_2ZnSn(S,Se)_4$ Solar Cells by Applying a Double In_2S_3/CdS Emitter. *Adv. Mater.* **2014**, n/a-n/a.

(114) Xin, H.; Vorpahl, S. M.; Collord, A. D.; Braly, I. L.; Uhl, A. R.; Krueger, B. W.; Ginger, D. S.; Hillhouse, H. W. Lithium-Doping Inverts the Nanoscale Electric Field at the Grain Boundaries in $Cu_2ZnSn(S,Se)_4$ and Increases Photovoltaic Efficiency. *Phys Chem Chem Phys* **2015**, *17* (37), 23859–23866.

(115) Yang, K.-J.; Son, D.-H.; Sung, S.-J.; Sim, J.-H.; Kim, Y.-I.; Park, S.-N.; Jeon, D.-H.; Kim, J.; Hwang, D.-K.; Jeon, C.-W.; Nam, D.; Cheong, H.; Kang, J.-K.; Kim, D.-H. A Band-Gap-Graded CZTSSe Solar Cell with 12.3% Efficiency. *J Mater Chem A* **2016**.

(116) Nakamura, M.; Yoneyama, N.; Horiguchi, K.; Iwata, Y.; Yamaguchi, K.; Sugimoto, H.; Kato, T. Recent R&D Progress in Solar Frontier's Small-Sized Cu (InGa)(SeS) 2 Solar Cells. In *Photovoltaic Specialist Conference (PVSC), 2014 IEEE 40th*; IEEE, 2014; pp 107–110.

(117) Gunawan, O.; Todorov, T. K.; Mitzi, D. B. Loss Mechanisms in Hydrazine-Processed Cu[sub 2]ZnSn(Se,S)[sub 4] Solar Cells. *Appl. Phys. Lett.* **2010**, *97* (23), 233506.

(118) Scragg, J. J.; Ericson, T.; Fontané, X.; Izquierdo-Roca, V.; Pérez-Rodríguez, A.; Kubart, T.; Edoff, M.; Platzer-Björkman, C. Rapid Annealing of Reactively Sputtered Precursors for Cu_2ZnSnS_4 Solar Cells: Rapid Annealing of Sputtered Precursors for Cu_2ZnSnS_4 Solar Cells. *Prog. Photovolt. Res. Appl.* **2014**, *22* (1), 10–17.

(119) Gokmen, T.; Gunawan, O.; Todorov, T. K.; Mitzi, D. B. Band Tailing and Efficiency Limitation in Kesterite Solar Cells. *Appl. Phys. Lett.* **2013**, *103* (10), 103506.

(120) Bär, M.; Schubert, B.-A.; Marsen, B.; Wilks, R. G.; Pookpanratana, S.; Blum, M.; Krause, S.; Unold, T.; Yang, W.; Weinhardt, L.; Heske, C.; Schock, H.-W. Cliff-like Conduction Band Offset and KCN-Induced Recombination Barrier Enhancement at the CdS/Cu2ZnSnS4 Thin-Film Solar Cell Heterojunction. *Appl. Phys. Lett.* **2011**, *99* (22), 222105.

(121) Terada, N.; Yoshimoto, S.; Chochi, K.; Fukuyama, T.; Mitsunaga, M.; Tampo, H.; Shibata, H.; Matsubara, K.; Niki, S.; Sakai, N.; Katou, T.; Sugimoto, H. Characterization of Electronic Structure of Cu2ZnSn(SxSe1−x)4 Absorber Layer and CdS/Cu2ZnSn(SxSe1−x)4 Interfaces by in-Situ Photoemission and Inverse Photoemission Spectroscopies. *Thin Solid Films* **2015**, *582*, 166–170.

(122) Rey, G.; Weiss, T. P.; Sendler, J.; Finger, A.; Spindler, C.; Werner, F.; Melchiorre, M.; Hála, M.; Guennou, M.; Siebentritt, S. Ordering Kesterite Improves Solar Cells: A Low Temperature Post-Deposition Annealing Study. *Sol. Energy Mater. Sol. Cells* **2016**, *151*, 131–138.

(123) Platzer-Björkman, C.; Frisk, C.; Larsen, J. K.; Ericson, T.; Li, S.-Y.; Scragg, J. J. S.; Keller, J.; Larsson, F.; Törndahl, T. Reduced Interface Recombination in Cu2ZnSnS4 Solar Cells with Atomic Layer Deposition Zn1−xSnxOy Buffer Layers. *Appl. Phys. Lett.* **2015**, *107* (24), 243904.

(124) Sun, K.; Yan, C.; Liu, F.; Huang, J.; Zhou, F.; Stride, J. A.; Green, M.; Hao, X. Over 9% Efficient Kesterite Cu_2ZnSnS_4 Solar Cell Fabricated by Using $Zn_{1-x}Cd_xS$ Buffer Layer. *Adv. Energy Mater.* **2016**.

(125) Repins, I. L.; Moutinho, H.; Choi, S. G.; Kanevce, A.; Kuciauskas, D.; Dippo, P.; Beall, C. L.; Carapella, J.; DeHart, C.; Huang, B.; Wei, S. H. Indications of Short Minority-Carrier Lifetime in Kesterite Solar Cells. *J. Appl. Phys.* **2013**, *114* (8), 84507.

(126) Wei, S.-Y.; Liao, Y.-C.; Hsu, C.-H.; Cai, C.-H.; Huang, W.-C.; Huang, M.-C.; Lai, C.-H. Achieving High Efficiency Cu2ZnSn(S,Se)4 Solar Cells by Non-Toxic Aqueous Ink: Defect Analysis and Electrical Modeling. *Nano Energy* **2016**, *26*, 74–82.
(127) Courel, M.; Pulgarín-Agudelo, F. A.; Andrade-Arvizu, J. A.; Vigil-Galán, O. Open-Circuit Voltage Enhancement in CdS/Cu2ZnSnSe4-Based Thin Film Solar Cells: A Metal–insulator–semiconductor (MIS) Performance. *Sol. Energy Mater. Sol. Cells* **2016**, *149*, 204–212.
(128) Siebentritt, S.; Rey, G.; Finger, A.; Regesch, D.; Sendler, J.; Weiss, T. P.; Bertram, T. What Is the Bandgap of Kesterite? *Sol. Energy Mater. Sol. Cells* **2015**.
(129) Urbach, F. The Long-Wavelength Edge of Photographic Sensitivity and of the Electronic Absorption of Solids. *Phys. Rev.* **1953**, *92* (5), 1324–1324.
(130) De Wolf, S.; Holovsky, J.; Moon, S.-J.; Löper, P.; Niesen, B.; Ledinsky, M.; Haug, F.-J.; Yum, J.-H.; Ballif, C. Organometallic Halide Perovskites: Sharp Optical Absorption Edge and Its Relation to Photovoltaic Performance. *J. Phys. Chem. Lett.* **2014**, *5* (6), 1035–1039.
(131) Grossberg, M.; Timmo, K.; Raadik, T.; Kärber, E.; Mikli, V.; Krustok, J. Study of Structural and Optoelectronic Properties of Cu2Zn(Sn1−xGex)Se4 (x=0 to 1) Alloy Compounds. *Thin Solid Films* **2015**, *582*, 176–179.
(132) Guc, M.; Levcenko, S.; Izquierdo-Roca, V.; Fontané, X.; Arushanov, E.; Pérez-Rodríguez, A. Polarized Raman Scattering Analysis of Cu2ZnSnSe4 and Cu2ZnGeSe4 Single Crystals. *J. Appl. Phys.* **2013**, *114* (19), 193514.
(133) Valakh, M. Y.; Kolomys, O. F.; Ponomaryov, S. S.; Yukhymchuk, V. O.; Babichuk, I. S.; Izquierdo-Roca, V.; Saucedo, E.; Perez-Rodriguez, A.; Morante, J. R.; Schorr, S.; Bodnar, I. V. Raman Scattering and Disorder Effect in Cu$_2$ZnSnS$_4$. *Phys. Status Solidi RRL - Rapid Res. Lett.* **2013**, *7* (4), 258–261.
(134) Caballero, R.; Garcia-Llamas, E.; Merino, J. M.; León, M.; Babichuk, I.; Dzhagan, V.; Strelchuk, V.; Valakh, M. Non-Stoichiometry Effect and Disorder in Cu2ZnSnS4 Thin Films Obtained by Flash Evaporation: Raman Scattering Investigation. *Acta Mater.* **2014**, *65*, 412–417.
(135) Kask, E.; Krustok, J.; Giraldo, S.; Neuschitzer, M.; López-Marino, S.; Saucedo, E. Temperature Dependent Electrical Characterization of Thin Film Cu$_2$ZnSnSe$_4$ Solar Cells. *J. Phys. Appl. Phys.* **2016**, *49* (8), 85101.
(136) Gunawan, O.; Gokmen, T.; Warren, C. W.; Cohen, J. D.; Todorov, T. K.; Barkhouse, D. A. R.; Bag, S.; Tang, J.; Shin, B.; Mitzi, D. B. Electronic Properties of the Cu2ZnSn(Se,S)4 Absorber Layer in Solar Cells as Revealed by Admittance Spectroscopy and Related Methods. *Appl. Phys. Lett.* **2012**, *100* (25), 253905.
(137) Mott, N. F. IMPURITY BAND CONDUCTION. EXPERIMENT AND THEORYTHE METAL-INSULATOR TRANSITION IN AN IMPURITY BAND. *J. Phys. Colloq.* **1976**, *37* (C4), C4–301.
(138) Kosyak, V.; Karmarkar, M. A.; Scarpulla, M. A. Temperature Dependent Conductivity of Polycrystalline Cu2ZnSnS4 Thin Films. *Appl. Phys. Lett.* **2012**, *100* (26), 263903.
(139) Hages, C. J.; Carter, N. J.; Agrawal, R.; Unold, T. Generalized Current-Voltage Analysis and Efficiency Limitations in Non-Ideal Solar Cells: Case of Cu2ZnSn(SxSe1−x)4 and Cu2Zn(SnyGe1−y)(SxSe1−x)4. *J. Appl. Phys.* **2014**, *115* (23), 234504.
(140) Yu, P. W. Excitation-Dependent Emission in Mg-, Be-, Cd-, and Zn-Implanted GaAs. *J. Appl. Phys.* **1977**, *48* (12), 5043.
(141) Levcenko, S.; Just, J.; Redinger, A.; Larramona, G.; Bourdais, S.; Dennler, G.; Jacob, A.; Unold, T. Deep Defects in Cu 2 ZnSn (S , Se) 4 Solar Cells with Varying Se Content. *Phys. Rev. Appl.* **2016**, *5* (2).
(142) Gershon, T.; Shin, B.; Gokmen, T.; Lu, S.; Bojarczuk, N.; Guha, S. Relationship between Cu2ZnSnS4 Quasi Donor-Acceptor Pair Density and Solar Cell Efficiency. *Appl. Phys. Lett.* **2013**, *103* (19), 193903.
(143) Gershon, T.; Shin, B.; Bojarczuk, N.; Gokmen, T.; Lu, S.; Guha, S. Photoluminescence Characterization of a High-Efficiency Cu2ZnSnS4 Device. *J. Appl. Phys.* **2013**, *114* (15), 154905.

(144) Lin, X.; Ennaoui, A.; Levcenko, S.; Dittrich, T.; Kavalakkatt, J.; Kretzschmar, S.; Unold, T.; Lux-Steiner, M. C. Defect Study of Cu2ZnSn(SxSe1−x)4 Thin Film Absorbers Using Photoluminescence and Modulated Surface Photovoltage Spectroscopy. *Appl. Phys. Lett.* **2015**, *106* (1), 13903.

(145) Luckert, F.; Hamilton, D. I.; Yakushev, M. V.; Beattie, N. S.; Zoppi, G.; Moynihan, M.; Forbes, I.; Karotki, A. V.; Mudryi, A. V.; Grossberg, M.; Krustok, J.; Martin, R. W. Optical Properties of High Quality Cu2ZnSnSe4 Thin Films. *Appl. Phys. Lett.* **2011**, *99* (6), 62104.

(146) Weiss, T. P.; Redinger, A.; Regesch, D.; Mousel, M.; Siebentritt, S. Direct Evaluation of Defect Distributions From Admittance Spectroscopy. *IEEE J. Photovolt.* **2014**, *4* (6), 1665–1670.

(147) Giraldo, S.; Neuschitzer, M.; Placidi, M.; Pistor, P.; Perez-Rodrıguez, A.; Saucedo, E. Cu2ZnSnSe4-Based Solar Cells With Efficiency Exceeding 10% by Adding a Superficial Ge Nanolayer: The Interaction Between Ge and Na. *IEEE JOURNAL OF PHOTOVOLTAICS 6* (3), 754–759.

(148) Suski, T.; Paul, W. *High Pressure in Semiconductor Physics. I I*; Academic Press: San Diego, 1998.

(149) Tinoco, T.; Rincón, C.; Quintero, M.; Pérez, G. S. Phase Diagram and Optical Energy Gaps for CuInyGa1- ySe2 Alloys. *Phys. Status Solidi A* **1991**, *124* (2), 427–434.